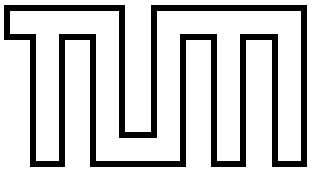

TECHNISCHE UNIVERSITÄT MÜNCHEN

MAX-PLANCK-INSTITUT
FÜR PHYSIK

Dissertation in Physics

Top Quark Threshold Scan and Study of Detectors for Highly Granular Hadron Calorimeters at Future Linear Colliders

Michal Tesař

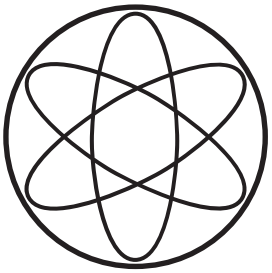

TECHNISCHE UNIVERSITÄT MÜNCHEN

MAX-PLANCK-INSTITUT
FÜR PHYSIK

Top Quark Threshold Scan and Study of Detectors for Highly Granular Hadron Calorimeters at Future Linear Colliders

Michal Tesař

Vollständiger Abdruck der von der Fakultät für Physik der Technischen Universität München zur Erlangung des akademischen Grades eines

Doktors der Naturwissenschaften (Dr. rer. nat.)

genehmigten Dissertation.

Vorsitzender:		Univ.-Prof. Dr. rer. nat. Martin Beneke
Prüfer der Dissertation:	1.	Hon.-Prof. Allen C. Caldwell, Ph. D.
	2.	Univ.-Prof. Dr. rer. nat. Laura Fabbietti

Die Dissertation wurde am 16.12.2013 bei der Technischen Universität München eingereicht und durch die Fakultät für Physik am 11.3.2014 angenommen.

I assure the single handed composition of this dissertation only supported by declared resources.

Munich, December 16, 2013 Michal Tesař

Abstract

Two major projects for future linear electron-positron colliders, the International Linear Collider (ILC) and the Compact Linear Collider (CLIC), are currently under development. These projects can be seen as complementary machines to the Large Hadron Collider (LHC) which permit a further progress in high energy physics research. They overlap considerably and share the same technological approaches. To meet the ambitious goals of precise measurements, new detector concepts like very finely segmented calorimeters are required.

We study the precision of the top quark mass measurement achievable at CLIC and the ILC. The employed method was a $t\bar{t}$ pair production threshold scan. In this technique, simulated measurement points of the $t\bar{t}$ production cross section around the threshold are fitted with theoretical curves calculated at next-to-next-to-leading order. Detector effects, the influence of the beam energy spectrum and initial state radiation of the colliding particles are taken into account. Assuming total integrated luminosity of $100\,\mathrm{fb}^{-1}$, our results show that the top quark mass in a theoretically well-defined $1S$ mass scheme can be extracted with a combined statistical and systematic uncertainty of less than 50 MeV.

The other part of this work regards experimental studies of highly granular hadron calorimeter (HCAL) elements. To meet the required high jet energy resolution at the future linear colliders, a large and finely segmented detector is needed. One option is to assemble a sandwich calorimeter out of many low-cost scintillators read out by silicon photomultipliers (SiPM). We characterize the areal homogeneity of SiPM response with the help of a highly collimated beam of pulsed visible light. The spatial resolution of the experiment reach the order of 1 μm and allows to study the active area structures within single SiPM microcells. Several SiPM models are characterized in terms of relative photon detection efficiency and probability crosstalk at the mentioned precision level.

The second experimental study investigates properties of plastic scintillators for an HCAL. Light collection homogeneity of square scintillator tiles with an area of a few cm^2 and a few mm in thickness is probed with a collimated electron beam from a radioactive ^{90}Sr source. The same experimental apparatus is used to quantify the light crosstalk between two neighboring scintillator cells. Two tile designs are tested and a high degree of homogeneity and low crosstalk level is demonstrated for one of the samples. Additionally, the sensitivity of the scintillators to neutrons is tested by irradiating the tiles with a ^{241}Am/Be neutron source. A substantial neutron sensitivity even with spectroscopic capabilities is observed. This measurement is compared with Monte Carlo simulation. A good agreement is demonstrated. It confirms that the experiment can be realistically described by taking into account only basic physical processes.

CONTENTS

PREFACE

The subject of particle physics is to study, understand and mathematically describe matter at subatomic scales. This comprises investigations of radiation, elements of matter itself and interactions between these constituents. A theoretical framework of particle physics was gradually developed, confronted with experimental reality and extended. A global scientific effort resulted in the second half of the 20th century in an extraordinarily successful theory called the Standard Model of particles physics. The last few decades of experimental research up to the present day are dedicated to confirm or disprove predictions and calculations based on the Standard Model. In spite of all the success of the theory, there are some inconsistencies with the observed physical reality. This leads to a further urge for theoretical extensions on one hand and experimental guidance by discoveries on the other hand. Highly precise measurements are one of the aims of particle accelerator experiments. A contemporary particle accelerator which is providing the most accurate data so far is the Large Hadron Collider (LHC) at CERN. Despite its great performance and the recent success of discovering a new particle which is likely the Higgs boson, a lepton collider experiment is in general capable of achieving an even better precision. A construction of a new lepton collider together with continual improvements of experimental methods and technology can contribute a lot to deepen our understanding of this material world.

There are two major future e^+e^- accelerator projects which are meant to be complementary machines to the LHC. These are the International Linear Collider (ILC) and the Compact Linear Collider (CLIC). Even though there are some significant differences between the two, many parts of the projects overlap and share the same technological approaches.

The goal of this thesis is to contribute to the ongoing research and development effort which will at the end results in a high-performance particle accelerator experiment. There are many aspects of such a project which have to be studied and prepared. In this work, we address two different topics with one common underlying connection.

Top quark physics is one of the important field of study at the LHC and also at future linear colliders (FLC). We present a simulation-based study of the FLC capability to perform precise measurements of the top quark mass. We determine the mass by using a threshold scan. It is based on the measurement of the $t\bar{t}$ pair production cross section in e^+e^- collisions in the vicinity of the threshold. The top mass itself was obtained from a

template fit of the cross section data. The study included also further unwanted physics and detector effects on the measurement. Statistical and systematic uncertainties of the top $1S$ mass determination at CLIC and the ILC were calculated and represent together the total uncertainty of the measurement. The strong coupling constant was also extracted by the template fit and its precision is presented as well.

A high jet energy resolution of a collider experiment is a crucial parameter for reaching a satisfactory top quark identification efficiency. To meet the desired precision, a completely new hadron calorimeter concept is required. A new technological approach needs also development on the hardware level. Characterization of elements of prototype hadron calorimeter units is the second topic presented in this thesis. An FLC will employ highly granular hadron sandwich calorimeters. One option for the active calorimeter part are plastic scintillators. In this case, a single cell must have a volume of just a few cm^3. To maintain compactness of the detector, usage of photomultiplier tubes is excluded. They must be replaced by much smaller silicon photomultipliers (SiPM). The areal homogeneity of SiPMs response was investigated in the first part of the technical studies. The homogeneity was probed by a highly collimated pulsed visible light beam. The spatial resolution of the experiment allowed to observe active area structures within single SiPM microcells. Hamamatsu Multi-Pixel Photon Counters (MPPC) were the main subject of interest.

The second studied element of the calorimeter units were the scintillators. The plastic scintillators in the calorimeter are square-shaped tiles and the scintillation light is read out from one side by a SiPM. Areal light collection homogeneity of the scintillator tiles was investigated with a collimated electron beam from a radioactive source. This method allows to characterize and compare different tile designs. Additionally, the sensitivity of the scintillator to neutrons was tested by irradiation of the tiles with a radionuclide neutron source. Our study was motivated by differences observed by the Tungsten Timing Test-Beam experiment experiment in the response of a calorimeter with steel and tungsten absorbers. This points to the importance of understanding neutron detection in hadron calorimeters.

This thesis is divided into three parts which logically separate the theoretical and introductory, experimental, and physics-simulation dedicated chapters. First, we give an overview of the Standard Model. The symmetry concepts of the theory and the Higgs mechanism are explained. Some shortcomings of the construction which are leading the scientists to introduce further extension like the Supersymmetry and which are putting completeness of the Standard Model into question are also addressed in chapter 1.

Chapter 2 gives an introduction to the topic of future linear colliders. It mentions the physics motivation of a new accelerator experiment as well as technical aspects of the machine. Possible choices of accelerating technology for the colliders are discussed. We also summarize the important parameters of the detector systems.

Information about the basic properties of silicon photomultipliers is given in chapter 3. The details of SiPM construction and operation are explained. Further, we present different options of quench resistor implementation. Impacts of operating conditions of the sensor and possible performance deterioration are described.

In chapter 4, we present the study of SiPMs. The areal response homogeneity of several

SiPM types was investigated with the main emphasis on Hamamatsu MPPCs. The technical aspects of the experimental apparatus and measurement data analysis are described in detail. Finally, the results are discussed. The complete results of SiPM measurements are summarized in appendix B.

The characterization studies of plastic scintillators are presented in chapter 4. Technical details of used experimental setups are given as well as a description of the analysis techniques. The characteristics and performance of two different scintillator tile materials and designs are compared and discussed. The experimental results of the neutron irradiation are also confronted with a Monte Carlo simulation.

In chapter 6, the simulation of the top quark threshold scan at CLIC and the ILC is presented. The data simulation and analysis process is described in detail. Several sources of systematic uncertainties like ambiguities in background level, strong coupling constant and theoretical cross section calculation are addressed. The simulation was performed for the top pole and $1S$ mass scheme with the focus on results for the $1S$ mass definition. The full summary of top mass measurement simulation results is shown in appendix C.

Lists of experimental equipment with some technical details are summarized in appendix A.

Parts of this thesis were already published in references [1] and [2].

Part I.

Introduction and Motivation

CHAPTER 1

STANDARD MODEL OF PARTICLE PHYSICS

The *Standard Model of particle physics* (SM) is the central theory of particles of the present day. It is a quantum field theory which describes all known elementary particles and three of the four known fundamental physical forces of the nature: the strong, the weak and the electromagnetic. The contemporary form of the SM has been established in the 70's of the 20th century. Since then, it has had major success in describing experimentally observed phenomena and predicting existence of further particles. The past predictions of particles were based on symmetry considerations. The ν_τ , the b, c and t quarks and the W and Z bosons were forecast this way and experimentally discovered later on. In the year 2012, another outstanding breakthrough has been achieved by the *Large Hadron Collider* (LHC) at the European Organization for Nuclear Research (CERN[1]) when the ATLAS [3] and the CMS [4] collaborations announced the discovery of a boson compatible with the Standard Model Higgs boson [5, 6] which is also predicted. However, the SM has some issues. For example, it cannot predict masses of elementary particles from first principles, it does not include gravity and it cannot explain dark matter and dark energy which form 95 % of "visible" universe. The Standard Model and its shortcomings will be discussed in this chapter.

1.1. Introduction

The SM is mathematically described by a scalar Lagrange density function (shortly Lagrangian). It is generally based on Yang-Mills Theory [7, 8] which requires invariance of the Lagrangian under local gauge transformations (up to constant terms). These transformations are in this case given by a representation of a special unitary gauge group $SU(n)$ of degree $n \in \mathbb{N}$ and have a general form

[1]The abbreviation "CERN" originates from the french name "Conseil européen pour la recherche nucléaire."

$$\psi \rightarrow \exp(-\mathrm{i}\alpha_a(x) \cdot \boldsymbol{T}_a)\, \psi, \tag{1.1}$$

where ψ is a field to be transformed, $\alpha_a(x)$ are real functions of a continuous parameter x, $a \in \{1, 2, \ldots, n^2 - 1\}$, and $\boldsymbol{T}_a$ are Hermitian operators which form a basis of a vector space with dimension $n^2 - 1$ [9]. Because these gauge transformations form a group which is isomorphic to $SU(n)$, $\boldsymbol{T}_a$ are called *group generators*. The $\alpha_a(x)$ are named *gauge functions*.

The symmetry of the Standard Model Lagrange density that matches experimental observations is

$$U_Y(1) \times SU_W(2) \times SU_C(3). \tag{1.2}$$

The $U_Y(1)$ symmetry is used instead of $SU(1)$ because $SU(1)$ is a trivial group with only one element. The meaning of the indices will be explained later on. The Lagrangian symmetry (1.2) is assured in the following way:

In the Yang-Mills theory, it appears that the Dirac Lagrangian is generally not gauge invariant. To fix this issue, additional massless so called *gauge fields* must be introduced in the Lagrange density [10]. The number of these new fields is equal to the dimension of the particular transformation group. As a consequence of the gauge invariance and presence of the gauge fields, a new term describing interaction between the fermionic gauge field arises. Furthermore, another *self-interaction* term appears for the $SU(2)$ and $SU(3)$ gauge group. It describes the interaction of the gauge fields themselves. These newly added fields are interpreted as bosons mediating a particular interaction between respective fermions in quantum theory. They are named *gauge bosons*.

The group $U_Y(1)$ reflects the symmetry of the *weak hypercharge* and gives rise to one gauge boson B^μ. The $SU_W(2)$ is the symmetry of the *weak isospin* and because the $SU(2)$ group has three generators, this gauge introduces three further bosons, W^1_μ, W^2_μ and W^3_μ. The symmetry $U_Y(1) \times SU_W(2)$ describes the *electroweak interaction*, however none of the B^μ and W^i_μ ($i \in \{1, 2, 3\}$) bosons is a physical particle. Linear combinations of these form the photon, $W^\pm$ and Z bosons. The $SU_C(3)$ gauge group represents the symmetry of *color charge* and describes the *strong interaction* mediated by eight gauge bosons called *gluons*.

The so far presented model comprises six fermions and twelve bosons. It is schematically depicted in figure 1.1. The fermions form matter and can be further divided into quarks, which are subjected to all interactions, and leptons, which do not interact strongly. Moreover, the explicit mass terms in the Dirac Lagrangian would violate the $SU_W(2)$ gauge invariance. Thus, they must be dropped. However, there is one major issue in the theory which contradicts experimental reality: all of the particles are massless. This problem is solved by the Higgs mechanism.

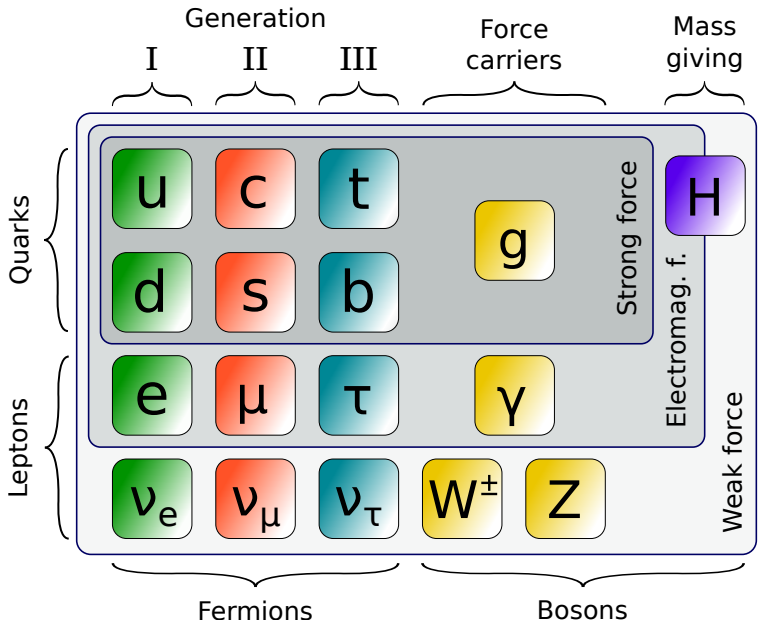

Figure 1.1.: Overview of Standard Model particles and forces.

1.2. Higgs Mechanism

Since the explicit mass terms violate the gauge invariance, they obviously cannot be used and the masses of the particles must be generated differently. This can be done by a rather complicated procedure which starts by introducing a new complex scalar two-component field ϕ into the SM Lagrangian. The field ϕ has a potential

$$V(\phi) = -\mu^2\phi^\dagger\phi + \lambda^2\left(\phi^\dagger\phi\right)^2, \tag{1.3}$$

where μ, $\lambda \epsilon \mathbb{R}^+$. It is required that the Lagrangian including the new field ϕ is invariant under $U_Y(1)\times SU_W(2)$ gauge. In a perturbation theory, particle interactions are described in terms of deviations from the vacuum ground state with the minimal energy. However, the potential (1.3) has a non-zero vacuum expectation value. Its depiction in two dimensions has the form shown in figure 1.2. Thanks to a proper redefinition of the field ϕ, so that perturbation series can be expanded around the minimum of the potential, the gauge bosons acquire mass. However, the field ϕ intrinsically includes four bosons. Three of them are massless and have unphysical coupling terms to the gauge bosons in the Lagrangian. They are called *Goldstone bosons* and they can be removed by a proper choice of a specific gauge function (defined in equation (1.1)) [11]. The fourth boson in ϕ is massive and its name is the *Higgs boson* [12].

As a consequence of this procedure, called the *Higgs mechanism* [13, 14, 15], the gauge bosons induced by $U_Y(1) \times SU_W(2)$ symmetry have acquired mass and a neutral scalar massive particle represented by a new *Higgs field* has appeared. One should keep in mind that the physical weak bosons and the photon are obtained by linear combinations of the unphysical gauge bosons in the Lagrangian. This leads to massive $W^\pm$ and Z bosons and a massless photon. The fermions acquire their masses through interaction with the Higgs

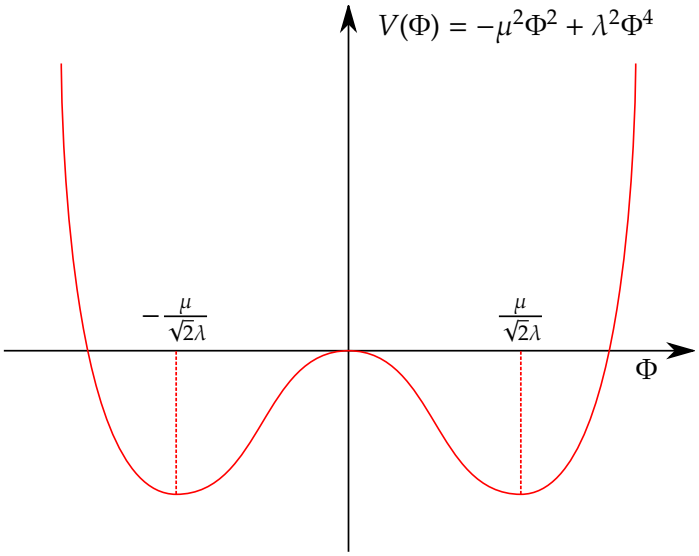

Figure 1.2.: Example of the Higgs potential in one dimension. Taken from [18].

field in further *Yukawa* terms which must be explicitly added to the SM Lagrangian [16, 17]. In the step where the field ϕ was redefined, the $U_Y(1) \times SU_W(2)$ symmetry has been broken to $U_Q(1)$, the symmetry of electromagnetism. Therefore, the Higgs mechanism is also called *spontaneous symmetry breaking*.

1.3. Shortcomings of the Standard Model

The Standard Model includes all known elementary particles and accurately describes most observations in particle physics today. However, the SM does not include gravity. In addition, there are phenomena which are not described by the SM and some SM calculations have to be treated very carefully to match the experimental results. Below, the most significant open issues of the SM will be addressed.

Dark matter and *dark energy* can be neither explained nor described by the SM at all. From measurements of tangential rotational velocities of galaxies (dark matter) [19] and universe expansion speed (dark energy), the existence of these subjects of unknown nature is implied. Since about 70 % of the universe consists of dark energy, 25 % of dark matter and only 5 % of the Standard Model particles, the SM evidently fails in giving a complete picture of the particles making up the material part of this world.

Assuming that equal amounts of matter and anti-matter were created during the Big Bang and facing the fact that the known universe is composed exclusively of matter, there must be some effect which caused this imbalance. The solution could be CP violation of the SM. However, it is not large enough [20] to explain the matter-antimatter asymmetry.

Moreover, the neutrinos in the SM are massless. The discovery of neutrino oscillations [21, 22] implies that at least two of the three SM neutrinos must be massive.

Another issue of the SM is the *hierarchy problem*. It was experimentally observed that the value of μ from equation (1.3) is roughly of the order of 100 GeV [23]. The problem is

that μ receives quantum corrections from the virtual effects of every particle that couples to the Higgs field. For example, a fermion f coupling to the Higgs field H leads through the $-\lambda_f H f \bar{f}$ term to a correction of

$$\Delta\mu_f^2 = -\frac{\left|\lambda_f\right|^2}{8\pi}\Lambda_{UV}^2 + \dots\,, \tag{1.4}$$

where λ_f is a Yukawa coupling constant. Λ_{UV}^2 is an ultraviolet cutoff and should be understood as an upper energy limit of SM validity. The disturbing fact is that if Λ_{UV}^2 is chosen close to the Planck scale, the correction originating from top quark coupling would be by 30 orders of magnitude higher than the current experimental value of μ^2. One of the ways how to overcome the quadratic Λ_{UV}^2 dependence without extending the SM is to use dimensional regularization instead of a momentum cutoff. However, the physical interpretation of Λ_{UV}^2 must be sacrificed in this case and the Λ_{UV}^2 has to be fine tuned without any physical motivation in order to match the experimental result of μ^2.

A solution to the hierarchy problem and some other troubles of the SM can be the theory of *Supersymmetry*.

1.3.1. Supersymmetry

A contribution to μ^2 (defined in equation (1.3)) correction induced by a massive complex scalar particle S coupling to the Higgs field H by a Lagrange density term of $-\lambda_S |H|^2 |S|^2$ has the form

$$\Delta\mu_S^2 = +\frac{\lambda_S}{16\pi}\Lambda_{UV}^2 + \dots\,, \tag{1.5}$$

where λ_S is a Yukawa coupling constant. From a comparison of equation (1.5) and (1.4), it is apparent that the correction terms have a very similar form and opposite signs. This gives a hint that if a further particle symmetry was introduced, the hierarchy problem could be possibly solved. The new symmetry called the *Supersymmetry* (SUSY) [23] assigns to each SM fermion a pair of newly established bosons (one for the right-handed and one for the left-handed fermion) with a Yukawa coupling fulfilling a condition

$$\left|\lambda_f\right|^2 = \lambda_S\,. \tag{1.6}$$

It is clear now that μ^2 corrections originating from the fermion f and two bosons S, $\Delta\mu_f^2$ and $2\Delta\mu_S^2$, respectively, cancel out.

Even though some more restrictions on the theory are needed to assure the higher order correction to vanish as well, the SUSY is a functional and elegant way how to solve the hierarchy problem. However, none of the supersymmetric particles have been experimentally discovered yet. This fact leads to suggestion that SUSY, if it exists, is a broken symmetry. It should be also stressed that SUSY is not the only possible extension of the SM. Other theories beyond the Standard Model are e.g. extra dimensions [24] or string theory [25].

1.4. The Top Quark

The top quark was introduced in 1973 [26] as an extension of the Standard Model to explain the observed CP-violation in kaon decays. 22 years later, in 1995, the existence of the top was confirmed experimentally by the discovery done by the CDF [27] and DØ [28] collaborations at the Tevatron accelerator. Nowadays, the top quarks are produced in large numbers at the LHC.

1.4.1. Role of the Top Quark in the Standard Model

The top quark plays in a certain sense a special role in the SM. With a mass of about 173.3 GeV (comparable to rhenium nucleus) it is by far the heaviest quark. Because of its large mass, it couples among all SM particles the most strongly to the Higgs boson. Therefore, it might be a good tool to probe the Yukawa coupling to the Higgs particle. Top physics is also very sensitive to corrections originating from yet unknown particles and thus it could contribute to possible new discoveries through precise measurements. The top mass cannot be calculated from the first principles of the SM, it is an input parameter. A precise knowledge of the top mass would be a very valuable information for precision electroweak analyses. By close theoretical studies of stability of the SM vacuum, it turns out that there is a possibility that today's vacuum might not be a true ground state but a local minimum of the Higgs potential [29, 30]. The phase diagram of the SM Higgs vacuum can be depicted in a Higgs-mass - top-mass plane. It is shown in figure 1.3. The dominant uncertainty in answering the question whether the vacuum is stable originates mostly from experimental uncertainties of the top mass. A more precise knowledge of this quantity would shed light also on the fundamental property of vacuum.

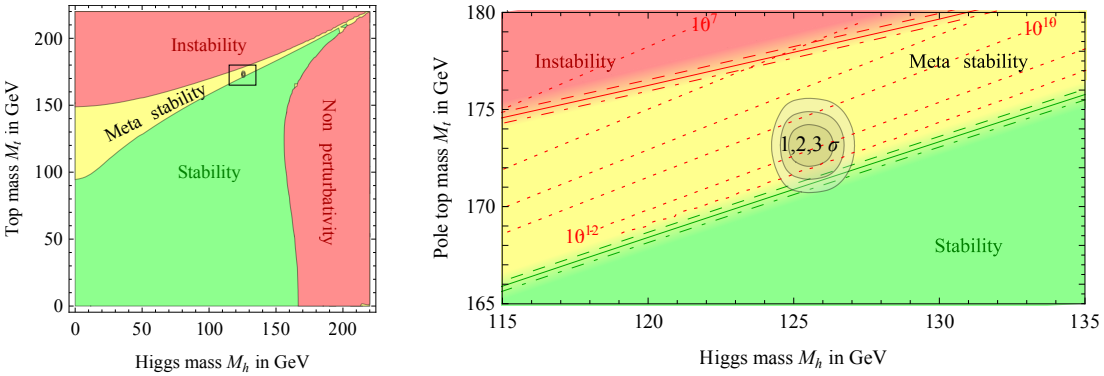

Figure 1.3.: Regions of absolute stability, meta-stability and instability of the SM vacuum in the $M_t - M_h$ plane plane. The right plot is a zoomed region of the left graph which is marked by the black rectangle. Recent experimental uncertainties of M_t and M_h are depicted by the concentric circles in the right. The three phase boundary lines correspond to $\alpha_s(M_Z) = 0.1184 \pm 0.0007$, and the grading of the colors indicates the size of the theoretical error. Taken from [30].

1.4.2. Mass Definitions

The large top mass causes also a very short lifetime of the particle which is at the order of 10^{-25} s [31]. However, the hadronization time scale $\Lambda_{QCD}^{-1} \approx (200\,\text{MeV})^{-1} \approx 10^{-23}$ s [32] is approximately by two orders of magnitude longer. That means that the top decays before being allowed to form any bound states like toponium or other hadrons. This fact has two major consequences. First, the top quark can be studied as an almost free particle which is not possible for other quarks due to quark confinement. Second, since the decaying top quark is always subjected to the interaction with its fellow anti-top, it is never a perfectly free particle. In other words, a part of the top mass is always absorbed in the binding of the $t\bar{t}$ pair. This leads to difficulties in the correct assignment of theoretical top mass definitions and experimentally accessible invariant mass. There are several top mass definitions, each of them with its own specific motivation.

Pole Mass and $\overline{\text{MS}}$ Mass

The *pole mass* m_p is defined as pole of the renormalized propagator of a given particle in the perturbation theory [33]. In the following, we assume the usage of the $\overline{\text{MS}}$ renormalization scheme [10, 34]. The general formula for the pole mass of a fermion is

$$m_p = \overline{m}_{MS} \left\{ 1 \; + \; A\left(\overline{m}_{MS}\right) \cdot \frac{\overline{\alpha}_S(\overline{m}_{MS})}{\pi} \; + \; B\left(\overline{m}_{MS}\right) \cdot \left[\frac{\overline{\alpha}_S(\overline{m}_{MS})}{\pi}\right]^2 \; + \; \ldots \right\}, \tag{1.7}$$

where $\overline{m}_{MS}$ is a parameter with the dimension of mass called the $\overline{\text{MS}}$ *mass*, $\overline{\alpha}_S(\overline{m}_{MS})$ is the renormalized strong coupling constant in the $\overline{\text{MS}}$ scheme and $A\left(\overline{m}_{MS}\right)$ and $B\left(\overline{m}_{MS}\right)$ are renormalization constants. In addition to that, $\overline{\alpha}_S(\overline{m}_{MS})$ is also a function of Λ_{QCD} which is an energy parameter named *QCD renormalization scale*. As a consequence, the overall uncertainty of the curly bracket in equation (1.7) is $O(\Lambda_{QCD})$. A physical interpretation of Λ_{QCD} is rather complicated and it is usually set to $\approx 200\,\text{MeV}$. A valid input parameter for further theoretical calculations is the $\overline{m}_{MS}$ and since the assignment between m_p and $\overline{m}_{MS}$ intrinsically suffers from an error of Λ_{QCD}, it would be favourable to measure the $\overline{m}_{MS}$ directly, rather than m_p. The $\overline{\text{MS}}$ renormalization procedure assumes energetic quarks. Hence, the usage of m_p and $\overline{m}_{MS}$ terms is not valid for calculations regarding low energy quarks. An example of such a situation can be quark-antiquark pair created just at its production threshold and hence being at rest.

$1S$ Mass

To describe low-energetic top quarks, the $1S$ mass definition $m_t^{(1S)}$ was introduced [35]. It is defined as one half of the perturbative mass of the fictitious 1^3S_1 ground state under the assumption that the top quark is stable. Mathematically, it can be expressed as

$$m_t^{(1S)} \equiv m_t^{(pole)} - \frac{1}{2} V_{t\bar{t}}, \tag{1.8}$$

where $m_t^{(pole)}$ is the top pole mass and $V_{t\bar{t}}$ is the potential between t and $\bar{t}$ in the 1^3S_1 state. This construction has two major advantages. First, it stabilizes the position of the $t\bar{t}$ pro-

duction cross section peak at the threshold with respect to the 1S mass. In other words, the peak is placed at $2m_t^{(1S)}$ (+ 200 MeV) which is not the case for other mass definitions. Second, the most important property of the 1S mass is that the ambiguity in the relation between $m_t^{(1S)}$ and the top $\overline{\text{MS}}$ mass $m_t^{(\overline{MS})}$ is only $O\left(\Lambda_{QCD}^2/m_t^{(1S)}\right)$. This low uncertainty makes the 1S mass a perfectly valid input parameter for theoretical calculations.

1.4.3. Mass Measurement Methods

Due to the mass definition issue, it is not a trivial task to measure the top mass in a clear way. The usual experimental practice for obtaining particle masses is to measure the invariant mass of the decay products of a given particle. There is a belief that the experimentally well-defined and well understood invariant mass roughly corresponds to the pole mass. The usage of this mass in theoretical calculations suffers from the intrinsic uncertainty of $O(\Lambda_{QCD})$. Moreover, the inaccuracy of the assignment between the invariant mass and the pole mass is even larger. For example, the 1S mass scheme is a theoretically well-defined concept, but it requires a different experimental approach. It can be measured from a $t\bar{t}$ production cross-section energy dependence around the $t\bar{t}$ pair production threshold. This method is utilized in the study presented in chapter 6.

CHAPTER 2

FUTURE LINEAR COLLIDERS

A future linear e^+e^- collider is a scientific tool which is needed to continue, extend and complement the recent high energy particle physics research done at the *Large Hadron Collider* (LHC). Furthermore, the energy scale of predicted and yet undiscovered "new" physics is still unknown and has to be investigated. The physics studies which can shed light on this question as well as give important parameters of the Standard Model require a high collision energy. From the processes of interest, one can name for example the Higgs pair production (threshold at $\sim$ 250 GeV), WW fusion ($\sim$ 350 GeV), top pair production ($\sim$ 350 GeV), $t\bar{t}H$ production ($\sim$ 500 GeV), etc. Also channels allowing Higgs self coupling determination need a collision energy higher than 200 GeV which was the maximum energy achieved by the *Large Electron-Positron Collider* (LEP), the most powerful lepton accelerator built so far. Due to these reasons, a new accelerator with flexible centre-of-mass energy in the range between 250 and 500 GeV with a possibility of a further energy upgrade would be the next logical step. The high collision energy puts also challenging demands on the accelerator and detector technology. Technical aspects as well as physics motivation for construction of such a machine will be presented in the following.

2.1. Motivation for a Linear e^+e^- Collider

A hadron collider, like the LHC, is a good discovery tool for yet unknown heavy particles. It can collide e.g. protons at very high energies and rates. However, the proton is a composite object consisting of further partons, three valence quarks, gluons and sea gluons. These constituents carry a variable fraction of the proton momentum which is described by the parton distribution function [36]. In a proton-proton collision, the high energy reaction involves just two partons. As a consequence, the initial state of the two partons can never be precisely known. Additionally, the partons which do not participate in the hard process hadronize into secondary particles which are also registered in the detector systems of the accelerator and form *underlying events*. The accelerated protons at the LHC are also grouped and collided in so called bunches. In every bunch crossing, about 30 *p-p* collisions take place. These individual interactions cannot be unambiguously separated

when their spatial distance is not high enough. The underlying events along with the event pile-ups overlay with the processes of interest and the extraction of important signal signatures is more complicated. The cross sections of different signal processes are also by 3 to 11 orders of magnitude smaller than the total cross sections of a *p*-*p* collision ($\sim 10^{15}$ fb) [37]. These environmental conditions require a sophisticated event triggering which might exclude detection of possible unexpected and unknown physics effects. The high QCD background leading to a small signal-to-noise ratio makes precise measurements of many interesting physical cases extremely difficult or even impossible.

In contrast to hadron accelerators, lepton colliders overcome these issues. Leptons are, according to present knowledge, truly elementary particles without any further inner structure. Advantages of this are the absence of QCD background events and much better defined initial state of the colliding particles. A lepton collider offers a very clean environment which allows precise measurement of various phenomena, e.g. accurate determination of Higgs particle properties. From this point of view, a lepton machine can serve as a complementary tool to the LHC and investigate the effects discovered in a hadron collider experiment in detail. The signal-to-background ratio is much more favourable for a lepton (e^+e^-) collider. The cross sections for signal processes are usually less than two orders of magnitude smaller than for background processes. On the other hand, there is a quite strong $\gamma\gamma \rightarrow$ hadrons background, in a e^+e^- machine. These real and virtual photons are emitted by the electrons and positrons in the beam. The cross section for the $\gamma\gamma \rightarrow$ hadrons events is few hundred nb which is about $4-5$ orders of magnitude more than for the interesting physics events. However, the experimental conditions are still very clean and allow a full reconstruction of events. The full event reconstruction enables also missing energy analyses. Thanks to the clean experimental conditions and relatively high signal cross sections, no triggering is required and events from all bunch crossings can be recorded. This also opens an opportunity for searches for yet undiscovered effects.

Lepton colliders in general or colliders using electrons and positrons have been described, so far. The electrons are indeed the most suitable leptons for a future linear accelerator experiment. The reasons are the following. A practical usage of the heaviest τ lepton (rest mass 1.78 GeV) is immediately excluded by its short lifetime of $2.9{\cdot}10^{-13}$ s and difficult production. Ideas for a muon accelerator already exist [38, 39], but there are still many issues like the fact that μ is an unstable particle with a mean lifetime of $2.2{\cdot}10^{-6}$ s. Working technology for a muon collider is not yet available. The remaining charged lepton is the electron. Its advantages are an easy production and stability. On the other hand, its low mass of 511 keV makes it unsuitable for ring accelerators, because the particle constantly accelerates due to its circular path. The energy loss ΔE of an ultrarelativistic particle with energy E, rest mass m_0 and charge Q on a circular trajectory with radius R due to synchrotron radiation during one revolution can be derived from Larmor's formula [40, equation (9.5.45)] like

$$\Delta E = \frac{1}{3\varepsilon_0} \cdot \frac{Q^2}{R} \cdot \left(\frac{E}{m_0 c^2}\right)^4, \tag{2.1}$$

where ε_0 is the premittivity of vacuum and c is the speed of light. It can be seen from equation (2.1) that the energy loss is inversely proportional to the fourth power of the particle rest mass which plays against light particles. Accelerating electrons in circular

machines has already met the technological limits at the LEP with 100 GeV per beam just because of the synchrotron radiation. The solution would be an accelerator with a larger radius. Unfortunately, it turns out that the collider would have to be enormous and thus technically demanding. A linear accelerator overcomes this problem completely. It has other disadvantages, on the other hand. The particles must be accelerated within one single passage through the machine and those particles which do not participate in the collision cannot be used again. The same issue regards the accelerating elements, they cannot be used multiple times to act on the same particle more than once. With the usage of nowadays available acceleration cavities which can reach gradients of the order of few tens of MV/m (see also table 2.1), a collider for TeV energies would need a long acceleration path. This increases the construction costs. The length of the machine can be reduced by employment of technologies with high acceleration gradients like the plasma-wakefield acceleration technique [41] which aims towards gradients of 1 - 100 GV/m. However, this equipment is not available yet, it still requires years of research and development. A linear e^+e^- collider with long acceleration paths is the only option for any near future lepton accelerator project.

2.2. Physics Potential

A lepton collider operating at centre-of-mass energies $\sqrt{s}$ between 250 GeV and 1 TeV or 3 TeV is a very powerful tool to study the regions of particle physics which are not investigated yet and are crucial for a complex understanding of contemporary theories and fundamental structure of matter. Since a boson compatible with light Higgs boson was recently discovered at the LHC [6, 5], the physics program for a future linear collider [42, 43] has even broadened.

A linear e^+e^- collider can provide measurements with sufficient precision to address questions regarding the Higgs sector. The Standard Model (SM) Higgs particle characteristics like mass, width, spin, and its CP properties can be measured in many ways and also model independently in some cases. Cross sections for some Higgs boson production channels in e^+e^- collisions as functions of centre-of-mass energy are shown in figure 2.1. In the lower energy range for $\sqrt{s} \approx 230\,\text{GeV}$, the highest statistics can be obtained in the so called golden channel $e^+e^- \to Z^* \to HZ$. For energies above $\sqrt{s} \approx 350\,\text{GeV}$, the fusion channels $e^+e^- \to ZZ \to He^+e^-$ and $e^+e^- \to WW \to H\nu_e\bar{\nu}_e$ are available, respectively. Further processes with lower cross sections like $e^+e^- \to t\bar{t}H$, $e^+e^- \to HHZ$ and $e^+e^- \to HH\nu_e\bar{\nu}_e$ provide access to the top quark Yukawa coupling and the Higgs self coupling. Further quantities which can be accurately measured are Higgs couplings to other known elementary particles. Higgs decay branching ratios which will be used for the determination of the couplings can be measured with high statistical precision. Higgs couplings to W, Z and b can be obtained model independently with a precision better than 2 %. The couplings to gauge bossons, fermions and Higgs itself are that important, because they are essential for testing of Higgs mechanism predictions regarding proportionality of the couplings to the masses of the given particles. An e^+e^- collider has also the capability of revealing whether any effects assumed by *Beyond Standard Model* (BSM) theories take part in the electroweak symetry breaking sector. The BSM physics can influence the Higgs sector for example by loop effects of BSM particles and cause a deviation from the SM predictions.

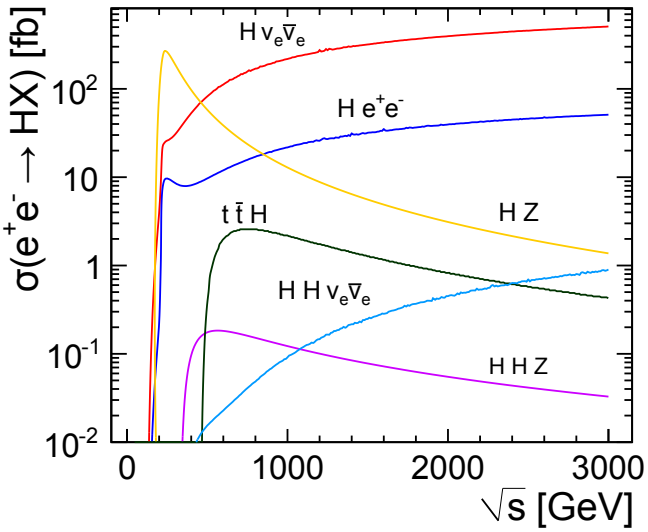

Figure 2.1.: Standard Model Higgs boson ($m_H = 120\,\text{GeV}$) production mechanisms and their cross sections in e^+e^- collisions. Taken from [44].

Another part of the physics program of the future linear colliders is top quark physics. The clean environment of the e^+e^- collisions allows to measure the top invariant mass with much better accuracy than at a hadron collider. However, the biggest benefit of an e^+e^- machine is the possibility of $t\bar{t}$ production threshold measurements which allows to obtain the top mass with high precision in a theoretically well-defined mass scheme. An accurate knowledge of the top mass plays an important role in predictions of many SM parameters and can potentially reveal effects of BSM physics. The top mass can be measured with a total uncertainty better than 50 MeV. For more details see chapter 6.

A further important topic of e^+e^- collider studies is the search for predicted and yet undiscovered "new" physics effects. An e^+e^- machine can contribute in three different ways: by performing deeper and more exact studies of phenomena discovered at the LHC, revealing new effects beyond the capabilities of the LHC and finding traces of BSM processes through high precision investigations of known effects and their deviations from the SM. The theory of Supersymmetry (SUSY) sketched in section 1.3.1 is arguably the most popular BSM physics theory. It offers a large number of predicted particles. Some of them, in particular colored ones, can be likely observed at the LHC if they exist. Unfortunately, non-colored particles, charginos, neutralinos and sleptons are not abundantly produced at the LHC. These particles might be found in cascade decays of strongly decaying SUSY particles. It is possible that not all of these particles will be accessible at the LHC. However, the LHC can identify the energy region of these reactions. An e^+e^- collider with sufficient centre-of-mass energy can subsequently investigate the given energy range for existence of further particles with electroweak charge. Parameters of the newly discovered particles such as mass, spin, couplings, etc. can be also accurately measured at a lepton collider. This kind of data can shed light on the correctness of BSM physics models and show potential sources of new physics.

Parameter	Unit	ILC	CLIC
Tunnel length	[km]	31	13
Luminosity	$[10^{34}\,\mathrm{cm}^{-2}\mathrm{s}^{-1}]$	1.8	2.3
Luminosity fraction in 1 % of $\sqrt{s}$	[%]	58	61
Acceleration gradient	[MV/m]	31.5	80
Bunch separation	[ns]	554	0.5
Luminosity pulse repetition rate	[Hz]	5	50
Power consumption	[MW]	163	272

Table 2.1.: Parameter overview of the 500 GeV version of CLIC and the ILC. The values were taken from [45] and [37], respectively.

2.3. Accelerator Concepts

Recently, there are two linear e^+e^- collider concepts in development. The *International Linear Collider* (ILC) aims for a centre-of-mass collision energy $\sqrt{s}$ = 500 GeV with a possible upgrade to 1 TeV. It relies on a well established accelerating technology using *superconducting radio-frequency cavities* (SCRF). On the other hand, the *Compact Linear Collider* (CLIC) plans to utilize a novel *two beam acceleration* (TBA) approach and it is intended to be constructed in stages. In the first stage, the maximal $\sqrt{s}$ will be either around 350 or 500 GeV. In the final step, the machine will be upgraded to 3 TeV. The first stage version with $\sqrt{s} \approx 350$ GeV is more favourable because it offers higher luminosities for lower energies. The gradual construction or a later upgrade of an accelerator has several advantages. It also allows the investigation of physics at lower energy scales below 500 GeV, providing valuable physics results earlier and spreads the overall cost over longer time span. In the following, these two linear collider proposals will be introduced.

2.3.1. Compact Linear Collider

The CLIC machine is planed to be constructed in three stages with centre-of-mass energies of 500 GeV, 1.5 TeV and 3 TeV. The basic parameters of the first, $\sqrt{s}$ = 500 GeV, version of CLIC as well as of the ILC are presented in table 2.1. Since CLIC aims to very high collision energies, employment of the super-conducting acceleration cavities with their limitations on electrical field intensity is excluded. In this case, an enormous machine would be required. To make the accelerator smaller, the TBA technology will be used. It is capable of reaching accelerating gradients up to 100 MV/m. The TBA needs a special configuration of the accelerator facility. A schematic overview is shown in figure 2.2. The *radio frequency* (RF) power for the *main linac* is extracted from a low-energy high-current *drive beam* which runs parallel to the main high-energy beam. The energy transfer from the drive to the main beam is performed by a sequence of *power extraction and transfer structures* (PETS). These elements transform the beam energy into RF waves which are subsequently transferred through waveguides into the main linac accelerating structures.

The drive beam at the final construction stage will be produced by two dedicated accelerators, each for one main linac arm. The first construction stage will use just one drive beam accelerator for both main linacs. The drive beam is first accelerated by an RF field

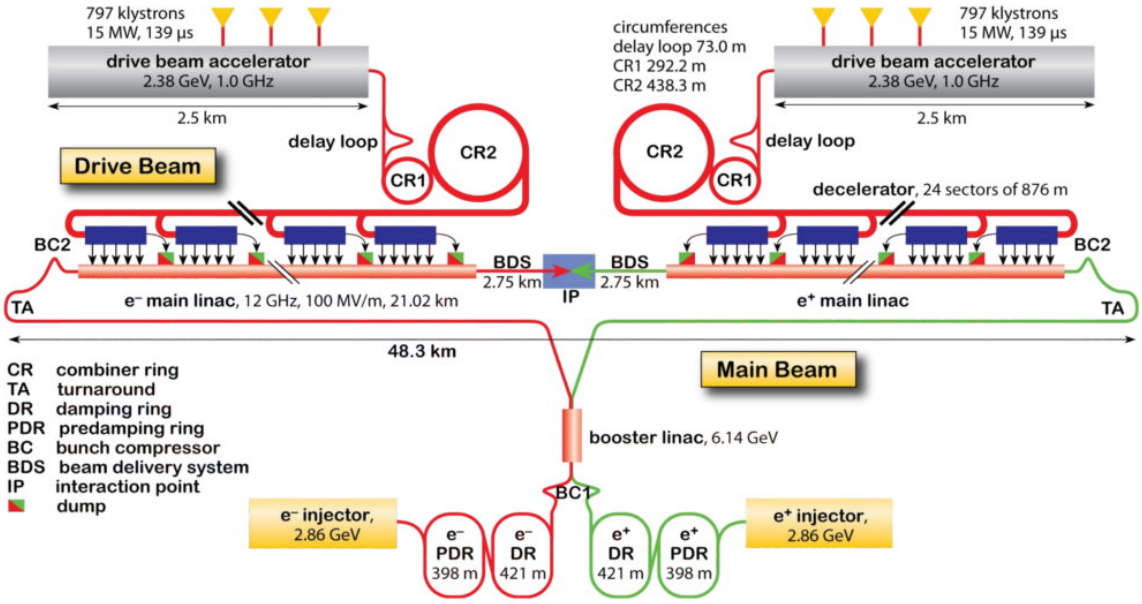

Figure 2.2.: Schematic layout of the 3 TeV CLIC. Taken from [46].

to 2.4 GeV. Afterwards, it is lead into a delay loop and two *combiner rings* which strongly enhance the current of the beam up to 100 A.

Each of the main linacs will consist of 70 000 accelerating structures with 23 cm in length. Theses elements will occupy almost 80 % of the total length of the accelerator. The particles for the main beams are produced in conventional electron and positron sources and accelerated to 2.9 GeV. The beam emittances are reduced in a *pre-damping* and a following *damping ring*. After that, the beam is compressed and accelerated by a *booster linac* to 9 GeV and fed into the main linac for the final acceleration. Subsequently, the beams collide with a crossing angle of 20 mrad. This angle provides enough space for placement of separate extraction lines.

As already mentioned, the power for the main linear accelerator is extracted from the drive beam by the PETS where it is decelerated from 2.4 GeV to 0.24 GeV. The energy is then lead through a waveguide to an accelerating structure. A drawback of the TBA using normal conducting cavities is the time spacing of the colliding particle bunches. It must be just 0.5 ns to reach a high efficiency. This puts very challenging requirements on the detector systems. The experimental proof-of-principle of the novel TBA technology has been already performed [45]. However, it is expected that several years of additional research and development will be required to build a full scale accelerator.

2.3.2. International Linear Collider

The ILC which is designed for $\sqrt{s}$ = 500 GeV will be capable of colliding electrons and positrons in continuous energy range between 200 and 500 GeV. Its basic parameters for a centre-of-mass energy of 500 GeV are listed in table 2.1. The total length of the accelerator tunnel will be 31 km and the beams will collide with a crossing angle of 14 mrad. A schematic overview of the ILC is shown in figure 2.3.

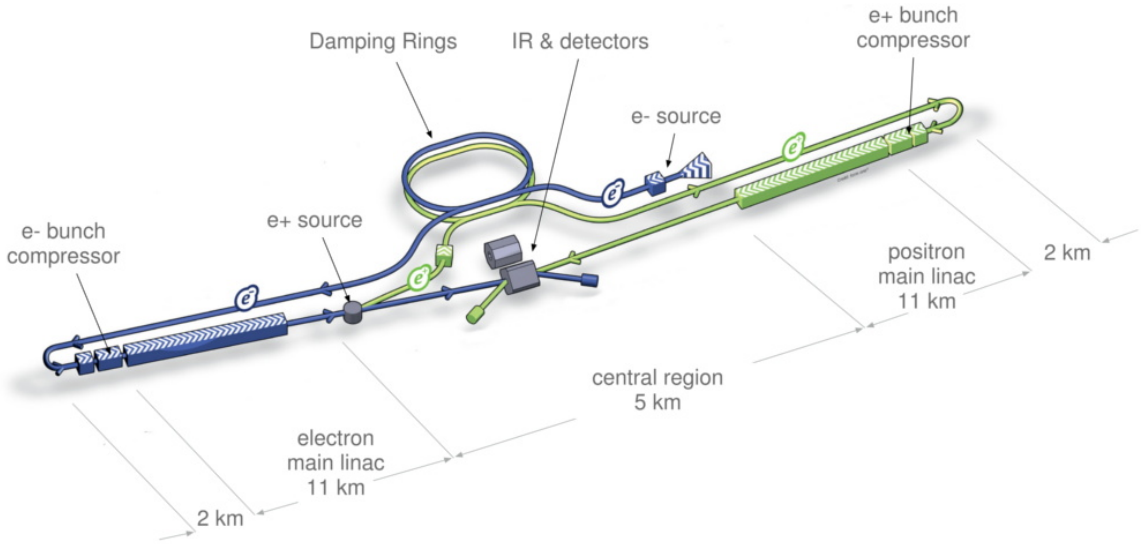

Figure 2.3.: Schematic layout of the ILC. Taken from [37].

Polarized electrons for the accelerator are produced on a laser-irradiated photocathode. Subsequently, they are put into bunches, accelerated by several SCRF to 5 GeV and injected into the electron *damping ring*. The positrons are obtained with the help of a 147 m long superconducting undulator placed along the part of the electron *main linac* where the electrons have an energy of $150 - 250$ GeV. The undulator produces γ-radiation of $10 - 30$ MeV which interacts with a titanium alloy target and converts into polarized electrons and positrons. This positron production scheme is used in order to obtain polarized e^+. The electrons and gammas are lead to a dump. The positrons are accelerated to 5 GeV and injected into the positron damping ring. The polarisation will be 90 % and 30 % for the electrons and positrons, respectively.

The ILC is equipped with two damping rings placed in the middle of the accelerator complex. These are put one on the top of the other and will be built in a "race track" geometry. The diameter of the ring curves will be 579 m and the straight parts will be 712 m long. Each ring will accommodate 12 SCRF and further devices in order to reduce the transverse and longitudinal emittance of the beams by several orders of magnitude.

From the damping rings, the beams travel to a transfer beam line called *ring to main linac*. It is the longest continuous beam line of the ILC complex and consists of several parts. Among others, it contains spin rotators to perform the final spin setting and bunch length compressors. In this line, the beam is accelerated from 5 to 15 GeV and finally injected into the main accelerator stage.

The two main linacs are 11 km long. Each is equipped with approximately 7400 pieces of $\sim$ 1 m long niobium 1.3 GHz SCRF operating at a temperature of 1 K. Focusing of the beam is assured by approximately 280 quadrupole magnets. The main linacs accelerate the particles from 15 to the final $100 - 250$ GeV. The maximum beam energy can be possibly increased up to 1 TeV by expanding the accelerator complex by further 20 km.

The last stage of the beam path is the *beam delivery system* (BDS). It assures the final focusing, alignment and refining of the beams. It is generally responsible for reaching the

demanded luminosity and polarisation. The BDS also transports the particles which did not take part in the collision to the main beam dump. Just for illustration of the total beam energy, the power which has to be absorbed by the main beam dump for the upgraded 1 TeV ILC will be 14 MW.

Due to the different acceleration technology used at both linear colliders, also the luminosities $\mathcal{L}$ and luminosity spectra (see also figure 6.5) of the machines differ considerably. A very important parameter of the luminosity spectrum is the fraction of the total $\mathcal{L}$ included in 1 % of the nominal $\sqrt{s}$. The values of this quantity for CLIC and the ILC are also given in table 2.1. If this fraction is small, the beam energy will be blurred and the uncertainty of the collision energy is large. Therefore, it is required to have an accelerator with most of the luminosity concentrated as close to the nominal energy as possible. It is also necessary to know the shape of the luminosity spectrum precisely in order to keep systematic errors of physics analyses under control.

2.4. Detector Systems

Unlike a circular collider, a linear accelerator does not allow to deploy several interaction regions (IR) along the beam path. Therefore, two interchangeable detector systems will be build at the IR of a future linear collider. They can be switched in a so called "push-pull" mode to perform independent measurements and they will equally share the beam time. The two detectors bring a scientific benefit for the facility, because they provide cross-checking and confirmation of the results. This increases reliability and introduces competition in the research.

The detectors proposed for the ILC are called the *International Large Detector* (ILD) [47] and the *Silicon Detector* (SiD) [48]. Both of them are multi-purpose detectors optimised for a broad range of physics investigations. They have a cylindrical geometry where the tracker as well as the novel highly granular calorimeters are placed inside of a super-conducting solenoid. The construction of the detector systems is governed by the particle flow concept which is presented in section 2.5.1. The most important aims of such a detector design are to maximize jet energy resolution and improve track and vertex reconstruction capabilities. These are crucial for separation of W and Z bosons and b and c quarks, respectively. Even though the SiD and ILD were designed for the ILC, they can be adapted for the CLIC machine conditions. These are mainly a higher collision energy and tighter bunch timing. The most significant differences of the CLIC and ILC version of ILD lie in the radius of the innermost detector and a different absorber material in the hadron calorimeter. The CLIC versions of ILD and SiD, the CLIC_ILD and the CLIC_SiD, respectively, are shown in figure 2.4. In the following, both detectors will be described in more detail with an emphasis on ILD. The CLIC_ILD model was used for the top quark threshold scan simulation presented in chapter 6.

2.4.1. International Large Detector

A complex detector system like ILD and SiD consist of several subsystems with highly specialized purposes. The assembly of these is shown in figure 2.4. The main parts of ILD and SiD will be now described.

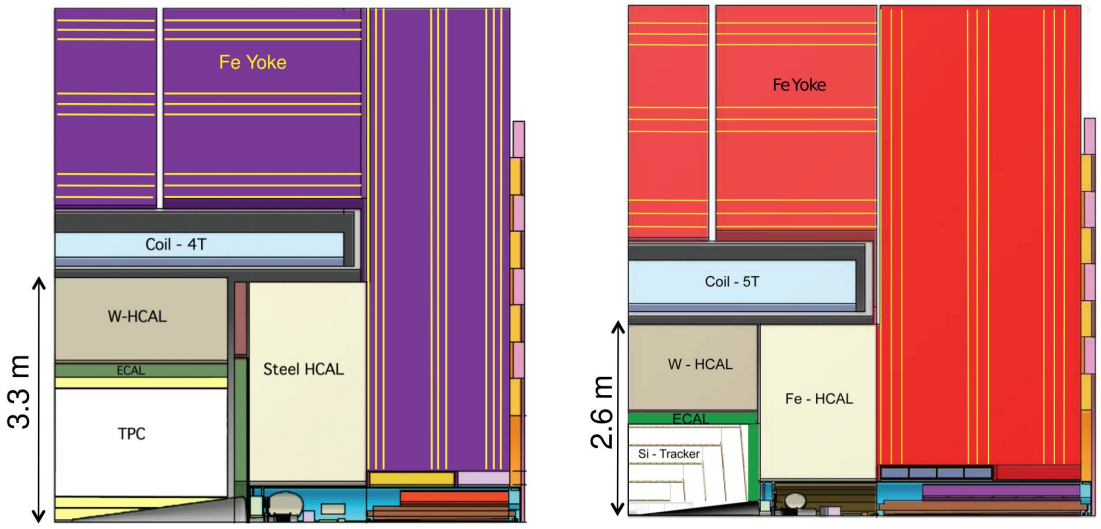

(a) CLIC_ILD (b) CLIC_SiD

Figure 2.4.: Longitudinal cross section of the one quadrant of the ILD (**b**) and the SiD (**a**) systems for the CLIC. Taken from [45].

Vertex Detector

The innermost detector system of the ILC is the *vertex detector* (VTX) which will consist of three double layers of silicon pixel detectors arranged in a barrel geometry. The goal of the VTX is to achieve a 3 µm single-point spatial resolution. It must have an extremely low mass, large geometrical coverage and sufficient heat removal system. In the case of CLIC_ILD, the inner radius of the VTX will be larger than for the ILC version. The reason is a reduction of occupancy caused by incoherent e^+e^- pairs emitted mainly along the beam pipe.

Time Projection Chamber

The main tracking device of ILD is the *time projection chamber* (TPC). It is a big lightweight gaseous detector with an inner and outer radius of 33 and 180 cm, respectively. It is optimized for three-dimensional track recording. The TPC will be capable of acquiring up to 224 points per track and perform particle identification based on characteristic energy loss $\mathrm{d}E/\mathrm{d}x$. It will provide tracking information and momentum measurement.

Silicon Trackers

The TPC will be surrounded by additional silicon strip and pixel detectors. Between the TPC and the VXT, two layers of silicon strip detectors (SIT) will be located. The forward regions of the VXT will be covered with two silicon-pixel and five silicon-strip disks. Their purpose is to extend the tracking acceptance up to small polar angles of 7 °. Between the TPC and the electromagnetic calorimeter and behind the TPC end-caps, a further silicon-

strip system will be mounted. Its task will be to improve tracking performance by providing additional high-precision space points along particles' paths.

Electromagnetic Calorimeter

The *electromagnetic calorimeter* (ECAL) will be a 17 cm thick sampling calorimeter with 30 longitudinal layers. It will be split into a barrel and an end-cap part. Tungsten was chosen as an absorber for the ECAL to meet the requirements of compactness of the detector and the ability of separating adjacent showers. Silicon strips and small $5.1 \times 5.1\,\mathrm{mm}^2$ scintillator pads read out by silicon photo-multipliers (SiPMs) or their combination are considered for the active medium of the calorimeter. The ECAL design is optimised for usage of particle flow algorithms.

Hadron Calorimeter

Like the ECAL, the *hadron calorimeter* (HCAL) will be a sampling calorimeter divided into a barrel and end-cap part. The ILD HCAL barrel for CLIC and the ILC will consist of 75 and 48 layers, respectively. At the ILC, steel will be used as an absorber in the entire calorimeter. At CLIC, due to its much higher target centre-of-mass energy, tungsten is considered to be utilized in the HCAL barrel and steel will be used in the end-caps.

There are several technologies considered for the active layers. One option are $3 \times 3\,\mathrm{cm}^2$ scintillator tiles with analog SiPM readout. The second possibility is a gaseous detector with $1 \times 1\,\mathrm{cm}^2$ cells based on resistive plate chambers (RPCs), Micro-Mesh Gaseous Structures (Micromegas) or Gas Electron Multiplier (GEM) foils with digital or semi-digital readout. An analog readout has the advantage of providing full information about the deposited energy. A detector read out digitally can estimate the energy deposition just from number of struck cells. The SiPM-based analog option of the CLIC_ILD HCAL was used in the detector model employed in the top quark study presented in chapter 6.

Magnet System

For successful particle identification and particle flow reconstruction, all above mentioned detectors are enclosed in a *superconducting solenoidal magnet* with a field of 4 T and 3.5 T in the case of CLIC and the ILC, respectively. A strong magnetic field parallel to the beam line is necessary to confine low-p_T particles originating from beam-induced background within the beam pipe, to reach a high momentum resolution and to separate different particle tracks coming from high energy jets.

The *iron yoke* which returns the magnetic flux of the solenoid will be equipped with nine track-sensitive layers made of either scintillator stripes or glass RPCs. With this instrumentation, the yoke serves also as a muon filter, muon detector and tail-catcher calorimeter. Thereby, the energy measurements of high energy hadrons will be slightly improved.

Very Forward Region Detectors

LumiCAL and BeamCAL (and LHCAL at the ILC) will be high-precision sandwich semiconductor-tungsten calorimetric detectors which will be installed at very forward angles

beyond the acceptance of the ECAL and the HCAL. The LumiCAL will perform accurate measurements of luminosity. The BeamCAL will serve as a tool for beam diagnostics. Because of very high radiation levels in the forward regions, both of these detectors will have to be extremely radiation hard. They will be exposed to doses in the order of MGy/y.

The very forward regions of the ILD will also contain quadrupole magnets of the beam delivery system for final beam focusing.

2.4.2. Silicon Detector

In the figure 2.4b, it can be seen that the design of SiD is very similar to that of ILD. SiD is also a general-purpose detector focused on excellent jet-energy reconstruction and particle flow reconstruction. All tracking detectors, the ECAL and the HCAL are nested in a superconducting solenoidal coil with magnetic field of 5 T. The solenoid is enclosed in an iron magnetic flux return yoke. The main differences between the SiD and ILD lie in the tracking system and in the choice of technology for the active layers of the electromagnetic and hadron calorimeter. The tracker is made exclusively of silicon detectors. It is divided into the barrel and disc section and it will utilize single-sided silicon microstrip detectors. The barrel contains five silicon layers with 20 μm pixel size. The forward and backward region consists of four silicon discs with pixel pitch of 50 μm. Three additional silicon pixel discs are located at a larger distance from the interaction point. Such a configuration provides a very good track pattern recognition and impact parameter resolution over the full solid angle. The outer radius of the main tracker barrel will be 1.25 m. Silicon detectors with $3.5 \times 3.5\,\mathrm{mm}^2$ hexagonal pixels were chosen for the active layers of the ECAL of SiD. The ECAL will consist in a total of 30 layers with tungsten as absorber. The SiD HCAL will use glass RPCs with $10 \times 10\,\mathrm{mm}^2$ readout pad size in its active layers. The other detector systems of SiD, like the BeamCAL, LumiCAL, muon system, etc., will be implemented in a similar way to the ILD.

2.5. Detector Requirements

The construction requirements for the detector system for future linear colliders are dictated by the necessary precision of the planned physics measurements. One of the important processes to be studied is the higgsstrahlung $e^+e^- \to HZ$ which is followed by a decay $Z \to \mu^+\mu^-$. To be able to determine the Higgs mass successfully under the conditions of $250 - 350\,\mathrm{GeV}$ CLIC, a momentum resolution of $\sigma_{p_T}/p_T^2 \lesssim 2 \cdot 10^{-5}\,(\mathrm{GeV/c})^{-1}$ is needed.

Another set of interesting physics processes results in final states consisting of jets created by hadronization of individual quarks. The capability of reconstructing the invariant mass of the jet is crucial for all measurements containing W and Z boson hadronic decays $W/Z \to q\bar{q}$. The separation of W and Z invariant mass peaks for different jet mass resolutions σ_m/m is depicted in figure 2.5a. To obtain $2.5\,\sigma$ separation of the W and Z, $\sigma_m/m \lesssim 3.5\,\%$ is required in the CLIC operational range between 50 GeV and 1 TeV. Additionally, BSM searches based on mass measurements will also benefit from a high jet energy resolution.

A further important parameter is the b quark flavor tagging ability which enables discrimination of c-, b- and light jets. The flavor tagging will play a substantial role in mea-

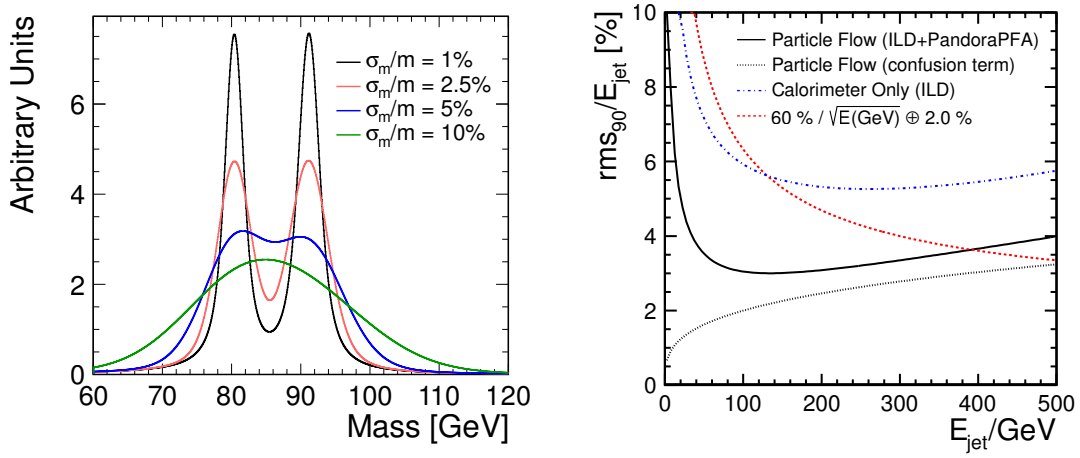

(a) W and Z invariant mass peak separation

(b) Jet energy resolution of the ILD

Figure 2.5.: (**a**): Separation of W and Z invariant mass peaks for different jet mass resolutions σ_m/m. (**b**): Jet energy resolution of ILD as a function of jet energy. *Solid black line*: the total resolution using PandoraPFA algorithm [49]. *Black dotted line*: an estimate of the confusion term contributing to the total resolution. *Blue dash-dotted line*: resolution obtained from calorimetric energy deposition. *Red dashed line*: the highest resolution achievable by traditional calorimetric approach ($60\,\%/\sqrt{E[\mathrm{GeV}]} \oplus 2.0\,\%$). Taken from [44] and [49].

surements of branching ratios and couplings of the Higgs particle. It is also needed for e.g. top quark studies. Performance of the b-tagging is strongly dependent on the impact parameter resolution σ_{IP}. This must be better than

$$\sigma_{IP} = 5\,[\mu\mathrm{m}] \oplus \frac{15\,[\mu\mathrm{m}]}{p\,[\mathrm{GeV/c}] \cdot \sin^{3/2}\theta}\,, \tag{2.2}$$

where p is the momentum of a given charged particle. The first term in equation (2.2) is given by the point resolution of the vertex detector, the second one is related to multiple scattering of the particles in the inner detector. Thus, it is important to reduce the amount of material in the innermost tracking detectors as much as possible.

To study SM processes which produce particles at low angles along the beam line, the detector coverage must be extended up to such low angles. Good coverage also helps to reject these processes in some BSM studies. For the BSM investigation and analyses of semi-leptonic decays, it is also important to be able to identify high energy leptons. The required lepton identification efficiency is $\geq 95\,\%$.

2.5.1. Particle Flow

It is known from the fragmentation measurements performed by LEP [50, 51] that the average particle composition of a jet is the following: $\sim 62\,\%$ charged particles (mainly hadrons), $\sim 27\,\%$ photons, $\sim 10\,\%$ long-live neutral hadrons and $\sim 1.5\,\%$ neutrinos. Usu-

ally, the jet energy measurement relies on the HCAL. Despite the fact that the HCAL resolution is limited to $\gtrsim 55\,\%/\sqrt{E}$, where E is the particle energy, the energy of about 72 % of the particles in the jet is determined in the hadronic calorimeter. The *particle flow* (PF) approach is a reconstruction technique to reach a high jet energy resolution σ_E/E. To improve the resolution, the PF algorithms reconstruct the four-momenta of all visible particles produced in each event. Some clusters of energy deposition in the calorimeter are assigned to charged particles using their tracking information. The remaining clusters serve for determination of four-momenta of neutral particles. Since the photon energies in the jet are measured in the ECAL and the neutrinos cannot be detected at all, only the energy of the neutral hadrons (10 %) is obtained from the HCAL. Performance of the PF reconstruction is not perfect in practise. For example, if a part of a charged hadron cluster is identified as a cluster deposited by a neutral particle, this energy is effectively counted twice since it is already contained in the charged particle momentum. This effect is called *confusion* and it is the limiting factor of particle flow calorimetry. However, with the help of this method, the required σ_E/E better than 3.5 % is achievable. Figure 2.5b shows performance of ILD using different calorimetric approaches. It also displays an estimate of the so called confusion term of the PF method. Apparently, the confusion is the driving factor of jet energy resolution in the PF approach.

To be able to take advantage of all the benefits of the PF method, the detector systems have to fulfil certain demands. The tracking detectors must have a very high spatial resolution to assign precisely the tracks of charged particles to the clusters of deposited energy in the calorimeter. An accurate tracking suppresses the confusion term. The ECAL and the HCAL must also have the capability of distinguishing showers of two nearby particles. This will be achieved by a very high granularity of the detectors. The proposed lateral cell size is $1 \times 1\,\mathrm{cm}^2$ for the ECAL and $3 \times 3\,\mathrm{cm}^2$ for the HCAL to reach a compromise between the jet energy resolution and technical feasibility. In addition to that, to maintain highly accurate tracking performance to be able to associate the tracker and calorimeter information, the dead material between these two detectors must be reduced as much as possible. This can be fulfilled by putting the entire calorimeter system in the solenoid. The high granularity calorimeters can basically provide a picture of an electromagnetic or hadronic shower. Due to that capability, they are sometimes called *imaging calorimeters*.

2.5.2. Timing Requirements at CLIC

The main background source at CLIC are incoherent e^+e^- pairs and $\gamma\gamma \rightarrow$ hadrons reactions. The incoherent e^+e^- pairs are created by a strong electromagnetic field of the electron and positron bunches. Particles from the incoherent pairs have a small transverse momentum p_T and hence strike mainly the vertex and the forward region. This background can be substantially reduced by applying a p_T cut. The real and virtual photons from the colliding beams can also undergo reactions which lead to hadronic finals states. These processes also produce particles with higher p_T which will form a dominant background in the main tracking detectors and calorimeters. Due to the high p_T particles, the $\gamma\gamma \rightarrow$ hadrons events cannot be easily excluded and pose a challenge for the data analysis. Because both of these backgrounds originate from beam interactions, their amounts scale with the number of integrated bunch crossings within the measurement time window. The total deposited energy in all detector systems integrated over the whole bunch train (312 bunch crossings,

156 ns) is about 19 TeV. This deteriorates the jet energy resolution and hence measurements of invariant mass.

Simulation results show that an acceptable background level corresponds to 5−10 bunch crossings which requires a time resolution better than 5 ns for all detectors [44]. However, regardless of technical feasibility, there is a physical limitation of the minimal time window, because the timescale of hadronic shower development is significantly longer than few ns. Furthermore, tungsten has a slower response than steel. This is due to more frequent nuclear processes in tungsten which take place during the shower development. The energy in the nuclear processes is not released instantaneously which slows down the overall shower process. Obviously, there are two contradictory requirements. The first one for a short measurement window to suppress the background and a second one for a long time window to record enough energy of the hadronic shower.

This issue can be resolved by using different timing requirements for separate subdetectors. The data of a whole bunch train will be acquired and analyzed offline. Candidates for hard interactions will be identified within the bunch train and the data in a given time window around the time of the hard process will be accepted for the event reconstruction. The time window for silicon detectors, ECAL and HCAL end-cap will be 10 ns and for the HCAL barrel 100 ns. The TPC cannot be triggered like this, because it integrates over the whole bunch train. The $\gamma\gamma \rightarrow$ hadrons background will be reduced roughly by a factor of 15 by the tracker 10 ns integration window. However, it can be suppressed even more by tighter time cuts based on time stamping of calorimeter clusters. Each energy deposition cluster will get a time stamp calculated as a truncated mean of the energy-weighted hit times within the cluster. A resolution of less than a nanosecond can be achieved with a highly granular particle flow detector. By applying tight timing cuts in the range of 1.0 − 2.5 ns, the background level can be reduced to about 100 GeV. The impact of the cutting on the physics processes of interest is negligible.

CHAPTER 3

SILICON PHOTOMULTIPLIERS

Silicon photomultipliers (SiPM) are sensors designed for detection of visible and near-visible light with very low intensities like a few up to a few hundred photons. They were invented in 1989 [52] and they find applications in medical imaging or experimental physics. SiPMs are the key element for construction of highly granular calorimeters for future linear colliders like CLIC and the ILC. They have several favourable features compared to photomultiplier tubes. SiPMs are very robust and small, with an area is few square millimeters and thickness about half a millimeter. They are insensitive to magnetic fields and require operation voltage up to 100 V. SiPMs are designed to operate at room temperature and do not require any kind of cooling. However, there are also some problematic points like high sensitivity to ambient temperature and low radiation hardness. There are several names for SiPMs depending on the producer like multi-pixel photon counters (MPPC), multi-pixel Geiger-mode-operated avalanche photo diodes (G-APD), solid state photomultipliers (SSPM) or avalanche photo diodes with metal resistance semiconductor structure (MRS APD). We will stick to the designation SiPM in most of the cases. The basic features and characteristics of the SiPM will be explained in this chapter.

3.1. Basic Layout and Working Principle

SiPMs are semiconductor photon detectors which are capable of detecting very small amounts of visible, ultra-violet (UV) and infrared (IR) light. An example photo of a SiPM is shown in figure 3.1a, further photographs can be found in appendix B.4. The sensor consists of a few tens up to tens of thousands individual p-n *avalanche photodiodes* (APD) arranged in an array and connected in parallel. Each of the diodes is called *pixel* or *microcell*. The typical area of the diode array is a few mm^2 and the physical distance of the centres of the pixels (*pixel pitch*) ranges between a few μm and a few hundred μm. The microcells are connected to a common output line as shown in schematic in figure 3.1b. They are operated with a reverse bias voltage a few volts above the breakdown voltage, in the so called *Geiger mode*. This means that if a breakdown of the semiconductor junction occurs, both charge carrier types, electrons and holes, are involved in the multiplication

process. The avalanche spreads across the whole diode, similarly to a discharge in gas Geiger tube. The part of the applied voltage exceeding the breakdown voltage is referred to as *over-bias voltage*. The SiPM design has a major advantage of the photon counting capability originating from a combination of two features. First, because every cell is operated in Geiger mode, it works as a binary detector. Either, it supplies a zero signal or, when triggered, it gives a signal which has always the same shape and amplitude. Second, thanks to the parallel connection and common readout of all cells, the output signals of all pixels are superimposed one on the top of each other. This two properties together allow determination of the number of microcells contributing to the output signal.

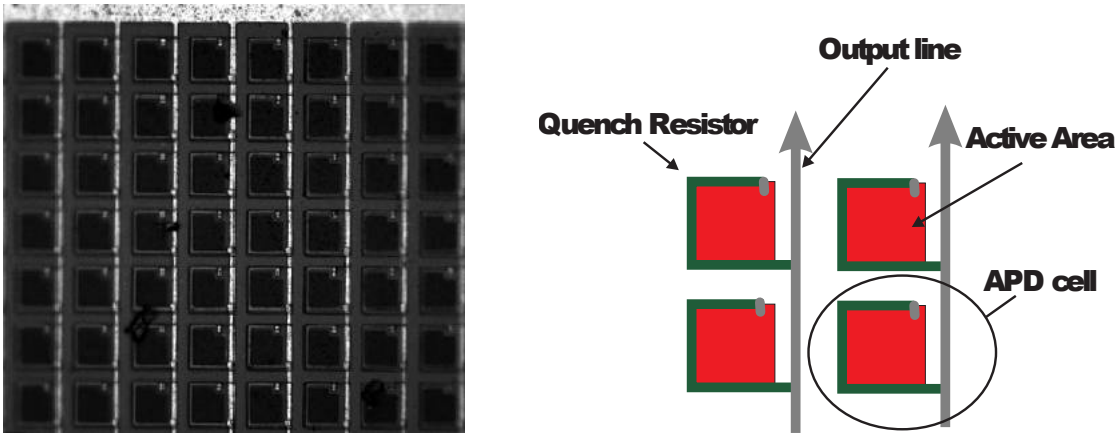

(a) SiPM chip with polysilicon quench resistor

(b) Sketch of four SiPM pixels

Figure 3.1.: Photograph of a SiPM chip with a polysilicon quench resistor (**a**) and a schematic sketch of four SiPM pixels (**b**). Taken from [53] and [54].

In a Geiger mode operated p-n junction, any single free electron or hole can trigger an avalanche independently from the partner. These charge carriers can be released due to an interaction with a photon or by thermal excitations. The applied electrical field acts on the free charges and accelerate them towards the respective electrodes. After a short distance, they gain enough energy to create electron-hole pairs through impact ionisation of atoms. Each new electron undergoes the same process and the avalanche evolves. This breakdown of a p-n junction is called *Geiger discharge* or simply the *"firing"* of a pixel. Without any further treatment, after a certain time of avalanche development, the diode current would saturate and the avalanche would sustain for a hardly predictable time period. In order to be able to stop the avalanche, the diode is biased through a *quench resistor*. A simplified electrical schematic of one SiPM microcell is depicted in figure 3.2. When the APD fires, the resulting current causes a voltage drop on the resistor, the bias voltage on the APD falls and the avalanche stops. The resistance R_Q of the resistor affects the magnitude of the bias voltage drop. Furthermore, the R_Q together with the diode capacitance C_D and the additionally manufactured capacitance C_C determines the duration of the output electrical pulse τ in the following way [55, equation (4)]:

$$\tau = R_Q \cdot (C_D + C_C). \tag{3.1}$$

During the time span τ after the breakdown, the bias voltage goes back to its initial value before the breakdown. Therefore, τ is called the *recovery time* of the pixel. During the recovery phase, the cell is still sensitive to incident photons which would cause another breakdown of the junction. However, because of the lowered bias voltage, the gain as well as the *Geiger efficiency* of the pixel (see below) are lower and ill-defined. As a consequence, the resulting pulse cannot be properly evaluated. To avoid this effect, SiPMs should be always used for detection of light intensities which are low enough, so that the cells have enough time to recover before being triggered again.

A more detailed description of the electrical properties of SiPMs can be found e.g. in [55].

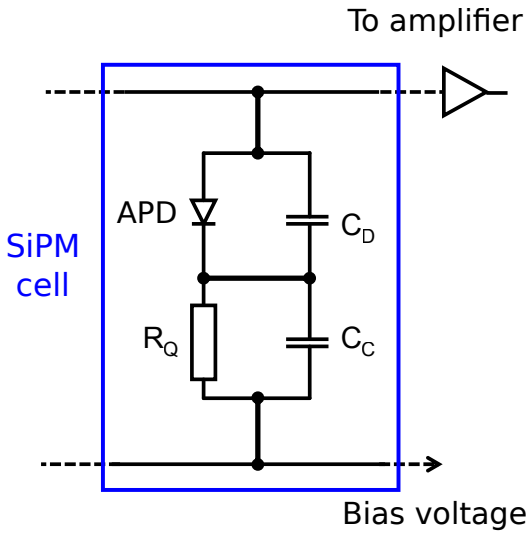

Figure 3.2.: A simplified electrical schematic of one SiPM microcell. *APD* represents the avalanche photodiode, C_D is the capacitance of the p-n junction, R_Q is the quench resistance and C_C is a additionally manufactured capacitance. Based on [56].

3.1.1. Quench Resistor

There are several ways how to implement the quench resistor. The most common approach is a resistor made of polysilicon. Another possibility, which is recently under development, is the usage of the silicon bulk beneath the sensitive region as a quench resistor. These two solutions will be now described.

Polysilicon Quench Resistor

The vast majority of nowadays commercially available SiPMs use a polysilicon quench resistor. It is made of a polysilicon stripe deposited on the surface of the silicon wafer. A schematic vertical cross section of a SiPM equipped with a polysilicon quench resistor is depicted in figure 3.3a. The high field region is formed in the p^+-n^+ junction. The diode is biased and read out via the aluminium line and the quench resistor. A drawback of

this solution is that the manufacturing of the polysilicon structure is a very complex and expensive process. The resistor as well as the aluminium conductor also occupies a certain area of the sensor surface and reduces the size of the entrance window. The dimensions of the polysilicon stripe and the metal line do not change considerably for pixels with different pitches. Therefore, the resistor covers a relatively larger area for small pixels compared with big ones. Furthermore, the resistivity of the polysilicon is temperature dependent [57].

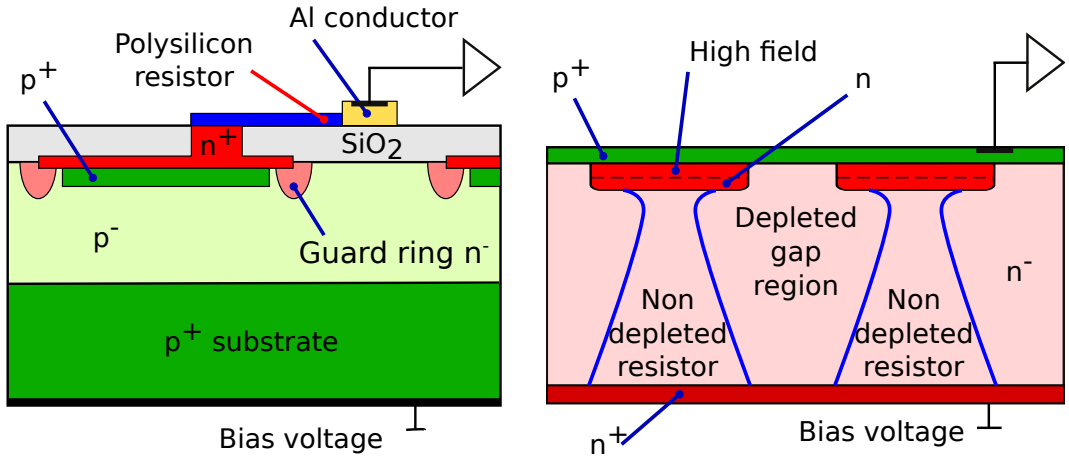

(a) SiPM with a polysilicon quench resistor (b) SiPM with a bulk-integrated quench resistor

Figure 3.3.: Schematic vertical cross section of a SiPM with a polysilicon (**a**) and a bulk-integrated (**b**) quench resistor. Drawings based on [58] and [59].

Quench Resistor Integrated in Silicon Bulk

Another approach is to use the silicon bulk as a quenching resistor [60, 61]. In figure 3.3b, a schematic cross section of a device a with bulk-integrated quench resistor is shown. The active volume of the sensor lies in the high field region at the junction of the common p^+ cathode and the n-type implantation beneath. After applying a bias voltage via the lower n^+ electrode, depleted and non-depleted regions are formed along the device. These are marked with blue curves in figure 3.3b. The depleted region in between the pixels serves as a barrier which separates the pixels electrically. The non-depleted space in the silicon bulk behaves like a quenching resistor. Magnitude of its resistivity depends mainly on pixel pitch, bulk material doping level, wafer thickness, and bias voltage. With increasing voltage the non-depleted region is getting thinner and thus its resistivity grows. According to pixel size, the bulk thickness and resistivity must be adjusted carefully to reach a proper resistance. For this reason, standard silicon wafers with thickness of a few hundred micrometers must be often thinned down. This additional but necessary step makes the fabrication procedure more complicated. However, manufacturing of these devices is still simpler and cheaper than of the sensors with polysilicon resistor. Another advantage of this technology is the absence of the polysilicon structure on the surface. When the common cathode is used, no metal lines and contacts in the entrance window are required. This makes it possible to achieve a larger active area. One of the disadvantages of this ap-

proach is the formation of a parasitic JFET[1] in the sensor structure [62]. This complicates the problem of the quenching resistor. It cannot be treated as a simple resistor in simulations and the recovery time is 3-4 times longer in comparison with SiPMs equipped with polysilicon resistors. Bulk resistors exhibit also a temperature dependence.

3.2. Gain

The *gain* is a multiplication factor between one initially liberated elementary charge and the output charge of the detector. An illustration of the gain of a semiconductor diode used as a light detector as a function of bias voltage U_{bias} is shown in figure 3.4a. A gain of 1 means no amplification. With increasing bias voltage, the detector enters an avalanche mode at some point. With further voltage increase, the gain grows steeply. When the breakdown voltage U_{break} is exceeded, the Geiger mode is reached. In Geiger mode, the gain increases only moderately with growing voltage. The gain G of SiPMs ranges between 10^5 and 10^7. The total avalanche charge Q_{av} of a Geiger mode operated device is independent of the initial amount of free charge in active volume of the junction. Q_{av} is determined by pixel capacitance C_{pix} and by the over-voltage U_{over}:

$$Q_{av} = G \cdot e = C_{pix}(U_{bias} - U_{break}) = C_{pix} \cdot U_{over}, \tag{3.2}$$

where e is the elementary electrical charge. It is obvious that the gain is directly proportional to the over-bias voltage and independent of the number of electron-hole pairs created by the incident particle. From this point of view, a higher operation voltage brings a benefit of high gain. However, the choice of a proper over-bias is a compromise between high gain and high dark noise (see below). The typical over-bias voltage level is ~10 % of the breakdown voltage.

[1] JFET - junction gate field-effect transistor

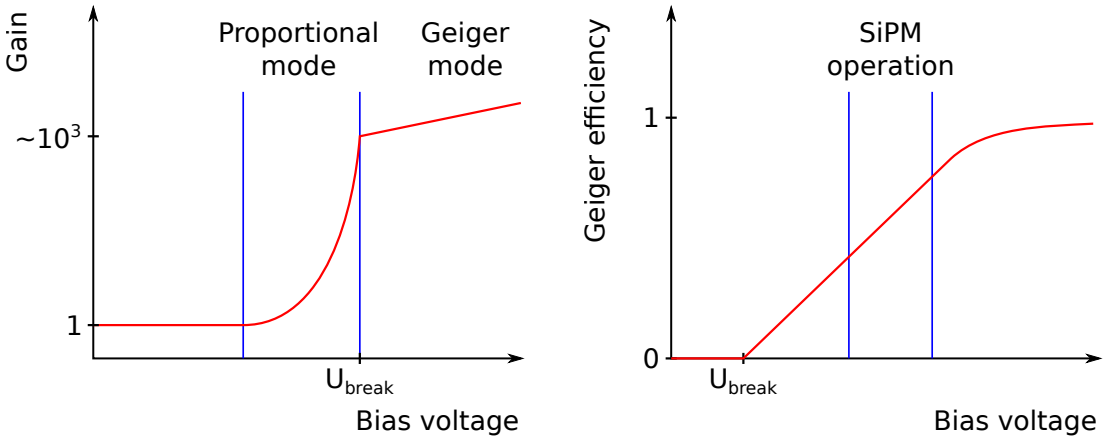

(a) Gain vs. bias voltage

(b) Geiger efficiency vs. bias voltage

Figure 3.4.: Bias voltage dependencies of gain (**a**) and Geiger efficiency (**b**) of a reverse-biased silicon p-n junction used as a photodetector. U_{break} stands for breakdown voltage. Scales of all axes are linear. Drawings based on [63, 64, 65].

3.3. Photon Detection Efficiency

The *photon detection efficiency* (PDE) η_{PDE} is the probability that an incident photon induces an avalanche in a photo-detector. For a Geiger mode operated detector, it is given by the product of the quantum efficiency η_Q, the Geiger or also breakdown efficiency η_B and the geometrical fill factor η_G of the sensor:

$$\eta_{PDE}(\lambda, U, T) = \eta_Q(\lambda) \cdot \eta_B(U, T) \cdot \eta_G, \tag{3.3}$$

where λ is the wavelength of incident radiation, U is the SiPM operation voltage and T is sensor temperature. The quantum efficiency is a probability that a photon creates an electron-hole pair in the high field region. The Geiger efficiency is a probability that an avalanche is initiated by an electron or hole in the active region. The geometrical fill factor is the ratio between the light sensitive area and the total area of a photodetector. It is given by the design of a particular detector.

The dependence of the Geiger efficiency on the bias voltage is sketched in figure 3.4b. The Geiger efficiency is zero until the breakdown voltage is reached. Then, it rises almost linearly and later turns into saturation. SiPMs are usually operated in the region of nearly linear growth of η_B before the onset of the saturation.

The PDE is also a function of wavelength of the incident photons. This dependence for Hamamatsu MPPCs is shown in figure 3.5. The wavelength sensitivity can be also affected by the choice of the SiPM design. Absorption length of photons in silicon is a function of their λ. Hence, photons with different energies are absorbed in different depths. The depth of the interaction of the photon in the silicon together with the layout of the p-n junction decides whether the avalanche is triggered by an electron or a hole. Since the Geiger efficiency differs for holes and electrons, the overall PDE is also affected. The standard SiPM structure is an n-doped implant on p-type substrate, as shown in figure 3.3a. This con-

figuration is the most suitable for detecting green to red light. Enhanced sensitivity for blue and UV light can be achieved by an inverted structure with a p-doped implant on an n-type substrate. The Hamamatsu MPPCs use the inverted structure approach. The blue and UV sensitivity is very favourable for scintillation light readout, because the emission wavelength of plastic scintillators is usually in this range. For examples of emission wavelengths of plastic scintillators see e.g. table 5.1.

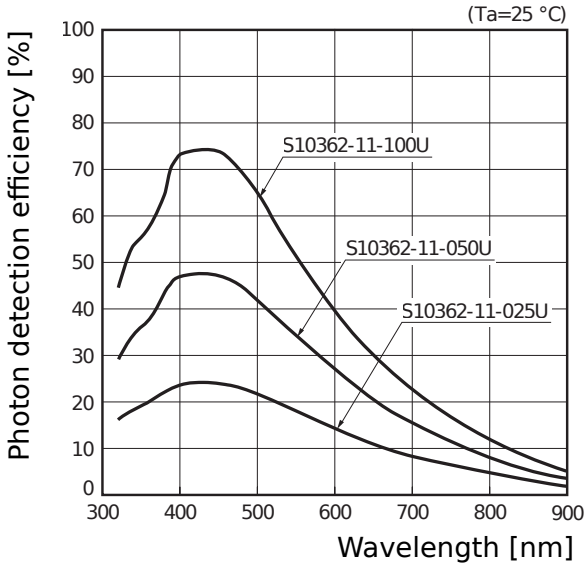

Figure 3.5.: Wavelength dependence of the photon detection efficiency of Hamamatsu MPPCs with pixel pitch of 25, 50 and 100 μm. Taken from [66].

3.4. Signal Response Function and Saturation

As mentioned above, the signals coming from different SiPM cells add up. Thanks to this, it is possible to determine the number of the fired microcells from the signal integral within a certain time window. This capability is demonstrated in figure 3.6a. The plot shows rates of events with a given integral of the SiPM output signal when a SiPM was illuminated by a weak light source. The first red-marked peak is caused by electronic noise and does not have a physical meaning. All other peaks represent events, in which the respective number of photo-electrons (p.e.) was detected.

However, since the number of pixels N_{tot} in a SiPM is limited and the recovery time of a microcell is finite, the relation between the number of generated and detected photoelectrons is not linear. This dependence is approximated by a signal response function of a SiPM [67]. Assuming light pulses much shorter than the microcell recovery time and a uniform illumination of the detector surface, the number of fired pixels (detected photoelectrons) N_{pix} can be described by

$$N_{pix} = N_{tot} \cdot \left(1 - e^{-\frac{N_{p.e.}}{N_{tot}}}\right), \tag{3.4}$$

where $N_{p.e.}$ is the number of generated photo-electrons. $N_{p.e.}$ is a function of the number of incident photons N_γ, the PDE η_{PDE} and the crosstalk probability κ of the SiPM [63]. It can be calculated like

$$N_{p.e.} = N_\gamma \cdot \eta_{PDE} \cdot (1 + \kappa)\,. \tag{3.5}$$

An illustration of the response function (3.4) and its comparison to a linear behavior is shown in figure 3.6b. The saturation behavior of the response function can be suppressed by the use of a sensor with a high number of smaller pixels which, on the other hand, brings other issues like a poor fill factor etc.

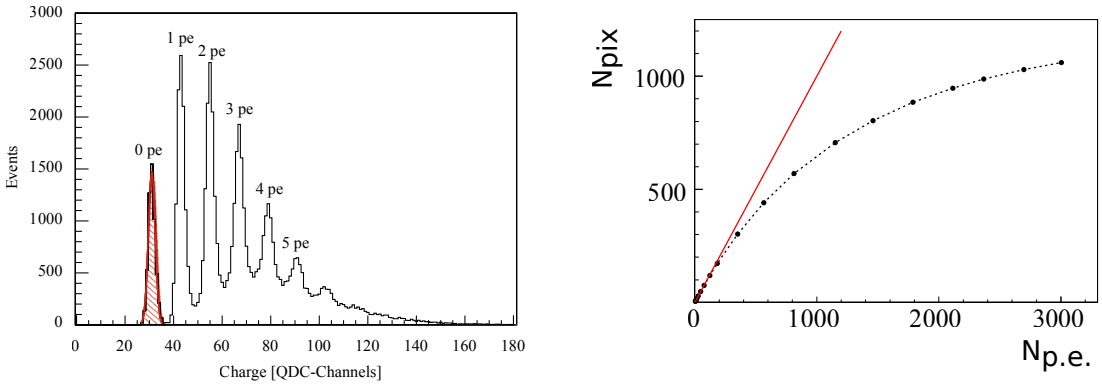

(a) Single photon spectrum

(b) SiPM response curve

Figure 3.6.: (**a**): Single photon spectrum obtained by illuminating a SiPM (Hamamatsu MPPC-50), noise peak is marked red. (**b**): Response curve of a SiPM showing saturation (dots). The red solid line shows an ideal linear behavior. $N_{p.e.}$ is the number of generated photo-electrons, N_{pix} is the number of fired pixels. Plots taken from [68] and [63].

3.5. Dark Noise and Afterpulsing

Electron-hole pairs are generated in the active region also by thermal excitations. When a device is operated above the breakdown voltage, the thermally liberated electrons-hole pairs can induce an avalanche. These events are called thermal pulses and they occur without any illumination of the pixels. Hence, the thermal pulses of a sensor enclosed in a perfect dark box are named *dark noise* and their rate is called *dark count rate*. The dark count rate depends on temperature, size of the active volume and Geiger efficiency. Dark noise also increases exponentially with growing bias voltage. Therefore, it plays an important role in setting of the most suitable operation voltage of a SiPM. A compromise between high gain and low dark count rate must be found. Furthermore, the dark count rate is strongly influenced by the quality and purity of the silicon wafer material which was used for the SiPM production. Typical dark count rate of a SiPM is roughly a few hundred kHz/mm^2.

Another effect causing fake signals is called *afterpulsing*. It arises due to existence of additional levels in a band gap region of semiconductor energy level structure [69]. Charge carriers can be trapped in these metastable levels for some period of time and released afterwards with some delay. These freed particles can trigger another avalanche and thus result in a fake pulse coming after a real one. The afterpulsing rate is inversely proportional to the pixel recovery time and temperature. Therefore, it becomes more significant when the device is operated at low temperatures.

3.6. Optical Crosstalk

When a p-n junction is reversely biased up to breakdown voltage, visible light is emitted from the junction [70]. This light is created in the spots where the breakdowns occur [71]. About 10^{-5} photons with a wavelength less than 1 µm are released from a breakdown avalanche per one electron crossing the junction [72]. The emitted photon can travel through the silicon. If it is absorbed in the active region of a neighboring pixel, it could initiate an avalanche. A subsequent breakdown of the neighboring pixel contributes to the output signal with a fake pulse. This effect is called *optical crosstalk*. It can be quantified by the *crosstalk probability*, which is defined as a ratio of the rate of ≥ 1 p.e. and the rate of ≥ 2 p.e. events for a SiPM which is not illuminated. According to the definition, the crosstalk probability can be extracted from dark noise amplitude spectrum. This method is allowed by the fact that one single cell does fire almost exclusively at a time due to thermal excitations. Hence, signals coming from two fired cells in the same moment originate almost entirely from the optical crosstalk. The effect of the optical crosstalk can be suppressed by adding trenches in between the pixels [73]. The crosstalk probability increases with growing gain. This is illustrated in figure 3.7a.

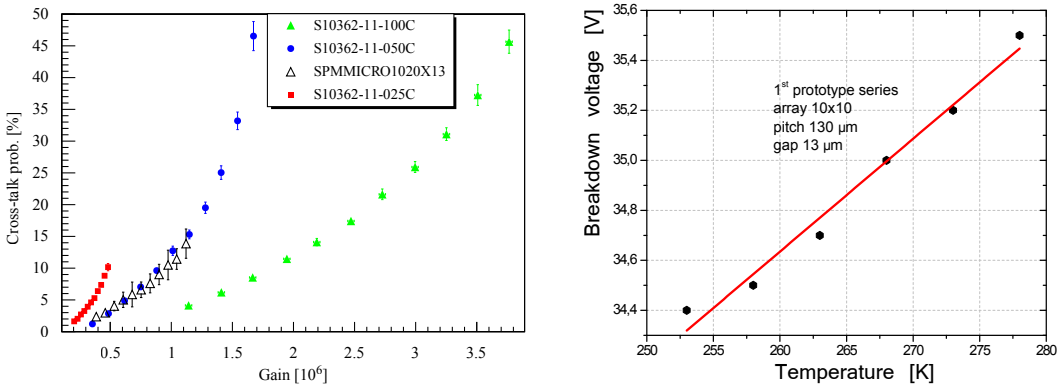

(a) Crosstalk probability vs. gain

(b) Breakdown voltage vs. temperature

Figure 3.7.: Crosstalk probability as a function of gain for different SiPMs (**a**) and breakdown voltage as a function of temperature of SiMPl detector (**b**). Taken from [68] and [74].

3.7. Temperature Effects and Light Intensity Measurement

One of the biggest issues of SiPM operation is their considerable sensitivity to temperature. It has been already mentioned that the dark noise, afterpulsing and PDE are temperature-dependent. Moreover, the breakdown voltage is a function of temperature as well. This dependence is demonstrated on experimental data in figure 3.7b. It has an extensive impact on the output characteristics, because gain, crosstalk probability and PDE are functions of over-voltage. If the operation voltage is kept fixed, a temperature change causes a variation of the over-bias voltage with all related consequences. For example, the breakdown voltage temperature gradient for an MPPC-50 is 56 mV/K [75].

It is clear from the described SiPM properties that for an absolute measurement of light intensities with a given SiPM the following parameters of the sensor must be known: Gain, photon detection efficiency, dark count rate and afterpulsing probability. In addition, the requirements of short light pulses (compared with the recovery time) and uniform sensor illumination must be fulfilled in order to compensate for non-linear behavior of SiPMs according to equation (3.4). Because the first three essential SiPM parameters are voltage dependent and all of them are a function of temperature, the operation conditions of the detector must be carefully controlled.

Part II.

Technology for Future Linear Colliders

CHAPTER 4

SILICON PHOTOMULTIPLIER HOMOGENEITY STUDIES

Silicon photomultipliers (SiPM) [76, 77, 67] (see also chapter 3) are modern semiconductor photon detectors with many possible applications, e.g. in medicine, astronomy or high energy physics. SiPMs are capable of detecting single photons, offer a high intrinsic gain of $10^5 - 10^7$ and fast timing resolution at the order of a few hundred ps. They are insensitive to magnetic field and are very compact and robust. These properties open a variety of new possibilities for a construction of detector systems for accelerator experiments. The SiPMs, thanks to their small size compared to *photomultiplier tubes*, can be employed for example in a very compact and highly granular calorimeter. Furthermore, the calorimeter can be placed in solenoidal coil of a complex detector system. This is a favorable option for several reasons given in section 2.5.1. Future linear e^+e^- colliders presented in chapter 2 intend to utilize a concept of such calorimeters equipped with SiPMs.

Since the SiPMs are still being extensively developed and steadily improved by many manufacturers, it is very important to characterize and understand them. The SiPMs can be studied from many points of view. In this chapter, we focus on one particular parameter, the *areal distribution of the relative photon detection efficiency*. Because the SiPMs consist of many individual microcells, it is very likely that some inhomogeneities in the photon detection efficiency (PDE) across the SiPM area will be present. By direct determination of the areal distribution of the PDE, precise dimensions of the active area of a sensor can be obtained. The quality, by means of PDE homogeneity, of a given device can be quantified by that information and compared with other samples. Furthermore, a precise PDE homogeneity measurement can provide important information during the development phase of a new SiPM, like the SiMPl device [59]. SiMPl is being developed in the Semiconductor Laboratory of the Max Planck Society in Munich, Germany.

Testing of new production series of these sensors motivated a construction of a new experimental apparatus for PDE homogeneity measurements. The setup has been successfully assembled as part of this thesis. It is based on scanning of the SiPM with a strongly focused beam of visible light and an excellent sub-microcell positioning precision. Our

experimental apparatus provides relative values of PDE of the examined device which can be obtained for a fixed wavelength given by the used light source. Besides testing of new devices, the setup offers also an opportunity to study and compare devices developed and produced by different manufacturers. This is very important for understanding and characterizing SiPMs which have been used in experiments such as the *Tungsten Timing Test-Beam experiment* (T3B) [78] and studies described in chapter 5.

In this chapter, we present a study of the areal distribution of the relative photon detection efficiency of different SiPMs. We focused on Hamamatsu Multi-Pixel Photon Counters (MPPC) which were used in the above mentioned experiments. For performance comparison of these sensors, corresponding tests of three further devices were done. A MEPhI[1]/Pulsar[2] prototype and two commercial SPMMicros manufactured by SensL were studied. Regarding the SiMPl device, tests of a few older prototypes of the second iteration series were performed, because the production of the next series was delayed by several years and did not take place before this thesis was finished.

4.1. Photon-Emission Measurement

The active and inactive area on a SiPM can be distinguished by measuring the breakdown distribution across the sensor surface. A method which can also tell where the breakdowns take place is a photon-emission measurement. When a pn-junction is reversely biased up to breakdown, visible light is emitted from the junction [70]. Furthermore, the light is created in the spots where the breakdowns occur [71]. The photon yield is about 10^{-5} photons per one electron crossing the junction during a breakdown avalanche [72]. This effect can be used to record a picture of breakdown distribution across a semiconductor device. The detection of these photons is what we call the photon-emission measurement. It can be conducted in a dark box with the help of a CCD[3] camera which integrates the emitted photons over a time period of hundreds to thousands of seconds. When a Geiger-mode-operated device is tested with this method, one obtains also a hint about high electrical field distribution, because a stronger electrical field makes the breakdowns more likely. The high field also directly influences the sensitivity of the SiPM to incident light, because the Geiger efficiency of a sensor grows with rising electrical field strength.

However, a drawback of this approach is that only the breakdowns caused by thermal noise are recorded and their distribution does not necessarily have to reflect the PDE distribution. Leakage currents also contribute in the recorded picture. Complementarily to the photon-emission measurement, a need of another testing apparatus arose.

The photon-emission measurement was performed for some of the devices which were tested with the new scan setup, too. These results are shown in appendix B.3. The photo-emission experiments were done with a Hamamatsu emission microscope PHEMOS-1000 [79]. An example of a photo-emission image of a Hamamatsu MPPC-50 is shown in figure 4.1.

[1] MEPhI - Moscow Engineering Physics Institute
[2] SUE "SPE Pulsar" - State Unitary Enterprise "Scientific and Production Enterprise Pulsar", Moscow
[3] CCD - charge coupled device

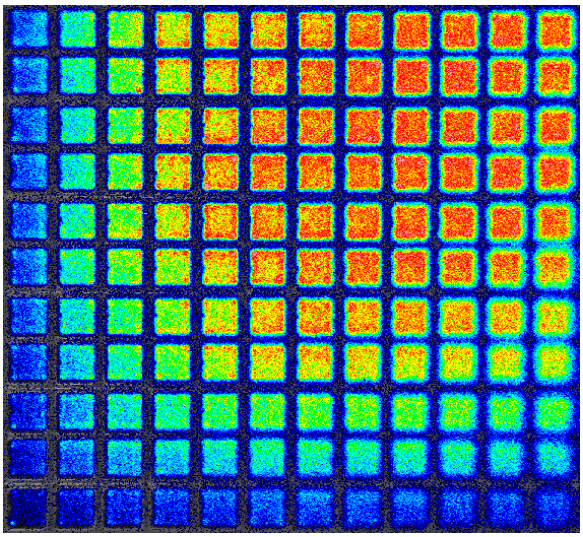

Figure 4.1.: Example photo-emission image of Hamamtsu MPPC-50.

4.2. Experimental Apparatus

The basic idea of the measurement of the areal PDE distribution of a SiPM is the following: An LED[4] emits a very short light pulse (ideally a single photon) in a strongly collimated beam on the examined SiPM. The response of the sensor is measured in coincidence with the LED pulse. This routine takes place several times on a single spot. Thereafter, the beam is moved to another position and the procedure is repeated. The entire area of a SiPM (or a part for short measurements) can be scanned this way.

To obtain information about the structure of the sensitive region inside of a single microcell, the dimensions of the incident light beam as well as the mechanical positioning precision must be much smaller than the SiPM pixel size. Fulfilling these requirements, our current experimental setup is capable of providing sensitivity maps of SiPMs with sub-pixel resolution of $\approx 1\,\mu m$.

The experimental apparatus is schematically depicted in figure 4.2. Its individual components and the working principle will be described in following paragraphs.

The light source is steered through the SiPM matrix by a three-axis micropositioning stage. Standard commercial LEDs are employed as a light source. One LED can be used at a time. It is attached to the top of a microscope tube. The light from the LED passes first through a small aperture in an aluminium foil which works as a collimator. Then, it continues to the microscope and it is focused on the surface of the sensor into a spot with $\leq 2\,\mu m$ in diameter. The measurement apparatus is placed in a dark box and the temperature in the box is monitored. The most important test stand characteristics are summarized in table 4.1. A photograph of the experimental setup is shown in figure 4.3.

The microscope is equipped with a beam splitter. It allows to shoot the light on the SiPM and to observe its surface with a CCD camera simultaneously. This feature is a key one for a successful measurement. It is used for a coordinate calibration, which is

[4]LED - light emitting diode

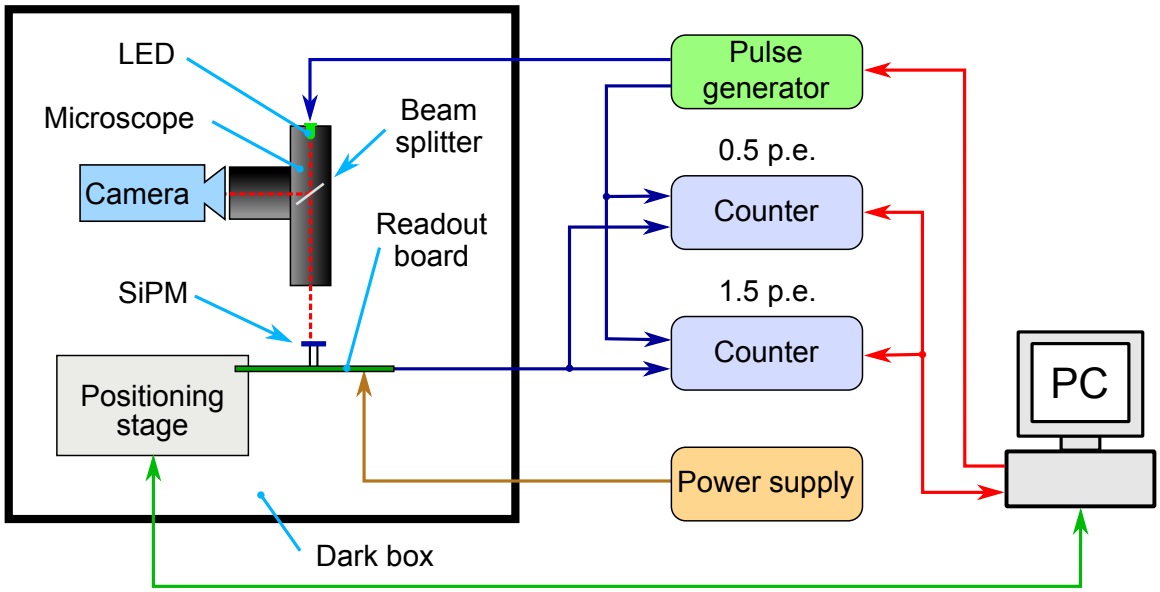

Figure 4.2.: Simplified SiPM scan setup schematic. The complete scheme can be found in [80].

Quantity	Value
Positioning precision	1 µm
Light beam diameter	≤ 2 µm
LED driver pulse length	10 ns
Max. # of pulses per position	65 534
Max. measurement rate	~ 7 steps/s

Table 4.1.: Parameters of the SiPM scan setup.

necessary to maintain the focus of the light spot in any position within the SiPM matrix during the measurement. The calibration is based on focusing the light beam in three points on the SiPM surface. These points must have known coordinates within the SiPM plane. The transformation function between the chip-plane coordinate system and the stage coordinate system is calculated subsequently. An additional major advantage of the calibration is that the scanned area can be well matched with the chip area which is intended to be investigated. Scanning just the area of interest without the surrounding dead surface decreases the measurement duration. The sensor edges are generally not aligned with any of the stage axes. When the calibration is utilized, the sensor edges are parallel with the measurement window. This feature allows further advanced analyses of the measurement data (see section 4.3.4). The calibration also overcomes some mechanical imperfections of the stage like positioning inaccuracies and the fact that the stage axes are not precisely orthogonal.

The SiPM is placed in the setup on a custom made simple preamplifier board. The output signal from the board is split by a T-adaptor into two to enable simultaneous measurements at two different threshold levels. The split signals are fed into two identical

chains of signal processing devices. The final element of each signal branch is a counter, which records the number of detected coincidences. The only difference between the two branches is the discriminating level. The counting is done for both discrimination thresholds separately. There are several units in the chain which are omitted in the block scheme in figure 4.2 for simplicity. These devices are used to overcome a low trigger rate of the counters which is less than 1 kHz. With usage of the additional modules, trigger rates up to ~ 430 kHz can be reached. For more technical details see table 4.1 reference [80].

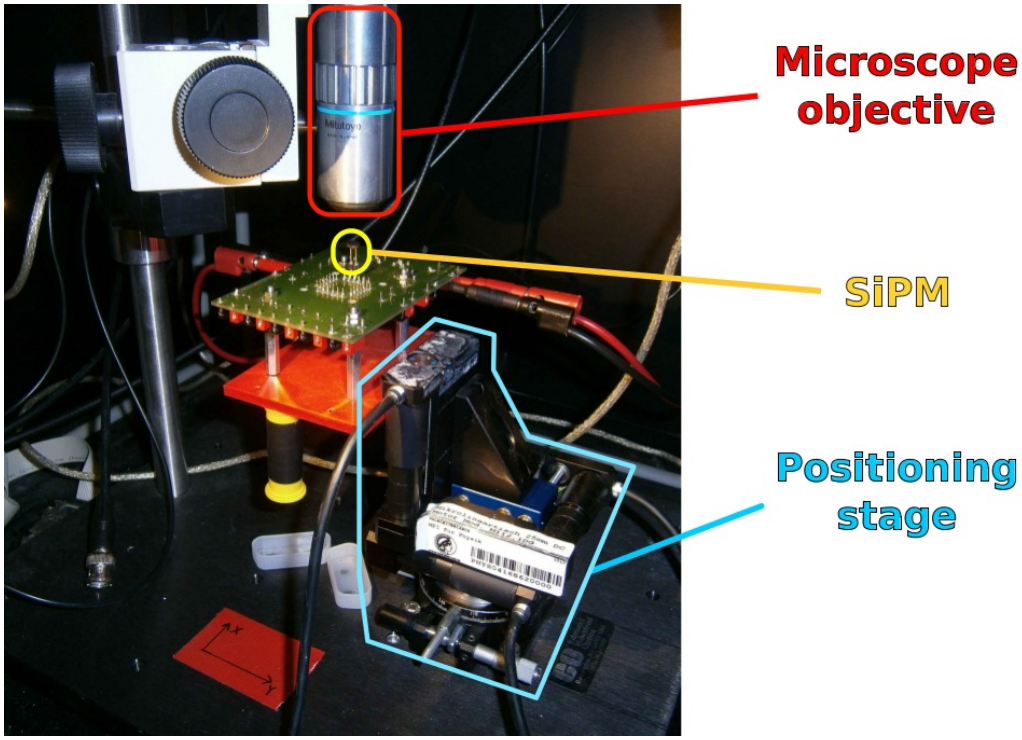

Figure 4.3.: Experimental setup for SiPM scanning.

The LED light source is driven by short electrical pulses coming from a pulse generator. This pulse generator also produces coincidence signals for both counters. Once the driving pulses are sent by the generator, the counters are set to a sensitive state for receiving coincidences from the SiPM for a certain time period. In practice, a given number of LED shots is fired in a single burst while the counters are sensitive. The counters record the number of times the signal passed over the threshold within the measurement time window. This procedure is repeated in for every single measurement point on the sensor surface.

The above mentioned devices are steered and synchronized by a PC[5] with LabVIEW [81]. This configuration offers a sufficient grade of measurement automation. A complete list of used equipment can be found in appendix A in table A.1.

In a typical measurement, the SiPM is scanned with 1 µm steps and 20 000 LED pulses with a length of 10 ns are shot in each position. The setup is working at a speed approximately 7 steps per second which implies a scan time for a typical $1 \times 1\,\mathrm{mm}^2$ SiPM of about 42 hours. Most of the measurement time is taken by the mechanical movement of the stage

[5]PC - personal computer

and communication between the PC and measurement devices. The time required for the light pulse burst itself represented about 7 % of the overall scan time in our case.

A limitation of the system is that the light output of the LEDs is not precisely known. Therefore, our measurements do not provide absolute PDE value but only a relative quantity which is directly proportional to the PDE. For this reason, with the abbreviation *PDE* we refer to *relative* PDE from now on in this chapter, unless explicitly specified. Furthermore, the wavelength distribution of the LED light pulse has also substantial uncertainties. The output wavelength is dependent on the electrical current and, in principle, it can be calculated when the LED is operated with direct current. However, in our case, the LED is driven with a very short electrical pulse and the voltage and current change in a wide range. According to the data sheets of the used LEDs [82, 83, 84], it can be estimated that during the rise of the current, the peak wavelength changes over $\sim 30\,\mathrm{nm}$. Additionally, the wavelength distribution for stable current has an uncertainty of $\sim 20\,\mathrm{nm}$. One more issue, which is not easy to control, are reflections and signal deformations in the cable connecting the LED to the pulse generator. This problem could be fixed by usage of a specialized dedicated LED driver e.g. the one used in [85]. However, the experimental setup can be still adjusted in a way that it is capable of conducting reasonable measurements and producing reliable data.

4.3. Data Analysis

There are several interesting characteristics which could be extracted from the experimental data. Areal distributions of various quantities across the SiPM array can be obtained. These distributions are called *maps* in the following. The basic one and also one of the most important maps is the total response measured at a discrimination level of 0.5 p.e. Besides this map, thanks to simultaneous measurement at two trigger levels, a crosstalk probability map and a response map corrected for crosstalk can be created. Furthermore, when individual pixels within the sensor map are recognized, each of them can be evaluated separately. Information about the integrated relative PDE of single pixels has a potential to reveal possible quality fluctuations between individual microcells. Operations which have been done to obtain this information, along with measurement data structure will be explained in this section.

4.3.1. Measurement Data

The raw data consist of two sets of numbers which form a map of the sensor. One is recorded at an amplitude discrimination level of 0.5 p.e. and the second at 1.5 p.e. In other words, the first mentioned map shows the number of all coincidence signals (above the noise of electronics) coming out of the detector where one or more cells are contributing. The second one comprises only those signals which correspond to two and more simultaneously firing cells. In an ideal case, if the sensor was not illuminated at all or just with single photons, events of more than one firing cell should originate only from crosstalk between neighboring pixels. Firing of two or more cells caused by only thermal noise or thermal noise and one incident photon at precisely the same moment is very unlikely unless the SiPM has extremely high dark count rate.

Since our light source aims only at a very tiny area which is significantly smaller than a single microcell, multiple-fired-cells events cannot be caused by the primary beam. However, in the case when more than one photon is emitted by the LED the light can be reflected from the chip surface towards the objective lens and back. It can be further scattered on surface structures of the sensor such as aluminium lines, its entrance window made of plastic, epoxy or glass, or epoxy protection layer. Under such conditions, photons emitted in one pulse can hit more than one cell and contribute to multiple-p.e. events. Despite these effects, crosstalk still forms the leading contribution to signals measured at 1.5 p.e. discrimination level. The amount of reflected and scattered photons is marginal and can be neglected almost in all cases.

The noise corrected SiPM maps recorded at 0.5 and 1.5 p.e. of all tested SiPMs are shown in appendix B.1.

4.3.2. Coincidence Distribution and Noise Subtraction

To the measured number of coincidences also contributes the thermal noise. Therefore, the noise is determined from the experimental data itself and subtracted from the coincidence count in each point. Both mentioned quantities are always scaled by the number of fired light pulses.

Because the dead area of the SiPM occupies a large fraction of the sensor surface, the noise level can be determined from a distribution of the measured coincidences. An example of a *coincidence distribution* is shown in figure 4.4a. The corresponding measured map from which it was derived is presented in figure 4.4b. The green color in the coincidence distribution in figure 4.4a marks signals originating from sensitive regions.

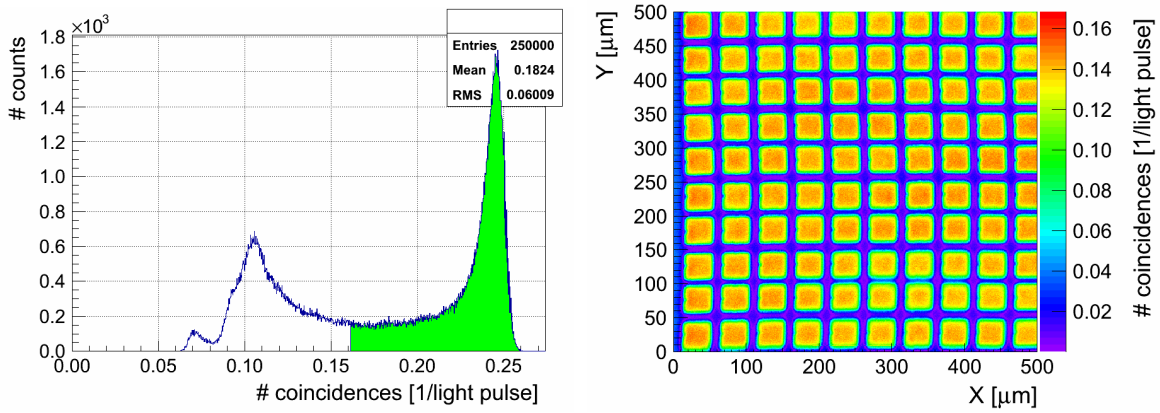

(a) Coincidence distribution example

(b) Measurement data example

Figure 4.4.: Examples of a coincidence distribution of a SiPM scan and a measurement map recorded at 0.5 p.e. threshold. Device: Hamamatsu MPPC-50, 1/4 of the full array, over-bias voltage 2 V.

In the coincidence distribution in figure 4.4a, three peaks are clearly visible. The first peak from the left at 0.07 arose due to the dead area stripe between 0 and ~ 10 µm on the left-hand side of the sensor map in figure 4.4b. The insensitive areas in between the pixels

are responsible for the second one at 0.11. The third peak at 0.24 is caused by the sensitive area of the microcells. It is obvious from the measurement map that the number of measured coincidences outside of the pixel matrix is lower than in between the microcells. This is a consequence of the reflections mentioned in section 4.3.1. The incident beam scattered on dead surface structures of the SiPM is more likely to be detected in the closest cells. This results in the separation of the first and the second peak. If the scan area does not include much of the insensitive area outside of the pixel matrix, the first peak in the coincidence distribution does not appear. The most probable value within the second peak is taken as the noise level. Its value is obviously somewhat higher than the pure dark noise of the device. However, we assume that the amount of reflections taking place inside and outside of a pixel is comparable. The reflections contribute to the output signal almost uniformly across the device irrespectively of whether a sensitive or insensitive area is hit. Presence of a third peak is a sign of large sensitive areas evincing small variations in PDE. For devices with bad pixel PDE homogeneity, the peak does not have to be formed at all. Generally speaking, any larger area of the same effective relative PDE can form a peak in the coincidence distribution. Origins of such areas can be various, dead area, area with high PDE, two or more different distances between neighbouring pixels, gain gradients over the matrix caused by temperature changes during the measurement or device design, repeating patterns in microcells, etc. In an ideal case, one would get two sharp peaks in the signal distribution, one for the thermal noise and one for the sensitive area. Separation of the two peaks also gives the signal-to-noise ratio.

The whole operation of obtaining the noise, subtracting it in every measurement point and scaling by the number of emitted LED pulses is called *noise subtraction*. We apply this procedure to both recorded data sets separately. This way, we get the two *basic maps* of the sensor. These maps are the starting point for creation of the crosstalk probability maps and crosstalk-corrected relative PDE maps.

The basic sensor maps recorded at 0.5 p.e. and 1.5 p.e. discrimination level corrected for crosstalk and coincidence distributions of tested SiPMs can be found in appendices B.1 and B.2. The map obtained at 1.5 p.e. is not presented for all examined devices, because some of the measurements were performed before the option of simultaneous measurement was implemented into the setup or because it was not possible to distinguish the 1.5 p.e. level precisely.

4.3.3. Crosstalk and Pure 1 p.e. Maps

The second map which is derived from the experimental data is the areal distribution of crosstalk probability. It can be obtained by dividing the 1.5 p.e. map by the 0.5 p.e. map in each separate measurement point. In other words, such an image depicts a probability that more than one cell will be fired, if we illuminate a particular spot on a sensor. This map shows for example the level of increase of crosstalk towards the pixel edges as presented in the example in figure 4.5a. It can also reveal *edge breakdowns*. This is an effect which tends to occur at the edges of the active area due to enhanced electrical field. The higher electrical field can be formed on a boundary between two implants with different doping profiles in the silicon. The stronger electrical field leads to a larger gain in this region and a more likely breakdown.

It is possible to obtain two further interesting maps of the chip from the available data.

The first one is a map of pure 1 p.e. response. This distribution displays only those signals, which have an amplitude corresponding to exactly one fired cell. This information is extracted by subtracting the raw map before noise subtraction obtained at 1.5 p.e. amplitude threshold from the one taken at 0.5 p.e. After this operation, the noise subtraction follows. The pure 1 p.e. map allows to distinguish spots in the SiPM which really evince a high PDE from those which just appear very sensitive due to a high crosstalk probability or edge breakdown. Keeping the crosstalk incorporated in the PDE distribution map also overestimates the PDE and distorts the sensitivity picture of a SiPM. An example of a pure 1 p.e. map is shown in figure 4.5b. From a comparison of the lower left corner of the pixel array in figures 4.4b and 4.5a, it is apparent that the corner pixel suffers from electric field inhomogeneity. It leads to a larger gain and hence signals with higher amplitude which are recognized as crosstalk.

All crosstalk maps and maps of pure 1 p.e. response of the tested devices are shown in appendix B.1.

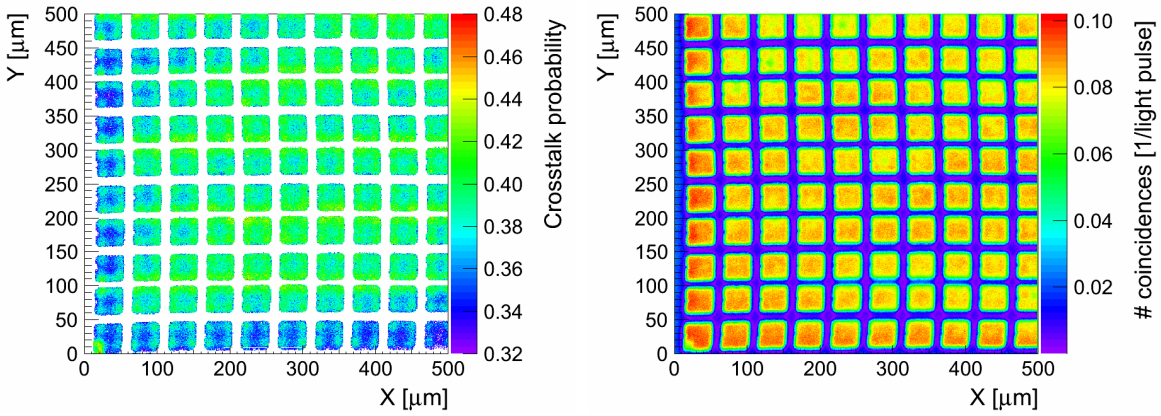

(a) Crosstalk probability example

(b) Pure 1 p.e. signal example

Figure 4.5.: Examples of crosstalk probability and pure 1 p.e. response map. Device: Hamamatsu MPPC-50, 1/4 of the full array, over-bias voltage 2.0 V.

4.3.4. Analysis of Single Pixels

Since the main goal of our study is to measure and quantify the PDE uniformity of SiPMs, it would be also very helpful to be able to analyze each individual microcell separately and to characterize the detector on the pixel level. In this approach, an area in a chosen sensor map which represents one pixel is defined and further analyses are conducted. This procedure is repeated for every single pixel.

The analysis works in the following way. In the first step, the noise-corrected basic sensitivity map recorded at 0.5 p.e. trigger level is overlaid with a rectangular grid. The grid is adjusted in such way that in each cell of the grid lies exactly one whole pixel. Positioning and cell size of the grid is determined with the help of automatic recognition of gaps between pixel rows and columns in the sensitivity map. Now, the microcells are localized and ready for processing.

In the next step, a threshold level is established. The purpose of this threshold is to separate the active and the dead area of the pixel. It can be displayed in the coincidence distribution in figure 4.4a and it lies at a certain position above the noise peak. If only the data above the threshold is shown in the map, just the sensitive area will be visible as demonstrated in figure 4.6a. The value of the threshold level is set manually. A zoomed view of a few pixels in the measured map is observed, while the discrimination level is being slowly raised. During this process, the spots with the lowest PDE start to "disappear" from the map. The threshold level value is accepted when the dead area vanishes from the map completely. This must be done because also the inactive areas of the SiPM exhibit an artificial non-zero PDE value even after noise subtraction. It is not wanted to include the reflections occurring on the dead surface, because it can bias the overall characteristic of a pixel.

By applying the threshold, the geometrical fill factor of the SiPM can be calculated immediately. We determine it as the ratio of the area lying above the discrimination threshold level and the total sensor area. This capability is one of the big advantages of our measurement method. The fill factor determination is based on the whole picture of the sensor, taking into account all imperfections of the particular device. Because of this feature of the threshold, it is called *fill factor cut* in further text. The fill factor cut is applied on the data, which will be further processed.

Two types of calculations will be now conducted for each pixel of the SiPM. One SiPM microcell is represented by one cell of the grid, which was laid over the pure 1 p.e. signal map. In both of these calculations, a new map of the device will be created. Every pixel (colored square) in the new maps will represent one microcell on the SiPM.

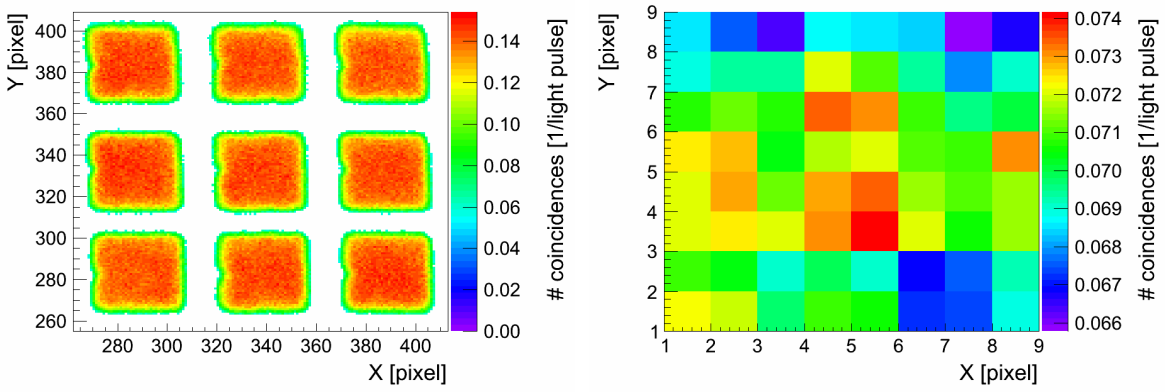

(a) Fill factor cut demonstration

(b) Single pixel integrated efficiency

Figure 4.6.: (**a**): Demonstration of the *fill factor cut*. Only the part of pixel which is considered sensitive is shown. (**b**): Example plot of integrated relative PDE of individual pixels. Device: Hamamatsu MPPC-50, 1/4 of the full array, over-bias voltage 2.0 V.

Integrated Detection Efficiency

The first quantity which will be obtained for every pixel is the *integrated detection efficiency*. In this calculation, the measured efficiency is integrated over a pixel and normalized by the mean number of measurement points inside of the pixel. The mean number of measurement points inside of one pixel is calculated from all grid cells in the map. The integrated detection efficiency represents, in fact, the fraction of detected pulses which would be detected in a particular pixel if the pixel was illuminated uniformly. This map has the capability of revealing "hot" pixels immediately or showing clusters of pixels with exceptional behavior. An example of an integrated detection efficiency map is shown in figure 4.6b.

The application of the fill factor cut and the mean number of measurement points within a pixel as a normalisation factor for integrated detection efficiency is necessary to get reliable results. The main reason for that is that the grid cells which define the pixels do not consists always of exactly the same number of measurement points. This is caused mainly by the grid placement accuracy, which is about 2 µm. For illustration, let us assume a scan of a SiPM with 25 µm pixel pitch, realistic fill factor and perfectly identical microcells. Let the step precision of the measurement be 1 µm. One pixel of this SiPM should comprise exactly 25×25 measurement points. However, due to limited grid placement precision, some grid cells can have a size of e.g. 26×26 and others e.g. 24×24 points. Obviously, the difference of the area of these two cells is 17 %. The resulting integrated efficiency of these pixels would be biased if the area of each grid cell would be used as a normalisation factor. Despite this discrepancy, both grid cells still include the same amount of active area. The active regions of the microcells are separated by a gap of dead area which is wide enough to compensate the grid inaccuracy. The bias caused by different grid cell sizes is completely suppresed by introducing the fill factor cut and normalisation of the integrated detection efficiency mentioned above.

The integrated detection efficiency map is created from the noise corrected map recorded at 0.5 p.e. discrimination level as well as from the crosstalk and noise corrected map. This approach opens further possibility to compare crosstalk impact on the PDE homogeneity. All resulting plots of this kind are to be found in appendix B.2.

Finally, the relative mean standard deviation of the integrated detection efficiency of every single pixel is calculated. It is used as a quality measure of a particular detector. This parameter for all sensors for which it could have been obtained is summarized in table 4.2.

Geometrical Fill Factor

The second type of pixel map depicts the geometrical fill factor of individual pixels. An example is given in figure 4.7. It is calculated as a ratio of sensitive area based on the fill factor cut and the mean pixel area introduced above. This SiPM map allows to see clearly whether there are large changes in active area size of pixels across the sensor. Such information can be also used to judge the production quality of a detector.

All resulting plots showing the geometrical fill factor of individual SiPM microcells can be found in appendix B.2.

Analogously to the integrated detection efficiency, the relative mean standard deviation of the fill factor obtained for every single pixel is calculated. It quantifies pixel quality

fluctuations within the microcell array. The relative mean standard deviation of the geometrical fill factor is also presented in table 4.2.

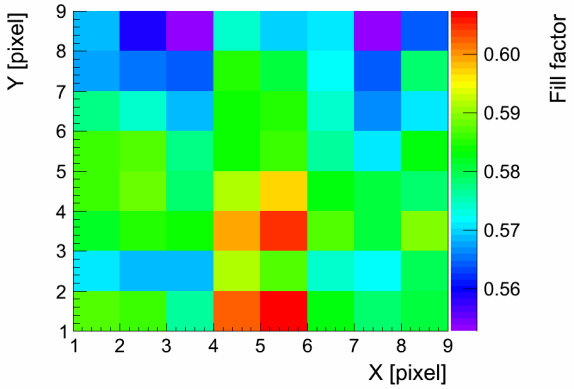

Figure 4.7.: Example of a map depicting geometric fill factor of individual pixels of Hamamatsu MPPC-50 (1/4 of the full array, over-bias voltage 2.0 V).

4.4. Results

In the following, the results of a detailed study of Hamamatsu MPPC-50 at different operation voltages are presented. These sensors were used in the T3B experiment and in the scintillator tile tests presented in chapter 5. The goal for this experiment was to obtain a picture of behavior of areal PDE and to investigate, if the size of the sensitive area changes with different bias voltages. In addition, the shape and homogeneity of active area of the SiMPl detectors was investigated. To provide a broader overview of different sensor types, gain experience with other designs and to make comparisons with Hamamatsu MPPCs and SiMPls, further sensor models were tested. Most of the detectors were probed with green light with a peak wavelength of 525 nm. Only the MEPhI-32 was scanned using red light with a peak at 625 nm. This thesis focuses on the studies of Hamamatsu MPPCs and SiMPls. For convenience, short names of the tested SiPM models are used the text. The full markings of the sensors along with detailed type information are listed in appendix A, tables A.2 and A.3. The most interesting plots are shown in this section. The full set of results for all tested SiPMs can be found in appendices B.1 and B.2.

4.4.1. Hamamatsu Multi-Pixel Photon Counters

Two types of Hamamatsu Multi-Pixel Photon Counters (MPPCs) were tested. The first of them was the MPPC-50. This MPPC type has a special plastic casing shown in appendix B.4, figure B.33 and is not commercially available. These sensors were produced specifically for scientific applications in high energy physics. The measurements were done with the highest possible positioning resolution of 1 µm for three different over-bias voltages of 1.0, 1.5 and 2.0 V.

In addition to this measurement, it was intended to perform a similar test of an MPPC-25 with similar transparent plastic casing and compare both results. Unfortunately, the

scanning of the MPPC-25 had to be aborted after several unsuccessful attempts. The sensitivity scan appeared to be unfeasible because of a blurred plastic entrance window which is shown in appendix B.4, figure B.34a. The blur made the coordinate calibration very difficult and less accurate. The bad quality of the entrance window also biased the measurement strongly. The differences in PDE of individual pixels and changes in sizes of sensitive areas of the pixels were dominated mainly by the imperfections of the plastic and did not reflect the real behavior of the silicon detector itself.

To show at least a basic comparison between an MPPC with 25 and 50 µm pitch, we present results of one full area scan at discrimination level of 0.5 p.e. of a commercially available U-type MPPC with 25 µm pixel pitch. The U-type MPPCs are originally equipped with a cylindrical metal casing with a glass entrance window. For the studied sensor, the glass window was removed to get direct access to the detector chip. The MPPC-25 sensors inside of both casing types should not be too different. However, since the manufacturer does not provide any detailed design information, we are unable to tell the exact difference between the two detectors.

Hamamatsu MPPC-25

In figure 4.8, the result of a scan of the whole MPPC-25 is shown. This map was recorded at 0.5 p.e. threshold. There are no homogeneity deviations across the diode array which would be visible with the naked eye in figure 4.8a. In a detailed view of four cells presented in figure 4.8b, the shape and the inner structure of the active region of the SiPM cells can be seen. One more thing which should be pointed out is the large dead area of this sensor and therefore low geometrical fill factor. This is given by the size of aluminium lines and polysilicon quench resistors placed on the silicon surface. It will become clear later on, that for larger pixel sizes, the fill factor is greater, because the space required for surface infrastructure stays approximately the same for a wide range of pixel sizes.

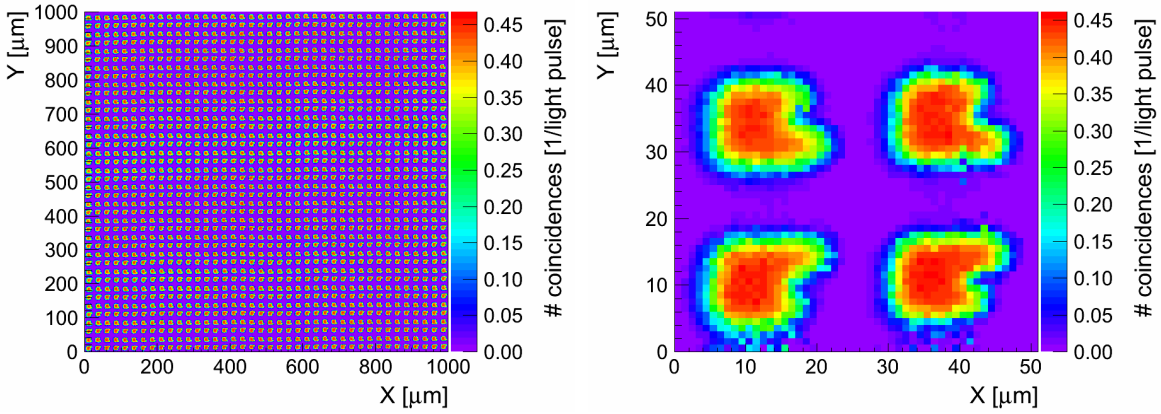

(a) Whole device

(b) Detail of four cells

Figure 4.8.: Sensitivity map of Hamamatsu MPPC-25U taken at 0.5 p.e. discrimination level. Full SiPM surface (**a**) and a detail of four corner cells (**b**) is shown.

The analysis of single pixels of the MPPC-25, which is shown in figure 4.9, has brought

very interesting results. Both the integrated efficiency map and the fill factor map exhibit very similar patterns over the whole sensor. Changing regions of lower and higher sensitivity are apparent. This effect can be caused by different gain in these regions, but why the gain is changing is unclear to us at the moment. One possible interpretation could be inhomogeneous doping levels across the chip or non-uniformities in the silicon wafer. A similar effect was also observed for the SensL-35 device shown in appendix B.2, figure B.28.

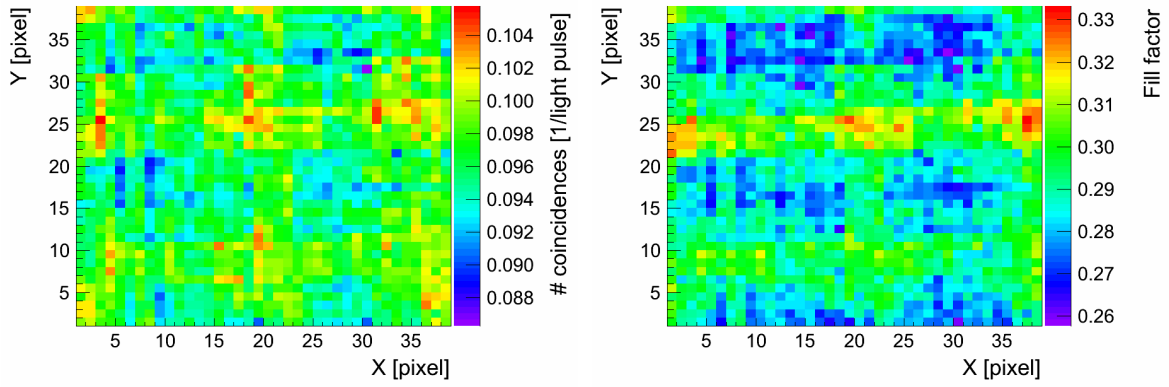

(a) Single pixel integrated efficiency

(b) Single pixel fill-factor

Figure 4.9.: Integrated PDE and geometrical fill factor for individual microcells of Hamamatsu MPPC-25. The outermost pixels of the SiPM are not included in the plot.

Hamamatsu MPPC-50

The studied type of Hamamatsu MPPC-50 is the model which was used in the T3B experimental setup and in other scintillator tile tests. A map of one quarter of this device operated at the manufacturer-recommended voltage taken at 0.5 p.e. threshold is depicted in figure 4.10a. It is clearly visible that the device has a higher photon detection efficiency on the outer edge of the outermost pixels. We believe that this excess is caused by the edge breakdown. In the edge region of these pixels, the electric field intensity might be higher than in the remaining area. This leads to a higher Geiger efficiency and therefore a larger overall PDE in the particular spot. Further consequence of the edge breakdown is a larger gain in this region. The signals induced by incident photon in this area have a higher output amplitude. Therefore, it seems that the edge suffers from a higher crosstalk since the single-cell signal amplitude can also exceed the 1.5 p.e. threshold. When the SiPM is operated at lower voltage, the edge breakdown becomes more severe. For a higher applied bias voltage, it is not pronounced that strongly.

The next high-resolution image of the sensor depicted in figure 4.10b is the pure 1 p.e. signal map. In this plot, the active lower left corner which is visible in the uncorrected map has vanished. The pixel homogeneity is slightly improved due to the crosstalk subtraction. The maps for different bias voltages presented in appendix B.1 show that the actual detection efficiency is not growing with rising bias voltage as fast as it may seem

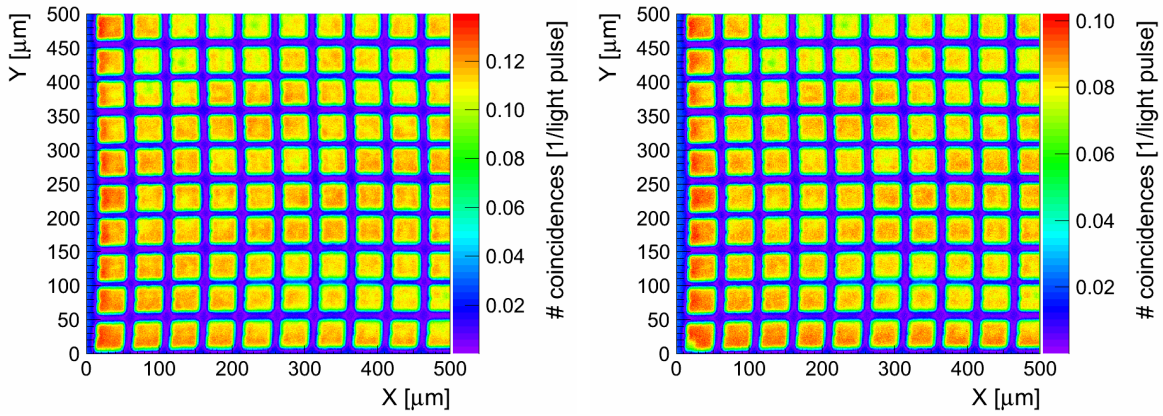

(a) Discrimination level = 0.5 p.e.

(b) Pure 1 p.e. signal

Figure 4.10.: Relative PDE map of MPPC-50 (1/4 of the whole area) recorded at discrimination level 0.5 p.e. without (**a**) and with (**b**) crosstalk correction applied.

from uncorrected measurements. The reason for this is a quadratic dependence of crosstalk on over-bias voltage, but just a linear dependence of gain.

The crosstalk probability distribution for the 1.0 V over-bias voltage is shown in figure 4.11a. The expected shape of the areal crosstalk distribution was observed. The edges of the inner pixels are more sensitive to crosstalk, because a secondary photon produced close to the microcell edge must travel a shorter distance to reach a neighboring pixel compared to a photon originating from central regions of a pixel. A hot spot is visible in the lower left corner which is most probably caused by exceptionally high edge breakdown. For higher operation voltage, as shown in appendix B.1, figure B.7b, the edge breakdown is not that distinct, because of the saturation of the Geiger efficiency. Consistently with natural assumptions, the outermost pixel rows exhibit a smaller crosstalk probability because of the lower geometrical probability that a secondary photon hits some other pixel. However, this expected behavior is violated by the present edge breakdown. The observation is one of the valuable results obtained in this study. The sensor producer does not mention this imperfection in the documentation at all.

The two plots for the Hamamatsu MPPC-50 shown in figure 4.12 depict results of the analysis of single pixels. For the purposes of these calculations, the outer pixels of the scanned area were excluded. This was done to avoid those pixels which were either cut by the border of the scan window or included additional dead area from outside of the pixel array. This restriction assured that only well-defined microcells were evaluated. The chosen data set is schematically depicted in figure 4.11b. The plots in figure 4.12 reveal deviations in sensitivity of separate pixels and their distribution over the sensor area. The impact of different over-bias voltages on these two maps was studied. The respective plots are shown in appendix B.2. It turned out that the patterns in both maps do not change significantly for all three tested bias voltages. The differences in PDE between pixels smear out with increasing bias voltage and the map is getting flatter. The device homogeneity slightly improves with increasing bias voltage. The results also showed that the area of the sensitive region within a single pixel does not change considerably with different bias

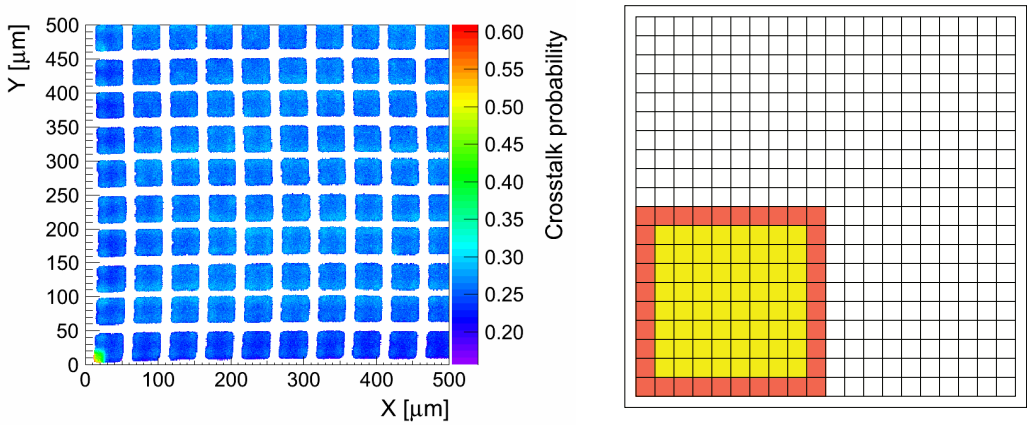

(a) Crosstalk probability (b) Scan area schematic drawing

Figure 4.11.: Crosstalk probability map of Hamamatsu MPPC-50 (1/4 of the full area, overbias voltage 1.5 V) (**a**). The figure (**b**) depicts a schematic of the scanned area (red ∪ yellow) of the MPPC-50, the data in the yellow area was used in the single pixel analysis.

voltages. This leads to a conclusion that the temperature and voltage dependence of the output signal is driven only by changes of gain and Geiger efficiency. No geometrical effects take place.

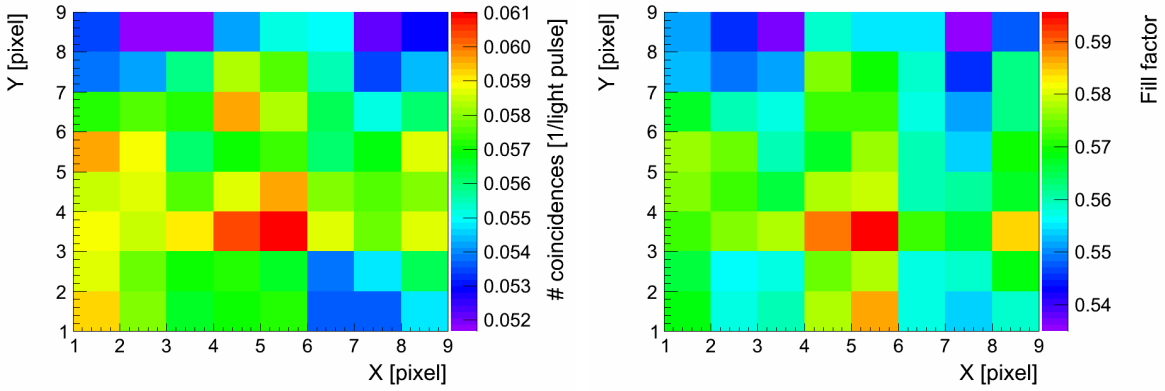

(a) Single pixel integrated efficiency (b) Single pixel fill factor

Figure 4.12.: Integrated relative PDE and geometrical fill factor map of individual pixels map of Hamamatsu MPPC-50.

4.4.2. Silicon Multi-Pixel Light Sensors

The next tested sensors were the Silicon Multi-Pixel light (SiMPl) devices. The SiMPl is being developed in the Semiconductor Laboratory of the Max Planck Society in Munich, Germany. These detectors are based on the concept of a bulk-integrated quench resistor

introduced in section 3.1.1. They have hexagonal pixels and no surface structures which would act as an obstacle in the entrance window. Thanks to this feature, a geometrical fill factor up to 85 % can be theoretically achieved which would enhance the overal PDE considerably [56].

Detector samples of the second production iteration were tested. All measurements of these detectors were performed just at one discrimination level of 0.5 p.e.. The reason for that was a poor signal quality and overwhelming noise rate of the sensors at room temperature. These circumstances did not allow us to find a clear 1.5 p.e. voltage level with the available experimental equipment. This issue could be solved by cooling the sensor to lower temperatures. An implementation of additional cooling in the experimental setup is not an easy task because of high sensitivity of the measurement to vibrations and limited maximum load of the stage. However, the next production series of SiMPls should be operational also at room temperature and all capabilities of the setup can be utilized.

The SiPMl prototypes are produced in several configurations of pixel arrays which are shown in appendix B, figure B.37b. The usual numbers of pixels in these arrays are 100, 19 and 7. In some of the larger ones, one or two pixels are occupied by a bond pad sometimes, reducing the sensitive area. We will now present the first relative PDE scans of three prototypes. Different design combinations of pixel size and width of gap between the microcells were tested. Results for one more SiMPl, which was also studied, can be found in appendix B.1. All tested SiMPls are listed in appendix A, table A.3.

SiMPl P15 (135 µm pitch, 15 µm gap)

In figure 4.13, sensitivity scans of three different SiPM structures with 100, 19 and 7 pixels are presented. The P15 chip carries several SiPM structures with 135 µm pixel pitch and 15 µm gap between pixels. This chip is exceptional, since it exhibits the lowest leakage current for the 19 pixel array among the prototype set which was available. Therefore, three structures were tested.

The first of them was a 10×10 pixel array. In the plot shown in figure 4.13a, it can be seen that the pixels are not very clearly distinguished from the dead area. This is caused by high thermal noise of the detector at room temperature and therefore low signal-to-noise ratio. Another effect, which is apparent, is the influence of temperature changes during the measurement. The test stand was located in a room without any temperature control. Unstable temperature caused a change in over-bias voltage (breakdown voltage is a function of temperature) which lead to a change in the output amplitude while the discrimination threshold stayed fixed. Our measurement showed that the shape of the active area looks as expected. However, it is hard to conclude something about homogeneity across the whole sensor because of the high temperature sensitivity.

The result obtained for the 7- and 19-pixel structures are presented in figures 4.13b and 4.13c, respectively. In both of them, variations of detection efficiency from pixel to pixel are clearly visible. Furthermore, the 19-pixel array gives a higher response in the outermost pixels. That is the opposite of what one would expect due to the lower crosstalk probability in these pixels. An explanation of this observation can be a different gap size between two pixels and a pixel and the aluminium line surrounding the whole microcell array. This line can be seen in appendix B.4, figure B.37b. The purpose of the aluminium line is to create an electrical field around the outermost pixels. Without the presence of this field,

the quenching resistor (in the silicon bulk) of the outer cells could not be formed properly and these pixels would not work correctly. The gap between the outer pixels and the aluminium line is the same for all prototypes, irrespectively of the actual pixel gap width. Because the gap width affects the size of the quenching resistor, its resistance can differ between the inner and the outer pixels for this sample.

For the 7-pixel device, a sensitivity gradient can be seen. It is probably caused by an inhomogeneous electrical field inside of the pixels. The same effect was also observed for all other tested SiMPls (P13, L01, O17). For the sample L01, an additional measurement was conducted to study this effect and to make sure that it is not caused by the measurement method. This test is discussed in the next paragraph which describes the results of L01 sample. The additional test supports the hypothesis that the electrical field in the microcells changes across the sensor.

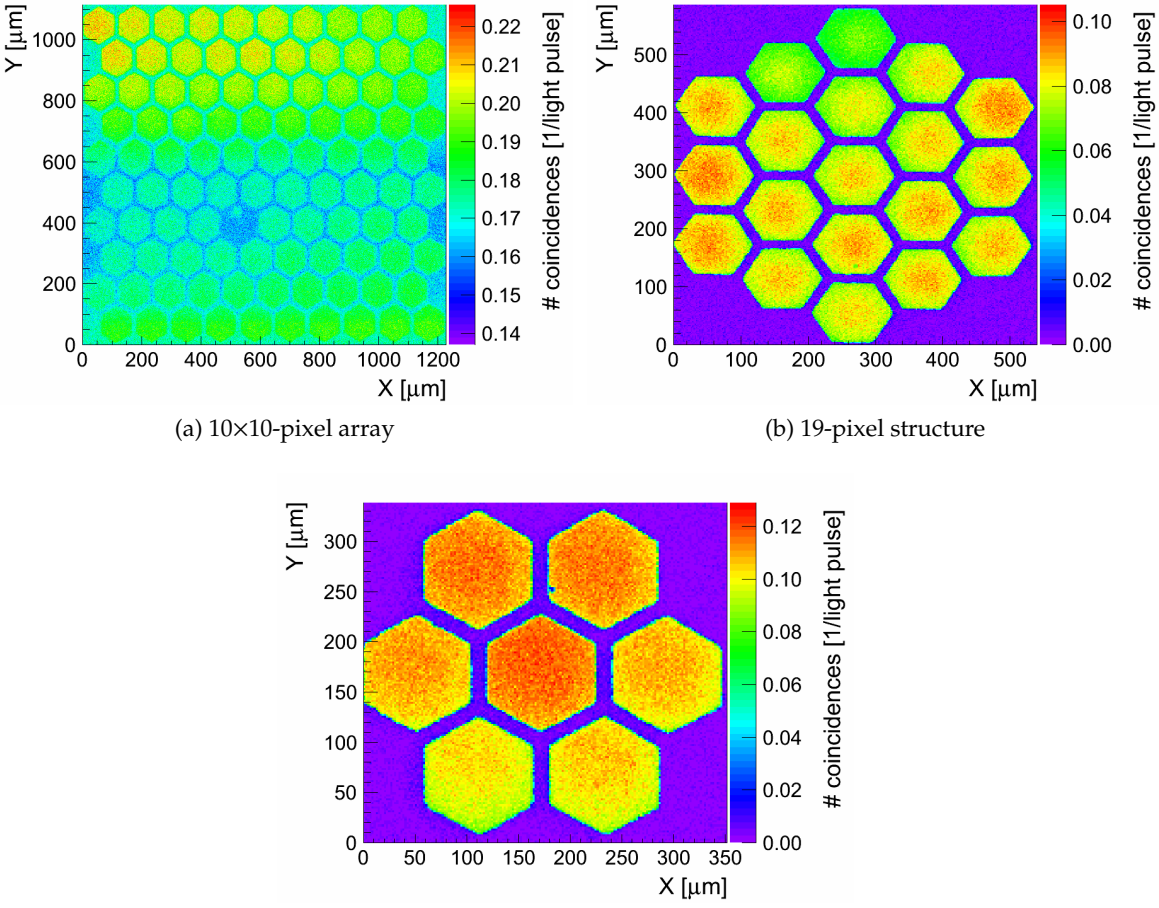

(a) 10×10-pixel array

(b) 19-pixel structure

(c) 7-pixel structure

Figure 4.13.: Sensitivity maps of different SiMPl P15 arrays. All measurement, except for (**a**), were corrected for noise. The noise of the 10×10 structure was very sensitive to temperature changes and was varying during the measurement.

SiMPl L01 (130 µm pitch, 10 µm gap)

Scans of the two following SiMPl prototypes were conducted to see properties and differences of two extremal gap widths of 10 and 20 µm. Arrays of 18 microcells was scanned. The resulting plot from a measurement of the L01 sample with 10 µm gap is shown in figure 4.14a.

The wedge-like shaped insensitive area in the pixel on the right-hand side of this plot is actually a shadow of a bond wire. Other small sharp local disturbances are most likely caused by dust particles or mechanical damage. A gradient of the PDE in X-direction is apparent and it is the strongest one among all tested SiMPls. To exclude that this is an effect of the scanning setup, predominantly the inaccuracy in coordinate calibration, the setup was recalibrated and the measurement wasrepeated. It brought the same results. The gradient also could not be caused by a changing temperature, because the measurement ran along the Y axis and therefore a temperature change would have created a gradient in this direction. To understand the observed effects, another measurement was performed.

The focused light beam was targeted on one pixel and the SiPM output signal amplitude was measured. This exam showed that the gradient observed in the sensitivity map is consistent with the change of the output signal amplitude as a function of beam position. It means that the pixels have in reality different gains. This result supports the hypothesis of a changing electrical field in the microcells across the sensor. However, the performed test is not sufficient to state a final conclusion about this effect. Further different measurements must be done to understand this issue completely. Moreover, a device with such a combination of pitch and gap was not expected to quench well [86]. However, the performance of this device appeared to be comparable to the other ones.

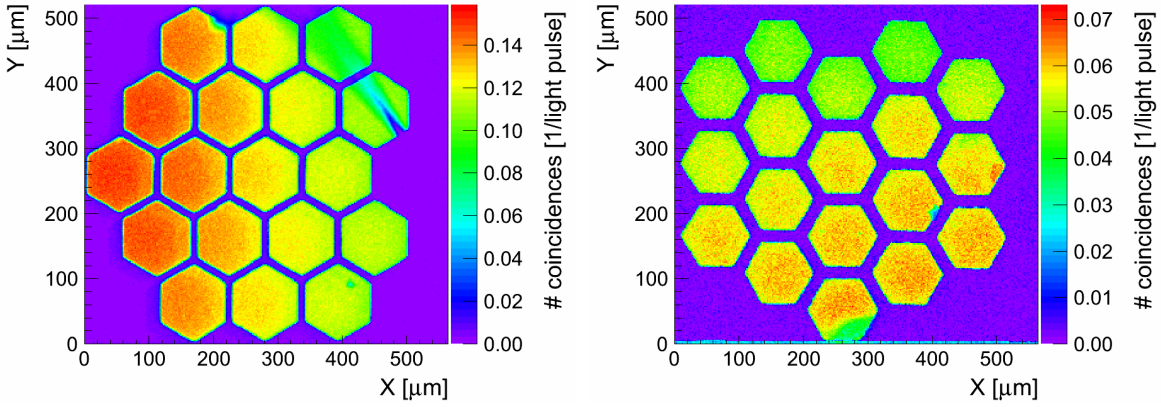

(a) SiMPl L01

(b) SiMPl O17

Figure 4.14.: Sensitivity maps of SiMPl L01 (**a**) and O17 (**b**), 18-pixel structures.

SiMPl O17 (130 µm pitch, 20 µm gap)

The device with the largest gap was the O17 and its sensitivity scan is presented in figure 4.14b. The surface quality is not perfect again. There might be some dust particles

or scratches, which cause irregularly shaped spots of lowered sensitivity. As well as for the previously described SiMPl devices, a sensitivity gradient in one particular direction was observed. Due to the orientation of the gradient and the scan direction, an influence of changing temperature is excluded. The lower overall relative PDE of O17 compared to L01 is caused by a much higher dark rate of O17. The most important result regarding O17 and L01 samples is that the measured width of the dead space between the pixels is in full agreement with the design value of this parameter. In other words, the gap between active areas of the neighboring pixels is as large as the gap in the implantation. This proves that the full microcell area is sensitive to incident light and the theoretically calculated fill factors can be possibly achieved.

4.4.3. MEPhI and SensL Devices

In addition to the above mentioned devices, SiPMs manufactured by two further producers were studied. The first one was a prototype MEPhI-32. The MEPhI-32 was an older sensor which was probably slightly mechanically damaged and some dust particles were scattered on its surface. This sample exhibited the worst homogeneity and geometrical fill factor of all tested sensors. This detector was scanned with a red light with a peak wavelength of 625 nm.

Two commercial SiPMs with different pixel sizes produced by SensL were tested. Both SensL-35 and SensL-100 exhibited a surprising structure of the sensitive regions. Active stripes with a width of ≈ 11 µm were observed inside of individual pixels of these devices. The performance of these was average compared to other samples.

Sensitivity maps of MEPhI-32 and SensL-35 recorded at 0.5 p.e. discrimination level are presented in figure 4.15. A more detailed discussion and complete results for MEPhI and SensL sensors and SiMPl P13 can be found in appendices B.1 and B.2. Further specifications of these detectors are listed in appendix A, table A.2.

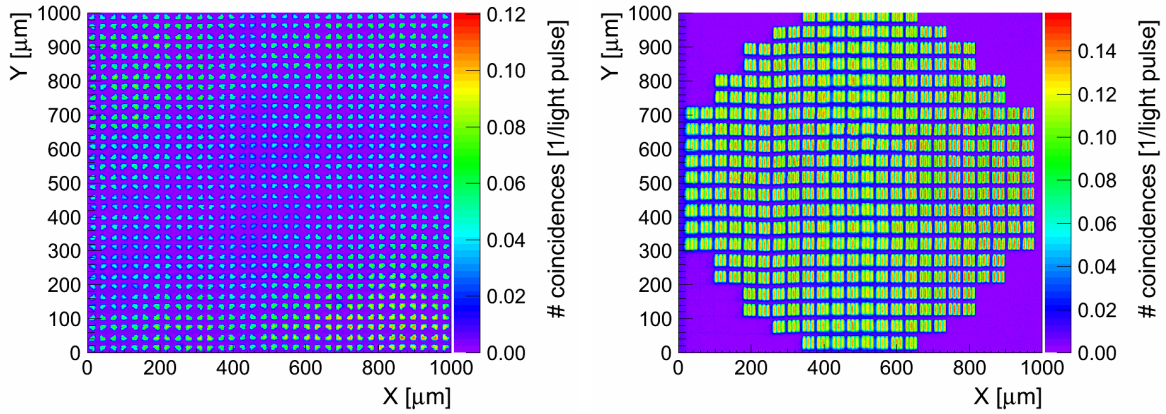

(a) MEPhI-32

(b) SensL-35

Figure 4.15.: Sensitivity maps of MEPhI-32 (**a**) and SensL-35 (**b**) taken at 0.5 p.e. discrimination level.

4.5. Summary

A new experimental setup was developed and assembled to provide relative photon detection efficiency maps of silicon photomultipliers with a spatial resolution up to 1 μm. The setup is capable of conducting simultaneous measurement at two different threshold levels. By proper setting of the levels and further offline analysis, crosstalk probability map for a particular sensor can be obtained and used for further corrections. As a result, a relative PDE map corrected for crosstalk and dark noise is extracted. Furthermore, a method which is capable of analyzing individual pixel separately was developed. It opens new possibilities to get additional quality measures of the SiPMs.

Using the new apparatus, several prototype sensors as well as commercial SiPMs were studied and compared. Being capable of investigating and understanding the SiPMs is very important for further development of calorimeters for the future linear e^+e^- colliders. During the tests, the main focus lied on the Hamamatsu MPPC with 50 μm pixel pitch, which was used in the T3B experiment and other projects of our group including the studies presented in chapter 5. A big importance had also a trial to characterise contemporary SiMPl detectors prototypes. This attempt was successful despite a high dark noise rate of the SiMPl sensors at room temperature. The first images of the sensitive regions which were experimentally obtained by such a method were presented.

The Hamamatsu MPPC-50 was tested also for different bias voltages to get information about the active region size in relation to the over-bias voltage. It was found out that the active area and therefore the geometrical fill factor do not change within a 1 V range around the recommended operation voltage. The other tested SiPMs with rectangular pixels, SensL, MEPhI and Hamamtsu MPPC-25U, were qualitatively compared with the MPPC-50. The results are shown in table 4.2. For the SiMPl devices, it was not possible to obtain some of the parameters shown below. Mainly, because of their poor performance at room temperature. The hexagonal pixel shape would also require a more complicated pixel recognition algorithm.

Device	**Dark noise**	**Crosstalk probability**	**Geometrical fill factor**	**PDE rel. mean standard dev.**	**Fill factor mean standard dev.**
Unit	[kHz]	[%]	[%]	[%]	[%]
MPPC-50	340	18	58	4	2
MPPC-25U	360	15	31	3	4
SensL-35	1300	24	31	4	4
SensL-100	1000	44	44	8	7
MEPhI-32	1450	17	22	37	18

Table 4.2.: Result summary of all successfully tested 1 mm^2 SiPMs with rectangular pixels. The last two columns are related to characteristics of whole pixels.

There is still space left for improvements of the experimental apparatus. One of the potential challenges is an ability to measure the absolute PDE. A very helpful upgrade would be a new pulse driver, which would assure a well-defined light pulse shape and

therefore a more controllable light yield. Another improvement would be an introduction of cooling of the SiPM. It would make possible studies of SiPMs at various temperatures. The cooling would also help to perform full-scale measurements of the prototypes which suffer from high dark rate.

CHAPTER 5

SCINTILLATOR TILE STUDIES

As a part of detector development for future calorimeters we performed a variety of different tests of scintillators and their light readout systems. Since the future sampling calorimeters should have a high granularity, the scintillators must be in a form of small tiles which are read out individually. Reasons for this requirement are discussed in section 2.5. One possible option for future accelerator projects is an analog calorimeter equipped with plastic scintillators. The plastic is easy to handle and machine, it has a high light output and its price is reasonable. The typical area of the scintillator tiles is about a few square centimeters and their thickness is a few millimeters. The scintillation light created by the passage of charged particles through the plastic is read out by a silicon photomultiplier (SiPM), which is attached to one of the faces of the tile. The large area of the tile face compared to the tiny SiPM active area brings certain challenges regarding the areal response uniformity of the tile. This property along with crosstalk between two adjacent scintillator tiles were studied with the help of a β-particle beam scans. The beam was provided by a ^{90}Sr radioactive source.

The *Tungsten Timing Test-Beam* (T3B) experiment [18, 78, 87] showed a significant differences in calorimeter response when tungsten or steel absorber is utilized. The discrepancy could originate from different production rate of secondary neutrons in tungsten and steel. One likely explanation of the enhanced response of a tungsten calorimeter is a higher emission rate of evaporated neutrons of the excited tungsten nuclei compared to iron. The emitted neutrons might deposit their energy in the scintillator and contribute to the output signal. It motivated us to conduct also an experiment with a goal to evaluate the sensitivity of the scintillators to neutron irradiation. This was done with a ^{241}Am/Be radioactive neutron source.

Detailed description of these experiments as well as their results will be presented in this chapter.

Tile type		T3B	ITEP
Dimensions	[mm^3]	$30 \times 30 \times 5$	$30 \times 30 \times 3$
Material		Polyvinyltoluene	Polystyrene
Emission max. wavelength	[nm]	391	430
Light output	[% anthracene]	64	56
Rise time	[ns]	0.5	0.5 - 0.9
Decay time	[ns]	1.5	2 - 3
Pulse FWHM	[ns]	1.3	N/A

Table 5.1.: Chosen parameters of studied scintillator tiles. Data about the T3B tile taken from producer's data sheet [88]. Equivalent product details are not available for the ITEP tile material [89], general polystyrene properties taken from [90] are listed.

5.1. Detector Layout

For tests of a scintillator, several additional components are required. First, a very sensitive light detector. Second, a coupling between the scintillator and the light detector which will assure the best possible transfer of the scintillation light to the sensor. Third, a reflector system which prevents the light from escaping from the scintillator tile. And fourth, adjacent readout electronics. These parts and their configuration will be described in the following.

5.1.1. Scintillator

Both two plastic scintillator prototypes, which were tested, have the same area of 30×30 mm^2. They do not employ any wavelength shifting fibers as some previous designs for calorimetry scintillator tile prototypes did. This solution is possible thanks to blue-sensitive SiPMs and it significantly simplifies the production process. The price, which is paid for the simpler manufacturing is worse response homogeneity. Both used scintillator tile prototypes will be described in the following text, their technical parameters are given in table 5.1.

T3B tile

The first tile sample was 5 mm thick and it was made of BC-420 material produced by Saint-Gobain [88]. It was machined from a larger piece of the material. A sticky 3M Radiant Mirror Foil which covered all sides of the scintillator was used as a reflector. The reflectivity of the foil was $>90\,\%$ for wavelengths >400 nm. This tile type was used in the T3B experiment which was our main motivation to perform these studies. Results obtained with this scintillator type also serve as a comparison for measurements with the other sample. In the following, we will denote this scintillator sample as *T3B tile*. The T3B tile is shown in figure 5.1a.

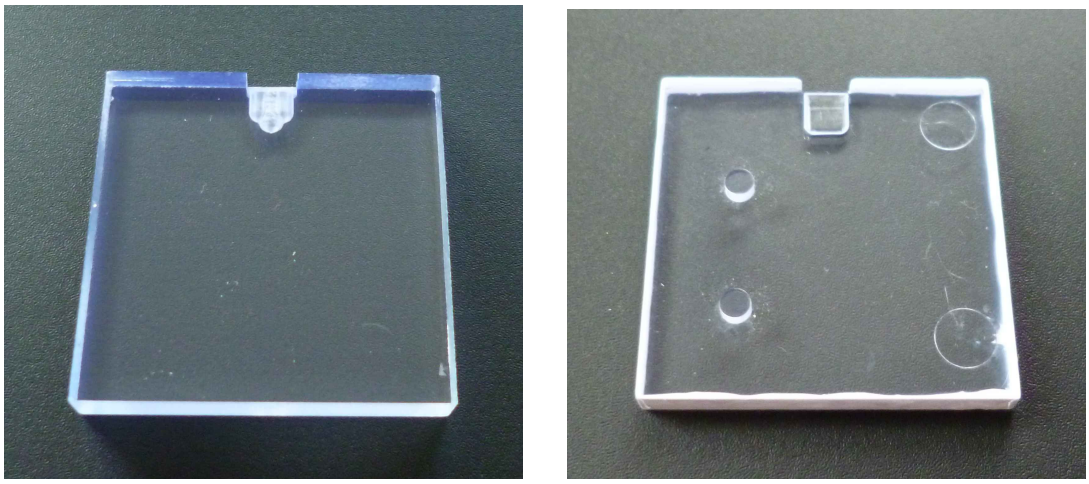

(a) T3B type (b) ITEP type

Figure 5.1.: Photographs of bare T3B (**a**) and ITEP tiles (**b**) without reflective foil cover.

ITEP tile

The second tile was 3 mm thick and it was made of BASF Polystyrene 143 [89, 91]. It was manufactured by injection molding technology. The four small narrow sides of the scintillator tile were manually coated with white reflective paint. Detailed specifications of the paint are not available. The big tile faces were either covered with the 3M foil in the same manner as for the T3B tile or the 3M foil was simply glued on another support material and laid on the scintillator surface. Which one of these reflector solution was used in current experiment will be specified in the respective sections. These tiles were designed in the Institute of Theoretical and Experimental Physics (ITEP), Moscow, and are intended to be used in the next version of the CALICE[1] AHCAL[2] [92]. In the following, we will denote this scintillator sample as *ITEP tile*. The ITEP tile is shown in figure 5.1b.

5.1.2. Silicon Photomultiplier

The main subject of interest in our study is the scintillator tile. However, the employed light sensor attached to the tile can strongly affect the overall detector performance. Let us name some examples. A long SiPM signal rise time can lower the time resolution, the size of the active area and the photon detection efficiency (PDE) determine directly the total number of detected photons. Therefore, in this perspective, a scintillator and a SiPM must be understood as one system. On the other hand, the dependence of the areal response homogeneity of the tile and the light crosstalk between two neighboring tiles on the detailed properties of the used SiPM is small. These things must be kept in mind while interpreting the results. From now on, we will describe and understand the scintillator and the SiPM together as one detector system.

[1] CALICE - Calorimeter for the Linear Collider Experiment
[2] Analog Hadron Calorimeter

Hamamatsu MPPC

In the vast majority of the conducted scintillator tests, Hamamatsu Multi-Pixel Photon Counter (MPPC) 50 P-type [66] were used for light readout. A photograph of this detector is shown in figure 5.2a. The same type of sensor was used in the T3B experiment. Therefore, its usage in our studies of T3B tiles assures consistency of both experimental setups. The distribution of the relative PDE of the Hamamatsu MPPC-50 was also studied. Further details regarding this topic are addressed in chapter 4.

KETEK SiPM

One test was performed with a scintillator tile which might be used in a next version of the CALICE AHCAL. Our intention was to partially reproduce a realistic configuration of the future experiment. The tile was equipped with a prototype KETEK SiPM. This light sensor was placed in a plastic casing with two metal pins for soldering as shown in figure 5.2b. The specifications of this sensor and the MPPC-50 are listed in table 5.2.

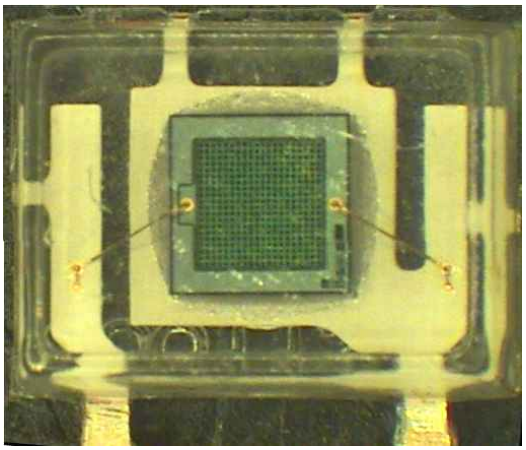

(a) Hamamatsu MPPC-50

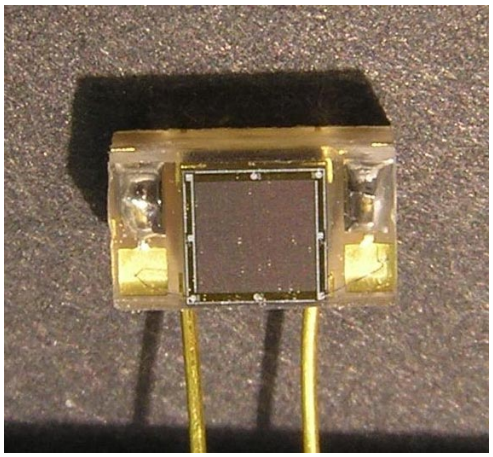

(b) KETEK SiPM

Figure 5.2.: Photographs of Hamamatsu MPPC-50 (**a**) and KETEK (**b**) SiPM.

5.1.3. Light coupling

As already mentioned, the SiPM is attached to one of the faces of the scintillator. To optimize the areal response uniformity of the tile, a small dimple is drilled or casted in the scintillator on the spot where the SiPM is attached. With the term *tile areal response* we mean the amount of detected photons as a function of the position of the passage of the charged particle through the tile. In an ideal case, this two-dimensional function will be flat. The additional dimple and its shape strongly affect flatness of this function. This is what we call tile *areal response homogeneity*. Dimple shapes have been extensively studied and adjusted in work [94].

The T3B and the ITEP tile use different dimple shapes. Also, the way of manufacturing of the dimples is different. The dimple for the T3B tile consists of three separately drilled

Parameter		MPPC-50	KETEK
Pixel pitch	[µm]	50	20
Sensitive area	[mm^2]	1×1	2.2×2.2
Number of pixels	[-]	400	12 100
Breakdown voltage	[V]	68 ± 10	≈ 24.6
Operation voltage	[V]	70 ± 10	32.5
Dark noise rate	[MHz]	0.8	< 2
Gain	[-]	$7.5 \cdot 10^5$	$9 - 11 \cdot 10^5$
Crosstalk probability	[%]	18	< 18

Table 5.2.: Specifications of Hamamatsu MPPC-50 and KETEK SiPM. Precise characteristics of MPPC-50 depend on a particular piece. Taken from [66, 93]. Crosstalk probability of MPPC-50 obtained from own measurement.

holes, their surface is opaque, due to the drilling. A detailed view on a dimple of the T3B tile is presented in figure 5.3a. On the other hand, the dimple of the ITEP tile, which is shown in figure 5.3b, is already incorporated in the casting form for the plastic. The inner surface of the dimple is therefore glossy. From previous measurements, it seems that an opaque surface is more favourable, because it causes light dispersion and avoids further unwanted reflections.

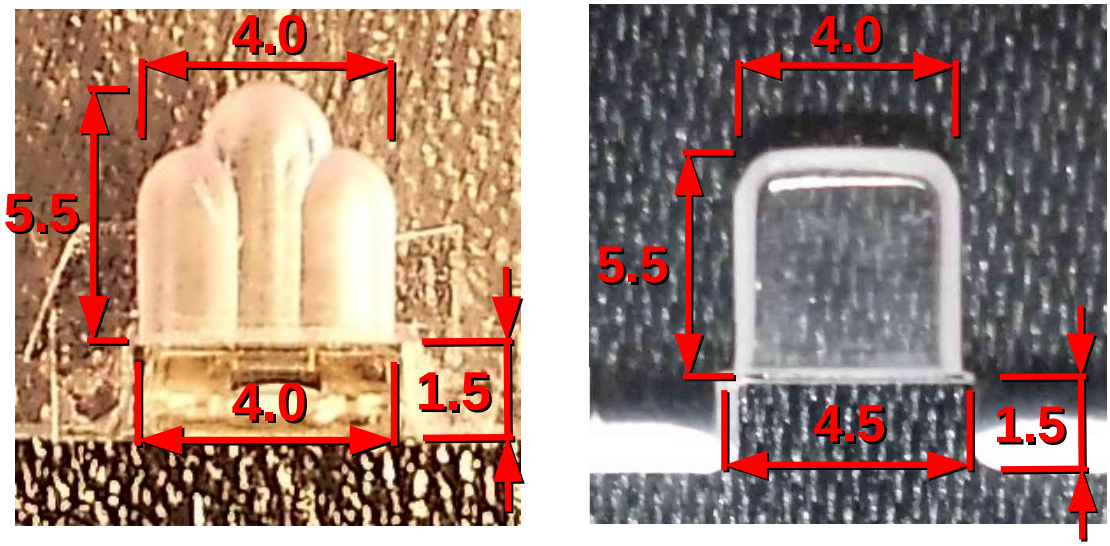

(a) T3B type

(b) ITEP type

Figure 5.3.: Photographs of dimples and the dimple dimensions in mm for the T3B (**a**) and the ITEP tiles (**b**).

5.2. Readout System

The same devices and a part of the data analysis tools which were employed in the T3B experiment were utilized for our data acquisition (DAQ). We will describe them shortly. A detailed list of the experimental equipment can be found in appendix A, table A.4.

Readout board

During all performed tests, we used the same type of a preamplifier readout board which is pictured in figure 5.4b. This printed circuit board (PCB) was developed in the electronics department of the Max Planck Institute for Physics (MPP) to have minimal input capacitance. The SiPM is therefore placed very close to the preamplifier which is the key element of the board. The low capacitance of the readout system provides good timing resolution for short SiPM signals. The board requires two supply voltages, +5 V for the amplifier unit and the bias voltage for the SiPM which is given by the specifications of the particular model.

The SiPM was soldered directly on the board. The scintillator was put on the top of the preamplifier board such that the SiPM was correctly positioned in the dimple. I our experiment, we wanted a β-particle beam to go through the scintillator. The particles passing through the tile must be also registered in a second coincidence detector beneath the tested scintillator. For this reason, the part of the PCB beneath the studied tile was cut away to prevent absorption of the ionizing particles. The removed PCB was replaced with a thin plastic foil to support the scintillator. The tile was lightly glued to the foil to be fixed in its position.

Oscilloscope

The DAQ of the test stand was performed with a Pico Technology screenless USB-controlled oscilloscope PicoScope PS6403 [95] shown in figure 5.4a. This device is capable of simultaneous waveform recording on its four input channels with a sampling frequency of 1.25 GHz per channel. The oscilloscope is equipped with a 1 GB internal buffer. Until the buffer is filled, the trigger frequency can be up to 1 MHz. When the buffer is filled, the accumulated data must be transferred to a computer. The PicoScope is fully driven by the USB port and works in the same way as an ordinary oscilloscope. To control the PicoScope, the DAQ software developed for the T3B experiment was utilized in all of our experiments. For our purposes, the PicoScope performance was more than sufficient.

(a) Oscilloscope

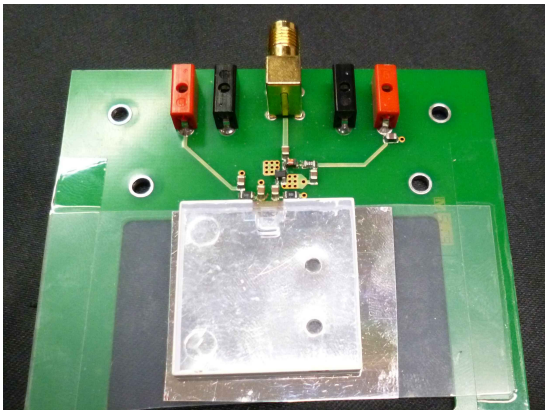

(b) SiPM readout board

Figure 5.4.: (**a**): Photograph of a Pico Technology PicoScope PS6000 series. Taken from [95]. (**b**): Picture of the used SiPM readout board with installed ITEP tile.

5.3. Tests with β-Source

We performed scintillator tile tests using a collimated ^{90}Sr radioactive source to create an electron beam. This beam can be pointed to any spot on the scintillator. The β-particles penetrate the tile material, interact with it, and the detector response is measured. A trigger detector is placed beneath the scintillator tile to ensure full penetration of the particles. Two kinds of tests were done.

The first one is a two-dimensional (2D) scan of the big side of the tile. The source is driven with a positioning stage in steps of 0.5 mm over the whole scintillator and its response is recorded as a function of the $X - Y$ position of the stage. The result is a map describing the tile response.

The second measurement employs the same experimental setup and methods. Two scintillator tiles of the same type are placed side by side, neighbouring on the small side in the same manner as it will be done in the future calorimeter. The electron beam goes in steps along a line perpendicular to the tile edge across the border region where the tiles touch as shown in figure 5.6. Both tiles are read out by the DAQ during the whole measurement. We are mainly interested in the response of the tile, which is not irradiated at the given moment. Because the tile is not irradiated, no ionizing particles can produce any scintillation light in this tile. Therefore, the SiPM detects just photons which originate from the irradiated tile and passed through the reflectors on the side where the tiles are in contact. We call this effect *light crosstalk*. Thermal noise of the SiPM also contributes to the number of measured photo-electrons (p.e.). To correct for this effect, the noise is recorded in a separate measurement and subtracted later on.

5.3.1. Experimental Apparatus

In the following, we will present the technical implementation of our experimental setup for β-source tile tests. The apparatus is schematically depicted in figure 5.5.

The readout board which carries a dedicated trigger detector and the ^{90}Sr source are

attached to a three-axis positioning stage. The geometry of the source and the trigger detector board holders is designed such that the electron beam always aims in the middle of the trigger. The trigger detector is a $5 \times 5 \times 5\,\mathrm{mm}^3$ large scintillator cube made of the same material as the T3B tiles and it is read out by a Hamamatsu MPPC-25P [66]. Two horizontal axes of the stage are controlled by a computer. Their range is 50 mm with a positioning precision of $50 - 100\,\mu\mathrm{m}$. The third axis with a range of 25 mm is operated just manually with the help of an electronic controller. It is used for adjusting the distance between the tile under test and the trigger detector.

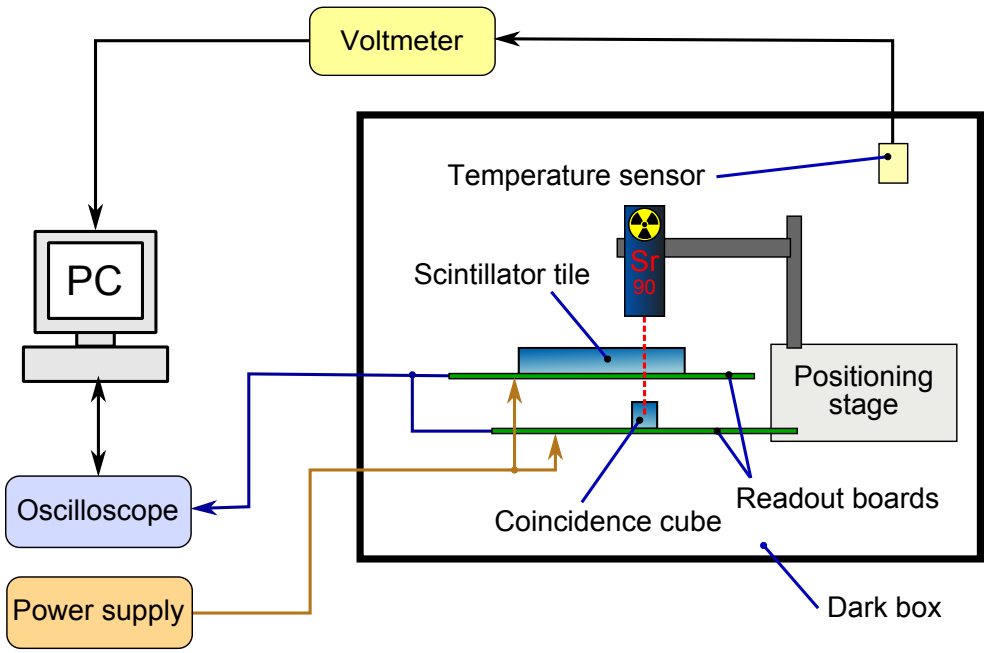

Figure 5.5.: Schematic of the tile scan experimental setup. Coincidence detector and the radioactive source are carried on a *XYZ*-stage while the tested scintillator is fixed. Both detectors are read out by an oscilloscope.

In between the radioactive source and the trigger detector is placed the tested tile which is attached to its own readout board. Its position can be adjusted such that the stage can cover the full area of the tile in a 2D scan. In a crosstalk measurement, two readout boards with two tiles are placed under the source such that their joint border lies in the middle of the range of the stage. Then, we can perform a symmetrical scan. A schematic drawing of the source path is show in figure 5.6.

All employed readout boards need their power supply lines for the amplifier and the SiPM. Their output signals were all read out by one PicoScope. Every SiPM is powered with an independent power supply to be able to adjust the SiPM gains separately. The stage as well as the oscilloscope communicated with the PC via a USB port. All the scintillators with their preamplifier boards, the ^{90}Sr source and the micro-positioning stage were enclosed in a light tight dark box to avoid any influence of outer illumination.

For temperature monitoring in the dark box, we used a resistance thermometer Pt1000. This sensor was read out by a dedicated voltmeter and the temperatures were acquired every 30 s by the PC via GPIB interface during the measurement. We used the Pt1000 during

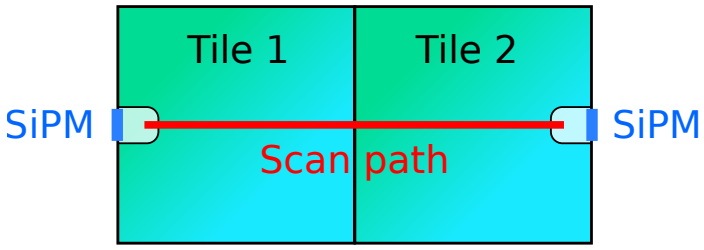

Figure 5.6.: Schematic drawing of the scan path in a crosstalk measurement.

the test to check the temperature stability, because bigger temperature fluctuations could affect the measurement through change of the SiPM gain. The temperature monitoring is also a valuable feature in the phase before the measurement is started. When the box is closed and the preamplifiers are turned on, the released heat warms up the box considerably. Thanks to the temperature sensor, we were able to start the measurement after the temperature was stabilized.

Figure 5.7 shows a photograph of the scan setup. The pictures portrays the configuration prepared for a crosstalk measurement of T3B tiles.

5.3.2. β-Source Properties

In all conducted tile scans, we employed a radioactive ^{90}Sr β-source [96, p. B32] with an activity of 13.9 MBq. The source is enclosed in a tungsten-copper capsule manufactured in the mechanics department of the MPP. The source is equipped with a removable collimator made of the same material as the capsule. The capsule opening is a hole with 1 mm in diameter. The source produces β-particles by a decay of the ^{90}Sr and ^{90}Y. ^{90}Y is a daughter product of ^{90}Sr. The electron energy spectrum of the ^{90}Sr/^{90}Y source is shown in figure 5.8. The first peak in the spectrum comes from electrons emitted by ^{90}Sr, the second one from ^{90}Y. To be really precise, the source should be denoted as ^{90}Sr/^{90}Y, because the ^{90}Y contributes to the overall electron rate significantly. However, this source will be called shortly ^{90}Sr for simplicity.

Profiles of the electron beam were experimentally obtained. A GAFCHROMIC EBT2 film [99] was used to fulfil this task. It is sensitive to β-radiation, it is self-developing and has an excellent dynamical range. We placed two layers of the film under the source and irradiated them for 63 hours. The distance between the source and the first film was about the same as the typical distance between the source and a scanned tile, i.e. ∼ 1 mm. The distance between the films was 1.4 mm. The resulting profiles are shown in figure 5.9. The strong dependence of the dose on the distance from the source is apparent. The measured dose shown in the figure has possibly about 30 % systematic error. On the other hand, the relative relations in the plot which are for us the most important are much more precise. The relative uncertainty is estimated to be about 5 %. We can conlude that the ≈ 1 mm wide electron beam is for our experiment narrow enough. Sufficient spatial resolution of the determination of the scintillator tile response uniformity can be achieved with this beam. The beam width measurement is also fully consistent with further measurement results at the edges of the tile [100]. As the beam leaves the scintillator area, a crossover region is apparent in the tile response plot. This region is roughly 1 mm wide. Further

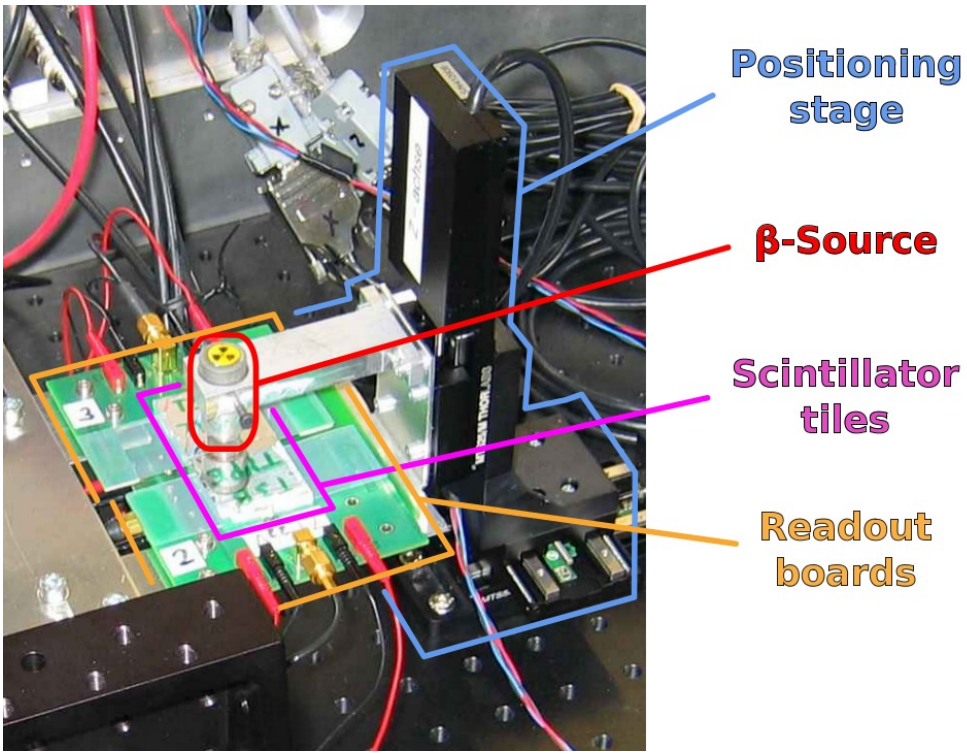

Figure 5.7.: Scintillator tile scan setup with the ^{90}Sr source. (In crosstalk measurement configuration.)

important characteristics of the beam are listed in table 5.3.

5.3.3. Trigger Configuration

The trigger during all β-source measurements was provided by the above mentioned trigger detector. We demanded a signal of 6 or more p.e. in the trigger. There are two reasons for triggering on one detector only. If a coincidence of both detectors would be required, in the moment when the beam runs out of the area of the scintillator, the trigger condition cannot be fulfilled any more. Since the scan runs in a window which is larger than the tile itself it is absolutely necessary to proceed with the measurement even when the beam is outside of the tested scintillator.

The second reason for the particular trigger choice was the crosstalk measurement.

Parameter	Value
Total activity	13.9 MBq
Collimator aperture	1 mm
Source - collimator opening distance	16 mm
Collimated beam rate	3.4 kHz

Table 5.3.: Parameters of used ^{90}Sr β-source.

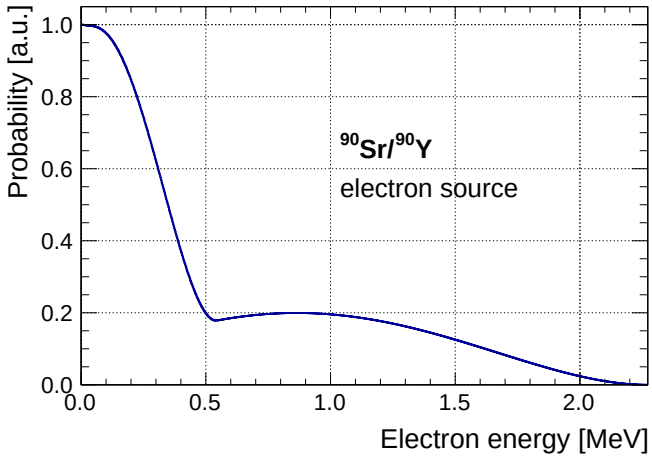

Figure 5.8.: Electron energy spectrum of ^{90}Sr/^{90}Y source calculated based on Fermi's theory of beta decay [97]. Plot from [98].

In this case, the scan is running through two independently read out tiles. The coincidence condition for this experiment would be *(tile 1* $\vee$ *tile 2)* $\wedge$ *trigger detector*. However, our DAQ does not allow to implement the logical disjunction between the two tiles easily. Furthermore, this condition can bias the data in the border region between the tiles. The electrons are there partially absorbed by the reflective coating. The coincidence triggering would lead to an unrealistic enhancement of the number of hits in this region.

The chosen trigger setting eliminates these issues and it also does not put any bias on the experimental data. Our assumption is that the particles which are detected in the trigger detector have interacted with the scintillator tile, too. The trigger level of 6 p.e. was chosen empirically as a compromise value. It suppresses the dark noise of the trigger detector sufficiently, while assuring a high enough trigger rate during the measurement.

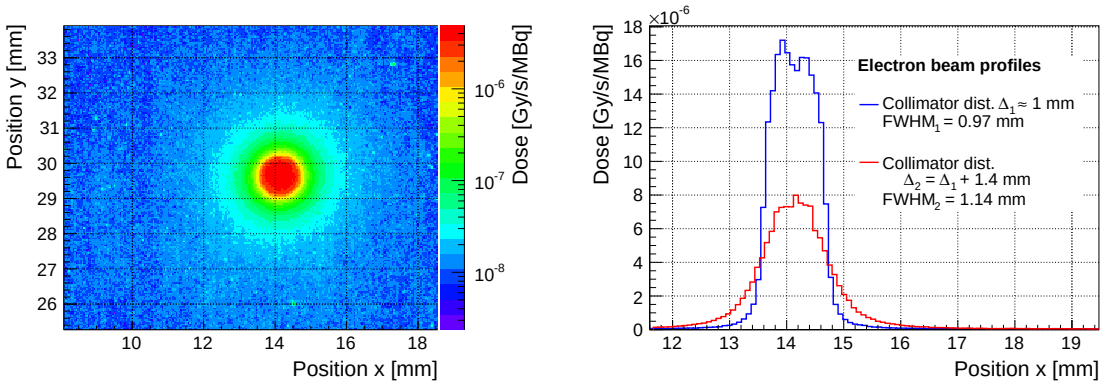

(a) 2D profile of the ^{90}Sr electron beam

(b) Profiles of the ^{90}Sr electron beam

Figure 5.9.: Two-dimensional profile of the used electron beam (**a**) at the usual distance of tile surface (~ 1 mm from the collimator) and two one-dimensional profiles (**b**) of the beam at the distance of the tile surface and 1.4 mm further.

5.4. Neutron Irradiation

This test was conducted with both tile types, the T3B and ITEP, at once. We irradiated them with an uncollimated ^{241}Am/Be neutron source. The point of the measurement was to check, whether the scintillators are sensitive to neutrons at all. And if this was the case, it would be further investigated, whether the tiles can give any spectroscopic information about the source. The tile irradiation experiment serves also as an independent check of the source activity.

The main motivation for this experiment was a discrepancy of results of the T3B experiment [78]. The T3B studied time structure of hadronic showers. It measured that the energy depositions in the case of usage of a tungsten absorber are enhanced compared to steel. A possible explanation of this observation is a higher amount of evaporation neutrons emitted by the denser tungsten [87].

During development of a hadronic shower, protons and neutrons with an energy of a few hundred of MeV are knocked out of the absorber nuclei in a spallation process. Neutrons are more likely to be released. Their energy is not high enough to induce further hadronic cascade. They are stopped by the absorber nuclei and incorporated in them. Due to the absorption of high energy particles, the nuclei are excited. After a period of time, the nuclei de-excite. One way of getting rid of the excess energy is releasing of evaporation nucleons. Because the neutrons do not have to overcome through the Coulomb barrier, they are emitted with a higher probability than the protons. The kinetic energy distribution of the neutrons has a Maxwell-Boltzmann shape with a mean value of 3 MeV. Moreover, the amount of the evaporation neutrons is larger for heavier elements.

Since the plastic scintillators consist entirely of hydrogen and carbon which have a high cross sections for elastic scattering with fast neutrons, a considerable sensitivity to the evaporation neutrons is expected. We prepared an experiment to investigate this issue by irradiating the scintillators with a neutron source which supplies neutrons with kinetic energies ranging between ~ 100 keV and ~ 10 MeV. The energy spectrum of the source

suits the task perfectly.

We also wanted to examine an impact of presence of tungsten shielding around the source on the measurement results. However, the source was enclosed in a tungsten capsule which could not be removed. The fast neutrons can also excite the tungsten nuclei which de-excite by emission of γ-radiation afterwards. To evaluate the impact of the secondary γ-radiation, we performed a further measurement with additional lead shielding.

5.4.1. Experimental Apparatus

The neutron experiment utilized almost all the equipment which was used in the tile scans except for the positioning stage. The mechanical support structure of the readout boards was slightly modified such that the tiles were in a vertical position to cover as much of the solid angle around the source as possible. The source was not collimated and therefore it radiated the neutrons isotropically in the full solid angle. To irradiate both tiles equally, a symmetrical experimental configuration was chosen. It is schematically depicted in figure 5.10, a photograph of the setup is shown in figure 5.11. Two measurements were performed. In the first of them, the source was enclosed in an additional lead container to shield the γ-radiation originating from the radioactive source and the a potential secondary radiation of the tungsten capsule. In the second one, the lead container was removed.

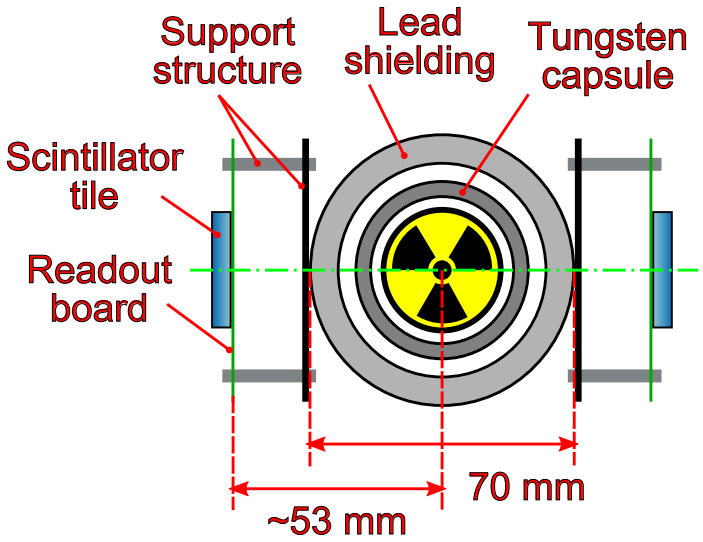

Figure 5.10.: Schematic top view of the neutron irradiation experiment. The ^{241}Am/Be neutron source itself is enclosed in a tungsten capsule. One of the two measurements was performed without the lead shielding.

5.4.2. Neutron Source Properties

We used as a neutron emitter a ^{241}Am/Be source [96, p. B6, capsule X.2]. The americium undergoes an alpha decay and the emitted α-particle can further react with the beryllium in the following way,

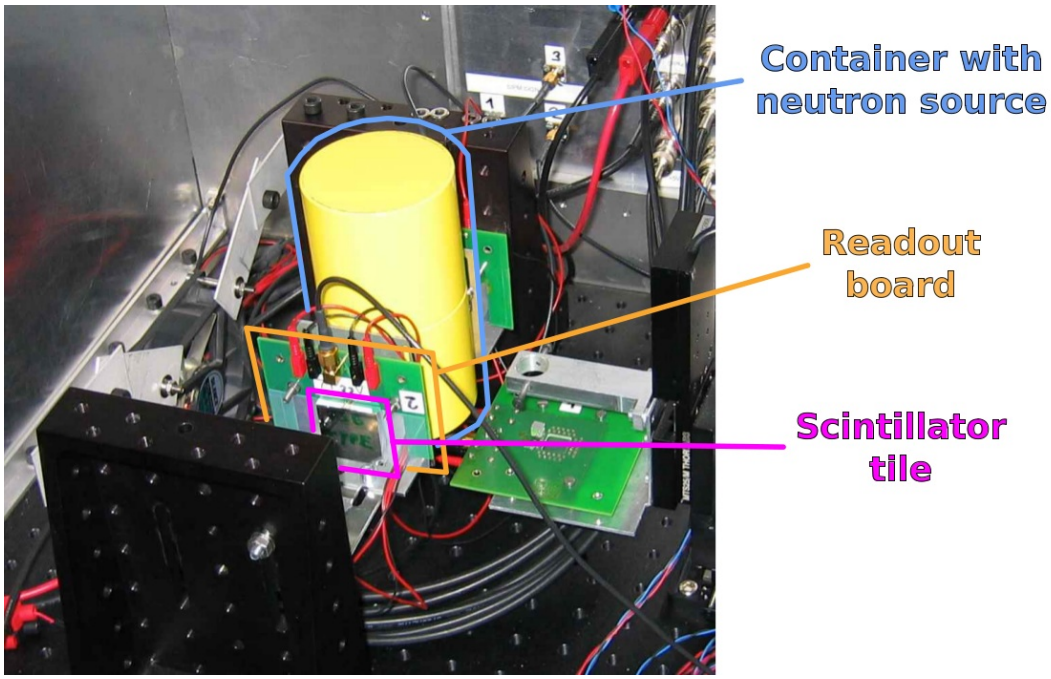

Figure 5.11.: View of the neutron irradiation experiment. The source is enclosed in the yellow lead container which was utilized as a lead shielding. The scintillator tiles are placed symmetrically in a vertical position along the source.

$$^{4}_{2}\mathrm{He} + ^{9}_{4}\mathrm{Be} \longrightarrow ^{12}_{6}\mathrm{C} + ^{1}_{0}\mathrm{n}, \tag{5.1}$$

and produce neutrons. The yield of the α-decay and the subsequent reaction (5.1) in the current Am/Be mixture is $\sim 6 \cdot 10^{-5}$ neutrons per one α-particle. In addition to that, in a thick source, reactions Be(n,2n)Be and Be(n,2n+α)He take place. These produce low energy neutrons and enhance the neutron output by a factor of 1.5 [98]. The energy spectrum of the emitted neutrons is shown in figure 5.12 and it does not include the Be(n,2n)Be and Be(n,2n+α)He reactions.

The ^{241}Am/Be source was enclosed in a tungsten-copper capsule. Unfortunately, further mechanical details of the capsule are not available. We estimate the thickness of its walls to be about 5 mm. The source itself is sealed in a $\sim$ 1 mm thick steel casing. These tungsten and steel metal layers are thick enough (mainly the tungsten) to absorb almost 100 % of the 59.5 keV γ-radiation emitted by the ^{241}Am. Hence the gammas do not pollute our measurements. However, in the reaction (5.1), further γ-photons with energy of 4.44 MeV are released. The contribution of these photons to the overall signal is of the order of 10 % [101, 102, 103]. The parameters of the Am/Be neutron source are listed in table 5.4.

5.4.3. Trigger Configuration

In this experimental configuration, the trigger detector was not used and we triggered directly on the output of the scintillators. Each tile was triggered independently. The emission of the radioactive source was isotropic and the whole area of the tiles was irradiated

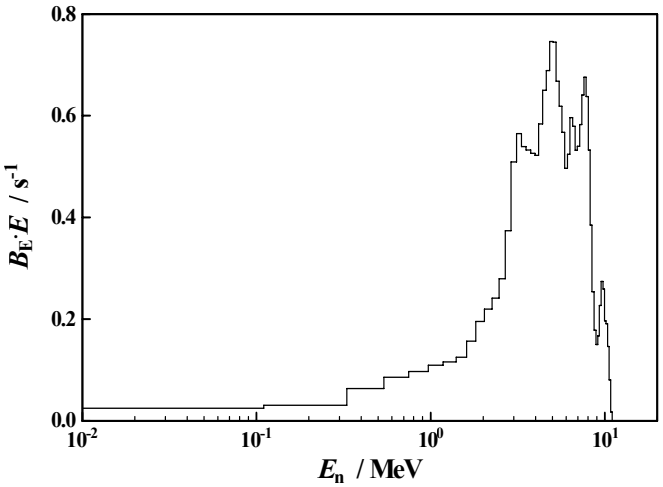

Figure 5.12.: Energy spectrum of neutrons emitted by a thin ^{241}Am/Be source. B_E is spectral source strength. Taken from [104].

Parameter	**Value**
^{241}Am activity	1.1 GBq
Neutron emission rate	100 kHz
Collimator	none
Neutron angular distribution	isotropic

Table 5.4.: Parameters of the ^{241}Am/Be neutron source.

at a time. The usage of a trigger detector in this configuration does not make any sense, because a neutron interacting with the scintillator is either stopped completely or deflected from the original direction. To be able to use independent triggers on two channels, we employed one PicoScope for each tile. Because the actual measured trigger rate of the neutrons was about 21 Hz, we had to set a high enough trigger threshold to suppress thermal noise of the SiPMs. Hence, we put the trigger threshold to 8 p.e. at which the SiPM noise dropped to $\sim$ 1.3 Hz. The higher threshold limits measurement of the lowest deposited energies to 400 keV for the T3B and 540 keV for the ITEP tile. However, this in not an issue, because the focus of the measurement was by the neutrons with an energy of several MeV.

5.5. Data Analysis Tools

As already mentioned, a significant part of the data analysis tools of the T3B experiment was used. We will describe the used methods briefly.

The data analysis can be divided into two stages, the *calibration* and the *analysis*. The output of the calibration is a precise information about every single recorded waveform: How many SiPM cells have fired, and a time stamp of every fired cell with a precision of $\approx$ 800 ps. The whole calibration framework was adopted from the T3B experiment and it is described in detail in [87]. The analysis stage of the data processing takes the output of the calibration stage as its input and produces final results. For each of the three conducted tile tests, the analysis stage was done in a different way and adjusted according to the requirements of the particular experiment.

To be able to understand steps of the calibration stage, the form of the experimental data will be explained.

5.5.1. Experimental data

There are two kinds of data acquired during all of the performed measurements. The DAQ records a given number of triggered events first. All these events have the same preset length in time and the time window consists of a pre- and post-trigger part. In this DAQ mode, we collect the information originating from the interaction of the radiation with the scintillator material. Therefore, we call this regime and the data *physics mode* and *physics data*, respectively. In the physics mode, the PicoScope is operated in the voltage range of ± 200 mV, which is the maximal applicable to keep a sufficient voltage resolution.

However, the SiPMs are very sensitive to temperature changes as discussed in section 3.7. If one wants to precisely determine the number of fired cells in a waveform in a long lasting run, a reference measurement to correct the waveform amplitude for changing temperature is needed. Therefore, after the physics mode, another set of data in a so called *intermediate run mode* (IRM) is recorded. In the IRM, the PicoScope is running in the smallest voltage range of ±50 mV providing the highest voltage resolution. The trigger condition is set on the output of the tile under test and its level is 0.5 p.e. This means, that the DAQ will collect all events with one or more firing pixels. The pixels are firing due to thermal noise with a much higher rate than the rate of events induced by the external irradiation of the tile. In the dark noise, the events with one firing pixel are the most frequent. As a result, the IRM picks up mostly dark-noise-originating waveforms with one

firing pixel. Based on this data, a so called *average 1 p.e. waveform* is calculated in the offline analysis. It is obtained by averaging a certain number of 1 p.e. waveforms. The average 1 p.e. waveform is used in the last step of the calibration later on to determine a precise number of fired pixels in the waveforms recorded in the physics mode. 2500 events in the IRM and 1000 events in the physics mode are typically recorded per one beam position in a ^{90}Sr measurement. In the experiment with the neutron source, we collected 10 000 events in the physics mode per one DAQ cycle. One such a bunch of data is called a *spill*. The name spill was adopted from the original application of the DAQ software. It was used by the T3B experiment at the Super Proton Synchrotron (SPS) at CERN. The accelerator was operated in a mode of separate 10 second long particle pulses and the data was acquired according to these particle bursts. At the SPS, each of the particle pulses was called a spill.

5.5.2. First Stage: Data Calibration

In the calibration stage, the data recorded in the IRM will be used to calibrate the physics data. The first step, the *synchronization*, serves to check consistency of the data collected by different oscilloscopes (the DAQ is capable of operating up to five PS6403 oscilloscopes at a time). However, we used more than one oscilloscope just in the neutron measurement and even in this case, the synchronization was not necessary. We mention this calibration step just for completeness.

The second step is the *pedestal subtraction*. The pedestal voltage of the waveforms recorded in both run modes is determined separately for every channel and every spill. It is subsequently subtracted from all waveforms at this point of the analysis.

In the *SiPM gain calibration*, the gain of all connected SiPMs is determined. This procedure is performed only on the IRM data and it is based on calculating of the mean values of waveform integrals for 1 and 2 p.e. signals. The difference of the two mean values gives the charge of one firing pixel. This charge expressed in elementary electrical charge units is the gain of the particular SiPM. Usage of amplifiers must be taken into account. The gain is calculated separately for every single spill and it is used in the next step of the calibration as a selection criterion for waveforms to be averaged.

The calculation of the *average 1 p.e. waveform* is performed as the fourth step of the calibration from the recorded IRM data. This process is the key one for later waveform decomposition. All recorded waveforms which have the integral within ±25 % around the gain value calculated in the previous step are added up and averaged over a every 3 spills. A single very smooth waveform is obtained for each spill set. The tailing edge of the signal has an exponential form and therefore it cannot be fully recorded within a limited time window. Hence, it is fitted with a proper function and is extended up to the point where the signal voltage drops below 5 μV.

The last stage of the calibration is the *waveform decomposition*. The precise number of fired pixels along with their timestamp in every waveform recorded in the physics mode is obtained here. The principle is following: At first, the position in time of the global maximum of the waveform is found. Then, the average 1 p.e. waveform is subtracted at this time point. In the next iteration, a new global maximum is found and the averaged 1 p.e. waveform is subtracted again, etc. This procedure is repeated as long as the waveform is not flat within certain limits. The time positions where the averaged waveforms were subtracted give the timestamp of each fired pixel. An illustration of this procedure is

depicted in figure 5.13. It displays one real event recorded during the neutron irradiation experiment and its decomposition into single detected scintillation photons.

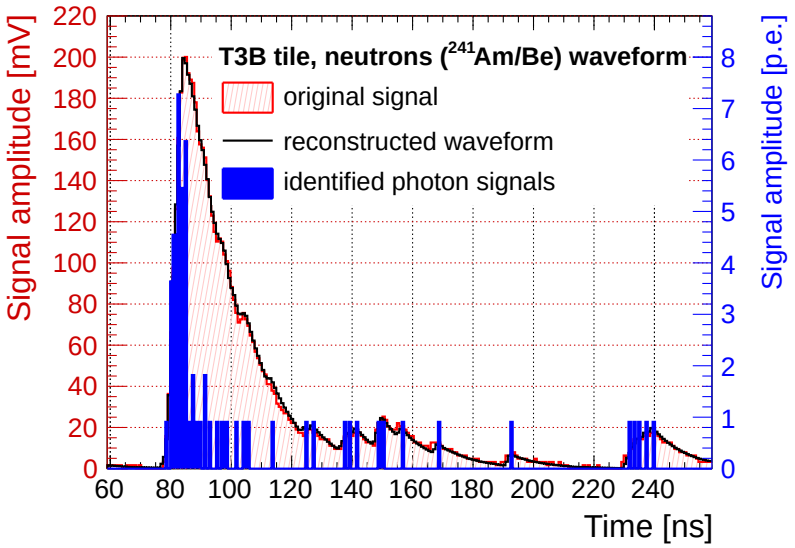

Figure 5.13.: Example of waveform decomposition demonstrated on waveform recorded during irradiation of a T3B tile with neutrons.

5.5.3. Second Stage: Calibrated Data Analysis

We performed several kinds of measurements, the scintillator tile scan with the electron beam and the test with the radioactive neutron source. In addition to that, we conducted also a *noise run* for the crosstalk tile scans and the neutron irradiation experiment. The purpose of the noise run was to determine the contribution of the thermal noise and crosstalk of the SiPM. We will now describe the data analysis methods for all these kinds of measurement modes.

Two-Dimensional Scintillator Tile Scan

In this kind of measurement, for each stage position a one thousand triggers was recorded. We are particularly interested in the number of detected scintillation photons originating from interactions of the electrons traversing the scintillator per one beam position. Because one spill characterizes one measurement point, the analysis evaluates every spill individually.

The mean number of fired pixels within a time window starting 0.8 ns before and ending 8.8 ns after the trigger is extracted from each waveform in a given spill. This particular time window choice was determined during the analysis of the T3B experiment [18]. It has been shown that this time span is long enough to integrat the instantaneous part of deposited energy. At the same time, it suppresses a part of afterpulsing of the SiPM. The final result of the analysis is a two-dimensional distribution of the mean numbers of fired pixels per electron beam position across the scintillator tile.

One-Dimensional Crosstalk Scan

The signals induced by the crosstalk photons originating from the neighboring scintillator cell overlay with the noise of the SiPM. Therefore, the noise must be precisely determined and subtracted. To be able to subtract the noise in a consistent way, the following analysis was performed.

The numbers of fired pixels in each recorded waveform are added up and the total number of fired cells within a spill is obtained. This quantity is normalized by the number of recorded waveforms in the spill. This particular normalization was chosen due to the following reasons.

Some of the recorded events do not contain any signals of firing pixels. This can happen, when the trigger detector is activated by its thermal noise or scattered particles. In these situations, no interaction of electrons in the scintillator tile takes place. Other kind of waveforms could be corrupted in some way, e.g. that the signal amplitude exceeds the voltage range of the oscilloscope. The waveform decomposition procedure can fail in evaluating such events. The outcome information is then that zero pixels have fired in that waveform. The normalization by the number of recorded waveforms takes the events with zero fired cells into account.

A normalization by the number of waveforms which contain at least one p.e. signal was also considered. However, such a normalization factor would vary from spill to spill and the noise subtraction would be more difficult. The noise value recorded in a dedicated measurement would have to be weighted by the variable normalisation factor as well. Furthermore, such a normalization would bias the results by neglecting the waveforms with zero outcome.

Noise Run for Crosstalk Scan

During the noise run for the tile scan, the β-source is removed to record just the noise of the SiPM which reads out the tile under study. The data is taken with a random trigger of the DAQ to eliminate any bias of the data. Typically, about 40 000 noise events were collected. From such a data set, the mean number of fired pixels in a waveform including the empty events is extracted. All other conditions like time window length, temperature, oscilloscope range, etc. stay the same as in the measurement with the radioactive source. In this case, the number of pixels which fired due to thermal noise and SiPM crosstalk can be subtracted from the mean number of detected scintillation photons which was obtained in the scan with the radioactive source. This way, we get the correction for the SiPM noise and crosstalk. Our experience has shown that the value characterizing the noise is rather stable. It is independent of the used scintillator. This shows that there are no background physics events present and the noise is caused entirely by the SiPM.

Neutron Irradiation

The trigger condition in the neutron measurement was a demand of at least eight simultaneously firing pixels of the SiPM which read out the studied scintillator tile. No coincidence was used. We were particularly interested in deposited energy spectrum in the neutron measurement. The energy was integrated within the same time window which

was used in the evaluation of the 2D scan measurement, i.e. a time interval starting 0.8 ns before and ending 8.8 ns after the trigger.

In this measurement, a noise run was performed as well. However, this noise run is different than the one described in previous section. All the DAQ settings including the trigger requirement were kept the same as in the measurement with the neutron source, but the source was removed. The noise run data were treated in the same way as the "neutron" data and both resulting spectra were properly scaled according to statistics and subtracted.

The last step of this analysis procedure was the calibration of the measured scintillator response from p.e. to units of energy. To accomplish this task, an additional energy calibration for both tested tiles was required. The calibration was done based on two parameters. The scintillator response in terms of the number of detected p.e. to a minimum ionizing particle (MIP) and the energy deposited by this particle in the particular scintillator tile are required.

The response of the tile to a well-defined energy deposition was extracted from the 2D scan of the tile performed with the electron beam. It is known that the measured energy deposition of β-particles obeys a Langau distribution which is a convolution of Landau and Gauss distribution [69]. The most probable value of this distribution gives the most probable number of fired SiPM cells when a β-particle hits the scintillator. This distribution in units of p.e. was available from the previous 2D scans with the electron beam. We conducted a Langau fit on that distribution for both tiles, and obtained the wanted quantity. The deposited energy distributions for both tiles are depicted in figure 5.14. The most probable value of the energy deposited by a β-particle from the ^{90}Sr source in the scintillator was acquired from a GEANT4 [105] simulation [106, 107]. The numerical values of these parameters for both scintillator tiles are listed in table 5.5. There are substantial differences between the T3B and the ITEP tile. The energy deposition is driven mainly by the thickness of the tile. In addition to that, the tile response is affected by the light yield of the scintillator material which is lower for the ITEP tile.

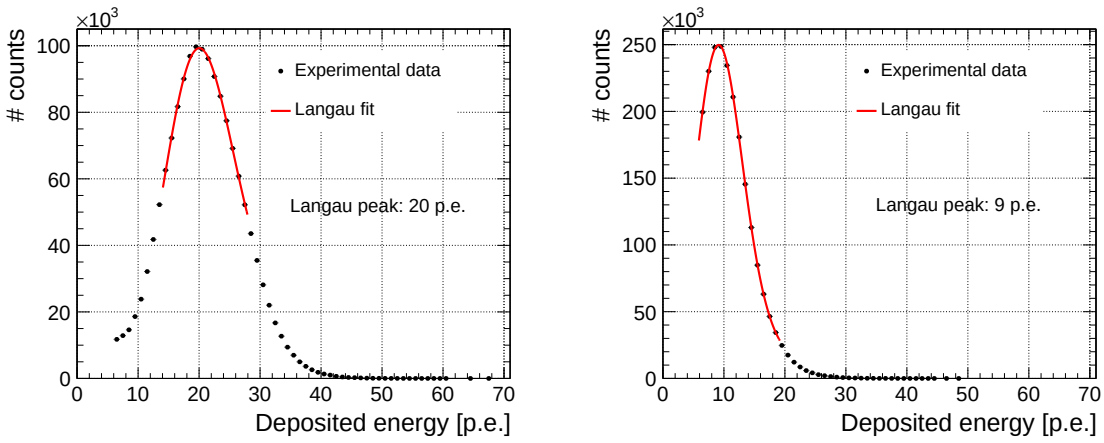

(a) T3B tile

(b) ITEP tile

Figure 5.14.: Langau fit of deposited energy spectra for T3B (**a**) and ITEP (**b**) tile.

Parameter	T3B tile	ITEP tile
Energy deposited by a ^{90}Sr electron	982 keV	570 keV
Num. of fired pixels for a ^{90}Sr electron	20 p.e.	9 p.e.

Table 5.5.: Values of parameters used for energy calibration of the neutron irradiation experiment. Obtained from [106] and electron beam scans.

5.6. Results

This section will present the results obtained in the set of experiments with scintillator tiles described above in this chapter. All measurements were done with both tiles, the T3B and ITEP type.

5.6.1. Two-Dimensional Tile Scans

The two-dimensional maps of tile response to β-particle beam for both tile samples are displayed in figure 5.15. These tiles were read out by Hamamatsu MPPC-50P. On the X and Y axis is the spatial coordinate in the tile plane. The Z axis shows the mean measured energy deposition when the particular spot is irradiated by the electron beam. The deposited energy is expressed in terms of the amount of detected scintillation photons. The mechanical step of the beam positioning was 0.5 mm in all of these measurements.

Regarding reproducibility and systematic uncertainties of the scans, the distance of the β-source from the tile under test plays an important role. A large distance reduces electron trigger rate significantly due to the divergence of the electron beam. This leads to enhanced number of triggers caused by noise of the detector. A consequence of these effects is a reduced mean number of collected scintillation photons. According to current capabilities of controlling this distance, we estimate the systematic error of the light output around 20 %. However, since we are mostly interested in relative quantities, the systematics do not play a significant role.

T3B Tile

The 2D scans of the T3B and the ITEP tiles are presented in figure 5.15. One can see here a direct comparison of performance of both tile types. The T3B tile response map shown in figure 5.15a. The uniformity is quite high over a large portion of its area. The region around the dimple evinces about 25% higher signal than the overall mean value. However, this region is only a few tens of mm^2 large which represents just a few per cent of the overall tile area. On the other hand, there are very few scintillation photons detected if the ionizing particle hits spots lying $\lesssim 2$ mm in front of the SiPM plane (placed at $X \approx 31.5$ mm) in the non-central region of the tile. In other words, if the hit occurs beyond position $X = 29.5$ mm, the amount of detected light will be very low.

ITEP Tile

The ITEP tile response map presented in figure 5.15b evinces a different behavior than the one for the T3B tile. The dimple is a bit wider and deeper. The scintillator material is considerably reduced at this spot, because the ITEP tile is 2 mm thinner than the T3B type. As a consequence, one can clearly see a lower light yield in the dimple area. On the other hand, there are three stripe-like regions of stronger response with an increase towards the dimple. The spots with the highest amount of collected light produce up to 56 % higher signal then the mean value. The effect of poor light collection from the parts lying behind the SiPM plane is apparent as well, comparable with the observation for the T3B tile.

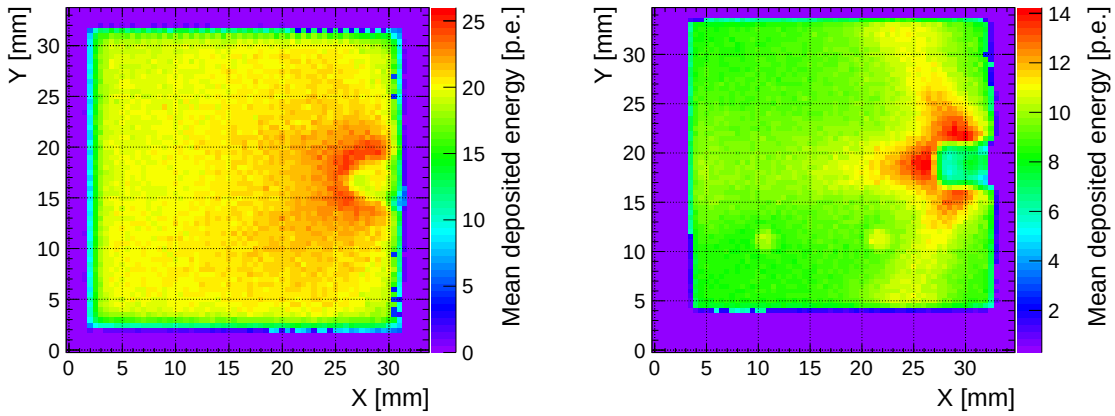

(a) T3B type

(b) ITEP type

Figure 5.15.: Response maps of T3B (**a**) and ITEP (**b**) scintillator tiles. Both tiles were read out by Hamamatsu MPPC-50P.

To be able to quantify the tile response homogeneity, another kind of plot was produced. Figure 5.16 shows the *deviation plot*. It portrays relative deviation of the response signal from the *overall mean signal height* (OMSH) across the tile. A table is also included in the plot to show how much of the tile area supplies signal values within the deviation interval ± 30, ± 20 and ± 10 % from OMSH. These numbers for all 2D scans are summarized in table 5.6. According to these numbers, both tiles have a comparable coverage at the ± 30 % level. At the ± 20 % level, the ITEP tile is worse by several per cent. The area giving signals within the ± 10 % deviation interval is by ≈ 17 % higher for the T3B tile compared to the ITEP scintilator.

The coverage factors are in fact not calculated for the full tile area. The edge regions were excluded from the analysis because of the beam profile. Since the beam has a finite width and divergence, there is an apparent crossover at the tile edge. The effect, which arises due to the beam properties, is unrelated to the tile construction and its response. Therefore the affected regions were not taken into account to avoid a bias of the results.

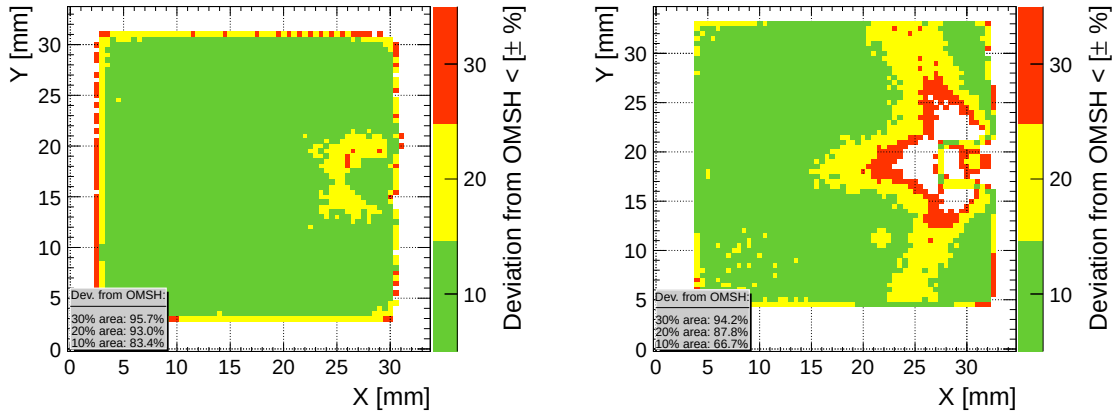

(a) T3B type

(b) ITEP type

Figure 5.16.: Representation of the relative deviation from overall mean signal height (OMSH) for T3B (**a**) and ITEP (**b**) scintillator tiles. Both tiles were read out by Hamamatsu MPPC-50P.

Deviation from OMSH	T3B tile	ITEP tile	ITEP tile with KETEK SiPM
± 10 %	95.7 %	94.2 %	94.7 %
± 20 %	93.0 %	87.8 %	88.6 %
± 30 %	83.4 %	66.7 %	68.3 %

Table 5.6.: Summary of tile response homogeneity measurements. Portions of the tile area which supply signals within given deviation from overall mean signal height (OMSH) are shown.

ITEP Tile Read Out with KETEK SiPM

An additional study has been performed with the ITEP tile read out with a KETEK SiPM. This SiPM is intended to be employed in the next CALICE version and is not commercially available at the moment. The 2D scan results are shown in figure 5.17. One can see that the character of the patterns in figure 5.17a is the same as for the ITEP tile coupled to a Hamamatsu MPPC presented in figure 5.15b. There is one difference between the two ITEP tiles, the one equipped the Hamamatsu has a cut for the light sensor which is 4 mm wide. The tile read out by the KETEK has a 6 mm cut. This is also visible in the response map. In the deviation plot in figure 5.17b, the dimple is almost surrounded by a region with response exceeding a ±30 % deviation from the OMSH. If we compare this with the result plot for the ITEP tile using an MPPC, depicted in figure 5.16b, it is apparent that in the KETEK case the area with high output signal is more smeared. This might be caused by the larger sensitive area of the KETEK SiPM which is 2.2×2.2 mm. However, the numerical values of the MPPC- and KETEK-equipped ITEP tile presented in table 5.6 do not exhibit any significant differences. It can be concluded that the type and size of used light sensor

has just minor impact on the areal response homogeneity of the tile. We also observe a fully expected increase of the mean number of detected photons per electron hit to 22 which is a consequence of 4.8 times larger active area of the KETEK compared to the MPPC.

Under the assumption, that the mean amount of light produced in the ITEP tiles is the same regardless of the used photo detector a rough estimate of photon detection efficiency (PDE) of the KETEK can be made. The ratio of the mean number of photons detected μ_i by the MPPC-50 and the KETEK can be written as a function of the PDE η_i and area S_i of the respective sensor $i \epsilon$ {MPPC, KETEK} like

$$\frac{\mu_{\mathrm{MPPC}}}{\mu_{\mathrm{KETEK}}} = \frac{S_{\mathrm{MPPC}} \cdot \eta_{\mathrm{MPPC}}}{S_{\mathrm{KETEK}} \cdot \eta_{\mathrm{KETEK}}} . \tag{5.2}$$

The absolute PDE of the Hamamatsu MPPC-50 is available from the data sheet [66] (see figure 3.5) and it is equal to $\approx 48\,\%$ for the emission wavelength of the ITEP tile material shown in table 5.1. Since the active area of the sensors is know and the μ_i was obtained from the measurement, the only unknown variable in equation (5.2) is η_{KETEK}, the PDE of the KETEK SiPM. From this consideration, a PDE of 11 % for the wavelength of 430 nm was calculated for the KETEK SiPM.

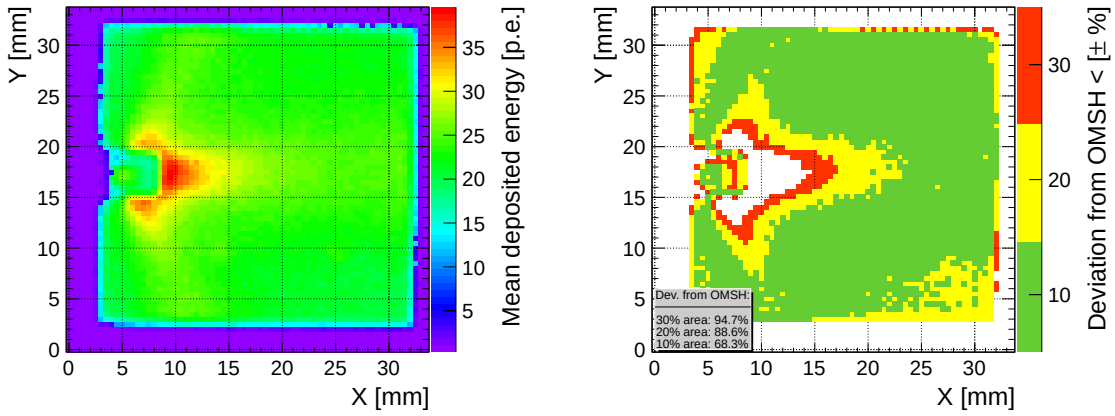

(a) Response map

(b) Relative deviation

Figure 5.17.: Response map (**a**) and relative deviation plot (**b**) of ITEP scintillator tile read out by KETEK SiPM.

5.6.2. Crosstalk Scans

In the second study with the electron beam scan apparatus, we tested the optical crosstalk level between two neighbouring tiles. The measurement was performed with a pair of both tile types read out by an MPPC-50. The results for the T3B and ITEP tile are presented in figures 5.18 and 5.19. The blue and the red lines describe the output signal of one of the tiles at a time. Because the level of the two graphs was not exactly the same, one of them was rescaled to match the other one. The discrepancy between the two tiles was less than 15 %. The different photon detection levels were caused by not exaclty the same quality

of the tiles and their reflectors. The position of the SiPM with respect to the tile can also slightly vary and influence the results. The main purpose of the renormalization was a later calculation of the width of the gap between the tiles. The black line in the upper part of the plots is a sum of both red and blue curves. It represents the behavior of the whole detector system.

In the lower part of the figures, crosstalk between the two tiles is depicted as function of the electron beam position. This is calculated as a ratio of the signal of the non-irradiated tile and the signal in the irradiated tile at the given position. The crosstalk is not calculated in the crossover region, because the electrons from the source are hitting both tiles and we cannot distinguish crosstalk from a primary signal contribution.

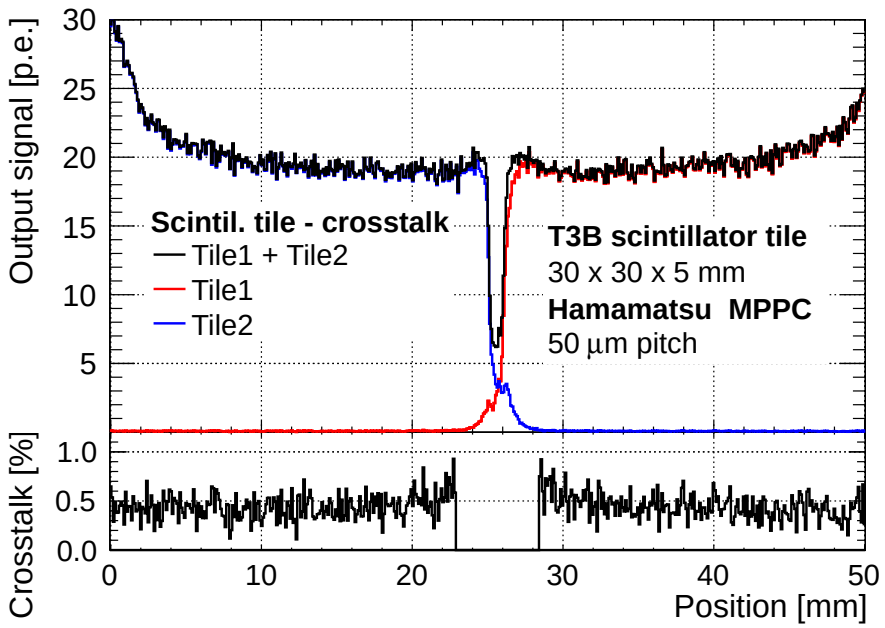

Figure 5.18.: Response of two neighbouring T3B scintillator tiles to the electron beam from ^{90}Sr (upper part) and their optical crosstalk (lower part) as a function of incident electron beam position.

The result for the T3B tile is depicted in figure 5.18. We see a crosstalk value oscillating with a rather big statistical fluctuation around a value of 0.5 % and it is slightly growing towards the crossover region. The crosstalk of 0.5 % is an excellent parameter of the detector. The crosstalk contribution is completely negligible compared to tile response inhomogeneities and statistical fluctuations of the energy deposition for given statistics. The value of the crosstalk is that small, because the photons must cross two layers highly reflective foil on their way from one tile to the other.

In the case of the ITEP tile, the observed crosstalk of ≈ 2 % is about 4 times larger than for the T3B tile. The respective plot is shown in figure 5.18. The reason for the higher crosstalk value can be a lower reflectivity of the paint on the sides of the ITEP tile. Another possibility are tiny uncovered spots in the crossover edge between the paint on the sides and the reflective foil on the top and the bottom of the scintillator. Statistical fluctuations

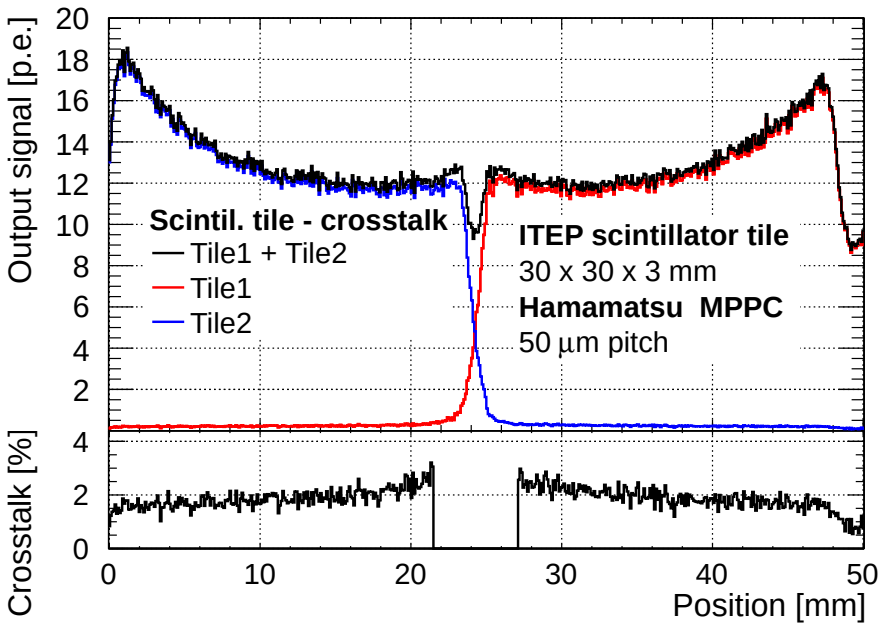

Figure 5.19.: Response of two neighbouring ITEP scintillator tiles to the electron beam from ^{90}Sr (upper part) and their optical crosstalk (lower part) as a function of incident electron beam position.

of the crosstalk are relatively smaller. The crosstalk also noticeably grows towards the border region where the tiles are neighbouring because more scintillation photons hit the neighbouring side directly. Even though the crosstalk is larger for the ITEP tile, its level is still reasonable. The crosstalk contribution is smaller than areal response inhomogeneties of the tile.

An additional parameter, which could be obtained from this measurement is an estimate of the size of the gap between the tiles. When considering a full scale calorimeter equipped with such scintillator tiles, the gap is a dead area in the detector and it deteriorates the shower energy resolution. The shape of the "gap" in the signal in the crosstalk measurement plot is strongly affected by the beam profile presented in figure 5.9 and it does not show directly the real mechanical gap width. However, the physical gap size can be calculated from the integral of the gap in the signal.

For each tile, two crosstalk scans were performed and gap sizes at the order of few hundred μm were obtained. Unfortunately, the numbers vary by more than 100 % and we cannot state any precise gap width size. The lowest gap widths measured for The T3B and the ITEP tile were $230 \pm 30_{(stat.)}$ μm and $190 \pm 20_{(stat.)}$ μm, respectively. The following discusion explains why the smallest experimental values of the gap between the tiles are most probably the closest to reality.

There is a hint why there are such strong systematic discrepancies. The reason could be the reflective foil, which is stuck on the large areas of all tiles. Because the foil is put in place by hand, its edges do not perfectly match the edges of the tile and there is an overlap of the foil over the tile edge. Due to this overlap, two tiles cannot be put tightly

together to have a full contact on the whole tile side. The possible situations are illustrated in figure 5.20. As one can see, the gap size can be changed due to the foils up to the order of 100 %. This is fully consistent with our results. To overcome this issue, a different reflector solution must be employed. One can e.g. utilize one piece of foil to cover the big sides of both neighboring tiles or just lie loosely one piece foil on the tiles. The second proposed reflector solution is even more realistic with respect to proposed design of the new CALICE version. On the other hand, it could increase the crosstalk level.

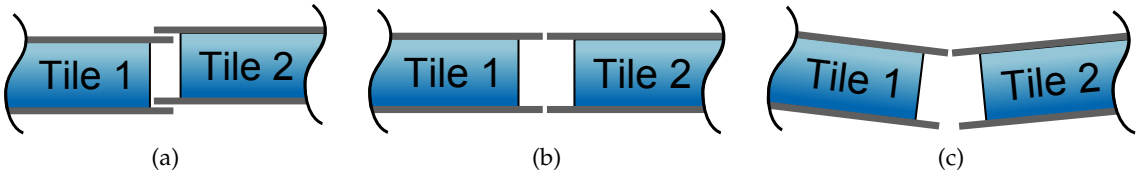

Figure 5.20.: Schematic drawing of three general possible scenarios of scintillator tile contact which strongly affect the gap width. Thick straight grey lines represent mirror foil stuck on the tile surface. The foil overlap is exaggerated for instructive reasons compared to reality.

5.6.3. Neutron Irradiation

In the last of the tile tests, we measured the tile response while being irradiated by an ^{241}Am/Be radioactive neutron source. The goal of this experiment was to examine the tile sensitivity to neutrons and to study potential spectroscopic capabilities. The test was performed twice, once with 1 cm lead shielding around the source capsule and once without. The source capsule was made of a few millimeters thick tungsten-copper alloy.

The resulting measured energy spectra for the T3B and ITEP scintillator tiles are presented in figures 5.21 and 5.22, respectively. The blue curve represents the measurement with the lead shielding, the red without. The plots clearly show a considerable sensitivity of the tiles to neutrons and even a change in the energy spectrum when additional shielding is used. The cutoff of the spectra in low energies is given by the used trigger level and the gradual onset of the spectra just above the lower limit is a trigger effect. The high energy cutoff is given by the signal amplitude acceptance of the DAQ. The reason for the small bump at the end of spectra recorded with the T3B tile are pile-ups due to the limited range of the oscilloscope.

If we compare the curves with and without shielding, a peak at about 500 keV is apparent in the spectra recorded with the lead shielding. An unambiguous interpretation of this peak is not an easy task. A very detailed evaluation of the spectrum is rather complex for various reasons.

First, the source in not monoenergetic. Second, the source is thick and hence also additional Be(n, 2n)Be and Be(n, 2n+α)He reactions occur which affects the neutron energy spectrum. This effect is not taken into account in the standard of the ^{241}Am/Be spectrum shown in figure 5.12. Third, the lead shield has a natural isotope composition, which is a mixture of ^{204}Pb, ^{206}Pb, ^{207}Pb and ^{208}Pb and many different processes can take place. One possible explanation of the enhancement around 500 keV in the measurements with lead

could be corresponding to a strong lead neutron capture emission line at 574 keV [108]. Further contribution could originate from annihilation photons with an energy of 511 keV. The annihilating positrons can be produced by photons created in lead through neutron capture. However, a precise and complex study of the spectrum is not the goal of this thesis. The valuable result is that the tested scintillator tiles can detect neutrons and that they are also sensitive to the shape of the neutron spectrum as well as to effects of metal shielding.

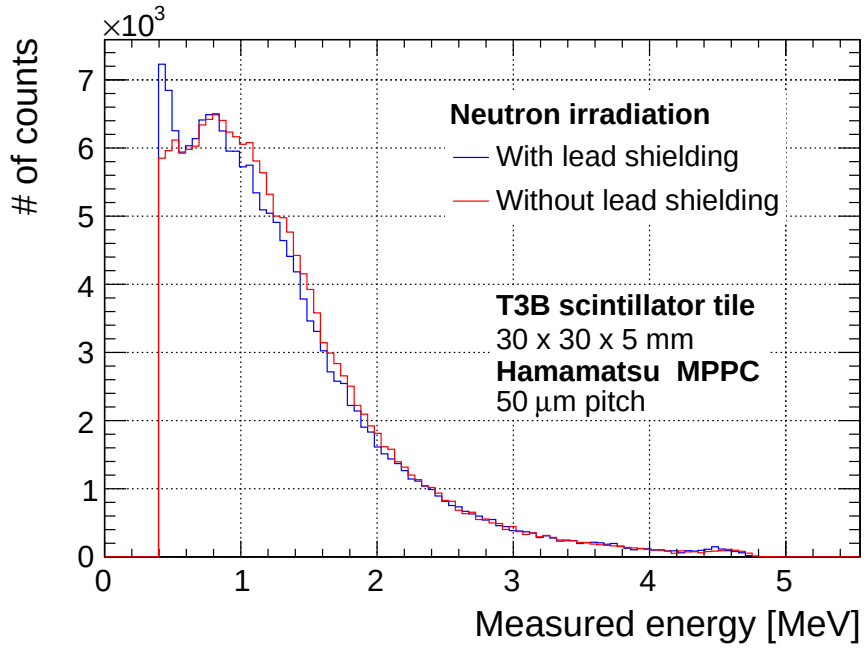

Figure 5.21.: Measured energy spectra of the neutron source with and without additional lead shielding obtained with the T3B tile.

In the energy spectrum measured with the ITEP tile and presented in figure 5.22 are the lower energies more pronounced compared to the T3B tile. Due to the lower thickness and different material, the ITEP tile has a different energy calibration which allows a wider energy range. Therefore, no pile-ups were observed in the upper part of the spectrum.

Comparison with Monte Carlo Simulation

In addition to the measurement, C++/ROOT based Monte Carlo (MC) simulation of the experiment was conducted [98] to cross-check the stated properties of the source [96, p. B6, capsule X.2]. The simulation results are shown in figures 5.23 and 5.24. The vertical axis of the graphs depicts the number of entries per one energy bin with a width of 66.8 keV per one neutron hit. This reflects the bin width of the performed measurement.

The starting point of the simulation was a spectrum of the neutron source [104]. In the first step, the spectrum was corrected for the Be(n,2n)Be and Be(n,2n+α)He reactions by enhancing the neutron yield at lower energies with a shallow exponential shape over the kinematically allowed neutron energy range of the reactions. The neutrons interact with

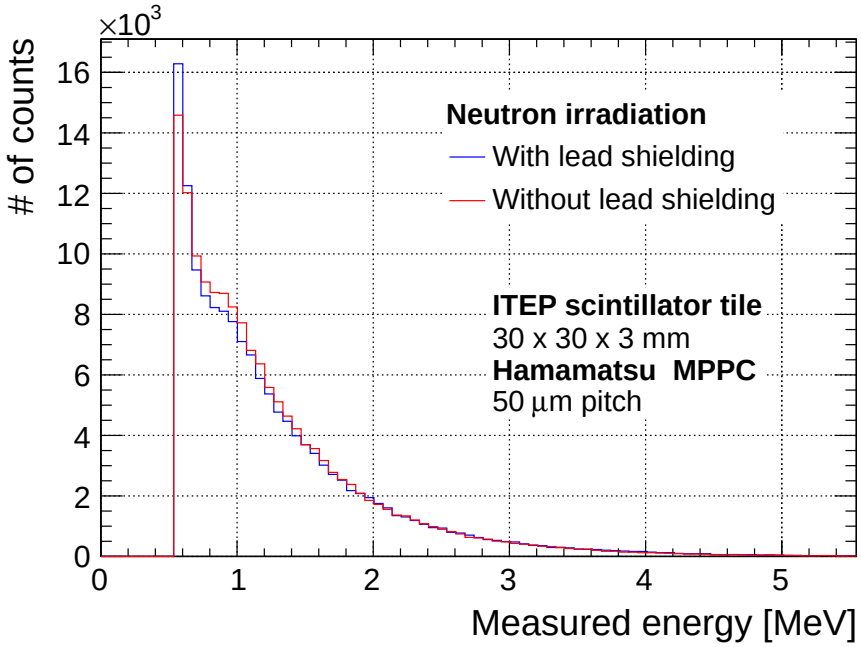

Figure 5.22.: Measured energy spectra of the neutron source with and without additional lead shielding obtained with the ITEP tile.

the tile mainly by elastic scattering on protons. This process was simulated by using realistic cross sections and the spectrum of the recoiled protons was determined. The recoiled protons decelerate and deposit their energy in the scintillator. Hence, the measured energy depositions reflect rather the energy spectrum of the recoiled protons. The spectrum of the recoiled protons is represented by the green line in the plots. Another important point is that a plastic scintillator was utilized in the experiment. The response of an organic scintillator is not linearly dependent on the energy deposited by an ionizing particle. The Birks' law [109] describes mathematically the relation between the organic scintillator response and the specific energy loss of a given particle. The black curve reflects the simulated measured energy spectrum when Birks' law is taken into account. In the last step of the simulation, the trigger and DAQ effects are applied. Following corrections are implemented: The DAQ trigger condition, which determines the low energy cutoff. The limited oscilloscope range, which causes the pile-ups and the cutoff for the highest measured energies. Furthermore, when the protons with energies close to the lower detection limit do not deposit their energy instantly. The signal amplitude therefore is not high enough to reach the trigger level and the event is not recorded. By implementing this effect into the simulation, a matching description of the slower onset of the experimental data at low energies is achieved. The blue line in the plots is the final result of the simulation. The experimental data collected without the lead shielding are depicted by the red points.

It is apparent that the simulation matches the experimental data very well. The MC simulation has shown two things at one time. First, that the source has really the properties, which were expected. And second, that our experiment can be described by a very clear model taking into account just fundamental laws. This proves that any obscure par-

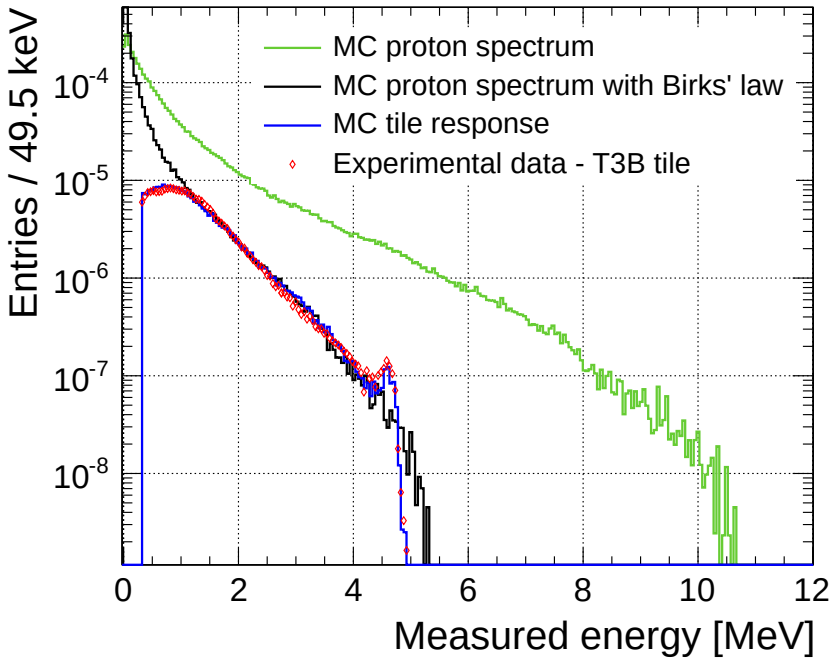

Figure 5.23.: Monte Carlo simulation of the experimental data obtained during a neutron irradiation of a T3B tile. Plot from [98].

asitic effects which would lead to a significantly deviant behavior of the system do not take place in the experiment. This gained knowledge can be used in further applications of these scintillation detectors. The results show that the neutron sensitivity has a predictable behavior. This is important for other experiments, which rely on the detection of neutrons in hadronic showers such as the T3B.

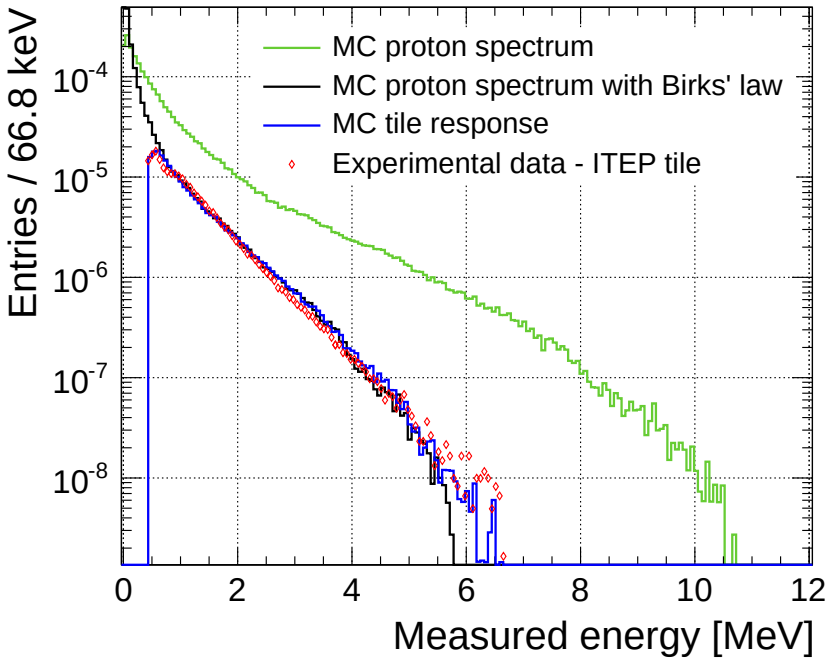

Figure 5.24.: Monte Carlo simulation of the experimental data obtained during a neutron irradiation of an ITEP tile. Plot from [98].

5.7. Summary

Two experimental apparatuses were utilized in an extensive study of plastic scintillator tiles. The investigation of the scintillators was a part of detector development process for future linear e^+e^- colliders. These machines intend to utilize the technology of scintillator tiles read out by silicon photomultipliers in construction of highly granular hadron calorimeters with unprecedented jet energy resolution. Two types of tiles were studied. The first one was the same type which was used in the T3B experiment. The second one was designed and produced at ITEP and it is planned to be used it in the next version of the CALICE detector prototype. In most of the performed experiments, the scintillation light from the tiles was read out by a Hamamatsu MPPC with 50 µm pixel pitch.

The goal of the first of our experiments was to characterize the tiles in terms of the areal response homogeneity across the scintillator. This method was based on irradiating the tile with a collimated electron beam in discrete steps and simultaneous measuring the tile output signal. The electron beam was produced by a ^{90}Sr radioactive source. The diameter of the beam and the positioning precision was high enough to supply tile response distribution with a spatial resolution of 0.5 mm. The homogeneity measurements have shown that the T3B tile evinces a better, but still comparable, response homogeneity level than the ITEP scintillator. This is given mainly by the different designs of the dimples which are drilled or casted in the tile at the place where the SiPM is attached. Purpose of the dimples is to enhance the light collection efficiency and uniformity. The ITEP tile exhibits also a light output magnitude which is by 65 % lower compared to the T3B scintillator.

The reason for this is that the ITEP tile is by 40 % thinner than the T3B tile. Moreover, the scintillation light yield of its scintillator material is by 13 % lower compared to the material of the T3B tiles. One homogeneity scan of the ITEP tile equipped with a KETEK SiPM prototype was conducted. No significant homogeneity changes were observed because of the different photosensor.

Besides the homogeneity scans, the apparatus was used to evaluate the amount of light crosstalk between scintillator tiles when tightly attached to each other. The two scintillator tile types also differ in the solution of the reflectors on the four smaller sides. The ITEP is covered with a white paint, while the T3B uses a reflective foil on all sides. The reflectors determine the light crosstalk between the neighboring tiles. The ITEP tiles evince a crosstalk factor of 2 % and the T3B scintillators 0.5 %.

The second experiment was built to examine sensitivity of the plastic scintillators to fast neutrons. This measurement was motivated by the results of the T3B experiment. It observed higher energy depositions in a calorimeter when a tungsten absorber was used instead of steel. This enhancement is probably caused a larger number of evaporation neutrons emitted by the tungsten during a hadron shower. The aim of our experiment was to test the neutron measurement capability of the tiles. For the neutron irradiation, a ^{241}Am/Be neutron source was utilized. The measurement showed that both scintillator tiles are sensitive to neutrons. Furthermore, the energy deposition measured by the tiles can be simulated by a simple straight-forward physical model. This result is particularly important for further understanding and evaluating of the experiments relying on measurements of the energy of hadron showers performed by plastic scintillators.

An additional information can extracted from the crosstalk measurement, the width of the gap between the neighboring scintillator tiles. This calculation was based on our experimental data. However, the systematic uncertainties of this quantity are overwhelming. Regarding this issue, a usage of a highly energetic and strongly collimated muon beam of well-defined energy for the measurement would be a perfect solution. With the muon beam and correspondingly precise positioning, it would be possible to determine the gap width in a detector prototype with high accuracy.

Part III.

Precise Top Quark Mass Measurement at Future Linear Colliders

CHAPTER 6

PRECISE TOP QUARK MASS MEASUREMENT AT FUTURE LINEAR COLLIDERS

The top quark plays a special role in the Standard Model, because it is far heavier than the other elementary fermions. Due to its big mass, it couples to the Higgs field most strongly and also offers potential sensitivity to Beyond Standard Model physics. The top mass together with the Higgs mass give stability constraints of the Standard Model [29]. The mass of the top cannot be calculated from the first principles within the Standard Model. It has to be obtained experimentally as precisely as possible to be used as an input parameter of theoretical calculations. In the case of the top quark, we have a unique opportunity to measure an almost free quark. Because its mean lifetime is shorter than the QCD hadronization time, it does not form any bound states. All other quarks hadronize before decaying.

The CDF experiment at Tevatron and CMS at LHC have measured the top mass like $173.20 \pm 0.51_{(\text{stat.})} \pm 0.71_{(\text{syst.})}$ GeV [110] and $173.36 \pm 0.38_{(\text{stat.})} \pm 0.91_{\text{syst.})}$ GeV [111], respectively. The total uncertainty of both results is at the order of 1 GeV and the dominating part of the error is the systematic one. One significant source of the systematics is a high hadronic background of both hadron colliders which contaminates the fully-hadronic decays of the top. Another one is the missing energy in the leptonic and semi-leptonic top decay channels. It is not expected that the systematic errors shrink dramatically with further analysis progress.

Due to a very short lifetime of the top quark, several mass definitions were introduced. Those which are relevant for our study were discussed in section 1.4.2. A general issue of top mass measurements is an unclear assignment of the invariant mass and the masses defined in quantum field theory. New methods must be employed to shed light on relations of the mass definitions and supply a precise value of the mass to theoretical models.

Future linear e^+e^- colliders like CLIC and the ILC offer an environment with lower multiplicity in cleaner e^+e^- collisions compared to hadron machines. Also an excellent jet energy reconstruction can be achieved thanks to new generation of highly granular calorime-

ters and particle reconstruction algorithms. There are two different ways how the top mass can be measured. The first one is a reconstruction of the top decay products' invariant mass. The invariant mass is an experimentally well-defined observable, but its relation to theoretically clean top mass definitions is not completely understood. The assignment between these masses suffers from an uncertainty of roughly 1 GeV. A theoretically well-defined top mass can be experimentally obtained in a top pair production threshold scan during which several cross section data points are measured and fitted with a theoretically predicted curve.

In this section, we will present a study which investigated capabilities of determining the top quark mass in a threshold scan at future linear colliders, CLIC and the ILC. The study was fully based on simulations. We have chosen the $1S$ top mass definition [35] for the threshold scan simulation, because it is the most suitable one for description of threshold behavior situation where the top quarks are produced almost at rest.

To take detector effects into account, information from an external full scale top quark reconstruction study at the CLIC were utilized. The vital points of this analysis will be briefly described in the following section.

6.1. Top Quark Identification and Reconstruction

To incorporate detector effects in the threshold scan simulation, the necessary information was obtained from a full detector simulation [112, 113]. This study consisted of event reconstruction followed by highly optimized top quark identification and reconstruction. In the following, we will briefly sketch the principles of the top reconstruction which gave us the crucial detector characteristics. At the same time we will describe the top quark production and decay channels relevant for the mass measurement. Important background processes will be addressed, too.

6.1.1. Key Physical Processes and Event Generation

The key signal process investigated in this study was the top quark pair production in e^+e^- collisions, $e^+e^- \to Z^*/\gamma^* \to t\bar{t}$ at the centre-of-mass energy $\sqrt{q^2}$ of 352 GeV at the CLIC accelerator. The cross section of this reaction at the given energy is 450 fb. The top quark decays almost exclusively into a W boson and a b quark [114]. The b quark originating from the t decay hadronizes and produces a jet. The W decays either leptonically into $l\nu_l$ with a branching ratio (BR) of 32 % or hadronically into a quark-antiquark pair (BR = 68 %) which also hadronizes and produces further jets. Based on the W decay mode, we clasify the top quark events into three groups, fully-hadronic (both Ws decay into hadrons), semi-leptonic (one W decaying into hadrons, one in leptons) and fully-leptonic (both Ws decay into leptons). The event classification is summarized in table 6.1.

The leptonic decays of W include also the channel with a τ lepton and the corresponding neutrino. The τ has a very short lifetime of 2.9×10^{-13} s which leads to its almost immediate decay into a lepton and a neutrino (BR = 35 %) or into one or more hadrons and a neutrino (BR = 65 %). The escaping neutrions would introduce additional missing energy in the analysis and the hadronic final states could cause confusion with other hadronic decays. Therefore, the leptonic decay channel with τ in the final state is excluded from the

Event class	$t\bar{t} \to WbWb$	Branching ratio
Fully-hadronic	$\to q\bar{q}b\,q\bar{q}b$	45.7 %
Semi-leptonic	$\to q\bar{q}b\,l\nu_l b$	43.8 %
Fully-leptonic	$\to l\nu_l b\,l\nu_l b$	10.5 %

Table 6.1.: Top quark decay channels and their respective branching ratios [33].

analysis. However, the signal data sample was simulated realistically with all top quark decay modes according to their branching ratios. This eliminates bias effects due to imperfect event clasification. The signal event sample was simulated with a top quark mass and width m_t = 174.0 GeV and Γ_t = 1.37 GeV, respectively.

To simulate a realistic collider environment, background processes with similar event topology as the top decays must be taken into account. The events were simulated and mixed with the signal data set. These processes and their cross sections for a collision energy of 352 GeV at the CLIC machine are shown in table 6.2. All mentioned event samples were generated for an integrated luminosity of 100 fb^{-1}. Two different event generators (WHIZARD [115] and PYTHIA [116]) were utilized for the signal and background processes, because none of these two tools is suitable to simulate all of them properly. The event generator which was employed for production of the particular process is also mentioned in table 6.2.

Process type	Event generator	$e^+e^- \to$	Cross section σ [fb]
Signal	PYTHIA	$t\bar{t}$	450
Background	WHIZARD	$q\bar{q}$	25 200
Background	PYTHIA	WW	11 500
Background	PYTHIA	ZZ	856
Background	WHIZARD	WWZ	10

Table 6.2.: Signal and background processes which were simulated for purposes of the top quark reconstruction. Cross sections for nominal energy 352 GeV in e^+e^- collisions are corrected for initial state radiation and collider beam energy spectrum.

Further beam-induced background sample in form of $\gamma\gamma \to$ hadrons events was generated with GEANT4 [105]. The real and virtual photons surrounding the colliding beams interact with each other and can produce hadronic final states. This process occurs 0.046 times per bunch crossing at 350 GeV nominal collision energy. A number of $\gamma\gamma \to$ hadrons events corresponding to 300 bunch crossings were overlaid with each signal event.

The detector model CLIC_ILD [44] was used to simulate the detector effects. Mokka [117] was employed to perform this simulation. The complete simulated data set was subsequently processed by tracking and particle flow event reconstruction algorithms which were performed with the help of PandoraPFA [49]. The PandoraPFA is an algorithm which was developed to study particle flow based calorimetry at the ILC and aims for a jet energy resolution of ~ 3 %. The data analysis was conducted on reconstructed particles after application of $\gamma\gamma \to$ hadrons background reduction cuts.

6.1.2. Top Quark Reconstruction

The goal of the original top quark reconstruction was to determine the t mass as precisely as possible. Moreover, the t signal significance, achieved through signal reconstruction and background rejection operations is a very valuable output for a threshold measurement simulation. From the point of view of threshold scan simulation, we are interested only in the signal significance. Therefore, only the steps leading to significance maximization will be presented in this work. Description of the top invariant mass reconstruction step will be omitted.

The data analysis of reconstructed events proceeds in several steps. In the first one, a *lepton finder* algorithm was employed. It classified the events according to table 6.1. An event was considered as fully-hadronic, semi-leptonic or fully-leptonic if no isolated lepton, exactly one isolated lepton or two isolated leptons were found, respectively. The lepton finding algorithm was optimized to find highly energetic (at least 10 GeV) charged leptons ($e^{\pm}$ or $\mu^{\pm}$) originating from W decay. Even after this procedure, the semi-leptonic events still include τ lepton decays of W bosons. Those will be suppressed in further steps. All events classified as fully-leptonic are excluded from further analysis. At this stage, about 11 % of all events are rejected.

In the next step, *jet clustering* was conducted. The events were split into two groups in this process. The particles in the full-hadronic and the semi-leptonic events except for the identified isolated lepton are clustered into six and four jets, respectively. The jet finding was done with the help of the k_t algorithm [118] implemented in the FastJet package [119, 120].

The *flavor tagging* procedure determines the flavor of the quark (b, c or light) which produced a jet. This is crucial for distinguishing of $t\bar{t} \to bq\bar{q}\,\bar{b}q\bar{q}$ and $t\bar{t} \to bq\bar{q}\,\bar{b}l\nu_l$ events from multi-fermion background. It is also essential for the correct assignment of the jets to the t decay product candidates in signal events. The flavor tagging algorithm is based on neural networks and provides b and c jet probabilities ("b-tag"). To perform the flavor tagging, the LCFI Flavor Tagging package [121] was used.

Subsequently, the jets of all event classes (fully-hadronic, semi-leptonic) undergo *jet pairing* and are assigned either to a parent W boson or b quark. The two jets with the highest b-tag are considered to originate from a b (b-jet) while the other are classified as light jets (created by c, u, d or s) coming from a W decay. In the case of a semi-leptonic (4-jet) event, there are two b-jets, two light jets which are unambiguously assigned to one W, one isolated lepton and an unmeasured neutrino. The neutrino carries all the missing energy in this type of event. Due to the missing energy, the W mass determined from in the leptonic decay of W is less constrained compared to hadronic decay of W where no missing energy is present.

Pairing of the jets in the fully-hadronic (6-jet) events is a bit more complicated. The event consists of two b-jets and four light jets which must be correctly assigned to the two W bosons. One of the three possible permutations of light jet pairing must be chosen. This is done according to the value of the function

$$v_{ijkl} = |m_{ij} - m_W| + |m_{kl} - m_W|, \tag{6.1}$$

where $m_W = 80.4\,\text{GeV}$ is the W mass and m_{ij} and m_{kl} is invariant mass of jets i, j and k, l,

respectively. The ν_{ijkl} function is calculated for all three jet permutations and the permutation with the lowest ν_{ijkl} is chosen to be used for the reconstruction of both W bosons.

Once the jets are correctly paired, a rather complicated procedure of *kinematic fitting* follows. It helps to group correctly the W bosons and the b quarks resulting from the previous step into t quarks out of two the combinations. The kinematic fit uses constraints based on $t\bar{t}$ event properties to improve the precision of quantities of interest. The constraints are four-momentum conservation, correct reconstruction of W masses and an equal mass of both top candidates. For the threshold scan, the main contribution of the kinematic fit is that it strongly rejects non-$t\bar{t}$ background. It excludes more than 97 % of $q\bar{q}$ background in both fully-hadronic and semi-leptonic events, more than 94 % of di-boson pair production events in the fully-hadronic branch and 94 % of ZZ and 86 % of WW events in the semi-leptonic branch. The WWZ background has a similar signatures and can have identical final products as a $t\bar{t}$ event. This results in lower rejection rates for this process compared to previous backgroung channels, 13 % for fully-hadronic and 25 % for semi-leptonic event classes.

The last step in the top quark reconstruction is an additional *background rejection* which utilizes a method of binned likelihood [122]. This technique calculates a likelihood measure to characterize how signal-like a given event is. The likelihood is a function of several observables. These observables are event sphericity, the highest b-tag and the total number of particles in the event, reconstructed W boson masses, difference of reconstructed top quark masses without the kinematic fit and a d_{cut} variable from the jet clustering algorithm. The d_{cut} characterizes how natural it is to cluster an event into a given number of jets rather than fewer jets. This background discrimination method removes 98.0 % and 96.7 % background events remaining after the kinematic fit in the fully-hadronic and the semi-leptonic event class, respectively.

The final signal reconstruction efficiency and background rejection efficiencies achieved in this data analysis are summarized in table 6.3. These results were used as input for the simulation of the top quark mass measurement in a threshold scan.

Event type $e^+e^- \rightarrow$	**Signal reconstruction efficiency [%]**	**Background rejection efficiency [%]**
$t\bar{t}$	70.2	-
$q\bar{q}$	-	99.9
WW	-	99.8
ZZ	-	97.8
WWZ	-	71.7

Table 6.3.: Signal reconstruction efficiency and background rejection efficiencies achieved in top quark reconstruction in a full scale detector simulation at CLIC [112]. Values from [123].

6.2. Top Quark Threshold Scan Simulation

The top quark threshold scan simulation was conducted as a performance study of the proposed future linear e^+e^- colliders CLIC and ILC. The input information for our study are the top identification efficiency, the non-$t\bar{t}$ background rejection efficiencies and $t\bar{t}$ production cross sections numerically calculated with the help of TOPPIK [35]. All other calculations were done with programmes created by us specially for this study. In this section, we explain the top quark threshold scan simulation and its results.

The main point of the study was to examine capabilities of CLIC and the ILC to measure m_t and investigate the achievable precision of α_s. There is a difference between te CLIC and the ILC is the beam energy spectrum shape. This is caused by diverse accelerating principles of the machines. The ILC plans to use superconducting cavities, whilst CLIC will employ two-beam-acceleration technology introduced in section 2.3.1. This difference is reflected in the beam spectrum of the collider. The ILC has a sharper nominal energy peak than CLIC. This difference was the motivation for our simulation It was not quite clear whether a sufficient measurement precision can be achieved at CLIC due to its broader luminosity peak.

There are also detector design differences between CLIC and the ILC which originate from a different maximal design center-of-mass energies. Let us list most important ones. The radius of the innermost layer of the silicon vertex detector is not the same for both colliders. At CLIC, the first layer is placed 9 mm further outwards (at a radius of 25 mm) compared to ILC to reduce the occupancy caused by the background of incoherent e^+e^- pairs. However, this difference is expected to have only a small effect on the b-tagging performance. Even though b-tagging is crucial for top quark identification, the overall top identification efficiency will not be changed considerably. The second difference in detector design is the calorimeter depth (in terms of radiation lengths X_0). The depth of the ILD designed for CLIC is higher than for the ILC due of the higher collision energy. Also this parameter should not be a problem, because it also does not affect the $t\bar{t}$ event identification.

To summarize, for purposes of our threshold scan study, we can assume that both detector systems will perform with negligible differences. The only characteristic which differs the two accelerators from each other is the beam energy spectrum.

A schematic illustration of the simulation procedure is shown in figure 6.1. In the first step, the $t\bar{t}$ production cross sections σ_{tt} are generated. These are corrected for *initial state radiation* (ISR) and *beam energy spectrum* (BS) effects through numerical folding. This data is handed to the *measurement data generator* which simulates the physics background based on the top identification and background rejection efficiencies and produces the *simulated measurement data*. The ISR- and BS-corrected cross sections calculated for a variety of different parameter values (m_t and α_s) form so called χ^2 *fit templates*. The templates are used by the subsequent χ^2 *template fit* algorithm to fit the simulated measurements. This step produces the final results. All parts of the simulation scheme will be described in detail in the following.

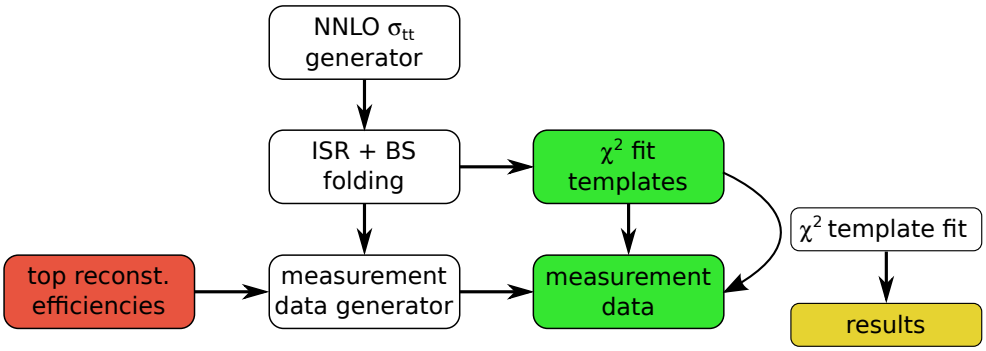

Figure 6.1.: Block scheme of the top quark threshold scan simulation. The red box represents external input data. White boxes symbolize software tools and the green ones represent intermediate output data.

6.2.1. Calculation of the $t\bar{t}$ Production Cross Sections

The key data for our study are precise values of $t\bar{t}$ production cross sections. The cross section is a function of many parameters, which could be in principal obtained in a threshold scan by fitting the cross section measurement points. However, the measurement capabilities regarding these parameters are restricted by the experimental precision of the cross sections. The main focus of our study lied on the top quark mass m_t. Since m_t is considerably correlated with the strong coupling constant α_s, capabilities of simultaneous determination of m_t and α_s were investigated. The other parameters were kept fixed in the analysis (Higgs mass, Yukawa coupling, top quark width). The possibility of the top quark width measurement was also tested. To generate the cross sections, we utilized a Fortran code TOPPIK [35, 124]. It is capable of numerical calculating of top-antitop production cross section with precision of leading order (LO), next-to-leading order (NLO) and next-to-next-to-leading order (NNLO). TOPPIK can calculate the cross sections $\sigma_{tt}^{(0)}$ using the input parameters mentioned above in the vicinity of the $t\bar{t}$ production threshold in $e^+e^- \to Z^*/\gamma^* \to t\bar{t}$ process for a given center-of-mass energy $\sqrt{q^2}$. The output of TOPPIK originally expressed in terms of vector current R^v and axial vector current R^a must recalibrated into picobarns [35, equation (8)] like

$$\begin{aligned}\sigma_{tt}^{(0)}(q^2) \;=\; \sigma_{pt}\left[Q_t^2 \;-\; 2\,\frac{q^2}{q^2-M_Z^2}\,v_e\,v_t\,Q_t \;+\; \left(\frac{q^2}{q^2-M_Z^2}\right)^2\left[v_e^2+a_e^2\right]\,v_t^2\right]R^v(q^2) \\ +\,\sigma_{pt}\left(\frac{q^2}{q^2-M_Z^2}\right)^2\left[v_e^2+a_e^2\right]\,a_t^2\;\;R^a(q^2),\end{aligned} \tag{6.2}$$

where

$$\sigma_{pt} \equiv \frac{4\pi\alpha^2}{3q^2}, \tag{6.3}$$

$$v_f \equiv \frac{T_3^f - 2\,Q_f \sin^2\theta_W}{2\,\sin\theta_W\,\cos\theta_W}, \tag{6.4}$$

$$a_f \equiv \frac{T_3^f}{2\,\sin\theta_W\,\cos\theta_W}. \tag{6.5}$$

The index f represents a fermion, M_Z is the mass of the Z boson, Q_f is the electric charge of a fermion f, T_3^f refers to the third component of the weak isospin of a fermion f and θ_W is the weak mixing angle. The product $Q_t^2 R^v$ is equal to the total normalized photon-induced cross section referred to as the R-ratio[1]. TOPPIK is capable of producing the cross sections for different top mass schemes, pole mass, 1S mass and potential-subtracted mass. For our purposes, we used the 1S top quark mass definition.

Two separate data sets are used in the study, the simulated measurement set and the fit templates. In the very first step of the simulation, the pure cross sections of the $t\bar{t}$ pair production which do not consider any further effects were generated. The simulated measurement set is based on one TOPPIK-generated curve using the default values of m_t and α_s. The fit template set is based on many curves, which are generated by TOPPIK for different choices of the input parameters m_t and α_s. Each cross section curve was generated in the energy range from 280 to 355 GeV with a step size of 1 MeV.

An example of cross sections calculated by TOPPIK with a demonstration of an influence of different m_t and α_s values on the output data is shown in figure 6.2. All parameters and their respective vales used for the calculation of the fit template set are listed in table 6.4. In the cross section curve which will be used for simulated measurement data calculation later on, m_t = 174.00 GeV and α_s = 0.1180 was chosen while the other parameters were the same as for the template sample.

For additional tests of experimental sensitivity to other parameters, further cross section sets were calculated. The TOPPIK configuration used for these tests is given in section 6.2.3. Because the numerical calculation of the cross sections is rather demanding in terms of computational power, the cross section generation was strongly parallelized. During the whole study, more than 8.5 million cross sections were calculated.

6.2.2. Corrections of the Cross Section

The NNLO calculations provide the cross sections for a fixed e^+e^- collision energy. In reality, this energy gets modified by two main effect: initial state radiation (ISR) and the finite width of the nominal energy peak in the luminosity spectrum. The TOPPIK-generated cross sections must be corrected for these. The two effects will be now described.

[1] the R-ratio is defined as $R \equiv \frac{\sigma\left(e^+e^-\to X\right)}{\sigma\left(e^+e^-\to\mu^+\mu^-\right)}$

Parameter	Value
Precision	NNLO
Top mass definition	1S
Top width	1.43 GeV
Top mass range	173.70 − 174.30 GeV
Top mass step	0.05 GeV
α_s range	0.1145 − 0.1216
α_s step	0.0007
Collision energy	280 − 355 GeV
Collision energy step	1 MeV
Yukawa coupling	disabled
Higgs mass	disabled

Table 6.4.: TOPPIK settings used in calculation for the fit template set of $t\bar{t}$ production cross sections.

Initial State Radiation

The ISR effect works in the following way. The incoming particles (e^+ and e^-) are constantly emitting and absorbing virtual and real photons of various energies. Because these photons carry a part of the energy of the particle, the kinetic energy of the particle is reduced. As a consequence, it is physically impossible to collide the particles in the beams at a precisely chosen energy, because it will be always somewhat lowered. The real collision energy E' distribution of two monoenergetic beams is therefore not a δ-function, as it would be in an ideal case, but it will be smeared towards lower values. The E' obeys a dependence shown in figure 6.3.

The ISR-corrected cross section $\sigma_{tt}^{(\mathrm{ISR})}$ at centre-of-mass (CMS) energy $\sqrt{q^2}$ can be obtained as a convolution of the cross sections $\sigma_{tt}^{(0)}$ calculated according to equation (6.2) with the structure functions $D_{e^\pm}$ of the incoming particles. In this theory [125], it is assumed that the electron or positron constantly emits and absorbs almost collinear photons. Based on this postulate, the $e^\pm$ structure function is built in a similar way as the structure functions in QCD. Subsequently, the cross section, which takes ISR into account, can be calculated like

$$\sigma_{tt}^{(\mathrm{ISR})}(q^2) = \int_0^1 \mathrm{d}x_1 \int_0^1 \mathrm{d}x_2 \; D_{e^-}(x_1, q^2)\, D_{e^+}(x_2, q^2)\, \sigma_{tt}^{(0)}(q^2, x_1, x_2), \tag{6.6}$$

where x_i, $i \in \{1, 2\}$ represents the momentum fraction of the original on-shell electron [125]. Unlike the hadron structure function in QCD, the $e^\pm$ structure functions can be determined from first principles in QED. To calculate the structure function $D_{e^\pm}$ of the $e^\pm$, a second order approximate Yennie-Frautschi-Suura solution $D_{(2)}^{YFS}$ [125, 126] of the Lipatov equation [127] was used:

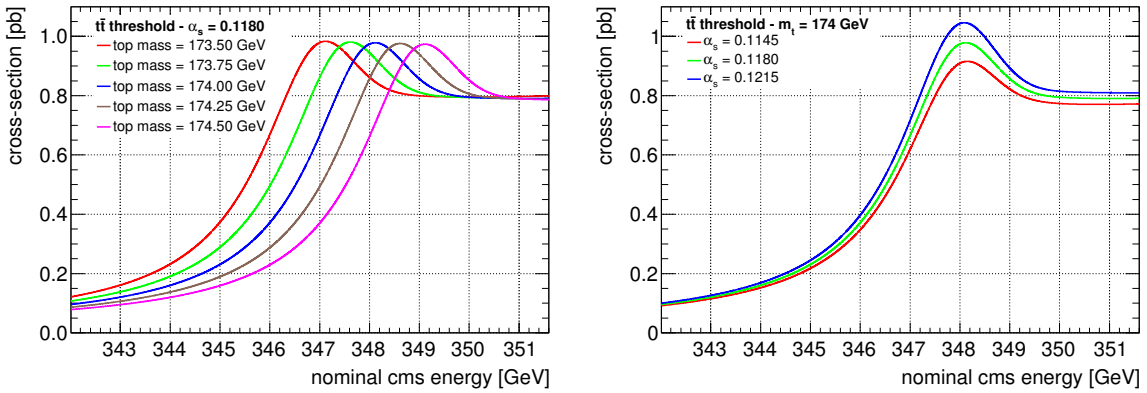

(a) Varying top mass

(b) Varying strong coupling constant

Figure 6.2.: TOPPIK output data. Influence of varying top mass m_t (**a**) and strong coupling constant α_s (**b**) on $t\bar{t}$ production cross sections as a function of e^+e^- centre-of-mass (CMS) energy.

$$D_{e^\pm}(x,q^2) \equiv D^{YFS}_{(2)}(x,q^2) = \frac{\exp\left(\frac{1}{2}\eta(\frac{3}{4}-\gamma)\right)}{\Gamma(1+\frac{1}{2}\eta)} \cdot \frac{1}{2}\eta(1-x)^{\frac{1}{2}\eta-1} \cdot \left[\frac{1}{2}(1+x^2) + \frac{1}{4}\frac{\eta}{2}\left(-\frac{1}{2}(1+3x^2)\ln x - (1-x)^2\right)\right], \tag{6.7}$$

where x is the momentum fraction, Γ is the Γ-function, $\gamma = 0.5772157$ and

$$\eta \equiv \eta(q^2) = \int_{m_e^2}^{q^2} \mathrm{d}z \frac{2\alpha(z)}{\pi z}. \tag{6.8}$$

In equation (6.8), m_e is the electron mass (colliding particle mass) and α is the running fine structure constant.

The folding of the NNLO cross section with ISR according to equation (6.6) was done numerically. The cross section curve around the $t\bar{t}$ production threshold after taking the corrections into account is shown in figure 6.4.

Beam Effects

As the last step in the procedure of getting realistic cross sections, the effects of the accelerator beam energy spectrum (BS) have to be taken into account. An ideal accelerator would deliver a purely monochromatic particle beam. For a real machine, this is not the case and the BS has a more complicated structure. It has a peak at the nominal energy and a tail towards lower energies. The spread of the nominal energy peak is caused by phase space acceptance of the accelerating structures. The tail arises through energy loss due to radiative effects prior to collision, primarily because of focusing of the beams to reach a high luminosity. The beam spectra of CLIC and the ILC are shown in figure 6.5.

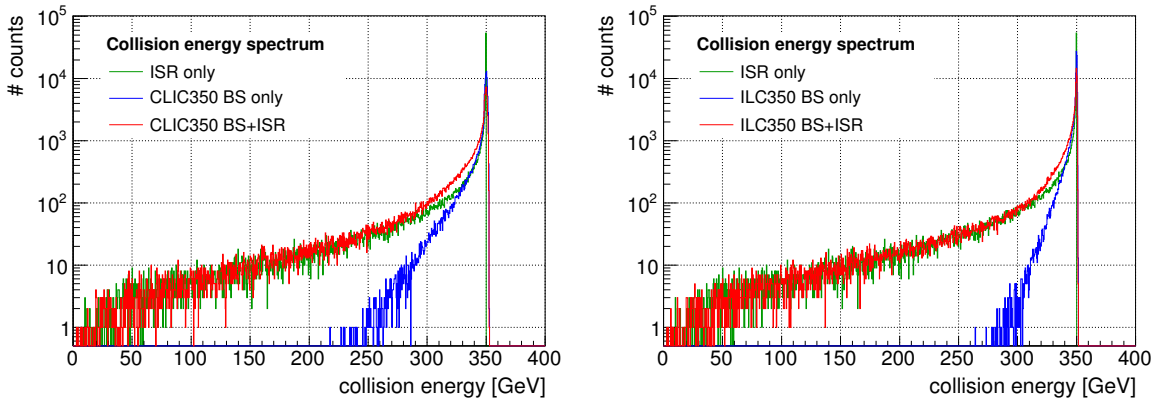

(a) CLIC (b) ILC

Figure 6.3.: Collision energy distribution after implementation of the ISR and beam effects (BS) for CLIC (**a**) and ILC (**b**).

The beam effects are applied to the cross section in a similar way as the ISR. The ISR-corrected cross section curve is numerically convoluted with the beam spectrum.

After folding with the corresponding BS, we obtain the $t\bar{t}$ production cross sections matching the environment of a particular accelerator, CLIC or the ILC. At this point of the study, the ISR and BS effects are applied to all TOPPIK generated data. We will call all of these files calculated for different choices of m_t and α_s *fit templates*, they will serve as reference cross section distributions for a later template fit.

6.2.3. Simulation of Data Points

The last missing part needed for the fit procedure is the simulated measurement of the $t\bar{t}$ cross section in the threshold region for both colliders. We want to create a realistic simulated cross section measurement consisting of ten discrete points in the vicinity of the $t\bar{t}$ production threshold. These points must reflect the ISR and BS of course. In addition to that, detector effects and integrated luminosity of the experiment must be taken into account.

To get the $t\bar{t}$ production cross sections $\sigma_{t\bar{t}}$, we pick one of the cross section dependencies corrected for ISR and BS which was calculated with the input parameters listed in table 6.5. To simulate the detector effects, the top quark reconstruction efficiency $\eta_{t\bar{t}}$ and the background rejection efficiencies $\eta^{(i)}_{bkg}$ for all background channels $i \in \{q\bar{q}, WW, ZZ, WWZ\}$ were used. We assumed that the cross section $\sigma^{(i)}_{bkg}$ of background processes i are constant in the collision energy range for which the measurement data was simulated. The integrated luminosity $\mathcal{L}_{int}$ for each measurement point was 10 fb^{-1} which gives a total integrated luminosity $\mathcal{L}_{int}$ = 100 fb^{-1} for the entire threshold scan. The collection of such an amount of data would take about ten months of the accelerator operation.

The calculation of the pseudo-random measurement points works in the following way. First, the mean numbers of signal and background events that go through the top identification procedure at given integrated luminosity $\mathcal{L}_{int}$ are calculated. The mean number of

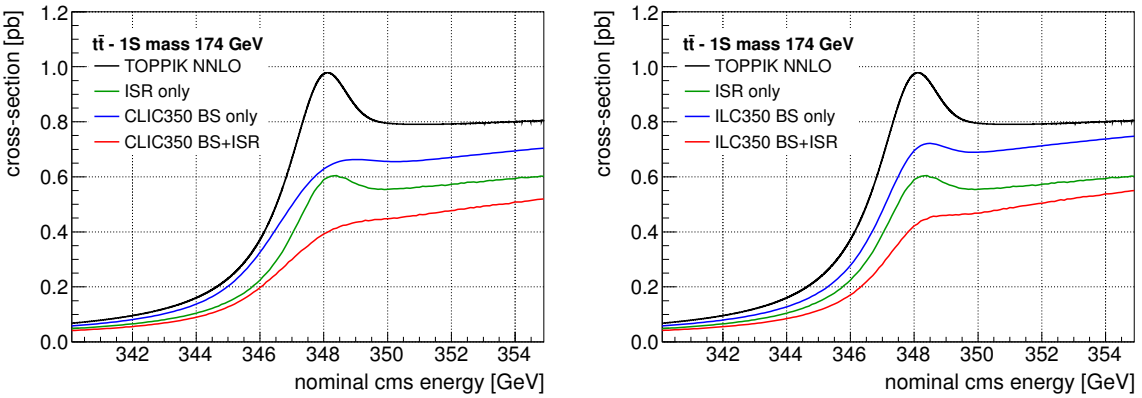

(a) CLIC (b) ILC

Figure 6.4.: TOPPIK generated cross sections with applied effects of ISR and beam spectrum shape (BS) for CLIC (**a**) and the ILC (**b**).

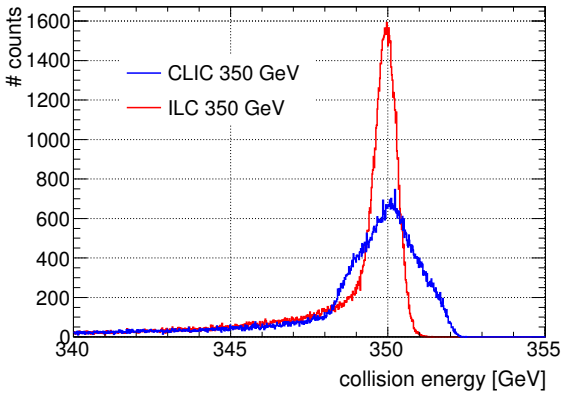

Figure 6.5.: Beam spectra of CLIC and the ILC at nominal center-of-mass energy 350 GeV.

signal events $\langle N_{sig} \rangle$ passing through is given by

$$\langle N_{sig} \rangle = \mathcal{L}_{int} \cdot \sigma_{t\bar{t}} \cdot \eta_{t\bar{t}}. \tag{6.9}$$

For background, the mean number of events $\langle N_{bkg} \rangle$ is calculated in the same way. It must be summed over all contributing processes i:

$$\langle N_{bkg} \rangle = \mathcal{L}_{int} \cdot \sum_i \sigma_{bkg}^{(i)} \cdot \eta_{bkg}^{(i)}. \tag{6.10}$$

After getting the mean event numbers, two Gaussian-shaped probability density distributions are created, one for the signal and one for the background. The distribution for the signal has a mean value at $\langle N_{sig} \rangle$ and its variance is $\sqrt{\langle N_{sig} \rangle}$. The distribution for background is built in the same way. Based on the distributions, a pseudo-random numbers of events $N_{sig}^{(R)} = N_{sig}^{(R)}(E)$ and $N_{bkg}^{(R)} = N_{bkg}^{(R)}(E)$ are picked for every single nominal collision

Parameter	Value
Top mass definition	$1S$
Top width	1.43 GeV
Top mass	174.00 GeV
α_s	0.1180
Collision energy	344 - 353 GeV
Collision energy step	1 GeV
Yukawa coupling	disabled
Higgs mass	disabled
$\mathcal{L}_{int}$ per point	10 fb^{-1}

Table 6.5.: Parameter values chosen for simulation of the top threshold scan. (α_s is the strong coupling constant, $\mathcal{L}_{int}$ is integrated luminosity.)

energy point E.

Now, we define two new quantities as follows:

$$N_{tot} = N_{sig}^{(R)} + N_{bkg}^{(R)} - \langle N_{bkg} \rangle, \tag{6.11}$$

$$N_{err} = \sqrt{N_{sig}^{(R)} + N_{bkg}^{(R)}}. \tag{6.12}$$

$N_{tot} = N_{tot}(E)$ is the total number of events identified as top events where the mean number of background events is subtracted. $N_{err} = N_{err}(E)$ is a poissonian uncertainty of the number of top events. It is assumed that in the experiment the $\langle N_{bkg} \rangle$ will be determined from measurements bellow the threshold and from theoretical calculations.

From these values, the simulated measured top pair production cross section $\sigma_{t\bar{t}}^{(meas)}$ and its statistical uncertainty $\sigma_{t\bar{t}}^{(err)}$ for each energy point E will be calculated. To obtain the cross section $\sigma_{t\bar{t}}^{(meas)}$, we will use formula (6.9) and substitute $\sigma_{t\bar{t}}$ by $\sigma_{t\bar{t}}^{(meas)}$ and $\langle N_{sig} \rangle$ by N_{tot}. To calculate the experimental error of $\sigma_{t\bar{t}}^{(meas)}$, the $\sigma_{t\bar{t}}^{(err)}$, we replace in equation (6.9) $\sigma_{t\bar{t}}$ by $\sigma_{t\bar{t}}^{(err)}$ and $\langle N_{sig} \rangle$ by N_{err}.

The so far described calculation of $\sigma_{t\bar{t}}^{(meas)}$ and $\sigma_{t\bar{t}}^{(err)}$ is repeated for every single energy measurement point in the scan. An example of a final simulated top quark pair production measurement for CLIC and the ILC is shown in figure 6.6.

Because we also want to study the statistical uncertainty of the quantities which will be determined from the template fit of the simulated threshold scan, we generate 5000 pseudo-random simulated measurements. Later on, we will apply the fit on all of them to derive the statistical uncertainties from the distribution of the fit results.

6.2.4. Template Fit

Up to now, we explained how we obtained all the simulated data needed for the analysis. Let us shortly repeat what we have at this moment. First, we generated 5000 pseudo-

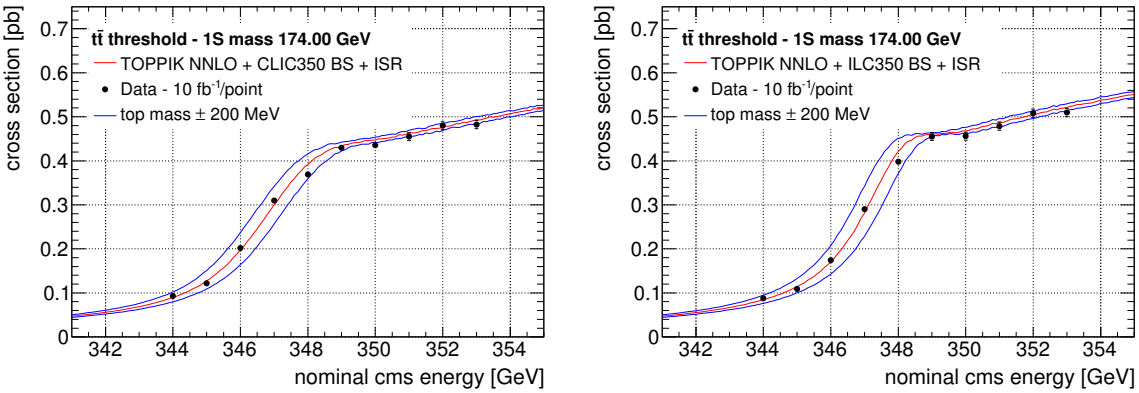

(a) CLIC (b) ILC

Figure 6.6.: Simulated measurement of top pair production cross section at the CLIC (**a**) and the ILC (**b**).

random sets of the top threshold scan simulated measurement data. Each set consists of 10 measurement points, 10 fb^{-1} of integrated luminosity each, i.e. 100 fb^{-1} in total. Every set represents one realistic measurement. We generated 5000 of them in order to study statistical uncertainties of the fit results. In a potential real experiment, only one such a set will be accumulated. The underlying idea behind the determination of the statistical error is that the fit is performed on many measurements where the cross sections are randomized in correspondence to statistical effects. The distribution of the fit results reflects their statistical uncertainty.

To be able to perform a template fit to determine the top quark mass m_t and the strong coupling constant α_s from the simulated data points, 143 fit templates were created. A fit template is a theoretically calculated cross section energy dependence with NNLO precision around the top quark pair production threshold taking into account ISR and collider specific beam spectrum. Each template is created with different values of input parameters, in our case m_t and α_s. All others stay fixed as listed in table 6.4. The templates were generated for 13 steps of 50 MeV in m_t and 11 steps of 0.0007 in α_s. In the template fit procedure, these theoretical curves are compared with the simulated measurement data and for each template χ^2 is calculated. Through a χ^2 minimization, values of m_t and α_s are obtained. The fit is performed for m_t while keeping α_s fixed and also for both parameters, m_t and α_s, simultaneously. This poses two different analysis methods. Their results can be compared later on to decide which approach is more favourable.

The χ^2 template fit is based on calculating the quantity χ^2 which in our case characterizes agreement of the simulated data points with theoretically determined cross section points. It is calculated according to

$$\chi^2 = \sum_{i}^{E\ bins} \left(\frac{\sigma_i^{(meas)} - \sigma_i^{(temp)}}{\Delta_i^{(meas)}} \right)^2 , \tag{6.13}$$

where $\sigma_i^{(temp)}$ represents the template cross section, $\sigma_i^{(meas)}$ the simulated measurement

cross section and $\Delta_i^{(meas)}$ is the statistical uncertainty of $\sigma_i^{(meas)}$ in the i-th nominal collision energy bin. The sum runs over all measurement points, i.e. collision energy bins. Smaller χ^2 values indicate a better agreement of the two compared data sets.

One-Dimensional Fit

In the first approach, one parameter will be fitted while keeping the others fixed. We will describe the fit procedure which is performed on one simulated top quark threshold scan. The χ^2 is calculated for templates generated with and fixed α_s and all available m_t values. Because the χ^2 is quadratically dependent on the difference of cross sections in the numerator of equation (6.13). The graph of χ^2 as a function of m_t has a parabolic shape as shown in figure 6.7a. This parabolic function is fitted and its minimum gives the resulting value of m_t.

We want to point out that the result obtained at this point is not the ultimate result of the whole study. The fit is done repeatedly for many simulated threshold scans and the statistical uncertainty as well as the final result of m_t is determined subsequently.

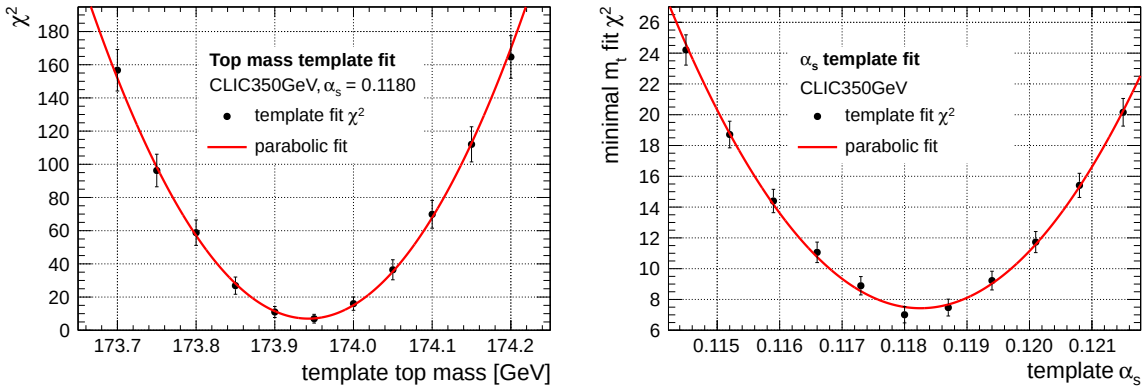

(a) Fit of m_t with fixed $\alpha_s = 0.1180$

(b) FIt of α_s from m_t fit χ^2 minima

Figure 6.7.: Examples of one-dimensional (1D) χ^2 template fits results fitted with a parabolas. The resulting values of the fit parameter lies at the minimum of the parabola. The χ^2 error bars are created artificially for purposes of the parabolic fit as $\sqrt{\chi^2}$. Plot (**a**) comes from the m_t 1D fit study, figure (**b**) is an example of one m_t slice of figure 6.8 taken from the 2D fit study.

Two-Dimensional Fit

The two-dimensional (2D) χ^2 fit is a straight-forward extension of the one-dimensional (1D) fit. The χ^2 is now calculated for templates with all possible discrete combinations of m_t and α_s within a given interval. χ^2 is now a function of m_t and α_s its graph is an elliptical paraboloid as presented in figure 6.8. It should be fitted with that two-dimensional function in the same manner is it was done in the 1D fit with one-dimensional parabola. ROOT [128], which was used for the data analysis, is unfortunately not capable of fitting a paraboloid properly.

A reliable way how to overcome this problem and to fit the $\chi^2(m_t, \alpha_s)$ is to split the 2D fit procedure into a sequence of several 1D fits. First, 1D χ^2 fit is performed for every α_s slice of the $\chi^2(m_t, \alpha_s)$ paraboloid. An example of such a fit is shown in figure 6.7a. The minimum of this parabolic fit function for each α_s slice is calculated. This minimum is characterized by a pair of values $\chi^2_{\text{min}}(\alpha_s)$ and $m_t^{\text{min}}(\alpha_s)$. By fitting the $\chi^2_{min}(\alpha_s)$ by a parabola, as depicted in figure 6.7b, we get the final χ^2-fit result for the strong coupling constant. The χ^2-fit result for the top quark mass is obtained by a linear interpolation from the $m_t^{\text{min}}(\alpha_s)$ function for α_s equal to the χ^2-fit result for the strong coupling constant.

As well as for the 1D fit, also this fit procedure is repeated 5000 times to obtain the final result of both fit parameters and their statistical uncertainties. Detail of these calculations are given in the following paragraph.

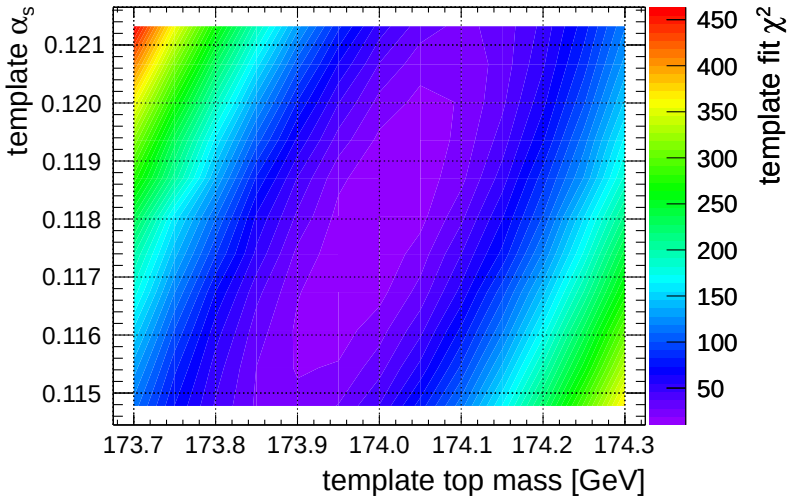

Figure 6.8.: χ^2 calculated in a simultaneous 2D template fit as a function of the top mass m_t and the strong coupling constant α_s.

Statistical Analysis

We described the fitting procedure of one simulated measurement so far. However, we want to get a result based on more than one simulated measurement to determine the statistical uncertainties of the m_t and α_s. For this purpose, we conduct the fit procedure on the set of the 5000 simulated threshold scans. The statistical evaluation of the fit results is the same for the one- and two-dimensional fit. If we put the fit results in a histogram, we will get a Gauss-shaped distribution of m_t for a 1D fit, and of m_t and α_s for a 2D fit. From a Gaussian fit of these distributions, we obtain the ultimate fit results. The mean value of the Gaussian is the final parameter (m_t or α_s) value and its sigma is the corresponding statistical uncertainty. Example plots illustrating statistical distributions of m_t and α_s in a 2D fit and the Gaussian fit results are shown in figure 6.9. It is expected that the mean values of the fit parameters will be the same as the input parameters. A deviation from the input would point to a bias in the fit itself.

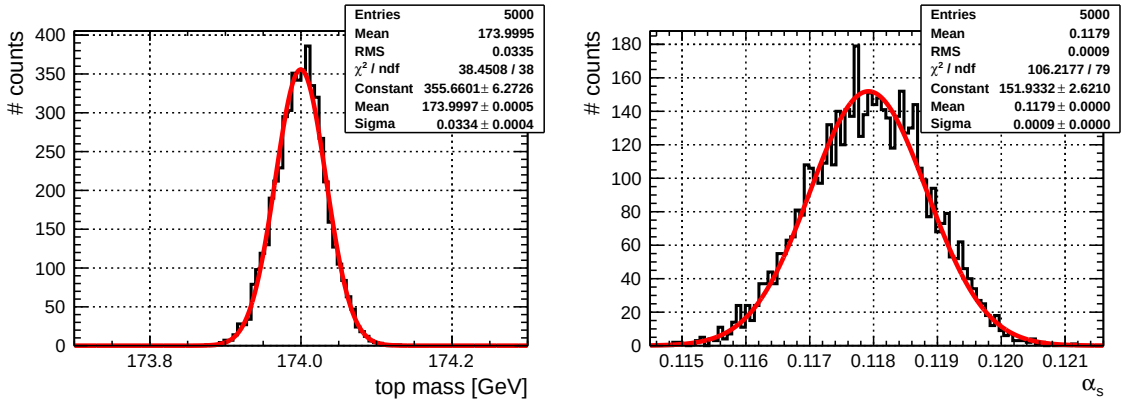

Figure 6.9.: Top quark mass m_t and strong coupling constant α_s distributions obtained from a 2D χ^2 template fit analyzing 5000 simulated measurements. Continuous red curves symbolize Gaussian fits.

Systematic Uncertainty Analysis

Additional effects, which can lead to systematic errors in the experiment were investigated too. We studied three and two quantities as a systematic uncertainty source in the 1D and the 2D fit, respectively.

The systematic error, which is relevant only for the 1D fit, is the one caused by the uncertainty of α_s. To study the α_s-induced systematic error, α_s was changed within the boundaries of the present experimental precision, which is ± 0.0007. This test was conducted by fitting the simulated cross section measurement with templates with different values of α_s than the one used to generate the measurement points. In other words, we fitted a measurement generated for $\alpha_s = 0.1180$ once with templates corresponding to $\alpha_s = 0.1187$ and once to $\alpha_s = 0.1173$. The difference between the top masses obtained for the original and shifted α_s template value gave us the systematic shift of the top quark mass due to present α_s experimental precision. This kind of systematics can be obviously studied only in the 1D m_t fit, because, in the 2D fit, the α_s is not an external parameter.

The next tested source of systematic errors was the theoretical uncertainty of the numerically calculated cross sections. It is caused e.g. by neglected higher order corrections. To test the sensitivity of the fit result to this issue, we simply modified the normalization of the cross section. Two scenarios were considered for the normalization. The more conservative one, assuming $\pm 3\,\%$ cross section error which approximates the present estimation. In the second and optimistic one, expecting additional future improvements in the theoretical calculations, we used an uncertainty of $\pm 1\,\%$. The systematic impact on the simulated measurement data was achieved by shifting the cross section points by the given percentage.

We also studied influence of precision of background level knowledge. The background must be properly subtracted to get reliable fit results. That means that it must be know as accurately as possible. Cases of $\pm 5\,\%$ and $\pm 10\,\%$ background determination uncertainty have been investigated. Reaching a statistical uncertainty of the background better than $5\,\%$ requires an accumulation of more than $5.7\,\mathrm{fb}^{-1}$ of background events listed in table 6.2.

This measurement should be done at a collision energy bellow the top production threshold. The systematic effect related to the background uncertainty was tested on specially generated measurement samples. These four sets of 5000 measurements each were simulated with accordingly bigger or smaller background level. The systematical uncertainties of m_t and α_s were obtained in the same way as in both previous cases.

The impact of decreasing the number of measurement points on the result was also tested. This is actually a very valuable information. If it were possible to reach acceptable experimental precision with less measured cross section points, one would be able to decrease the total integrated luminosity needed for the threshold scan and this would save time and resources. To implement this scenario, we dropped the last four of the ten points from the simulated cross section measurements and conducted the fit.

Further test was to shift all the measurement points by 0.5 GeV towards higher energies. The goal was to probe whether the used positioning of the points leads to any bias of the fit result. No systematic influence caused by this shift was observed.

The results of all so far mentioned studies of systematical uncertainties are presented in section 6.3.

Another important error source could be the precision of beam energy spectrum knowledge. Let us give one example. If the main luminosity peak of the beam energy spectrum had a Gaussian shape with a variance of σ, a 20 % error of σ would lead to a 70 MeV systematic uncertainty for m_t obtained in a 1D fit. This topic was investigated just briefly and will require a deeper study in the future. However, our results show that precise knowledge of the beam energy spectrum will play a significant role in keeping systematic effects under control.

6.3. Results

In this section, we will present results obtained from the template fit of simulated $t\bar{t}$ pair production cross sections measurement at the production threshold. At first we will show how the parameters like Higgs mass, top width and Yukawa coupling influence the cross section. Then, we will present fit results of the top mass m_t with fixed strong coupling constant α_s and values obtained by fitting m_t and α_s at the same time. In the end, we will discuss some systematic effects which will be relevant in future experiments. All of the studies were done with a statistical sample of 5000 threshold scans, 100 fb^{-1} each, to determine statistical uncertainty of the results.

6.3.1. Influence of Simulation Input Parameters on Cross Section Curve

A test of the influence of all TOPPIK input parameters on the shape of the $t\bar{t}$ cross section was conducted. The parameters which can be changed in addition to m_t and α_s, are the Higgs mass m_H, the Yukawa coupling λ and the top quark width Γ_t. We plotted the cross section curves with varying one parameter at a time while keeping the others fixed to see the sensitivity of the curve shape to the particular parameter. This tells us, whether it is potentially possible to determine the parameter with a reasonable accuracy from the fit of the threshold within the given cross section measurement precision. It also reveals whether fluctuations of the parameter in the boundaries of current experimental errors

may systematically affect the result of the m_t and α_s fit. Besides these variations, for Γ_t and m_H, we picked also one value of the parameter which is more distant from the current state of knowledge to see the tendency of the shape change. We will demonstrate the impact of the parameter variations on the cross sections already corrected for ISR and the CLIC beam energy spectrum, to make a comparison under real experimental conditions.

Figure 6.10a shows the influence of m_t on the cross section curve. It is the most strongly affecting one of all parameters. The significant change is favorable for the fit and it indicates that it should be possible to reach a highly precise fit result. A change in m_t causes a shift of the whole curve along the horizontal axis, as one would expect. Note that in this case the m_t change was about five times smaller than the current experimental precision.

The next examined parameter was α_s. The corresponding plot is depicted in figure 6.10b. The change in the cross section curve is not so pronounced as for the top quark mass. However, it is still large enough compared to the error bars of the measurement points so that a successful template fit can be conducted reaching a statistical precision slightly worse than the present-day experimental uncertainty.

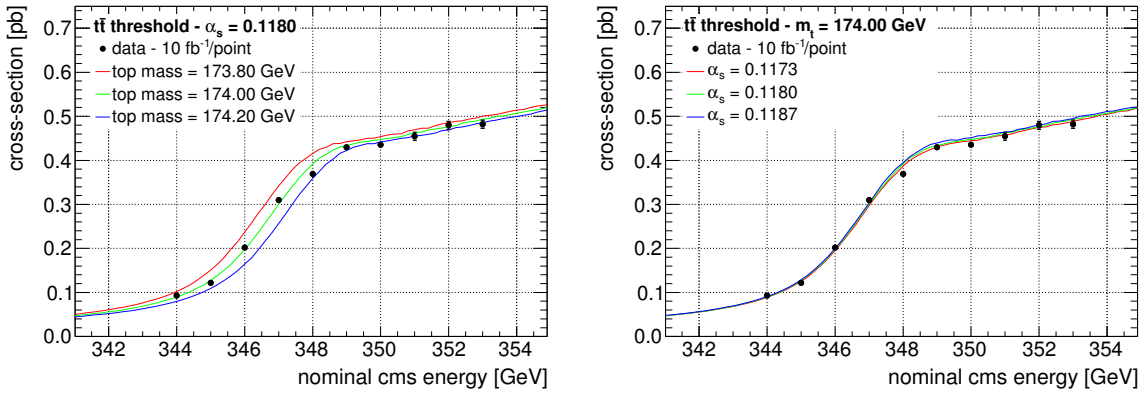

(a) Top mass influence

(b) Strong coupling constant influence

Figure 6.10.: Simulated measurement of $t\bar{t}$ production cross section at CLIC along with curves generated for different values of input parameters, the top quark mass (**a**) and the strong coupling constant α_s (**b**).

The influence of the top quark width Γ_t on the cross section curve shape is depicted in figure 6.11a. The curve marked as *default* is the one used in all other studies. Around the default choice, two further curves were generated with Γ_t variation of $\pm 2.8\,\%$. Clearly, all three mentioned curves cannot be really distinguished from each other. Therefore, we plotted two further curves with even larger deviations in Γ_t to see the dependence on this parameter. The graph shows that the threshold measurement using the cross section alone can potentially provide some sensitivity to the Γ_t. However, the precision of Γ_t will not reach a few percent level. We did not explore this possibility further in this work.

The sensitivity to the Higgs boson mass is even smaller than to the top quark width. As presented in figure 6.11b, no significant accuracy of Higgs mass measurement cannot be achieved within the given statistics. Only extreme deviations from the already experimentally observed mass of $\approx 125\,\text{GeV}$ would lead to detectable changes of the cross sections.

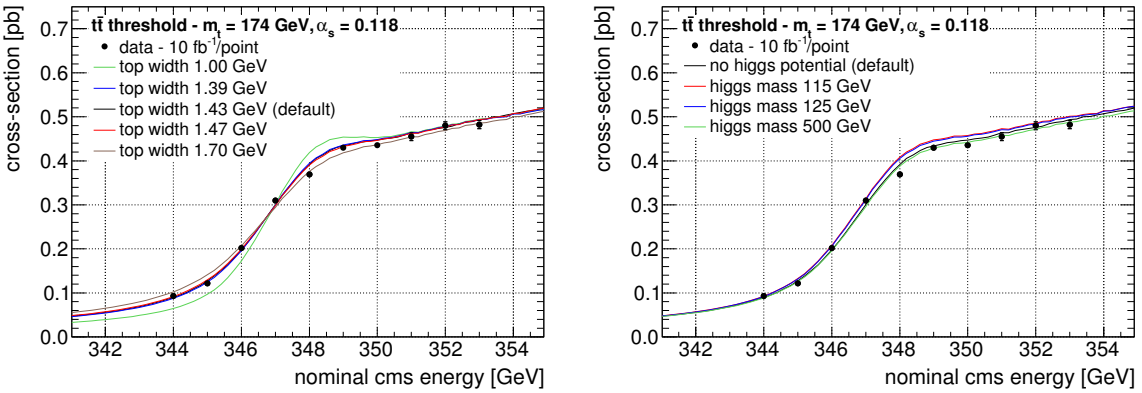

(a) Top width influence

(b) Higgs mass influence

Figure 6.11.: Simulated measurement of $t\bar{t}$ production cross section at CLIC along with curves generated for different values of input parameters, the top quark width (**a**) and the Higgs mass (**b**).

The last examined parameter was the Yukawa coupling constant λ. The respective plot is shown in figure 6.12. There is only a very small separation between the curves if we vary λ by $\pm 40\,\%$. An attempt was done to fit the λ in this range with nine specially generated templates with $10\,\%$ step in λ while keeping m_t and α_s fixed. This fit did not result in a valuable outcome. The differences between the curves are simply too small compared to statistical variations of the cross section measurement. For this reason, a fit of the $t\bar{t}$ cross sections at the threshold cannot provide a sensitive determinarion of the Yukawa coupling.

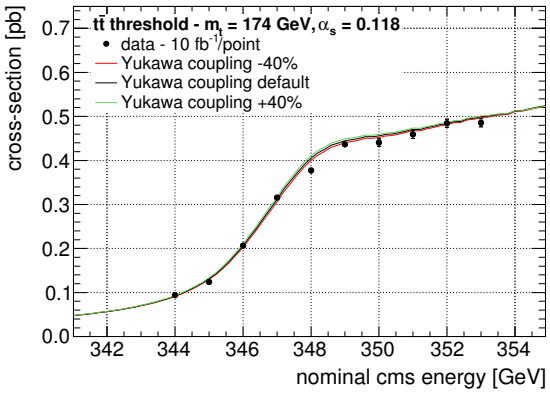

Figure 6.12.: Simulated measurement of $t\bar{t}$ production cross section at CLIC along with curves generated for different values of the top quark Yukawa coupling.

6.3.2. Single m_t Fit

The statistical error of top quark mass m_t and the potential systematic bias of the fit were determined with the help of the one-dimensional template fit. The strong coupling con-

stant was fixed to $\alpha_s = 0.1180$. Thirteen fit templates with m_t ranging between 173.70 and 174.30 GeV with a step of 50 MeV were used in this evaluation. All template parameters are listed in table 6.4. The 1D template fit result summary is shown in table 6.6 and the outcome will be discussed in the following. The detailed 1D fit results including a threshold scan with decreased integrated luminosity are to be found in appendix C.2.

Accelerator	**Fit result**	**Stat. error**	**Theor. sys. err. 1% / 3%**	**Backgnd. sys. err. 5% / 10%**	**α_S-induced sys. err.**
	[GeV]	[MeV]	[MeV]	[MeV]	[MeV]
CLIC	174.003	21	18 / 56	38 / 76	21
ILC	174.007	18	15 / 47	31 / 62	18

Table 6.6.: 1S top mass result summary of 1D fit.

Statistical Uncertainties

The reached statistical uncertainty is roughly by one order of magnitude smaller than the present-day one measured at the LHC [129] which is a substantial improvement. Despite the expected reduction of statistical uncertainty of the LHC results in the future, the systematic errors, which dominate, are foreseen to decrease only slowly as the analyses progress. The ILC is capable of achieving 15 % smaller statistical errors than CLIC thanks to sharper beam energy spectrum depicted in figure 6.5. If we turn from the ten-point scan to a six-point scan, the statistical errors will stay unchanged for both colliders.

Systematic Uncertainties

In the following paragraphs we will describe systematic effects affecting the 1D fit results. The analyses of systematics were performed on the full simulated measurement set consisting of ten cross section points.

If we assume the *theoretical cross section uncertainty* to be 1 %, the systematic error of the resulting m_t is as large as up to 85 % of the statistical error. For the 3 % case, which is the present estimation, the systematic error grows up to 2.6 times the statistical uncertainty. This systematic error is substantial. For this reason, it is highly important to reduce the theoretical uncertainty as much as possible, preferably at least to 1 %. To reach a better cross section precision, additional theoretical work is required. The impact of this systematic effect was simulated in a very simple way. A more detialed study should be performed to obtain the uncertainty with higher accuracy.

Regarding the *background-induced systematic uncertainty* of the fit result, if the subtracted background differs by 5 % from the original one, it leads to an error which is by a factor 1.8 larger than the statistical error. By turning to background uncertainty of 10 % the systematic error grows by anothe factor of two, up to 3.6 times the statistical error. Such values would deteriorate the measurement precision considerably. Hence, the accuracy of background determination must fulfill high requirements. The uncertainty of the background should be smaller than 5 % to keep the systematic error on the same scale as the statistical one.

If we vary the *strong coupling constant* α_s within its current experimental uncertainty, the respective systematic error is almost exactly as large as the statistical uncertainty. This systematic influence does not deteriorate the fit result too much and we can also hope for precision improvements of α_s in the future.

Further studies show, that the systematic errors are generally reduced by 9 % if the fit is conducted just with the first *six measurement points* in the scan. All statistical and systemtic uncertainties using six measurement points are presented in appendix C.2, table C.1. From this we see that the influence of systematic effects on the last four cross section points above the threshold is for the fit more significant. By reducing the number of measurement points in this way, we can reach lower sensitivity to all investigated kinds of systematics while keeping statistical uncertainties the same. Another major advantage of the usage of the lower number of points is a reduction of the required integrated luminosity and therefore accelerator time.

The fit result which is not subjected to any systematic influences is also shifted by a few MeV from the input value of m_t. This deviation is caused by the systematic bias of the fit algorithm itself. However, this is not an issue, because the magnitude of this error is still much smaller than the statistical uncertainty of the result.

The 1D fitting algorithm converged in 100 % cases in all performed studies. This excludes systematic biases of the results due to an unsuccessfull termination of the fit.

6.3.3. Simultaneous m_t and α_S Fit

In the second step, we extended the fit procedure so that we fitted both m_t and α_s simultaneously. We use in total 143 templates with 13 steps in m_t, and 11 steps in α_s. All template parameters are listed in table 6.4. The 2D template fit was conducted in all cases on 5000 simulated measurement samples. For the 2D fit, the same systematic studies as in the case of the 1D fit were performed except for testing of the α_s-induced error. The experimental uncertainties of m_t and α_s determine the accuracy of the conversion of the 1S mass into the $\overline{\text{MS}}$ mass [35]. The advantage of the 2D fit is a consistent extraction of m_t and α_s and their errors. The 2D template fit results for m_t and α_s are summarized in tables 6.7 and 6.8, respectively. The results with all details are given in appendix C.3.

Accelerator	**Fit result**	**Stat. error**	**Theor. sys. err. 1% / 3%**	**Backgnd. sys. err. 5% / 10%**
	[GeV]	[MeV]	[MeV]	[MeV]
CLIC	174.000	33	6 / 8	16 / 33
ILC	174.005	27	6 / 8	11 / 24

Table 6.7.: 1S top mass result summary of 2D combined fit of m_t and α_s.

Statistical Uncertainties

The order of magnitude of the statistical uncertainty of the top quark mass m_t resulting from the 2D template fit is a few tens of MeV for both investigated accelerators. For CLIC,

Accelerator	Fit result	Stat. error	Theor. sys. err. 1% / 3%	Backgnd. sys. err. 5% / 10%
CLIC	0.1179	0.0009	0.0009 / 0.0022	0.0008 / 0.0015
ILC	0.1180	0.0008	0.0008 / 0.0021	0.0008 / 0.0015

Table 6.8.: Strong coupling constant result summary of 2D combined fit of m_t and α_s.

it is about 1.9 times larger than the error obtained in the 1D fit. For the ILC, the uncertainty is by 20 % smaller than for CLIC.

The statistical error of α_s is larger than the current experimental uncertainty, almost by 30 % for CLIC and by 14 % for the ILC. This result shows that he precision of α_s can probably not be improved in a top quark threshold scan with the parameters considered in this work. If we compare the results for both colliders, at the ILC, the α_s uncertainty is by 12 % smaller than at CLIC.

As for the 1D fit, only six cross section measurement points were also used for the fitting. In the case of m_t, this led to a 18 % larger uncertainty for CLIC and 14 % for the ILC compared to the ten-point scenario. For the measurement of α_s, the influence is even larger, for CLIC the uncertainty has grown by 44 % and for the ILC by 38 %. Apparently, the precision of α_s is strongly affected by the cross section points lying in the flatter region above the $t\bar{t}$ production threshold. However, the result of the top mass, which is of the biggest interest, did not change that dramatically, even though the total integrated luminosity was reduced by 40 %.

The 2D fit algorithm converged for more than 99 % of the threshold scan measurement samples in all studies of statistic uncertainties. This excludes bias of the results caused by fit instability.

Correlation plots of m_t and α_s for both colliders calculated by using all ten points in the scan are shown in figure 6.13. They depict one and two sigma correlation ellipses of m_t and α_s based on the statistical uncertainties of these quantities determined in the 2D fit. Further plots comparing contours resulting from the six-point and ten-point scan are shown in appendix C.1, figure C.1.

Systematic Uncertainties

It was observed that the m_t is generally less sensitive to systematics in the 2D fit than in the 1D fit. The systematic change of the simulated data influences rather the α_s result. This is connected to the way of how a variation of m_t and α_s affects the energy dependence of the cross section. As seen in figure 6.10, the cross section curve moves up along the vertical axis with increasing α_s, while growing m_t causes a shift of the whole curve to the right along the horizontal axis.

On the other hand, the *theoretical cross section uncertainty* is simulated by modifying the normalization of the cross sections. The *background uncertainty* is implemented by varying the assumed background level which basically results in adding a positive or negative constant to the cross section energy dependence. Both of these systematic effects have an impact of the simulated cross sections similar to a change of α_s. Therefore, the sensitivity of α_s to these error sources is enhanced.

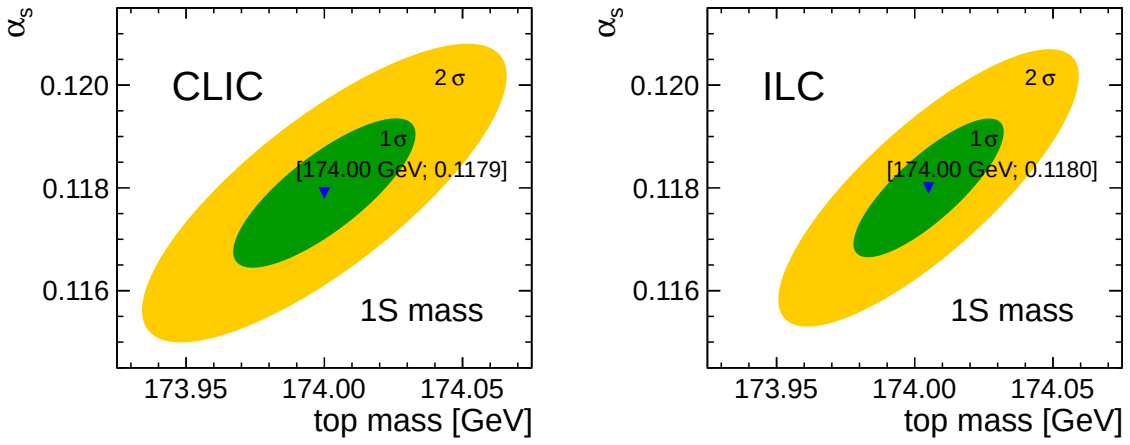

(a) CLIC (b) ILC

Figure 6.13.: One and two sigma correlation contour for the top mass $1S$ and the strong coupling constant α_s resulting from a simultaneous fit using 10 points in the threshold scan, shown for CLIC (**a**) and the ILC (**b**).

When we drop the last four points in the threshold scan from the analysis, the α_s systematic uncertainties are reduced by approximately 30 % for CLIC and by 15 – 35 % for the ILC for all systematics types. For m_t, the theory-induced uncertainties were strongly decreased, by 70 – 90 %. On the other hand, the background-related systematics have grown by 30 – 40 % for both colliders. In other words, by dropping the last four points in the scan, we gain lower sensitivity of α_s to all the systematics and of m_t to theory-induced systematics. The cost of this improvement is a bigger background-induced uncertainty of m_t and enhanced statistical errors of both α_s and m_t.

The general statement about the size of the systematic uncertainties is that all of them are of the same order of magnitude as the statistical errors. Moreover, in most cases they are even smaller. The only situations where the systematic error of m_t is slightly larger than statistical uncertainty are the scenarios with 10 % background error. For α_s, it happens for 10 % background error in the ten-point scan scenario and for the 3 % theoretical cross section uncertainty. A part of the systematic errors of m_t is in the 2D fit absorbed by the α_s compared to the 1D fit. The α_s uncertainty also contributes to the error of the assignment between $1S$ and $\overline{\text{MS}}$ mass and therefore its systematics play an importat role, too. According to [35, equation (84)], the conversion errors are 100 and 142 MeV for the 1D and 2D fit, respectively. This comparison shows the 1D fit to be more favourable under current conditions. In the calculation based on the 1D fit result, a total α_s uncertainty of 0.0007 was assumed. This number reflects the current world average error.

The fit-caused systematic error of the top mass is < 1 MeV for CLIC and 5 MeV for for ILC. It is reduced compared to the 1D fit and also significantly smaller than the statistical error. Regarding the strong coupling constant α_s, the fit-induced bias is < 0.0001 at the ILC. At CLIC, it is as large as 11 % of the statistical uncertainty. All these errors are reasonably small and acceptable.

The stability of the 2D fit is due to its complexity a bit lower than for the 1D fit. However, the 2D success rate was usually better than 96 % and it was never lower than 86 %. The fit stability was in all cases good enough to avoid significant biasing of the results by the fit instability. Detailed values of the fit convergence rates are given in tables in appendix C.

6.4. Top Quark Pole Mass

All results presented up to this point regarded the 1S top mass definition in the simulated data and fit templates. We also examined how the experimental errors change when the pole mass scheme is used. The pole mass concept is explained in section 1.4.2. The same simulated measurements, calculated with the 1S mass definition, were fitted with a new complete set of 143 templates. These templates were generated using the pole mass definition in the cross section calculation with TOPPIK. Subsequently, the full scale study was conducted for the pole mass as well. All the simulation and analysis steps were performed exactly in the same way as for the study with the 1S mass.

The complete results for the pole mass study can be found in appendix C, in tables C.2 (single m_t fit), C.5 (two-dimensional fit, m_t) and C.6 (two-dimensional fit, α_s).

The top quark pole mass $m_t^{(pole)}$ resulting from the 1D fit is 175.36 GeV at both colliders. It corresponds to the input top 1S mass of 174.00 GeV. As expected, the statistical error and all systematic errors, except for α_s-induced uncertainty, are the same as those ones obtained in 1D fit for 1S templates. The pole mass is much more sensitive to variations of α_s.The α_s induced error is by a factor of two larger than in the 1S case.

In the 2D fit, the top pole mass of 175.35 and 175.37 GeV was obtained for the CLIC and the ILC, respectively. The statistical uncertainties of both mass definitions as well as the correlation between the top mass and α_s are depicted in figure 6.14. In this plot, the correlation contours are expressed in terms of statistical deviations of the investigated quantities. The statistical errors of the pole mass are by a factor of two larger in comparison to the 1S mass. Apart from this, the correlation between the pole mass and the α_s is also stronger. In the case of the 2D fit, it is not possible to make a general statement about systematic error change with respect to the study using the 1S mass definition. The precision in the pole mass scenario is strongly deteriorated when the theoretical uncertainty of $t\bar{t}$ production cross section is taken into account. This systematic uncertainty is larger by a factor of four and six for CLIC and the ILC, respectively. On the other hand, the sensitivity to background determination error is moderately decreased. The 2D fit results of the strong coupling constant do not differ considerably from the ones obtained in the 1S mass study. The α_s fit is particularly sensitive to the of the cross section points above the threshold and their position does not change significantly due to mass definition.

The pole mass study showed that it is possible to perform the template fit with our tools successfully also for other top quark mass definitions obtaining consistent results. When all the $m_t^{(pole)}$ measurement errors are added up, even for the most pessimistic scenarios, they do not exceed the intrinsic uncertainty of the $m_t^{(pole)}$ and $\overline{\text{MS}}$ mass assignment. This transformation is governed by the QCD scale parameter $\Lambda_{QCD} \approx 200$ MeV. The experimental precision at the future linear colliders is obviously sufficient for a successful $m_t^{(pole)}$ measurement. Moreover, accurate determination of the pole mass in a threshold scan can

shed light on the relation between invariant mass and pole mass and allow further comparisons with LHC results. On the other hand, the usage of the 1*S* mass scheme offers by definition higher measurement precision.

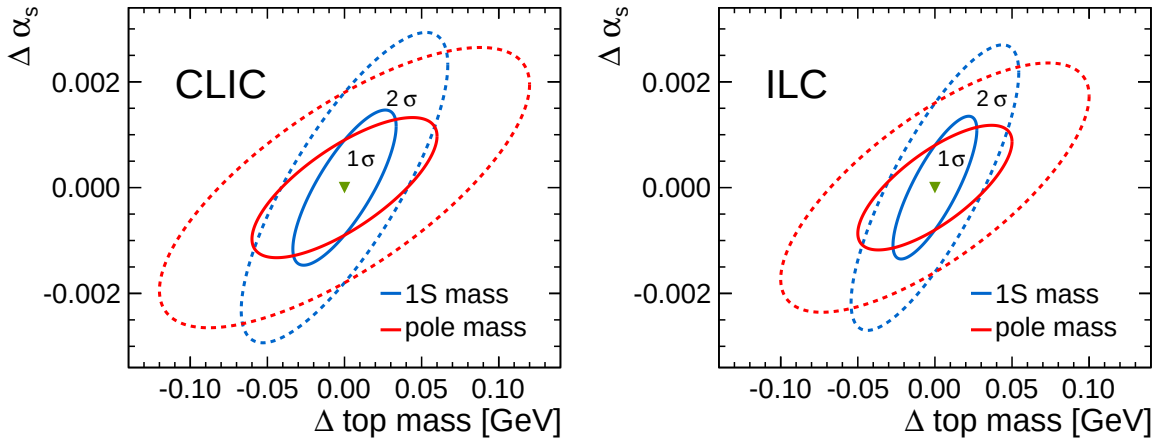

(a) CLIC (b) ILC

Figure 6.14.: Comparison of one and two sigma correlation contours based on statistical uncertainties for 1*S* and pole mass scheme expressed in terms of deviations of the correlated quantities, the top mass and the strong coupling constant α_s. Results obtained from a simultaneous fit are shown for CLIC (**a**) and the ILC (**b**) using 10 points in the threshold scan.

6.5. Summary

The top quark couples most strongly to the Higgs boson and may also provide sensitivity to Beyond Standard Model physics. The mass of the top quark is a very important input parameter of the Standard Model. Future linear colliders, CLIC and the ILC, provide the capabilities of precise measurement of the top quark mass in different ways. In the presented study, the highest reachable experimental precision of the top mass was investigated. A top pair production threshold scan was utilized for this purpose. The study was based on NNLO-precision numerical cross section calculations and realistic GEANT4 detector simulations including physics and machine-induced backgrounds. The analysis was performed for an integrated luminosity of 100 fb^{-1}.

In the threshold scan approach, different top quark mass definitions can be used for the interpretation of the result. Our choice was the theoretically well-defined 1*S* mass. The achieved top mass statistical precision at CLIC was 33 MeV, when fitted simultaneously with the strong coupling constant. The statistical error obtained for the strong coupling constant was 0.0009. Besides the statistical errors, also several systematic uncertainties were studied. The error induced by the theoretical top pair production cross section normalization uncertainty is considerably smaller than the top mass statistical error. For the

strong coupling constant, this kind of systematic effect causes comparable or larger errors than the statistical one. The second investigated source of systematics was the background determination error. For both the top mass and strong coupling constant, this led to uncertainties of the same magnitude or smaller compared to their statistical errors. The statistical errors obtained under conditions of the ILC are reduced by 20 % due to a narrower beam energy spectrum of the ILC.

To conclude, at future linear e^+e^- colliders, it will be possible to measure the top quark $1S$ mass with a total uncertainty of less than 50 MeV. Compared to recent Tevatron [110] and LHC [129] results, which evince combined precision of 1.0 GeV and 1.2 GeV, respectively, the linear e^+e^- colliders would bring a great improvement in measurement precision. The statistical accuracy reached in the threshold scan is also by more than two times better than the statistical precision of top invariant mass reconstruction at CLIC [112]. Furthermore, an experimental determination of a theoretically well-defined top mass like $1S$ can shed light on relation of the $1S$ and the experimentally well-defined invariant mass. The top $1S$ mass can be immediately employed in theoretical calculations. It should be stressed that the above cited experiments measured the top invariant mass which roughly corresponds to the pole mass. On the other hand, cross section measurement precision is not good enough, neither at the CLIC, nor at the ILC, to make it possible to determine further parameters like Higgs mass or Yukawa coupling from the top threshold scan. The top width may be measured. However, this issue requires further investigations.

A further valuable extension of our study could be the investigation of a systematic impact of the uncertainty of the knowledge of the beam energy spectrum of the collider. Our preliminary tests of systematics related to the inaccurate description of the beam energy spectrum show that this factor might be a non-negligible source of experimental errors. Improved realism of the simulations thanks to new calculations is expected to become available in the future including a more sophisticated treatment of theoretical uncertainties. It might be also useful to investigate various configurations of energy points and of uneven distributing of the total integrated luminosity between the measured data points in the scan. An optimization of this could bring increased precision and reduce necessary integrated luminosity at the same time.

CONCLUSIONS

The subject of thesis were studies of detector performance and a determination of experimental precision with which the top quark mass can be measured at future linear e^+e^- colliders (FLC). During the detector tests, we investigated properties of plastic scintillator tiles manufactured for a prototype hadron calorimeter and silicon photomultipliers which are used for the readout of these tiles.

The FLCs are designed with the intention to complement and extend the measurements performed at the Large Hadron Collider. To meet these goals, a new level of measurement precision must be established. This demand requires also novel detector solutions and analysis methods. The particle flow concept is an analysis technique which allows to assign a four-momentum vector to all particles (except for neutrinos and potentially other "invisible" particles) in a particle collision. For employing of this reconstruction method, very finely segmented calorimeters are necessary. A design option for such a hadron calorimeter are many interleaved layers of absorber and active layers. For the absorber, a metallic material with high density will be utilized. One alternative for the active calorimeter part are plastic scintillators in a shape of a prism with volume of a few cm^3. To maintain compactness of the detector, usage of photomultiplier tubes is excluded and they must be replaced by much smaller silicon photomultipliers (SiPM).

In our experimental work, we studied the areal homogeneity of SiPM response with a highly collimated pulsed visible light beam. Our focus was on Hamamatsu Multi-Pixel Photon Counters (MPPC) because of their usage in our further scintillator studies and in the Tungsten Timing Test-Beam (T3B) experiment performed by our group. We managed to obtain sensor images in terms of relative photon detection efficiency (PDE) and crosstalk probability for several SiPM models. The spacial resolution of these pictures was of the order of 1 μm which allowed to observe active area structures within single SiPM microcells. Our method enables to measure directly the geometrical fill factor of a SiPM. Additional analysis studied the homogeneity by calculating the relative PDE and geometrical fill factor for every single pixel of the sensor. This approach resulted in characteristics given by spread of relative PDE and fill factor of individual pixels. Our study showed that the best performing tested SiPM was the Hamamatsu MPPC with 50 μm pixel size. Another benefit of the developed experimental apparatus is that it can be employed in the future for

relatively quick tests of different SiPMs. This would be a very useful option once another prototype series of the Silicon Multi-Photon Light Sensors (SiMPl) will be produced at the Semiconductor Laboratory of the Max Planck Society. However, since the light source used in the setup is not calibrated and the pulse width cannot be precisely controlled, it is only possible to measure the relative PDE. A usage of a calibrated light source with a well-defined pulse length would allow to obtain absolute PDE which would be a major improvement of the method.

In the second technical study, we investigated properties of plastic scintillators which could be used in a hadron calorimeter for linear collider experiments. Two different scintillator tile designs were tested. The frontal area of both of them was $30 \times 30\,\mathrm{mm}^2$ and they were 5 and 3 mm thick, respectively. The thicker one was machined and the thinner one was manufactured by injection molding. These scintillators differed also in the used material and in the shape of the light collection dimple. The tiles were read out from one side by a SiPM. The light collection levels were measured while irradiating discrete positions of the frontal area with a collimated electron beam from a radioactive ^{90}Sr source. Advanced analysis techniques which resolve individual single photon events in the detector were employed. We obtained maps of the tiles in terms of number of detected scintillation photons in order to evaluate areal homogeneity of the output signal. The results show a better homogeneity in the case of the thicker 5 mm tile. The result was mainly influenced by the shape of the light collection dimple. The used measurement technique allowed also to compare the mean light yield of both sample scintillators. With the same equipment, we did an additional measurement of light crosstalk between two neighboring tiles mimicking a geometry in a full detector. Both tile types were covered with a different reflective coatings on the adjacent side which lead to different crosstalk levels. However, both tile designs evince a crosstalk of a magnitude lower than 2 % which is reasonably small. The thicker tile exhibited a more favourable crosstalk of about 0.5 % due to the used reflective foil. A further investifation of scintillator tile properties was done by irradiating the samples by an uncollimated ^{241}Am/Be neutron source. This experiment proved a considerable sensitivity to a broad energy spectrum of neutrons by both tiles even with a spectroscopic potential. This leads to a conclusion that the neutrons detected directly in the scintillator cannot be neglected in a calorimeter experiment. Additionally, the measurement results were confronted with a Monte Carlo simulation showing a good agreament with a straight-forward theoretical model. This result shows that the neutron interaction with plastic scintilators can be very well described and simulated by considering just basic physical proceses.

In the field of top physics, we performed a simulation of the top quark mass measurement under the conditions of FLC, namely the Compact Linear Collider (CLIC) and the International Lineal Colliders (ILC). Since the top mass cannot be calculated from first principles of the Standard Model (SM) of particle physics, a precise knowledge of this parameter can shed light on some open questions of the present day and improve further theory-based results. An interesting example of a question where the top quark mass plays a distinct role is the issue of SM vacuum stability. An accurate knowledge of the top mass has the potential to decide whether the vacuum is in a meta-stable or unstable state. The top quark has an unusual property of a very short lifetime, shorter than hadronization time. Therefore, it decays before forming any bound state and it can be directly identified and reconstructed by its daughter products. The peak position in the distribution of

the top invariant mass measured in an experiment roughly corresponds to the pole mass parameter in quantum field theory. Unfortunately, the $\overline{\text{MS}}$ mass parameter is needed for theoretical calculations and the relation between the pole mass and the $\overline{\text{MS}}$ mass is loaded with an intrinsic uncertainty of the order of Λ_{QCD}. To overcome this problem, the top mass must be measured using another method to obtain a theoretically well-defined parameter. At the same time, this must be convertible to the $\overline{\text{MS}}$ mass with high precision. The $1S$ top mass has these properties and can be experimentally determined in a threshold scan.

We performed a simulation of such a measurement by using the template fit approach. Top-antitop pair production cross sections in $e^+e^- \rightarrow Z^*/\gamma^* \rightarrow t\bar{t}$ process were obtained with a next-to-next-to-leading-order (NNLO) theory-based numeric calculation using the $1S$ mass scheme. These were corrected for the effect of initial state radiation and beam energy spectrum of the given accelerator. To simulate realistic experimental data, the uncertainty of the cross section measurement was based on top reconstruction and background rejection efficiencies obtained from an extensive study regarding direct invariant top mass reconstruction. Ten measurement cross section points were simulated around the threshold with a total integrated luminosity of $100\,\text{fb}^{-1}$ ($10\,\text{fb}^{-1}$ each).

The template fit of these data points lead to following results. The combined, statistical and systematic, uncertainty of the $1S$ top mass obtainable with this method is better than 50 MeV. The investigated systematic effects included 5 % uncertainty in background determination and 1 % error of the theoretical caldulation of $t\bar{t}$ production cross section. Specifically, a precision of $33_{(\text{stat.})} \oplus 17_{(\text{syst.})}$ MeV can be achieved at CLIC. The ILC will have, due to a different acceleration technology, a sharper nominal energy peak in the beam energy spectrum. Therefore, the statistical as well as the systematic error is moderately reduced resulting in $27_{(\text{stat.})} \oplus 12_{(\text{syst.})}$ MeV. These measurement precisions would be a great improvement compared to present day CDF and CMS results, $173.20 \pm 0.51_{(\text{stat.})} \pm 0.71_{(\text{syst.})}$ GeV and $173.36 \pm 0.38_{(\text{stat.})} \pm 0.91_{(\text{syst.})}$ GeV , respectively. The significant additional benefit of the FLC measurements is that the top mass could be obtained in a theoretically well-defined scheme. The presented uncertainties are assuming an optimistic scenario of keeping systematic effects well under control. The template fit procedure was performed simultaneously for the top mass and the strong coupling constant α_s. α_s can be extracted with an error of $0.0009_{(\text{stat.})} \oplus 0.0012_{(\text{syst.})}$ which is not competitive with contemporary world average. However, this simulation method supplies top mass and α_s uncertainties in a consistent way so that they can be utilized in further calculations. To reach the maximal precision of the $\overline{\text{MS}}$ mass under the conditions assumed in our study, α_s should be rather an input parameter of the fit. Moving from the NNLO cross section calculations to NNNLO accuracy in the future will bring a better understanding of theoretical uncertainties and can possibly improve precision of top mass determination.

Within the adopted detector reconstruction capabilities, the sensitivity of the threshold scan to the Higgs mass and top quark Yukawa coupling is not high enough to determine these quantities with a reasonable accuracy. It might be possible to measure the top quark width. To clarify this issue, further studies are required.

Acknowledgments

I thank especially my supervisor Dr. Frank Simon for a competent advising of my projects. He was always opened to constructive discussions and he was bringing inspiring ideas and suggestions which were a great motivation and challenge for me.

I also thank Prof. Allen Caldwell for accepting to be the official supervisor of this thesis.

Further, I would like to thank Dr. Sven Menke for his selfless support during measurements with radioactive sources and their characterization. His priceless advices and work on Monte Carlo simulations helped me to deepen my understanding of these experiments and the underlying physics.

Big thanks belong to Dr. Paola Avella for her unselfish help during language corrections of my thesis.

I also would like to thank Dr. Rainer Richter for his willingness to help me to improve those parts of the thesis which regard silicon detectors.

I thank Christian Jendrysik who contributed to a nice working atmosphere during my stay in the Semiconductor Laboratory and who was also a source of valuable ideas.

Special thanks belong to Sebastian Paßehr for his patience and kindliness to discuss and clarify issues of quantum field theory.

I am also very grateful to my colleagues Miroslav Gabriel, Dr. Katja Seidel, Dr. Christian Soldner, Marco Szalay and Dr. Lars Weuste for enriching my everyday working life and being always very helpful.

Finally, I thank all people who were supporting me during my doctoral studies and helped me to be strong enough during hard times.

Appendix

APPENDIX A

LISTS OF USED EXPERIMENTAL EQUIPMENT

SiPM Scan Apparatus

Device type	Model
Microscope	Infivar CFM-2 with 50/50 beam splitter
Objective	Mitutoyo M Plan Apo 50×/0,55
CCD camera	µEye UI145x-C
Micropos. stage axis	PI M-112.1DG (3×)
Micropos. stage controler	PI C-843
Pulse generator	Agilent 81110A 165/330 MHz
Counter	Agilent 53131A 225 MHz (2×)
Power supply	Töllner TOE 8842
Amplifier	NIM Foto Multiplier Amplifier
Discriminator	NIM LeCroy Model 623B
Coincidence unit	NIM LeCroy Model 622
SiPM readout board preamp.	MAR-8ASM 03/06
Oscilloscope	LeCroy WaveRunner 64Xi 600 MHz, 10 GS/s
LED (red, 625 nm)	WU-8-56SEC
LED (green, 525 nm)	Nichia NSPG500S
LED (blue, 470 nm)	Nichia NSPB500S

Table A.1.: List of equipment used in the PDE scan setup.

Types of Scanned SiPMs

Full SiPM name	Pixel pitch [μm]	Short name
Hamamatsu MPPC-10-25N-F	25	MPPC-25
Hamamatsu MPPC-S10362-11-025U	25	MPPC-25U
Hamamatsu MPPC-S10943-8584(X)	50	MPPC-50
SensL SPMMicro1035X13	35	SensL-35
SensL SPMMicro1100X13	100	SensL-100
MEPhI/Pulsar SiPM576#1 (prototype)	32	MEPhI-32

Table A.2.: List of SiPMs tested with the PDE scan setup. The presented short names are used in text of the thesis for simplicity.

SiMPl prototype name	Pixel pitch [μm]	Gap between pixels [μm]	Number of pixels
P15	135	15	100/19/7
P13	135	13	19
L01	130	10	18
O17	130	20	18

Table A.3.: List of SiMPl prototype structures of second production series tested with the PDE scan setup. The table shows their pixel pitch and gap size and number of pixels of the currently scanned detector.

Scintillator Tile Test Apparatus

Device type	Model
Oscilloscope	PicoScope PS6403 (2×)
Power supply	Keithely 2400 Source Meter (2×)
Power supply	Agilent E3620A (2×)
Power supply	Tektronix PWS4323
Micropos. stage axis (X, Y)	ThorLabs MTS50X/M (2×)
Micropos. stage axis (Z)	ThorLabs MTS25/M-Z8
Micropos. stage axis controller	ThorLabs TDC001 (3×)
Micropos. stage axis power supply	ThorLabs TPS001 (3×)
Temperature probe	Pt1000
Voltmeter (Pt1000 readout)	Agilent 34411A
Tile-under-test readout SiPM	Hamamatsu MPPC-S10943-8584(X) (2×)
Coincidence scintillator readout SiPM	Hamamatsu MPPC-S10362-11-025U
SiPM readout board preamp.	Infineon BGA614

Table A.4.: List of equipment used in the scintillator tile study.

APPENDIX B

SILICON PHOTOMULTIPLIER MEASUREMENT SUMMARY

B.1. Relative PDE and Crosstalk Maps

Hamamatsu MPPC-25U

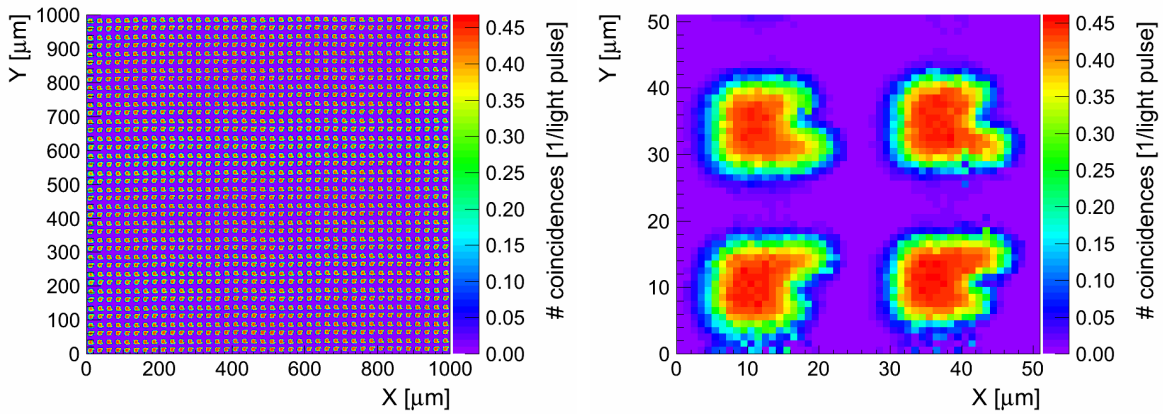

(a) Whole device

(b) Detail of four cells

Figure B.1.: Sensitivity map of Hamamatsu MPPC-25U taken at 0.5 p.e. discrimination level. Full SiPM surface (**a**) and a detail of four corner cells (**b**) is shown. Over-bias voltage 1.8 V (recommended by the manufacturer). Resolution 1 µm, 10 000 green LED pulses per step. Noise subtracted. Values on the *Z* axis are not comparable with other measurements because of different operation mode of the LED in this measurement.

Hamamatsu MPPC-50

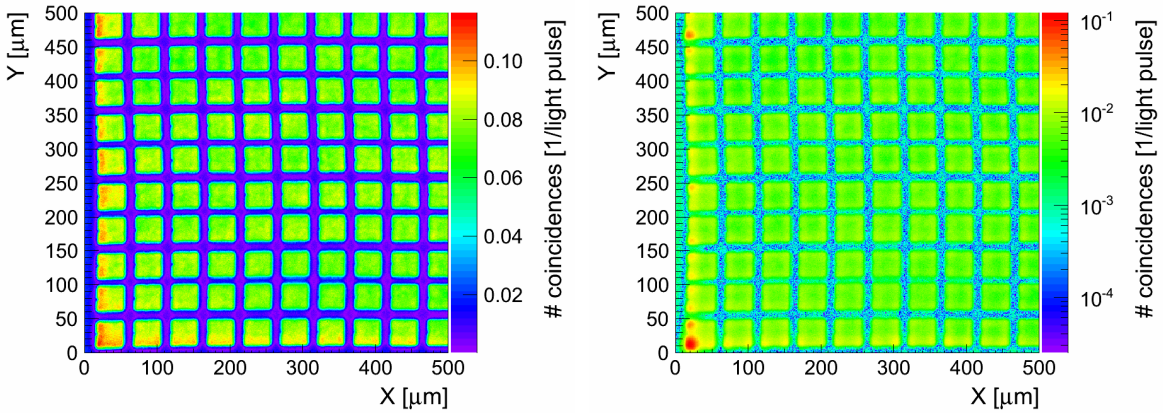

(a) Discrimination level = 0.5 p.e.

(b) Discrimination level = 1.5 p.e.

Figure B.2.: Sensitivity maps of Hamamatsu MPPC-50 (1/4 of the full array) taken at two different discrimination levels. Over-bias voltage 0.5 V. Resolution 1 µm, 20 000 green LED pulses shot per step. Noise subtracted.

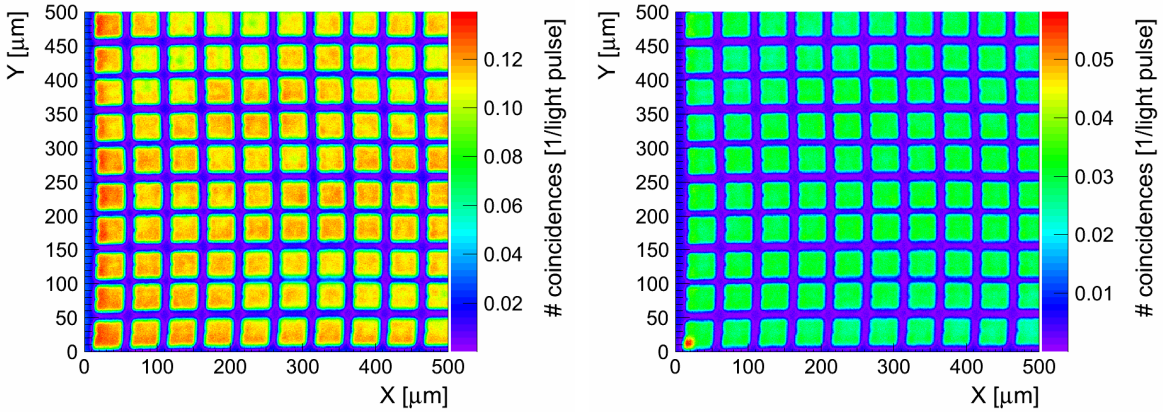

(a) Discrimination level = 0.5 p.e.

(b) Discrimination level = 1.5 p.e.

Figure B.3.: Sensitivity maps of Hamamatsu MPPC-50 (1/4 of the full array) taken at two different discrimination levels. Over-bias voltage 1.5 V. Resolution 1 µm, 20 000 green LED pulses shot per step. Noise subtracted.

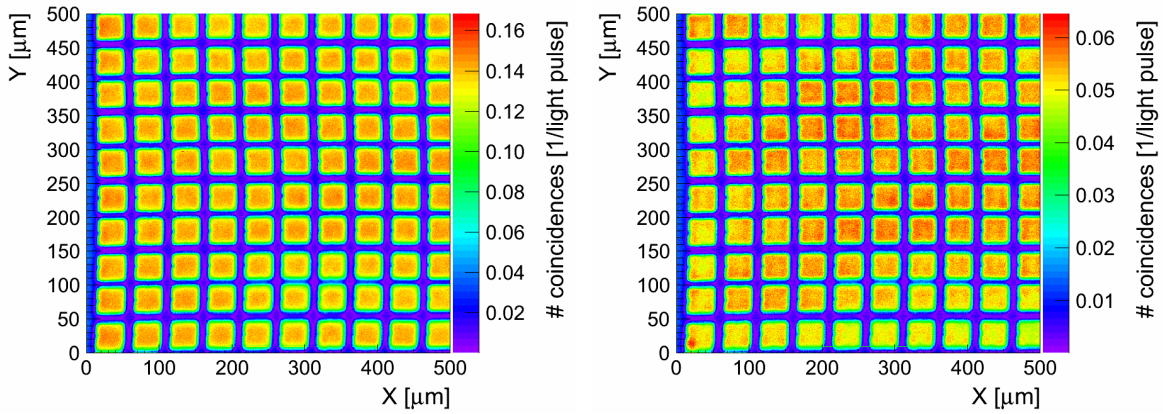

(a) Discrimination level = 0.5 p.e.

(b) Discrimination level = 1.5 p.e.

Figure B.4.: Sensitivity maps of Hamamatsu MPPC-50 (1/4 of the full array) taken at two different discrimination levels. Over-bias voltage 2.0 V. Resolution 1 µm, 20 000 green LED pulses shot per step. Noise subtracted.

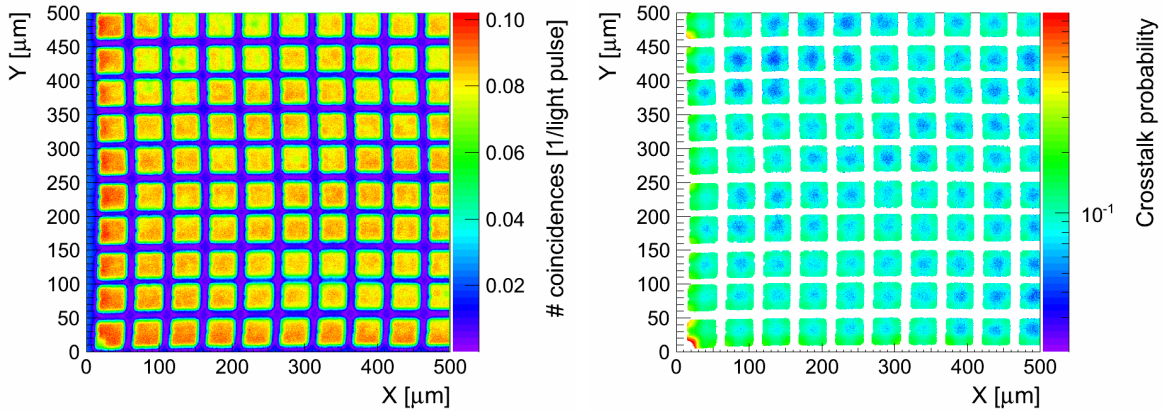

(a) Pure 1 p.e. signal

(b) Crosstalk probability

Figure B.5.: Pure 1 p.e. response and crosstalk probability maps of Hamamatsu MPPC-50 (1/4 of the full array). Over-bias voltage 1.0 V. Resolution 1 µm, 20 000 green LED pulses shot per step.

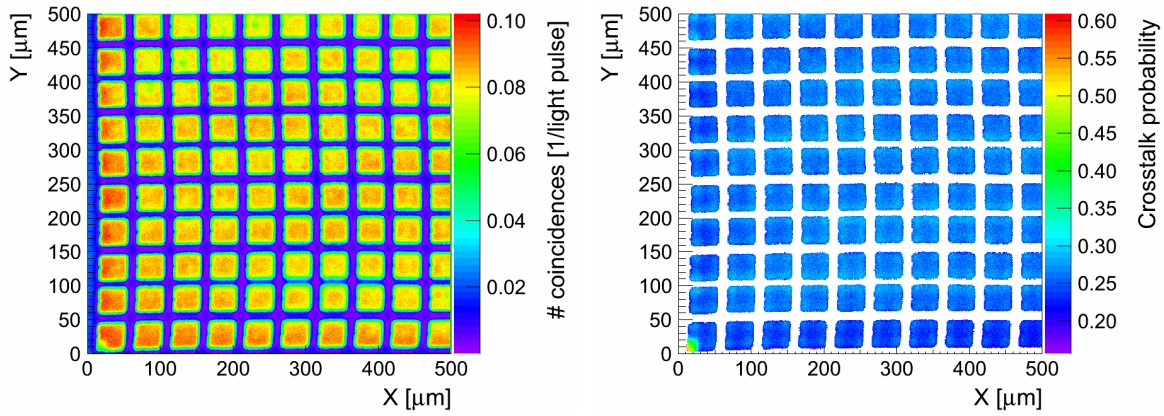

(a) Pure 1 p.e. signal

(b) Crosstalk probability

Figure B.6.: Pure 1 p.e. response and crosstalk probability maps of Hamamatsu MPPC-50 (1/4 of the full array). Over-bias voltage 1.5 V. Resolution 1 µm, 20 000 green LED pulses shot per step.

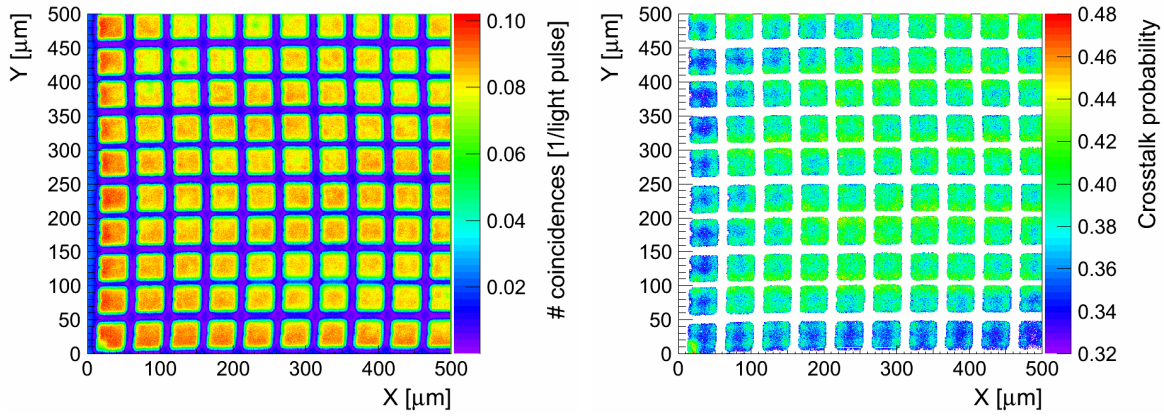

(a) Pure 1 p.e. signal

(b) Crosstalk probability

Figure B.7.: Pure 1 p.e. response and crosstalk probability maps of Hamamatsu MPPC-50 (1/4 of the full array). Over-bias voltage 2.0 V. Resolution 1 µm, 20 000 green LED pulses shot per step.

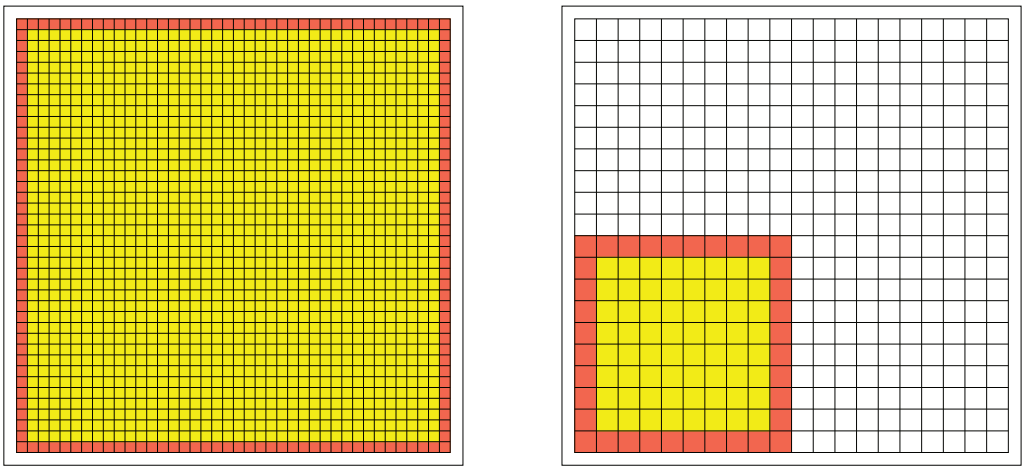

(a) Hamamatsu MPPC-25U

(b) Hamamatsu MPPC-50

Figure B.8.: Schematic illustration of scanned area of the Hamamatsu MPPC-25U (**a**) and Hamamatsu MPPC-50 (**b**). Union of red and yellow area represents scanned part of the chip. Data from the yellow area was used for analysis of single pixels (see results in section B.2).

SiMPl P15 (135 µm pitch, 15 µm gap)

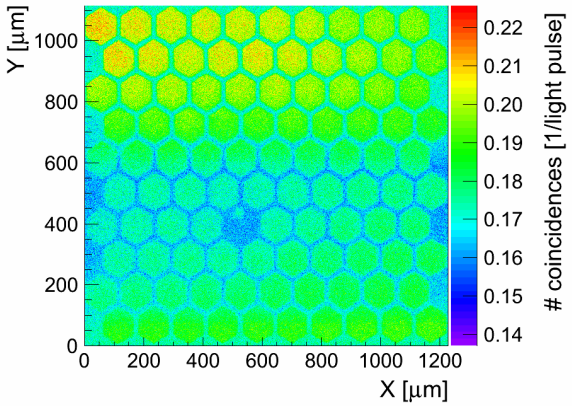

(a) 10×10-pixel array

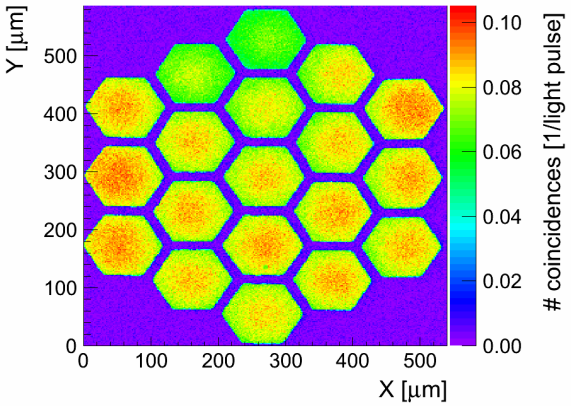

(b) 19-pixel structure

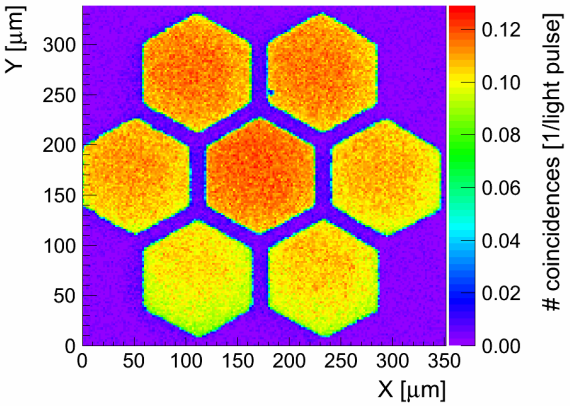

(c) 7-pixel structure

Figure B.9.: Sensitivity maps of different SiMPl P15 arrays. All measurement, except for (**a**), were corrected for noise. The noise of the 10×10 structure was very sensitive to temperature changes and was varying during the measurement. Overbias voltage 2 V. Resolution 1 µm, 20 000 green LED pulses per step.

SiMPl P13 (135 µm pitch, 13 µm gap)

The P13 sample (19 pixel structure) was scanned with a higher precision then other SiMPl devices, because the edge breakdown was observed in photo-emission images. The intention was to examine, whether this effect will affect light detection. As can be see in figure B.10, no significant inhomogeneities in PDE along the pixel edges are recognizable. Also, the inner pixels evince an enhanced PDE. This could be caused by a higher crosstalk probability for the pixels which are neighbouring with another microcells at each side. Further reason might be a different gap size. The gap between pixels and the gap between the outermost pixels and an aluminium line surrounding the whole pixel array (visible in figure B.37b) have a different width. Because the gap width affects size of the quenching resistor, its resistance can differ for the inner and the outer pixels.

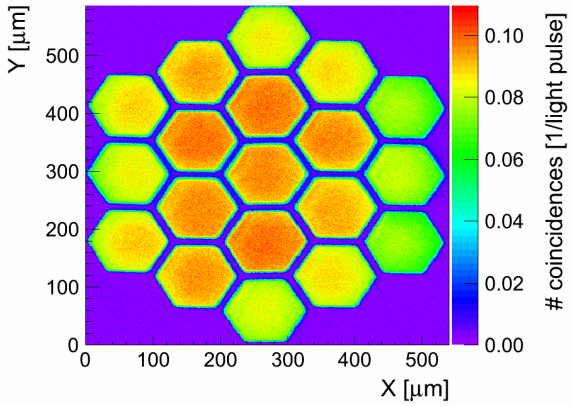

Figure B.10.: Sensitivity map of SiMPl P13, 19-pixel structure. An effect of edge breakdown can be seen very weekly (best visible in inner pixels at "10-to-11 o'clock" position). Over-bias voltage 2 V. Resolution 1 µm, 20 000 green LED pulses shot per step. Noise subtracted.

SiMPl L01 (130 µm pitch, 10 µm gap)

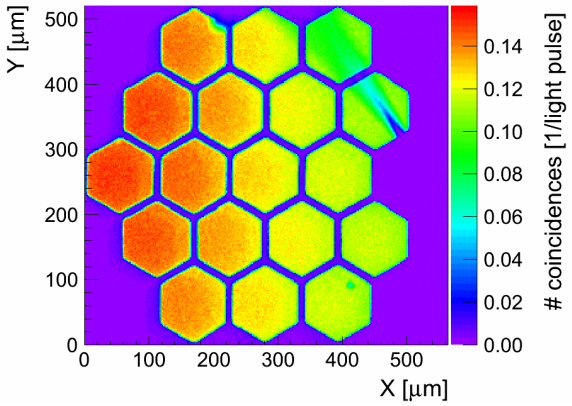

Figure B.11.: Sensitivity map of SiMPl L01, 18-pixel structure. The "cut" and the "shadow" in the pixels placed in upper right position is caused by a bond wire crossing active area of the sensor. Other small sharp local disturbances are most likely caused by dust particles or mechanical damage. Over-bias voltage 2 V. Resolution 2 µm, 20 000 green LED pulses shot per step. Noise subtracted.

SiMPl O17 (130 µm pitch, 20 µm gap)

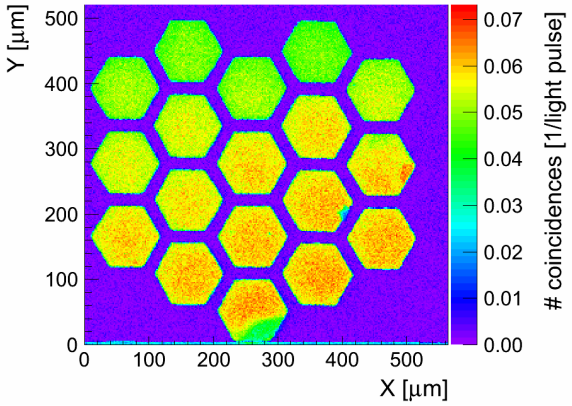

Figure B.12.: Sensitivity map of SiMPl O17, 18-pixel structure. Small sharp local disturbances are most likely caused by dust particles od mechanical damage (e.g. the lowermost pixel). Over-bias voltage 2 V. Resolution 2 µm, 20 000 green LED pulses shot per step. Noise subtracted.

MePhI-32

Scan results for the MePhI-32 SiPM are shown in figures B.13 and B.16. This device exhibited the lowest observed homogeneity of all studied detectors. It should be mentioned, that this particular piece is already rather old and was used by many people before which could lead to some mechanical damage. It can be recognized on the map taken at 0.5 p.e. threshold, shown in figures B.13a and B.15a, that the detector is more sensitive in the upper left and lower right corner than in the rest of the array. This effect becomes more apparent in the integrated efficiency and fill factor plot for single pixels depicted in figure B.26. In these two plots and in the map taken at 1.5 p.e., presented in figure B.26b, are apparent two visible parallel stripes of low efficiency and fill factor. We do not know where they come from, but it may be a signature of a mechanical damage. The crosstalk probability maps are given in figures B.14b and B.16b. For such a small pixel size we do not observe any specific structure of crosstalk inside of the active area. There is also no outstanding qualitative difference between the active area shape in pure 1 p.e. map and the 0.5 p.e. map.

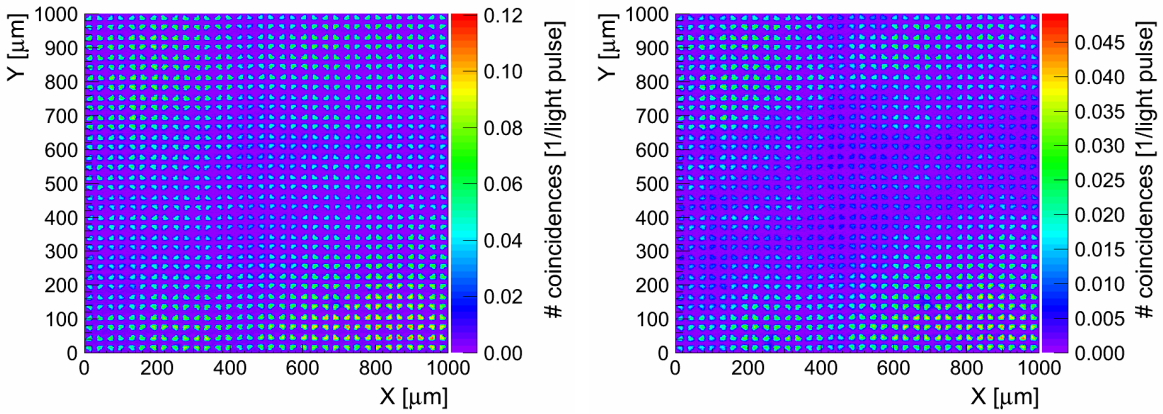

(a) Discrimination level = 0.5 p.e.

(b) Discrimination level = 1.5 p.e.

Figure B.13.: Sensitivity maps of MePhI-32 taken at two different discrimination levels. Over-bias voltage 2 V. Resolution 1 µm, 20 000 red LED pulses shot per step. Noise subtracted.

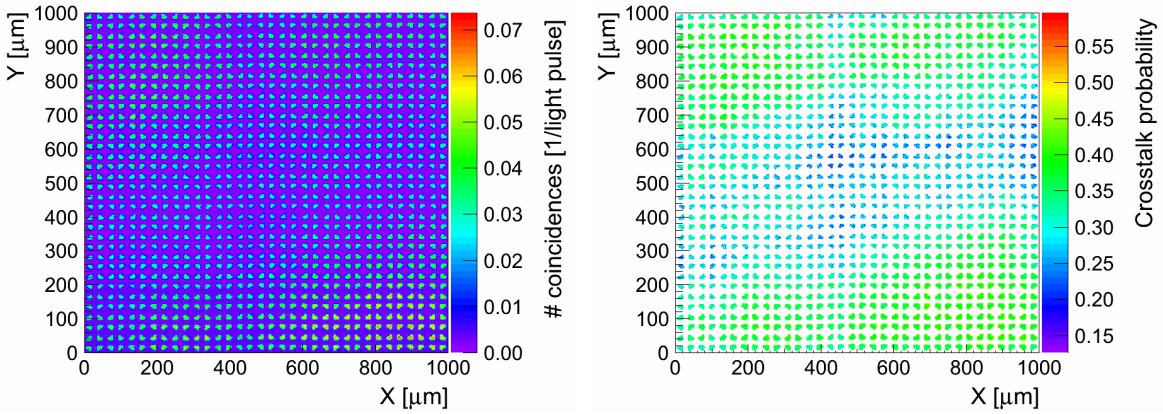

(a) Pure 1 p.e. signal

(b) Crosstalk probability

Figure B.14.: Pure 1 p.e. response and crosstalk probability maps of MePhI-32. Over-bias voltage 2.0 V. Resolution 1 µm, 20 000 red LED pulses shot per step.

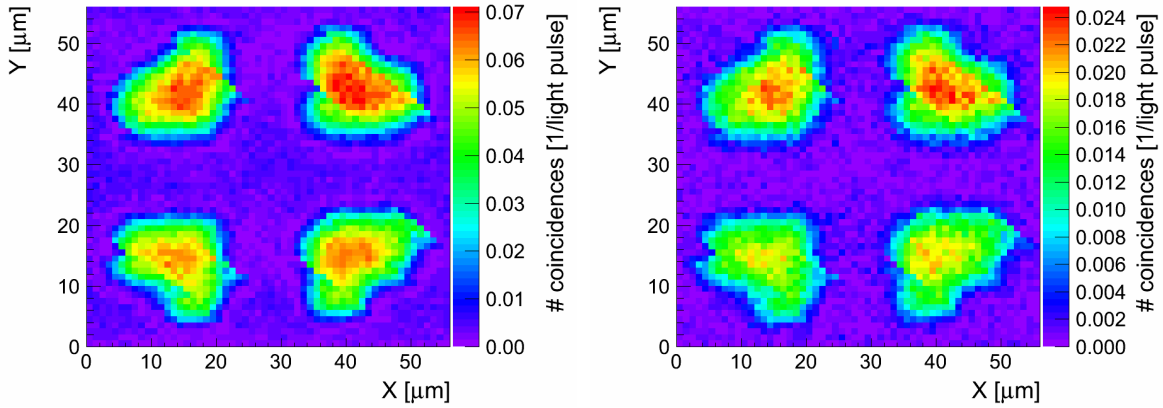

(a) Discrimination level = 0.5 p.e.

(b) Discrimination level = 1.5 p.e.

Figure B.15.: Sensitivity maps of MePhI-32 (detail on four cells taken from the full scan) taken at two different discrimination levels. Over-bias voltage 2 V. Resolution 1 µm, 20 000 red LED pulses shot per step. Noise subtracted.

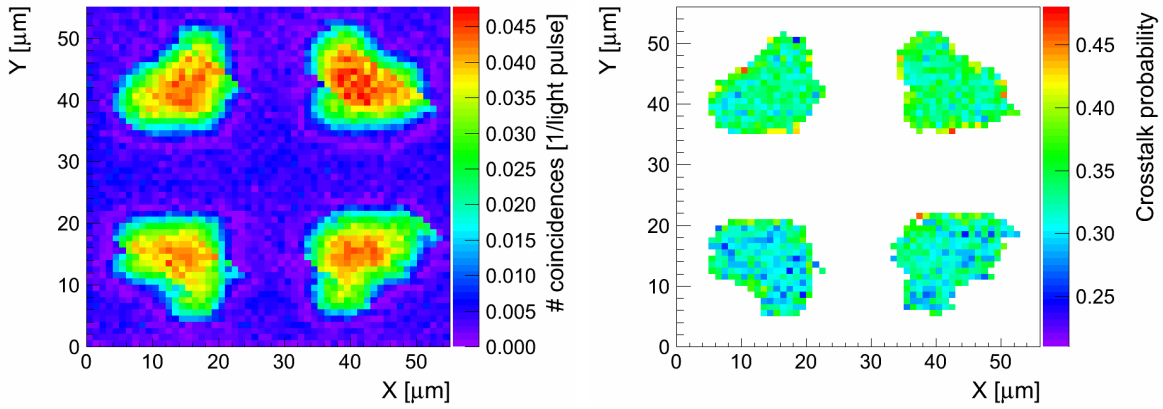

(a) Pure 1 p.e. signal

(b) Crosstalk probability

Figure B.16.: Pure 1 p.e. response and crosstalk probability maps of MePhI-32 (detail on four cells taken from the full scan). Over-bias voltage 2.0 V. Resolution 1 µm, 20 000 red LED pulses shot per step.

SensL

SiPMs manufactured by the SensL company are commercial devices. Two types of them with different pitches were tested. Both detectors evince a surprising active area structure inside of single microcells. The high field region in the pixels is not a continuous area as it was seen by all other investigated devices, but it is divided into $\approx 11\,\mu m$ wide stripes. Furthermore, some pixels in the array are not functional, probably on purpose. However, this fact is not mentioned in the manufacturer's data sheet.

SensL-100

This device evinces the second largest observed inhomogeneity. The MePhI-32 has even worse results, but it was not operated at the most proper over-bias voltage and it could have been also mechanically damaged. In contrast to that, the SensL-100 was completely new and operated at the recommended voltage level. However, the homogeneity level of the SensL-100 is closer to the one of Hamamatsu MPPCs then to MePhI-32. Already in the map recorded with 0.5 p.e. discrimination threshold which is depicted in figure B.17a, it is visible that some pixels have evidently a significantly higher PDE than others. This is even more pronounced in the integrated efficiency and fill factor plot in figure B.27. An interesting thing is the enhanced fill factor in the middle part of the device. One can recognize, that these pixels are actually smeared out in the 0.5 p.e. map. The smearing is caused by some defects in the epoxy protection layer which scatter the incident light. This observation shows that locally increased fill factor can be also a sign of an obstacle in the entrance window.

In the signal distribution plot for this sensor presented in figure B.27d, another peak in the middle of the distribution appeared. This peak reflects a relatively large crossover area between the active stripes within the pixels. This middle peak was not comprised in the fill factor calculation, because it was decided during the fill factor tuning procedure (explained in Sec. 4.3.2) that it does not represent a valid sensitive area.

In the map recorded at 1.5 p.e. and in the crosstalk map which are shown in figures B.17b and B.18b, respectively, can be seen that the right and left edges of the pixels are suffering from extremely high crosstalk probability up to 100 %. A question is, whether this is a real crosstalk or an effect of edge breakdown. The "hot" edges lead to a significant drop in efficiency recalculated to pure 1 p.e. signal as can be seen in figure B.18a.

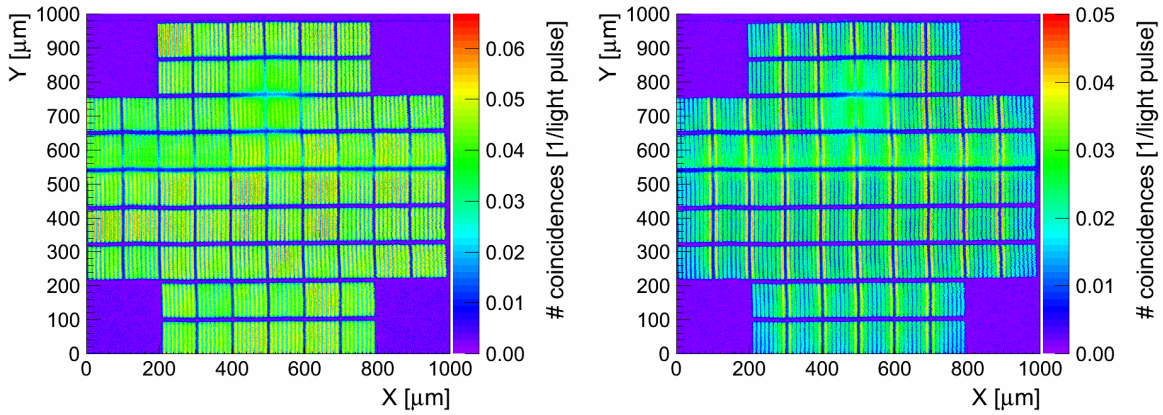

(a) Discrimination level = 0.5 p.e.

(b) Discrimination level = 1.5 p.e.

Figure B.17.: Sensitivity maps of SensL-100 taken at two different discrimination levels. Over-bias voltage 2 V. Resolution 1 µm, 20 000 green LED pulses shot per step. Noise subtracted.

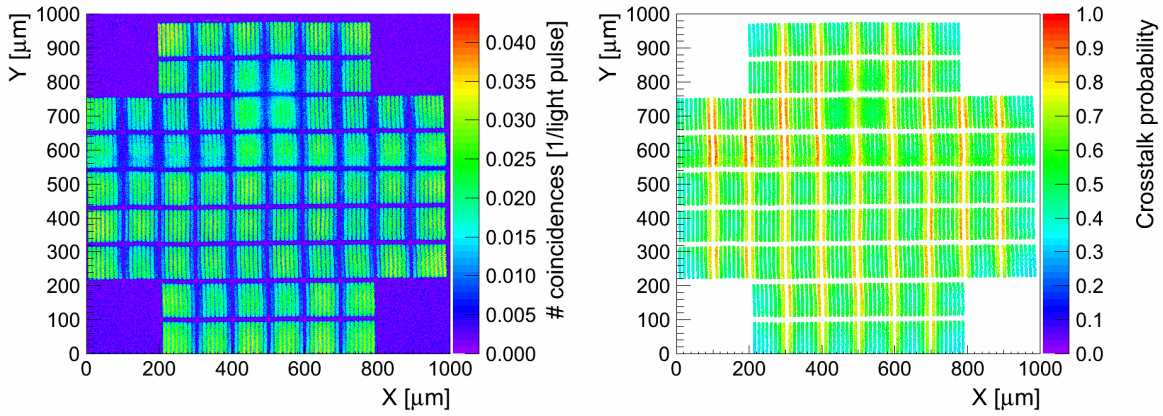

(a) Pure 1 p.e. signal

(b) Crosstalk probability

Figure B.18.: Pure 1 p.e. response and crosstalk probability maps of SensL-100. Over-bias voltage 2 V. Resolution 1 µm, 20 000 green LED pulses shot per step.

SensL-35

Inhomogeneity of the SensL device with 35 μm pixel pitch is slightly better than the inhomogeneity of the SensL-100. In the 0.5 p.e. maps of the SensL-35 detector shown in figures B.19a and B.19b, as well as in the pure 1 p.e. map in figure B.20a and the crosstalk map in figure B.20b it can be seen, that the active stripes at the pixel edges do not suffer from such a high crosstalk probability as those ones of the SensL-100. Further, the outermost active regions of the sensor evince lower crosstalk which is expected.

In the single pixel analysis plots presented in figure B.28, a "hotter" vertical stripe is apparent. It is probably caused by a higher temperature in that particular moment of the measurement (summer noon). This is consistent with the right-to-left measurement direction. There is also a slight sign of horizontal stripes of changing more and less effective regions. These are similar to the stripes in the single pixel maps for Hamamatsu MPPC-25 depicted figure B.21.

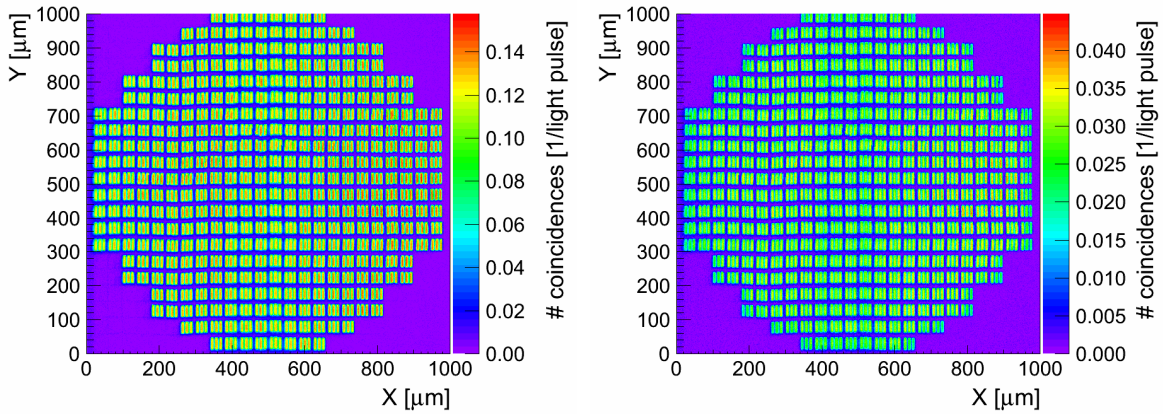

(a) Discrimination level = 0.5 p.e.

(b) Discrimination level = 1.5 p.e.

Figure B.19.: Sensitivity maps of SensL-35 taken at two different discrimination levels. Over-bias voltage 2 V. Resolution 1 µm, 20 000 green LED pulses shot per step. Noise subtracted.

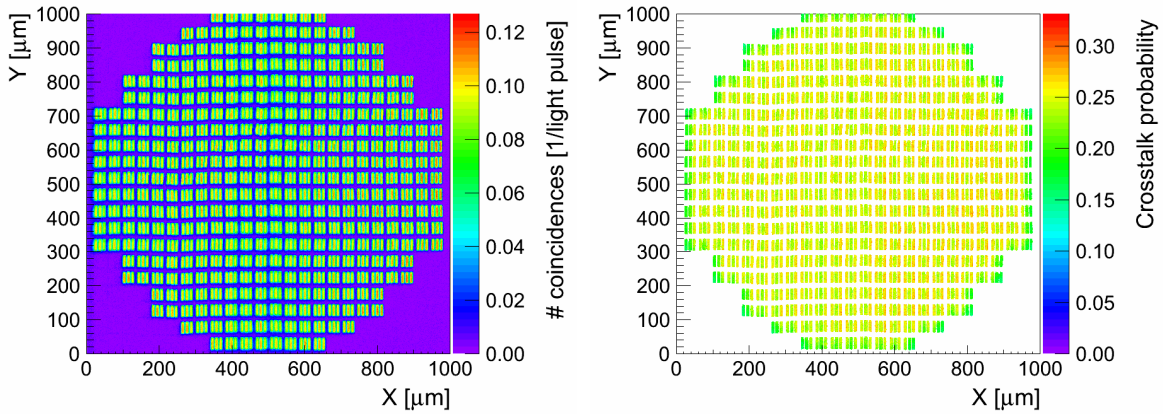

(a) Pure 1 p.e. signal

(b) Crosstalk probability

Figure B.20.: Pure 1 p.e. response and crosstalk probability maps of SensL-35. Over-bias voltage 2 V. Resolution 1 µm, 20 000 green LED pulses shot per step.

B.2. Single Pixel Analysis Plots and Coincidence Distributions

In this section, complete results of individual SiPM pixel analysis are comprised. In all cases, except for the Hamamatsu MPPC-25U, four kinds of plots are shown for every SiPM type or bias voltage: Normalized integrated pixel efficiency map without and with correction for crosstalk, map of fill factor of single pixels and coincidence distribution with marked data above the fill factor cut. This part of the spectrum represents the active area of the SiPM. The fill factor map is not crosstalk corrected. More explanations to these plots can be found in sections 4.3.2 and 4.3.4.

Hamamatsu MPPC-25U

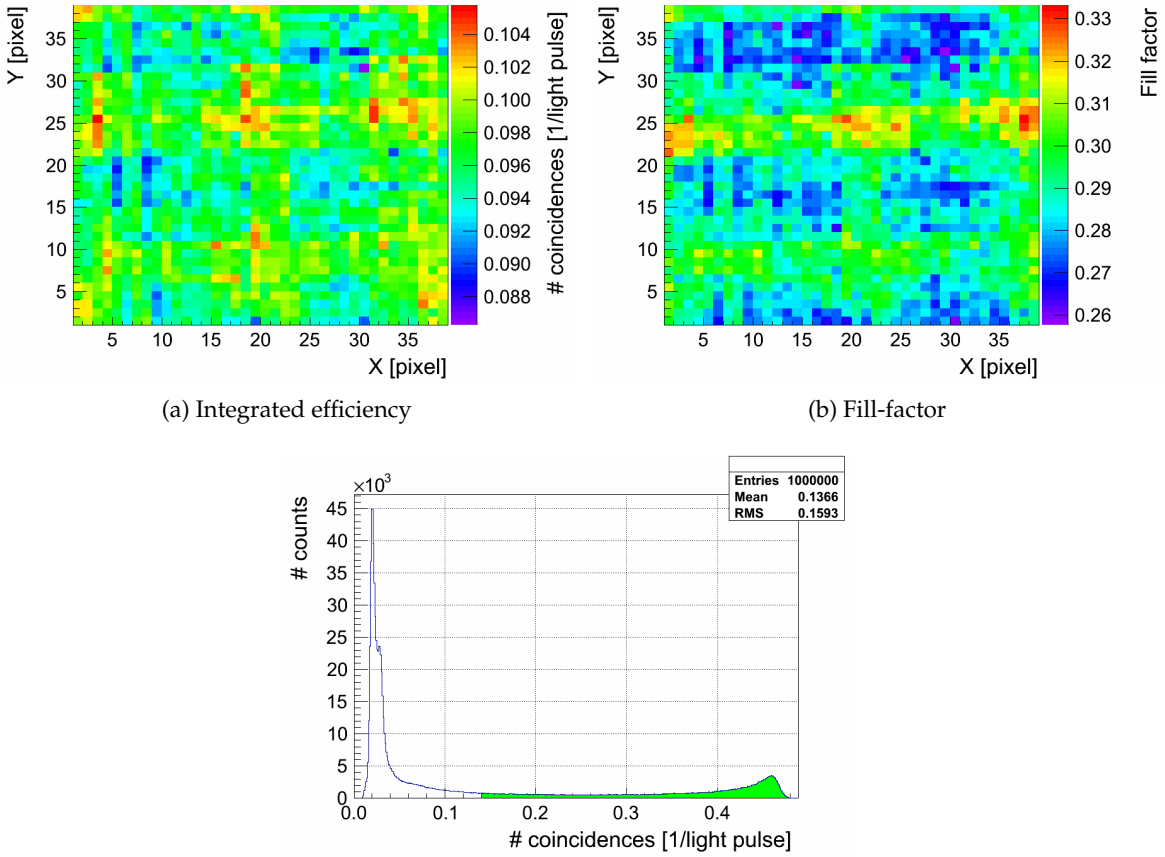

(a) Integrated efficiency

(b) Fill-factor

(c) Count distribution

Figure B.21.: Three output plots from single pixel analysis of Hamamatsu MPPC-25U. The sensor was operated at a voltage recommended by manufacturer (1.5 V overbias). As the data source, the map shown in figure B.1a with restriction depicted in figure B.8a was used.

Hamamatsu MPPC-50

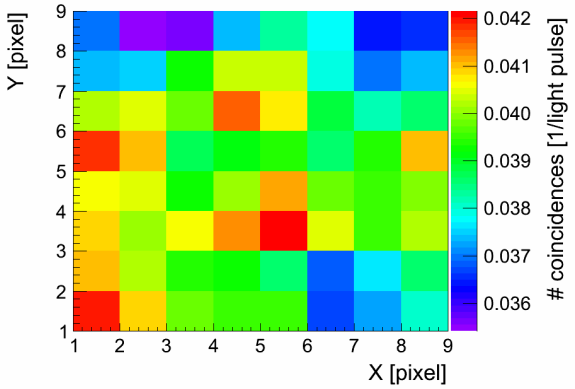

(a) Over-bias voltage = 1.0 V

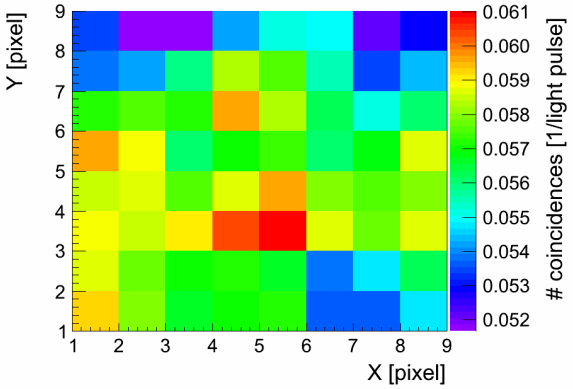

(b) Over-bias voltage = 1.5 V

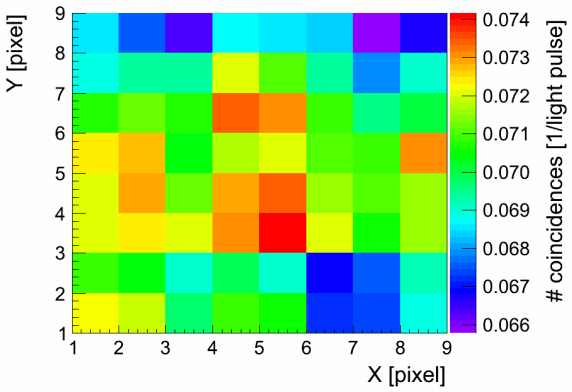

(c) Over-bias voltage = 2.0 V

Figure B.22.: Single pixel sensitivity maps of a part (see figure B.8b) of Hamamatsu MPPC-50. On Z axis is shown a value of the normalized fraction of detected pulses integrated over a particular (physical) pixel. The fill factor cut was applied, it is graphically shown in figure B.25. As the data source, the maps taken at 0.5 p.e. shown in figures B.2a, B.3a and B.4a were used.

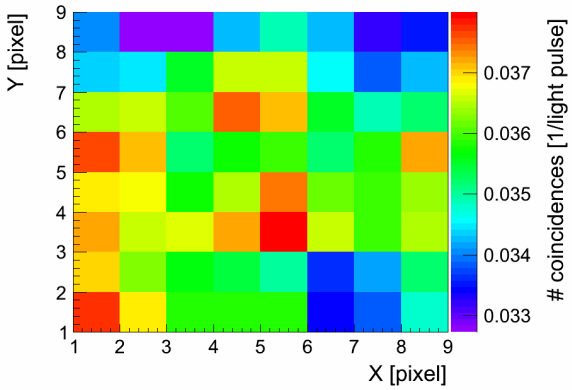

(a) Over-bias voltage = 1.0 V

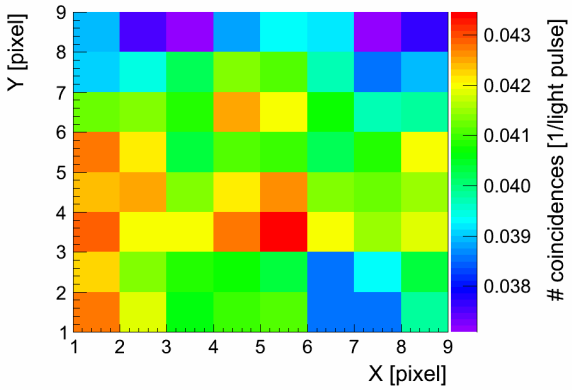

(b) Over-bias voltage = 1.5 V

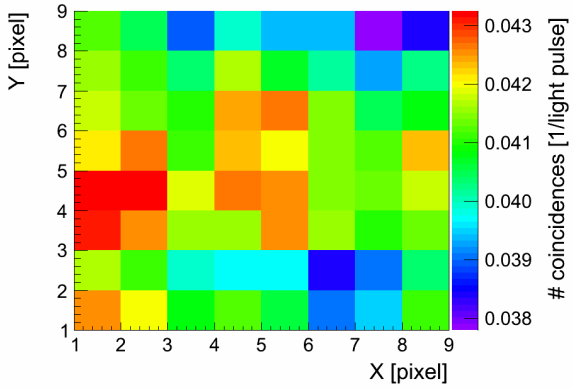

(c) Over-bias voltage = 2.0 V

Figure B.23.: Single pixel sensitivity maps of a part (see figure B.8b) of Hamamatsu MPPC-50 corrected for crosstalk. On the Z axis is shown a value of the normalized fraction of detected pulses integrated over the particular SiPM microcell. As the data source, the maps of pure 1 p.e. signal shown in figures B.5a, B.5a and B.5a were used.

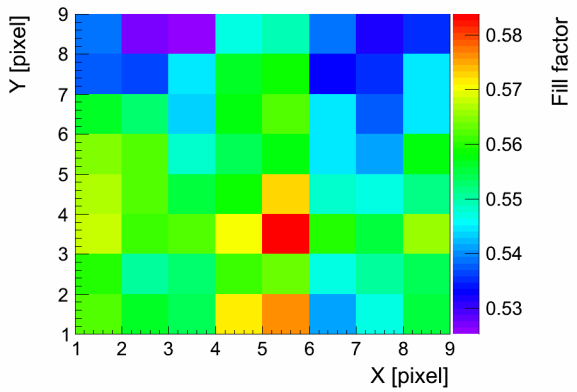

(a) Over-bias voltage = 1.0 V

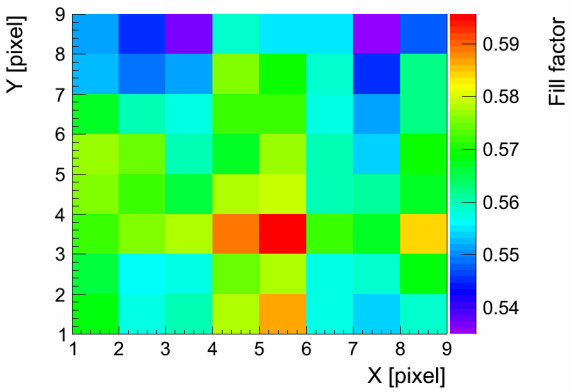

(b) Over-bias voltage = 1.5 V

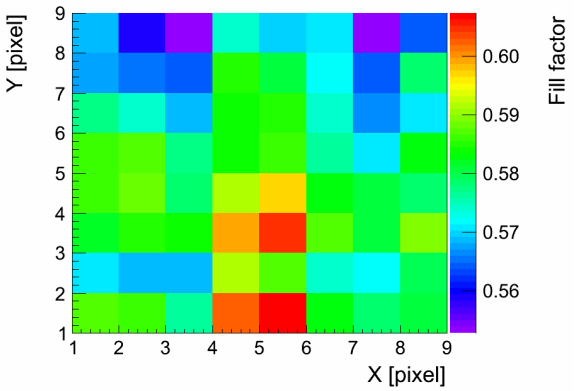

(c) Over-bias voltage = 2.0 V

Figure B.24.: Maps depicting fill factor of individual pixels of a part (see figure B.8b) of Hamamatsu MPPC-50 for different over-bias voltages. On Z axis is shown geometrical fill-factor calculated for each separate SiPM microcell. As the data source, the maps shown in figures B.2a, B.3a and B.4a were used.

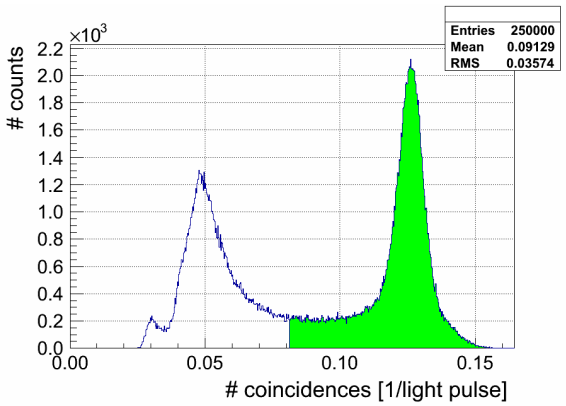

(a) Over-bias voltage = 1.0 V

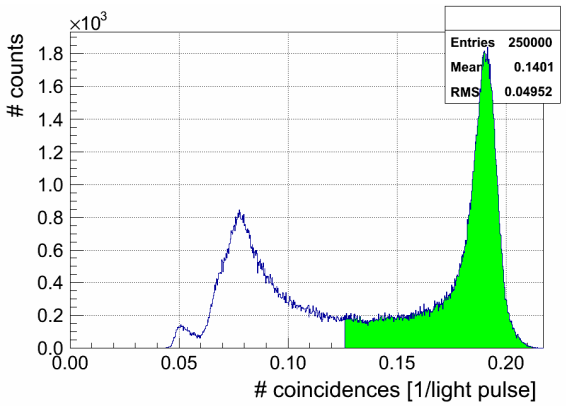

(b) Over-bias voltage = 1.5 V

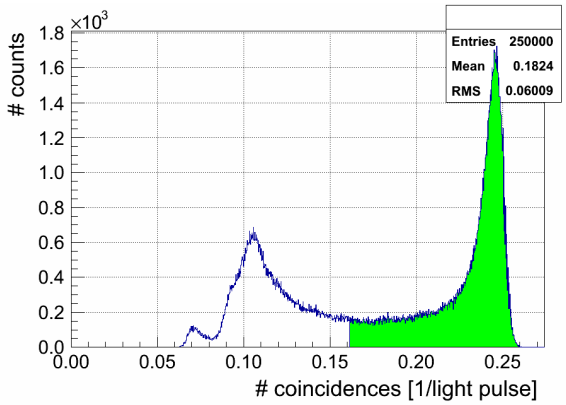

(c) Over-bias voltage = 2.0 V

Figure B.25.: Coincidence distributions obtained from a scan of Hamamatsu MPPC-50 at discrimination level of 0.5 p.e. for different over-bias voltages. The green filling marks data above the fill-factor cut which represent sensitive area of the sensor.

MePhI-32

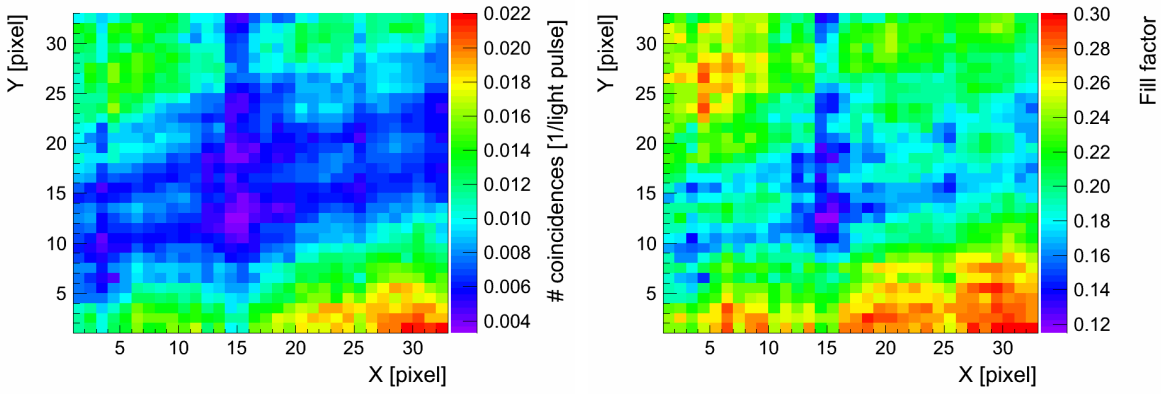

(a) Integrated efficiency

(b) Fill-factor

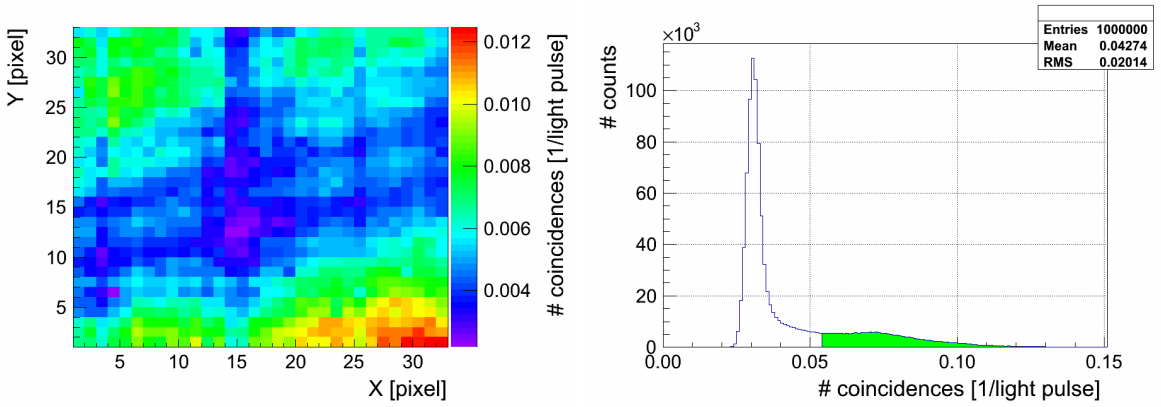

(c) Integrated efficiency, crosstalk corrected

(d) Count distribution

Figure B.26.: Four output plots from single pixel analysis of MePhI-32. As the data source, the maps shown in figures B.13a (**a**) and B.14a (**c**) were used. The outermost pixel were excluded from the analysis. Over-voltage of 2.0 V.

SensL-100

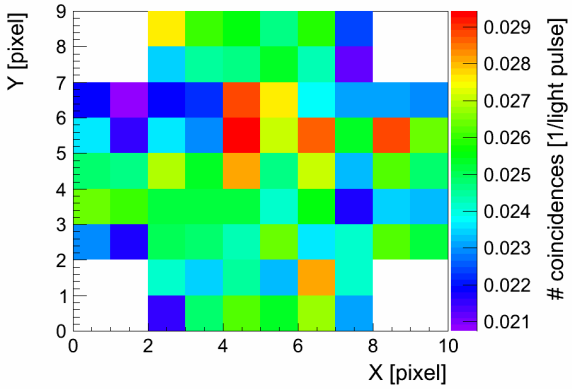

(a) Integrated efficiency

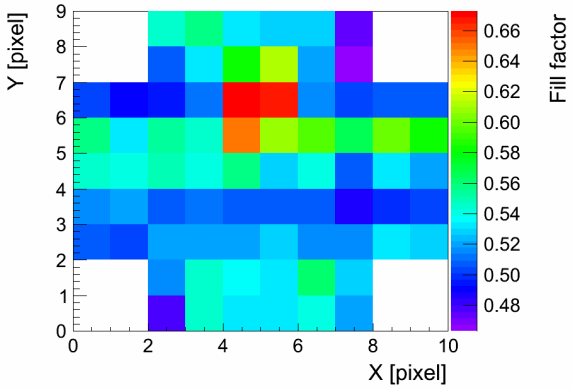

(b) Fill-factor

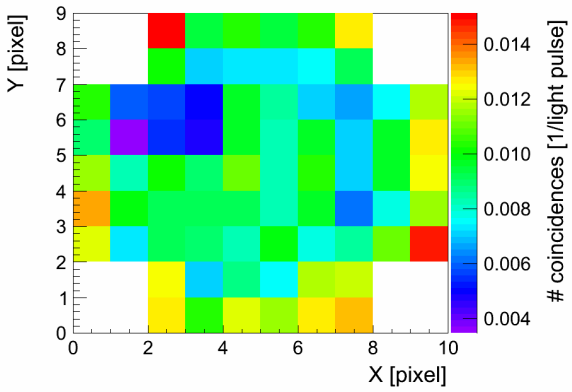

(c) Integrated efficiency, crosstalk corrected

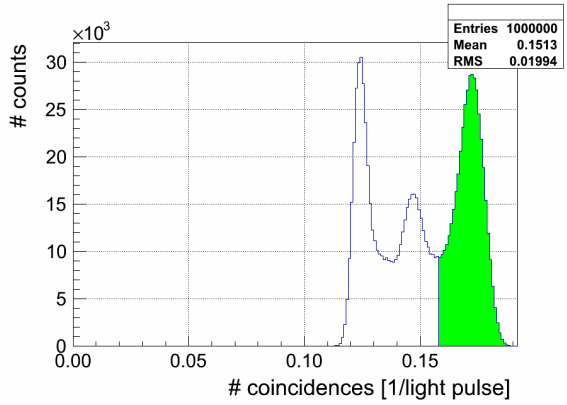

(d) Count distribution

Figure B.27.: Four output plots from single pixel analysis of SensL-100. As the data source, the maps shown in figures B.17a (**a**) and B.18a (**c**) were used. Over-voltage of 2.0 V.

SensL-35

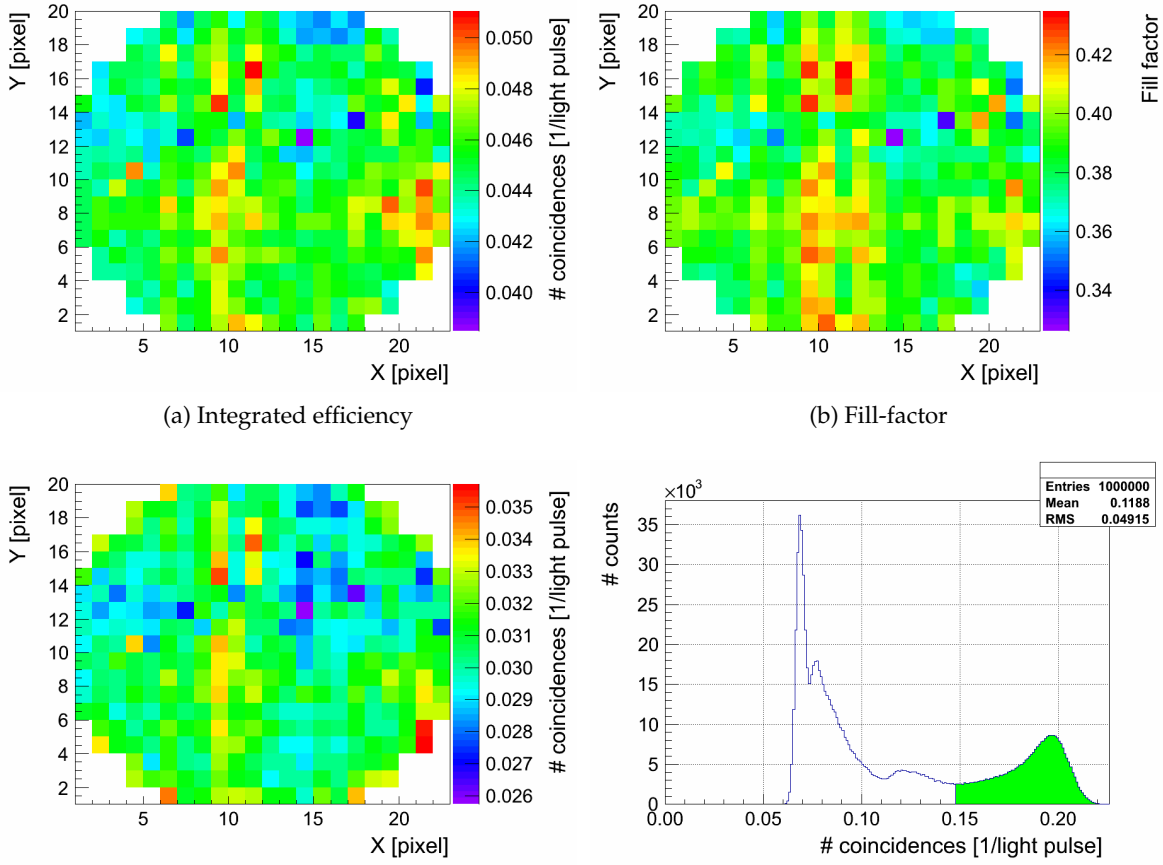

(a) Integrated efficiency

(b) Fill-factor

(c) Integrated efficiency, crosstalk corrected

(d) Count distribution

Figure B.28.: Four output plots from single pixel analysis of SensL-35. The measurement ran exceptionally from the right to the left in this case. As the data source, the maps shown in figures B.19a (**a**) and B.20a (**c**) were used. The outermost pixel are excluded from the analysis. Over-voltage of 2.0 V (recommended by the manufacturer). The "hotter" vertical stripe in the middle of the array is probably caused by higher temperature in that particular moment of the measurement (summer noon).

B.3. Photo-Emission Images Overlaid with SiPM Photographs

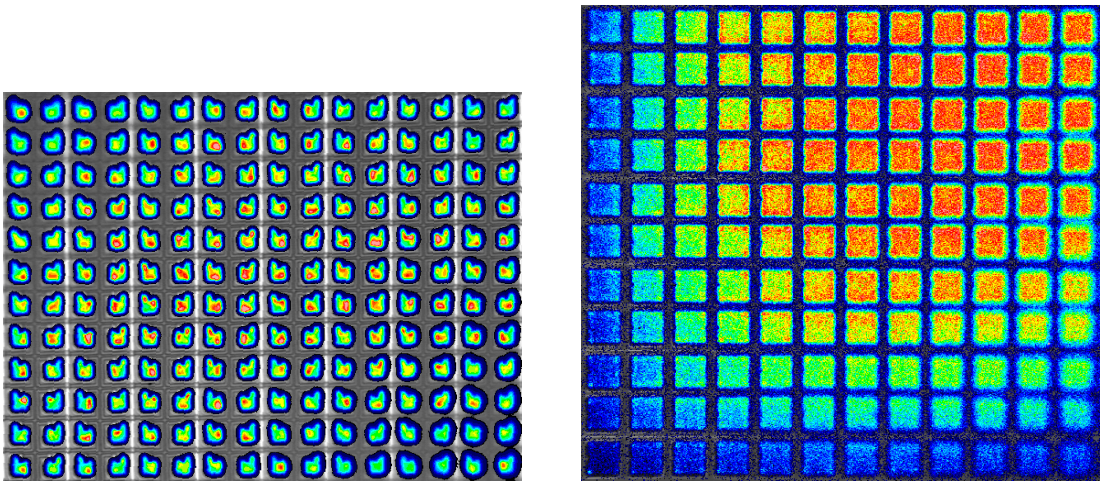

(a) MPPC-25 (b) MPPC-50

Figure B.29.: Photo-emission image of Hamamtsu MPPC-25 (**a**) and MPPC-50 (**b**). Some parts of the chip are not in focus and therefore blurred. Scale of the pictures is not the same.

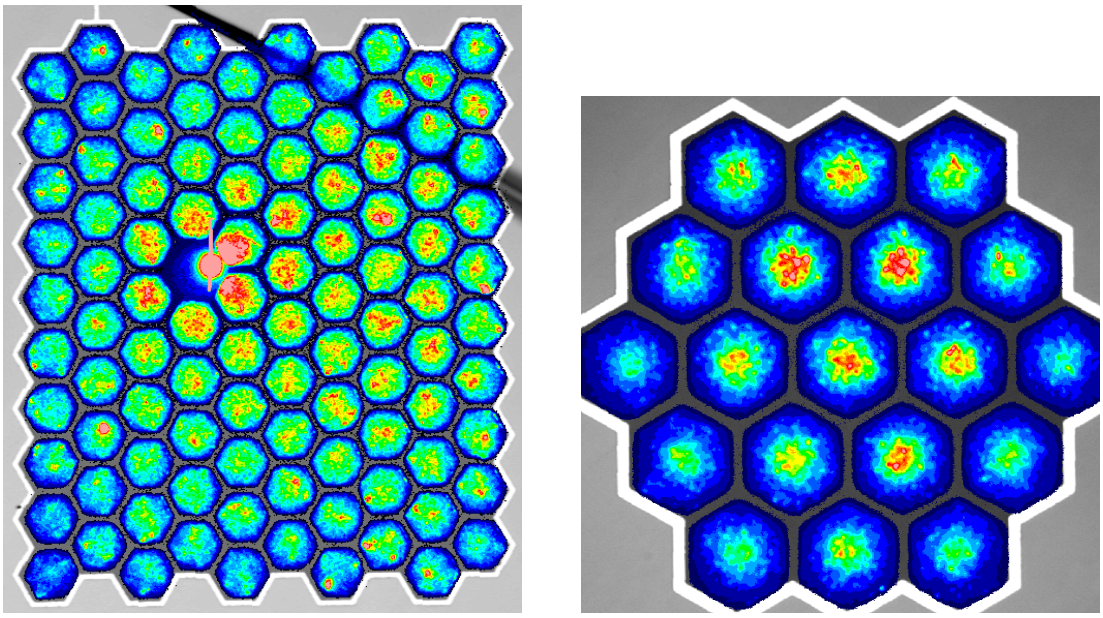

(a) SiMPl P15 (b) SiMPl P13

Figure B.30.: Photo-emission image of SiMPl P15 (**a**) and P13 (**b**). Scale of the pictures is not the same.

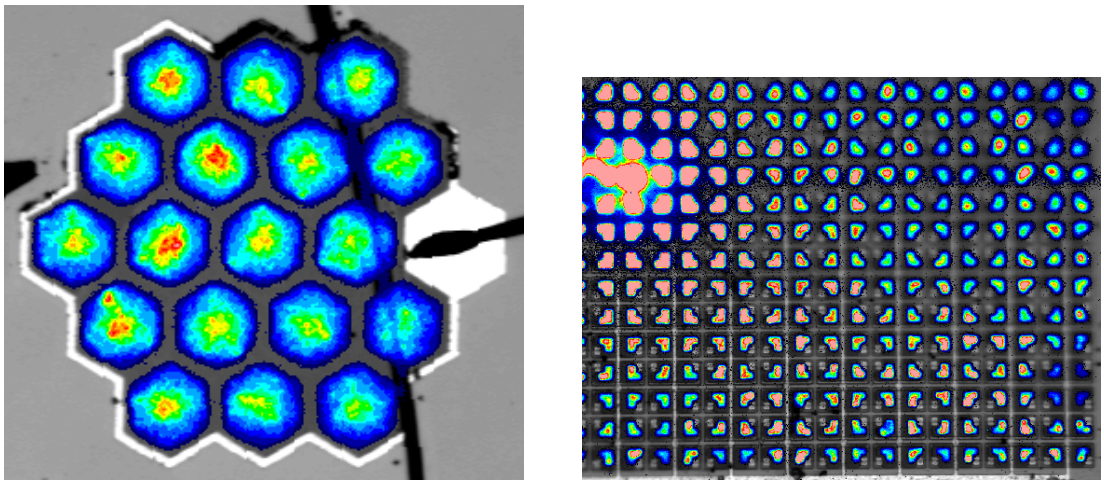

(a) SiMPl O17 (b) MePhI-32

Figure B.31.: Photo-emission image of SiMPl O17 (**a**) and MePhI-32 (**b**). Scale of the pictures is not the same.

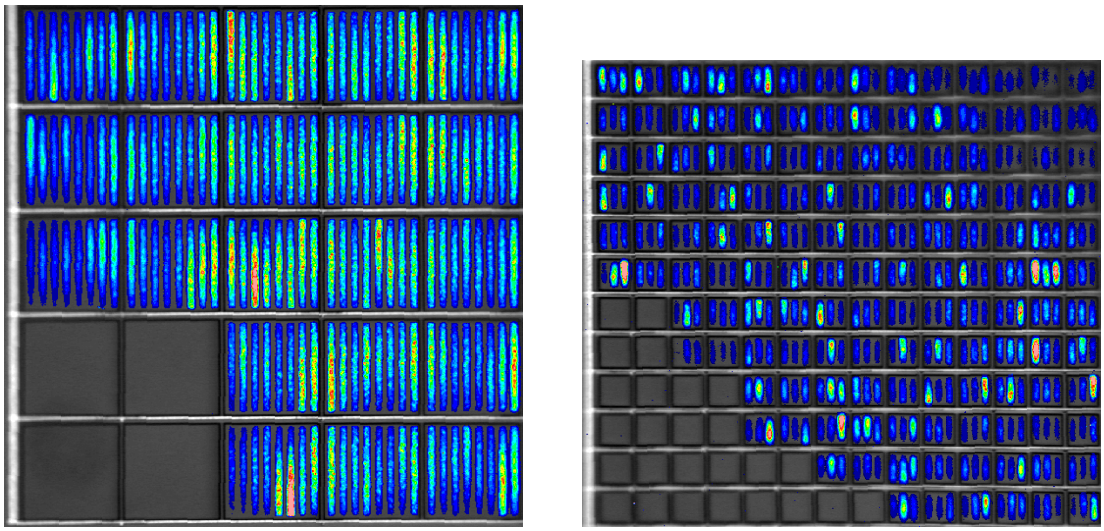

(a) SensL-100 (b) SensL-35

Figure B.32.: Photo-emission image of SensL-100 (**a**) and SensL-35 (**b**). Scale of the pictures is not the same.

B.4. Photographs of SiPM

Hamamatsu MPPCs with Plastic Casing

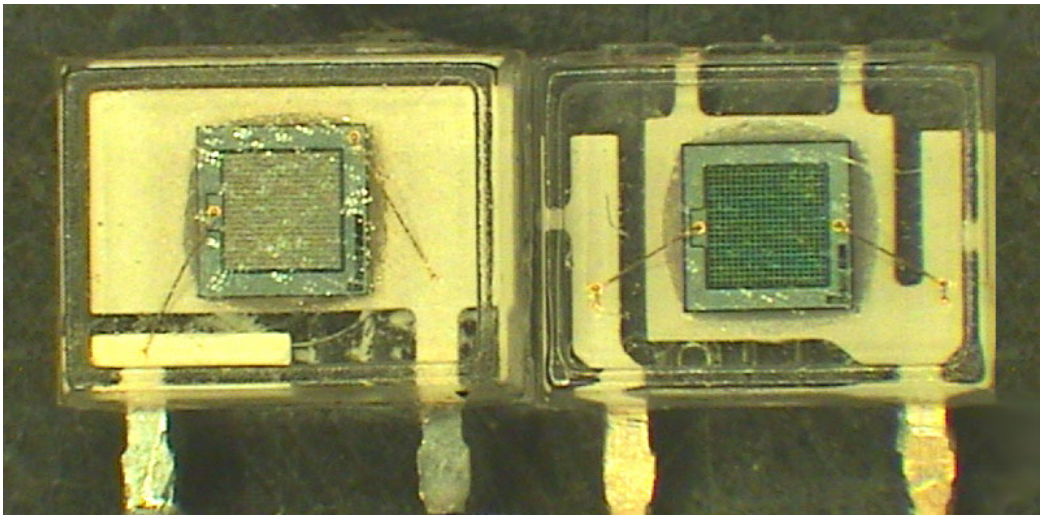

Figure B.33.: Hamamatsu MPPCs with transparent plastic casing. **Left:** MPPC-25, **right:** MPPC-50

.

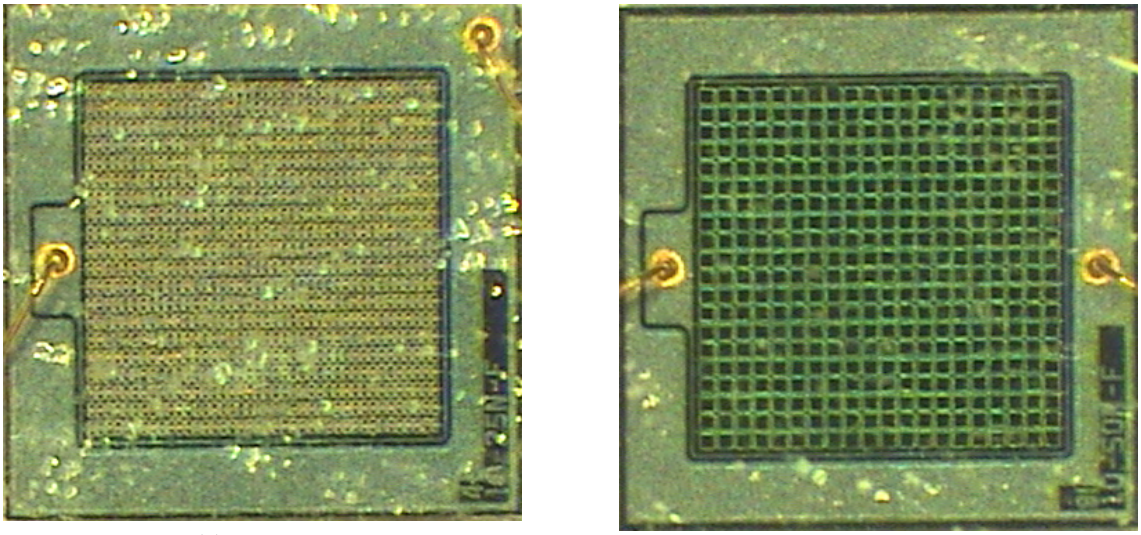

(a) MPPC-25

(b) MPPC-50

Figure B.34.: Detailed comparison of plastic casing transparency of Hamamatsu MPPC-25 (**a**) and MPPC-50 (**b**). (The camera was focused on the entrance window.)

Photographs of Tested SiPMs

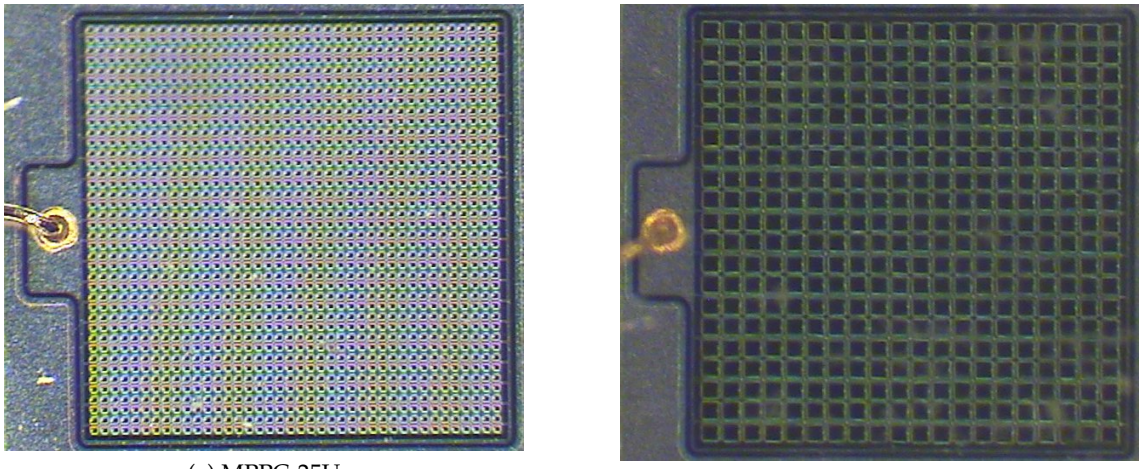

(a) MPPC-25U (b) MPPC-50

Figure B.35.: Photograph of surface of two Hamamatsu MPPCs with 25 (**a**) and 50 μm pixel pitch (**b**).

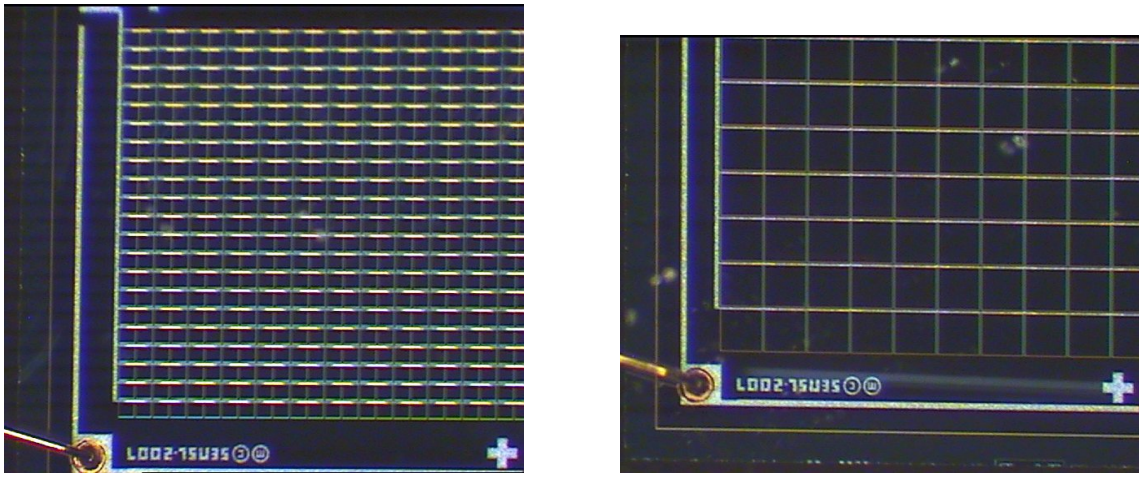

(a) SensL-35 (b) SensL-100

Figure B.36.: Photograph of surface of SensL-35 (**a**) and SensL-100 (**b**).

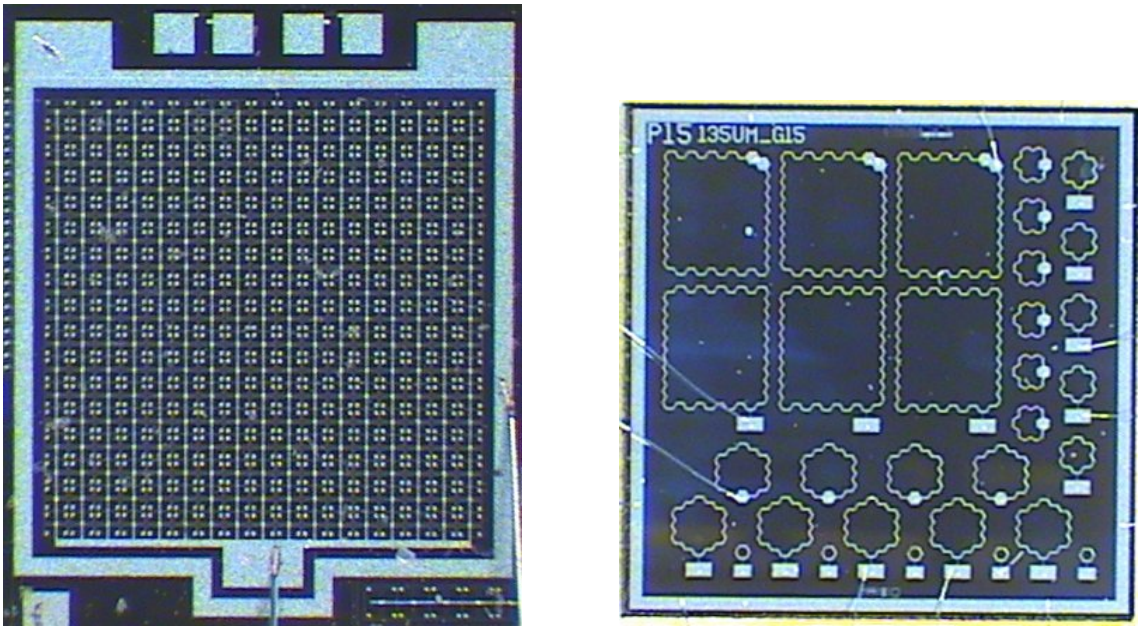

(a) MePhI-32 (b) SiMPl P15 wafer

Figure B.37.: Photograph of surface of a MePhI-32 photomultiplier (**a**) and a P15 wafer carrying various SiMPl prototypes (**b**).

APPENDIX C

TOP QUARK MASS MEASUREMENT SUMMARY

C.1. Two-Dimensional Template Fit Contour Plots

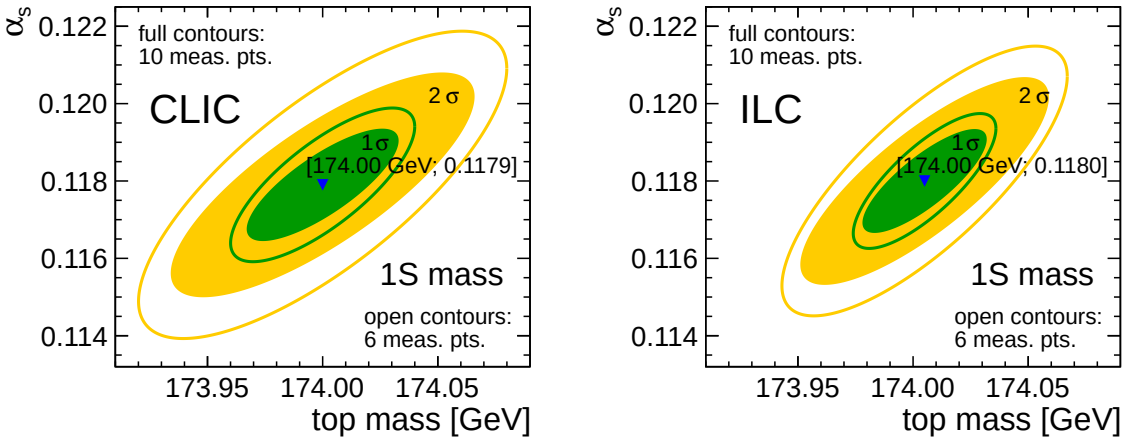

(a) CLIC

(b) ILC

Figure C.1.: Comparison of one and two sigma correlation contours of the top 1*S* mass m_t and the strong coupling constant α_s when ten and six simulated cross section points are used in a simultaneous 2D fit. The graphs are presented for CLIC (**a**) and the ILC (**b**).

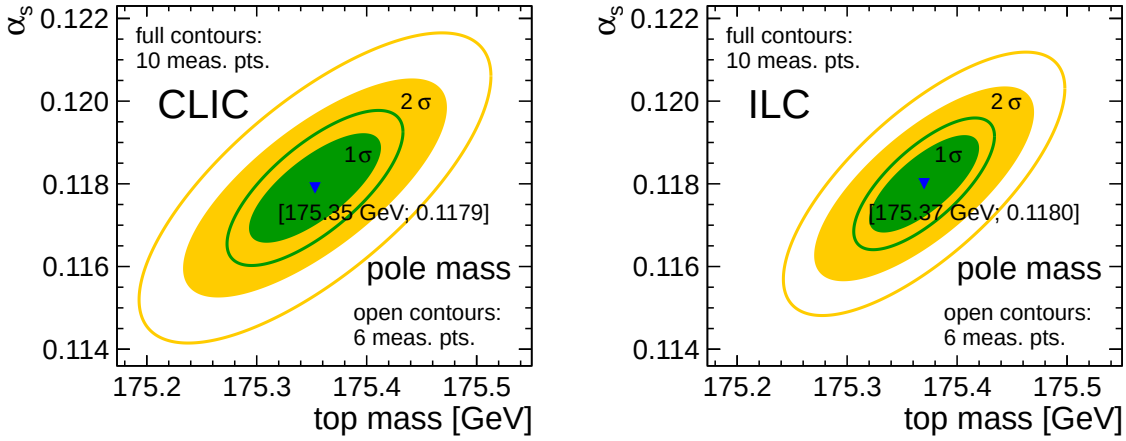

(a) CLIC

(b) ILC

Figure C.2.: Comparison of one and two sigma correlation contours of the top pole mass m_t and the strong coupling constant α_s when ten and six simulated cross section points are used in a simultaneous 2D fit. The graphs are presented for CLIC (**a**) and the ILC (**b**).

C.2. Complete Result Summary of One-Dimensional Template Fit

1D top mass m_t fit, α_s fixed, 1S mass scheme

accelerator	**number of scan points**	**fit result** $m_t^{(1S)}$	**stat. error**	**theor. sys. err.** **± 1% / ± 3%**		**backgnd. sys. err.** **± 5% / ± 10%**		α_S**-induced sys. err.**	**fit stability**
unit		[GeV]	[MeV]						[%]
CLIC	10	174.003	± 21	± 18	$^{+55}_{-56}$	$^{+37}_{-38}$	$^{+75}_{-76}$	$^{+22}_{-20}$	100
	6	174.004	± 21	$^{+15}_{-16}$	$^{+46}_{-48}$	$^{+35}_{-36}$	$^{+70}_{-71}$	$^{+20}_{-19}$	100
ILC	10	174.007	± 18	± 15	$^{+46}_{-47}$	± 31	± 62	± 18	100
	6	174.007	± 18	± 13	$^{+38}_{-39}$	$^{+28}_{-29}$	± 57	$^{+16}_{-17}$	100

Table C.1.: Result summary of one-dimensional fit of the top mass obtained from the threshold scan at CLIC and ILC, using 1S mass scheme. The systematic uncertainty originating from α_s is induced by the current world average error of 0.0007. Simulation input values: $m_t^{(1S)} = 174.000\,\text{GeV}$, $\alpha_s = 0.1180$.

1D top mass m_t fit, α_s fixed, pole mass scheme

accelerator	**number of scan points**	**fit result** $m_t^{(pole)}$	**stat. error**	**theor. sys. err.** **± 1% / ± 3%**		**backgnd. sys. err.** **± 5% / ± 10%**		α_S**-induced sys. err.**	**fit stability**
unit		[GeV]	[MeV]						[%]
CLIC	10	175.361	± 21	$^{+18}_{-19}$	$^{+56}_{-57}$	$^{+38}_{-39}$	$^{+77}_{-78}$	± 44	100
	6	175.361	± 21	$^{+15}_{-16}$	$^{+46}_{-48}$	$^{+35}_{-36}$	$^{+71}_{-72}$	$^{+41}_{-43}$	100
ILC	10	175.364	± 18	$^{+16}_{-15}$	± 47	$^{+32}_{-31}$	± 63	± 41	100
	6	175.364	± 19	± 13	± 39	± 29	± 58	± 40	100

Table C.2.: Result summary of one-dimensional fit of the top mass obtained from the threshold scan at CLIC and ILC, using pole mass scheme. The systematic uncertainty originating from α_s is induced by the current world average error of 0.0007. Simulation input values: $m_t^{(1S)} = 174.000\,\text{GeV}$, $\alpha_s = 0.1180$.

C.3. Complete Result Summary of Two-Dimensional m_t and α_S Template Fit

2D combined fit of top mass and strong coupling constant: top mass m_t, 1S mass scheme

accelerator	**number of scan points**	**fit result $m_t^{(1S)}$**	**stat. error**	**theor. sys. err. ± 1% / ± 3%**		**backgnd. sys. err. ± 5% / ± 10%**		**fit stability**
unit		[GeV]	[MeV]					[%]
CLIC	10	174.000	± 33	$^{-7}_{+6}$	$^{-14}_{-2}$	± 16	$^{+32}_{-34}$	$100/^{100/88/100/99}_{100/100/100/100}$
	6	174.000	± 40	∓ 1	$^{+3}_{-2}$	± 24	± 48	$99/^{99/88/99/98}_{97/86/96/93}$
ILC	10	174.005	± 27	$^{-6}_{+5}$	$^{-13}_{-3}$	$^{+10}_{-11}$	$^{+22}_{-26}$	$100/^{100/93/100/100}_{100/100/100/100}$
	6	174.005	± 31	$^{-1}_{+2}$	± 0	± 16	$^{+31}_{-32}$	$100/^{100/95/100/99}_{98/98/96/100}$

Table C.3.: Top 1S mass $m_t^{(1S)}$ result summary of two-dimensional fit. It was obtained from the threshold scan at CLIC and ILC. Simulation input values: $m_t^{(1S)} = 174.000\,\text{GeV}$, $\alpha_s = 0.1180$.

2D combined fit of top mass and strong coupling constant: strong coupling constant α_s, 1S mass scheme

accelerator	**number of scan points**	**fit result α_S**	**stat. error**	**theor. sys. err. ± 1% / ± 3%**		**backgnd. sys. err. ± 5% / ± 10%**		**fit stability [%]**
CLIC	10	0.1179	± 0.0009	$^{-0.0009}_{+0.0008}$	$^{-0.0025}_{+0.0019}$	$^{-0.0008}_{+0.0007}$	∓ 0.0015	$100/\,^{100/88/100/99}_{100/100/100/100}$
	6	0.1179	± 0.0013	$^{-0.0006}_{+0.0007}$	∓ 0.0020	$^{-0.0004}_{+0.0005}$	∓ 0.0009	$99/\,^{99/88/99/98}_{97/86/96/93}$
ILC	10	0.1180	± 0.0008	∓ 0.0008	$^{-0.0024}_{+0.0017}$	$^{-0.0008}_{+0.0007}$	$^{-0.0015}_{+0.0014}$	$100/\,^{100/93/100/100}_{100/100/100/100}$
	6	0.1180	± 0.0011	∓ 0.0006	∓ 0.0018	$^{-0.0005}_{+0.0006}$	∓ 0.0011	$100/\,^{100/95/100/99}_{98/98/96/100}$

Table C.4.: Strong coupling constant α_s result summary of two-dimensional fit (top 1S mass scheme used). It was obtained from the threshold scan at CLIC and ILC. Simulation input values: $m_t^{(1S)} = 174.000\,\text{GeV}$, $\alpha_s = 0.1180$.

2D combined fit of top mass and strong coupling constant: top mass m_t, pole mass scheme

accelerator	**number of scan points**	**fit result** $m_t^{(pole)}$	**stat. error**	**theor. sys. err.** $\pm 1\%$ / $\pm 3\%$		**backgnd. sys. err.** $\pm 5\%$ / $\pm 10\%$		**fit stability**
unit		[GeV]	[MeV]					[%]
CLIC	10	175.353	± 60	$^{-28}_{+36}$	$^{-41}_{+63}$	$^{-12}_{+22}$	$^{-12}_{+30}$	$100/^{100/100/95/99}_{100/100/92/90}$
	6	175.358	± 80	$^{-19}_{+20}$	$^{-47}_{+54}$	$^{+16}_{-11}$	$^{+24}_{-16}$	$99/^{98/91/93/99}_{97/82/93/84}$
ILC	10	175.366	± 50	$^{-33}_{+35}$	$^{-53}_{+54}$	$^{-12}_{+22}$	$^{-23}_{+27}$	$100/^{100/100/100/99}_{100/100/94/98}$
	6	175.370	± 64	$^{-21}_{+20}$	∓ 54	∓ 1	$^{-1}_{+5}$	$100/^{100/97/100/10}_{99/91/99/94}$

Table C.5.: Top pole mass $m_t^{(pole)}$ result summary of two-dimensional fit. It was obtained from the threshold scan at CLIC and ILC. Simulation input values: $m_t^{(1S)} = 174.000\,\text{GeV}$, $\alpha_s = 0.1180$.

2D combined fit of top mass and strong coupling constant: strong coupling constant α_s, pole mass scheme

accelerator	number of scan points	fit result α_S	stat. error	theor. sys. err. ±1% / ±3%		backgnd. sys. err. ±5% / ±10%		fit stability [%]
CLIC	10	0.1179	±0.0009	$^{-0.0007}_{+0.0009}$	$^{-0.0017}_{+0.0019}$	$^{-0.0008}_{+0.0010}$	$^{-0.0015}_{+0.0018}$	$100/^{100/100/95/99}_{100/100/92/90}$
	6	0.1180	±0.0014	$^{-0.0007}_{+0.0006}$	$^{-0.0018}_{+0.0020}$	∓0.0004	$^{-0.0008}_{+0.0010}$	$99/^{98/91/93/99}_{97/82/93/84}$
ILC	10	0.1181	±0.0008	$^{-0.0007}_{+0.0008}$	$^{-0.0018}_{+0.0017}$	$^{-0.0007}_{+0.0010}$	∓0.0015	$100/^{100/100/100/99}_{100/100/94/98}$
	6	0.1181	±0.0011	$^{-0.0006}_{+0.0007}$	$^{-0.0017}_{+0.0019}$	$^{-0.0005}_{+0.0006}$	$^{-0.0010}_{+0.0013}$	$100/^{100/97/100/10}_{99/91/99/94}$

Table C.6.: Strong coupling constant α_s result summary of two-dimensional fit (top pole mass scheme used). It was obtained from the threshold scan at CLIC and ILC. Simulation input values: $m_t^{(1S)} = 174.000\,\text{GeV}$, $\alpha_s = 0.1180$.

BIBLIOGRAPHY

[1] K. Seidel et al. Top quark mass measurements at and above threshold at CLIC. *Eur. Phys. J.*, C73:2530, 2013.

[2] M. Tesař et al. Study of detection efficiency distribution and areal homogeneity of SiPMs. *PoS*, PhotoDet 2012:063, 2012.

[3] G. Aad et al. Expected Performance of the ATLAS Experiment - Detector, Trigger and Physics. arXiv: 0901.0512 [hep-ex], 2009.

[4] G.L. Bayatian et al. CMS physics: Technical design report. CERN-LHCC-2006-001, 2006.

[5] G. Aad et al. Observation of a new particle in the search for the Standard Model Higgs boson with the ATLAS detector at the LHC. *Phys. Lett.*, B716:1–29, 2012.

[6] S. Chatrchyan et al. Observation of a new boson at a mass of 125 GeV with the CMS experiment at the LHC. *Phys. Lett.*, B716:30–61, 2012.

[7] R. L. Mills. Gauge fields. *Am. J. Phys.*, 57(6):493–507, 1989.

[8] C.-N. Yang and R. L. Mills. Conservation of Isotopic Spin and Isotopic Gauge Invariance. *Phys. Rev.*, 96:191–195, 1954.

[9] H. Georgi. *Lie Algebras in Particle Physics, Second Edition*. Westview Press, 1999.

[10] J. Chýla. Quarks, partons and Quantum Chromodynamics, 2009. `http://www-hep2.fzu.cz/~chyla/lectures/text.pdf`.

[11] D. Griffiths. *Intrododuction in Elementary Particles, Second, Revised Edition*. WILEY-VCH Verlag, 2008.

[12] P. W. Higgs. Spontaneous Symmetry Breakdown without Massless Bosons. *Phys. Rev.*, 145:1156–1163, May 1966.

[13] F. Englert and R. Brout. Broken Symmetry and the Mass of Gauge Vector Mesons. *Phys. Rev. Lett.*, 13:321–323, August 1964.

[14] P. W. Higgs. Broken Symmetries and the Masses of Gauge Bosons. *Phys. Rev. Lett.*, 13:508–509, October 1964.

[15] G. S. Guralnik et al. Global Conservation Laws and Massless Particles. *Phys. Rev. Lett.*, 13:585–587, November 1964.

[16] T. Teubner. The Standard Model, 2008. `http://hepwww.rl.ac.uk/hepsummerschool/Teubner-%20Standard%20Model%202008.pdf`.

[17] S. Paßehr. Countertermbeiträge zum anomalen magnetischen Moment des Myons im minimalen supersymmetrischen Standardmodell. Master's thesis, Technische Universität Dresden, 2010.

[18] L. Weuste. *Time Measurement of Hadronic Showers and Mass Measurement of Right-Handed Scalar Quarks for the Compact Linear Collider*. PhD thesis, Ludwig-Maximilians-Universität München, 2013.

[19] A. H. Broeils. The mass distribution of the dwarf spiral NGC 1560. *Astron. Astrophys.*, 256:19, 1992.

[20] M. Peskin. High-energy physics: The matter with antimatter. *Nature*, 419:24, 2002.

[21] B. T. Cleveland et al. Measurement of the Solar Electron Neutrino Flux with the Homestake Chlorine Detector. *Astrophys. J.*, 496(1):505, 1998.

[22] Y. Fukuda et al. Measurements of the solar neutrino flux from Super-Kamiokande's first 300 days. *Phys. Rev. Lett.*, 81:1158–1162, 1998.

[23] S. P. Martin. A Supersymmetry primer. arXiv: 9709356 [hep-ph], 1997.

[24] V.A. Rubakov. Large and infinite extra dimensions: An Introduction. *Phys. Usp.*, 44:871–893, 2001.

[25] M. B. Green et al. *Superstring Theory. Vol. 1: Introduction. Vol. 2: Loop Amplitudes, Anomalies & Phenomenology*. WILEY-VCH Verlag, 1988.

[26] M. Kobayashi and T. Maskawa. CP Violation in the Renormalizable Theory of Weak Interaction. *Prog. Theor. Phys.*, 49:652–657, 1973.

[27] F. Abe et al. Observation of Top Quark Production in $\overline{p}p$ Collisions with the Collider Detector at Fermilab. *Phys. Rev. Lett.*, 74:2626–2631, Apr 1995.

[28] S. Abachi et al. Search for High Mass Top Quark Production in $p\overline{p}$ Collisions at $\sqrt{s}$ = 1.8 TeV. *Phys. Rev. Lett.*, 74:2422–2426, Mar 1995.

[29] G. Isidori et al. On the metastability of the standard model vacuum. *Nucl. Phys.*, B609:387–409, 2001.

[30] G. Degrassi et al. Higgs mass and vacuum stability in the Standard Model at NNLO. *JHEP*, 1208:098, 2012.

[31] T. A. Aaltonen et al. A Direct Measurement of the Total Decay Width of the Top Quark. *Phys. Rev. Lett.*, 2013.

[32] S. Willenbrock. The Standard model and the top quark. arXiv: 0211067 [hep-ph], 2002.

[33] J. Beringer et al. Review of Particle Physics. *Phys. Rev. D*, 86:010001, 2012.

[34] F. Olness and R. Scalise. Regularization, Renormalization, and Dimensional Analysis: Dimensional Regularization meets Freshman E&M. *Am. J. Phys.*, 79:306, 2011.

[35] A. H. Hoang and T. Teubner. Top-quark pair production close to threshold: Top-quark mass, width, and momentum distribution. *Phys. Rev. D*, 60:114027, Nov 1999.

[36] R. Plačakyté. Parton Distribution Functions. arXiv:1111.5452 [hep-ph], 2011.

[37] The International Linear Collider, Technical Design Report, 2013. `http://www.linearcollider.org/ILC/Publications/Technical-Design-Report`.

[38] Muon Collider at Fermilab. 2013. `http://www.fnal.gov/pub/muon_collider`.

[39] Muon Ionization Cooling Experiment. 2013. `http://mice.iit.edu`.

[40] I. Štoll and J. Tolar. *Teoretická fyzika*. Vydavatelství ČVUT, 2004.

[41] A. Caldwell et al. Proton-driven plasma-wakefield acceleration. *Nature Physics*, 5:363–367, 2009.

[42] G. Weiglein et al. Physics interplay of the LHC and the ILC. *Physics Reports*, 426:47–358, 2006.

[43] J. E. Brau et al. The Physics Case for an e^+e^- Linear Collider. arXiv: 1210.0202 [hep-ex], 2012.

[44] L. Linssen et al. Physics and Detectors at CLIC: CLIC Conceptual Design Report. arXiv: 1202.5940 [physics.ins-det], 2012.

[45] P. Lebrun et al. The CLIC Programme: towards a staged e^+e^- Linear Collider exploring the Terascale, CLIC Conceptual Design Report. arXiv:1209.2543 [physics.ins-det], 2012.

[46] M. Aicheler et al. A Multi-TeV Linear Collider Based on CLIC Technology: CLIC Conceptual Design Report, 2012. `http://project-clic-cdr.web.cern.ch/project-clic-cdr/CDR_Volume1.pdf`.

[47] T. Abe et al. The International Large Detector: Letter of Intent. 2010. arXiv: 1006.3396 [hep-ex].

[48] H. Aihara et al. SiD Letter of Intent. arXiv: 0911.0006 [physics.ins-det], 2009.

[49] M. A. Thomson. Particle Flow Calorimetry and the PandoraPFA Algorithm. *Nucl. Instrum. Meth. A*, 611(1):25 – 40, 2009.

[50] I.G. Knowles and G.D. Lafferty. Hadronization in Z^0 decay. *J. Phys.*, G23:731–789, 1997.

[51] M. G. Green et al. *Electron - positron physics at the Z*. IoP Publishing, 1997.

[52] A. Gasanov et al. *Sov. J. Microelectron.*, 18:88, 1989.

[53] J. Ninković. Silicon Photomultiplier: a new device for frontier detectors. Conference talk, MAGIC Collab. Meeting Munich, 2008.

[54] A.N. Otte. *Observation of VHE γ–Rays from the Vicinity of magnetized Neutron Stars and Development of new Photon-Detectors for Future Ground based γ–Ray Detectors*. PhD thesis, Technische Universität München, 2007.

[55] S. Cova et al. Avalanche photodiodes and quenching circuits for single-photon detection. *Applied Optics*, 35(12):1956–1976, 1996.

[56] C. Jendrysik. Performance studies of Silicon Photomultipliers with quench resistors integrated to silicon bulk. Conference talk, PhotoDet. 2012. `http://indico.cern.ch/contributionDisplay.py?contribId=3&confId=164917`.

[57] B. P. Tyagi and K. Sen. Grain Size and Temperature Dependence of the Electrical Behaviour of Polysilicon. *Physica Status Solidi A*, 85(2):603–608, 1984.

[58] P. Buzhan et al. An advanced study of silicon photomultiplier. *ICFA Instrum. Bull.*, 23:28–41, 2001.

[59] J. Ninković et al. The first measurements on SiPMs with bulk integrated quench resistors. *Nucl. Instum. and Meth. A*, 628:407 – 410, 2011.

[60] J. Ninković et al. SiMPl - Novel high QE photosensor. *Nucl. Instum. and Meth. A*, 610:142 – 144, 2009.

[61] G.Q. Zhang et al. Demonstration of a silicon photomultiplier with bulk integrated quenching resistors on epitaxial silicon. *Nucl. Instrum. and Meth. A*, 621:116–120, 2010.

[62] J. Ninković et al. SiMPl - An avalanche diode array with bulk integrated quench resistors for single photon detection. *Nucl. Instrum. and Meth.*, A617:407 – 410, 2010.

[63] N. Feege. Silicon Photomultipliers: Properties and Applications in Highly Granular Calorimeter. Master's thesis, Universität Hamburg, 2008.

[64] R. J. McIntyre. The distribution of gains in uniformly multiplying avalanche photodiodes: Theory. *IEEE Transactions on Electron Devices*, 19(6):703–713, 1972.

[65] W. G. Oldham et al. Triggering Phenomena in Avalanche Diodes. *IEEE Transactions on Electron Devices*, 19(9):1056 – 1060, 1972.

[66] Multi Pixel Photon Counter (series S10362), Data sheet, 2010.

[67] E. Garutti. Silicon photomultipliers for high energy physics detectors. *JINST.*, 6(10):C10003, 2011.

[68] P. Eckert et al. Characterisation Studies of Silicon Photomultipliers. *Nucl. Instrum. Meth.*, A620:217–226, 2010.

[69] W. R. Leo. *Techniques for nuclear and particle physics experiments: A how to approach*. Springer, 2nd edition, 1994.

[70] R. Newman. Visible light from a silicon p-n junction. *Phys. Rev.*, 100:700 – 703, 1955.

[71] A. G. Chynoweth and K. G. McKay. Photon emission from avalanche breakdown in silicon. *Phys. Rev.*, 102:396 – 376, 1956.

[72] R. Mirzoyan et al. Light emission in Si avalanches. *Nucl. Instrum. and Meth. A*, 610:98 – 100, 2009.

[73] A. Mathewson et al. Photodetectors and Power Meters, SPIE proc. 2022, 132, 1993.

[74] M. Tesař. Vertex detectors for heavy flavor physics. Master's thesis, Czech Technical University in Prague, 2010.

[75] S. Uozumi. Study and Development of Multi Pixel Photon Counter for the GLD Calorimeter Readout. PoS (PD07) 022, 2007.

[76] D. Renker. Geiger-mode avalanche photodiodes, history, properties and problems. *Nucl. Instrum. Meth.*, A 567:48–56, 2006.

[77] D. Renker and E. Lorenz. Advances in solid state photon detectors. *JINST*, 4:P04004, 2009.

[78] F. Simon. Measurements of the Time Structure of Hadronic Showers in a Scintillator-Tungsten HCAL. 2011. arXiv: 1109.3143 [physics.ins-det].

[79] Hamamatsu Corporation. Emission microscope PHEMOS-1000, 2013. `http://www.hamamatsu.com/eu/en/PHEMOS-1000.html`.

[80] M. Tesař. *Setup for SiPM Detection Efficiency Measurement, User Manual*, 2012. `https://www.mpp.mpg.de/~tesar/SiPM_scan_setup_manual.pdf`.

[81] National instruments labview. `http://www.ni.com/labview`.

[82] WU-8-56SEC, red LED.
http://www.produktinfo.conrad.com/datenblaetter/175000-199999/186597-da-01-en-ALINGAP_LED_ROT_5MM.pdf.

[83] Nichia Corporation. NSPG500S, blue LED.
http://pdf1.alldatasheet.com/datasheet-pdf/view/240288/NICHIA/NSPG500S.html.

[84] Nichia Corporation. NSPB500S, blue LED.
http://pdf1.alldatasheet.com/datasheet-pdf/view/240264/NICHIA/NSPB500S.html.

[85] J. Zálesák. Calibration System with Optical Fibers for Calorimeters at Future Linear Collider Experiments. arXiv: 1201.5762 [physics.ins-det], 2012.

[86] Jelena Ninković. Private communication, 2011.

[87] S. Soldner. *The Time Development of Hadronic Showers and the T3B Experiment*. PhD thesis, Ludwig-Maximilians-Universität München, 2013.

[88] Saint-Gobain Crystals. *BC-418, BC-420, BC-422 Premium Plastic Scintillators, Data Sheet*, 2008.
http://www.detectors.saint-gobain.com/uploadedFiles/SGdetectors/Documents/Product_Data_Sheets/BC418-420-422-Data-Sheet.pdf.

[89] Say Polymers. *Polystyrol 143 E, Data sheet*, 2005.
http://www.saypolymers.com/Products/PS/PS_Basf_%20Polystyrol_143E.pdf.

[90] Amcrys-H. Plastic scintillators.
http://www.amcrys-h.com/plastics.htm.

[91] M. Groll. *Construction and commissioning of a hadronic test-beam calorimeter to validate the particle-flow concept at the ILC*. PhD thesis, Universität Hamburg, 2007.

[92] C. Adloff et al. Construction and Commissioning of the CALICE Analog Hadron Calorimeter Prototype. *JINST*, 5:P05004, 2010.

[93] M. Danilov. Tile and SiPM studies at ITEP. Conference talk, CALICE electronics and DAQ and AHCAL main meeting. 2012.

[94] S. Soldner. Scintillator Tile Uniformity Studies for a Highly Granular Hadron Calorimeter. Master's thesis, Ludwig-Maximilians-Universität München, 2009.

[95] PicoTech homepage.
http://www.picotech.com.

[96] Nuclitec GmbH. Source catalog.
http://www.dtechnology.com.hk/media/pdf/sourcecat_nuclitec.pdf.

[97] F. L. Wilson. Fermi's Theory of Beta Decay. *Am. J. of Phys.*, 36(12), 1968.

[98] Sven Menke. Private communication, 2013.

[99] Gafchromic EBT2 Self-Developing Film for Radiotherapy and Dosimetry. 2009. `http://online1.ispcorp.com/_layouts/Gafchromic/content/products/ebt2/pdfs/GAFCHROMICEBT2TechnicalBrief-Rev1.pdf`.

[100] F. Simon. Edge Non-Uniformities in ^{90}Sr Tile Scans. In *AHCAL Main Meeting*, 2011. `http://agenda.linearcollider.org/getFile.py/access?contribId=2&sessionId=4&resId=0&materialId=0&confId=5418`.

[101] J. H. Hubbell and S. M. Seltzer. Tables of X-Ray Mass Attenuation Coefficients and Mass Energy-Absorption Coefficients from 1 keV to 20 MeV for Elements Z = 1 to 92 and 48 Additional Substances of Dosimetric Interest, 1996. `http://www.nist.gov/pml/data/xraycoef/index.cfm`.

[102] S. Croft. The Use of Neutron Intensity Calibrated ^{9}Be(α,n) Sources as 4438 keV Gamma-Ray Reference Standards. *Nucl. Instum. and Meth.*, A281:103–116, 1989.

[103] Z. Liu et al. The 4.438 MeV gamma to neutron ratio for the Am–Be neutron source. *Appl. Radiat. and Isot.*, (12):1318 – 1321.

[104] International Standard ISO/DIS 8529-1, 2000.

[105] GEANT4 homepage. `http://www.geant4.org/geant4`.

[106] Frank Simon. Private communication, 2013.

[107] F. Simon and the CALICE Collaboration. Studies of Scintillator Tiles with SiPM Readout for Imaging Calorimeters. *J. of Phys.: Conf. Ser.*, 293(1):012074, 2011.

[108] E. T. Jurney et al. Gamma-Ray Spectrum from ^{204}Pb(n,γ)^{205}Pb. *Nucl. Phys. A*, 94:351–365, 1967.

[109] J. B. Birks. Scintillations from Organic Crystals: Specific Fluorescence and Relative Response to Different Radiations. *Proceedings of the Physical Society A*, 64:874–877, 1951.

[110] R. Y. Peters. Top Quark Mass Measurements at the Tevatron. 2013. arXiv: 1309.5783 [hep-ex].

[111] C. Battilana. Top quark Physics at the LHC. arXiv: 1309.5307 [hep-ex], 2013.

[112] K. Seidel. *Top Quark Pair Production and Calorimeter Energy Resolution Studies at a Future Collider Experiment*. PhD thesis, Ludwig–Maximilians–Universität München, 2012.

[113] K. Seidel et al. Top Quark Production at a 500 GeV CLIC Collider. LCD-Note-2011-026, 2012.

[114] Review of Particle Physics Booklet, 2012.
`http://pdg.lbl.gov/2012/download/rpp-2012-booklet.pdf`.

[115] WHIZARD homepage.
`http://whizard.hepforge.org`.

[116] PYTHIA homepage.
`http://home.thep.lu.se/~torbjorn/Pythia.html`.

[117] Mokka homepage.
`http://polzope.in2p3.fr:8081/MOKKA`.

[118] S. D. Ellis and D. E. Soper. Successive combination jet algorithm for hadron collisions. *Phys. Rev. D*, 48:3160–3166, Oct 1993.

[119] S. Kistryn et al. Evidence of the Coulomb-force effects in the cross-sections of the deuteron-proton breakup at 130 MeV. *Phys. Lett. B*, 641(1):23 – 27, 2006.

[120] M. Cacciari et al. FastJet User Manual. *Eur. Phys. J.*, C72:1896, 2012.

[121] D. Bailey et al. The LCFIVertex package: Vertexing, flavour tagging and vertex charge reconstruction with an ILC vertex detector. *Nucl. Instrum. Meth. A*, 610(2):573 – 589, 2009.

[122] K. Ackerstaff et al. Search for the Standard Model Higgs boson in e^+e^- collisions at $\sqrt{s}$ = 161–172 GeV. *Eur. Phys. J. C*, 1(3):425–438, 1998.

[123] Katja Seidel. Private communication, 2012.

[124] Thomas Teubner. Private communication, 2012.

[125] M. Skrzypek and S. Jadach. Exact and approximate solutions for electron nonsinglet structure function in QED. *Z. Phys. C*, 49:577–584, 1991.

[126] D. R. Yennie et al. The infrared divergence phenomena and high-energy processes. *Annals Phys.*, 13:379–452, 1961.

[127] L.N. Lipatov. The parton model and perturbation theory. *Yad. Fiz.*, 20:181, 1974.

[128] ROOT homepage.
`http://root.cern.ch`.

[129] The ATLAS and CMS Collaborations. ATLAS-CONF-2012-095, CMS-PAS-TOP-12-001, 2012.

LIST OF FIGURES

LIST OF TABLES